

REPORT DOCUMENTATION PAGE

AFRL-SR-BL-TR-02-

0037

Public Reporting burden for this collection of information is estimated to average 1 hour per response, including the time gathering and maintaining the data needed, and completing and reviewing the collection of information. Send comments of information, including suggestions for reducing this burden, to Washington Headquarters Services, Directorate for Information Operations and Reports, 1204 Army Pentagon, Arlington, VA 22202-4302, and to the Office of Management and Budget, Paperwork Reduction Project (O

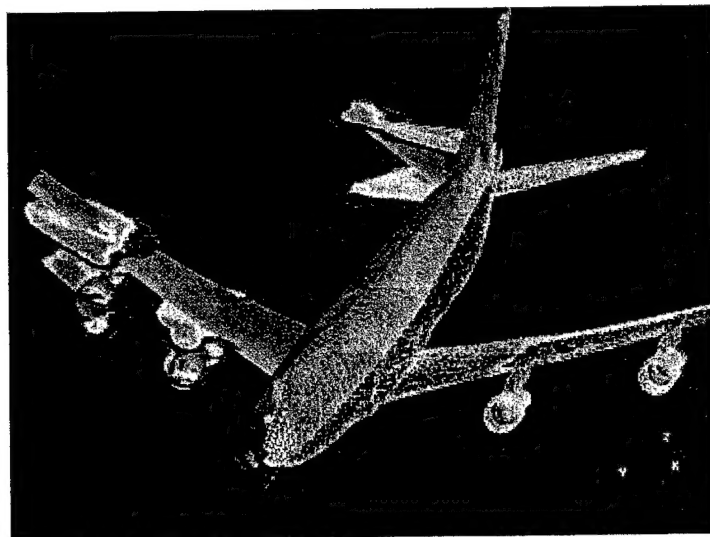
1. AGENCY USE ONLY (Leave Blank)				2. REPORT DATE November 2001		3. REPORT TYPE AND DATES COVERED Final Report for 4/1/98 - 3/31/01	
4. TITLE AND SUBTITLE Predicting the Nonlinear Response of Aerospace Structures Using Aeroelastic NS Solutions on Deforming Meshes				5. FUNDING NUMBERS F49620-98-1-0396			
6. AUTHOR(S) R. Panneer Selvam ZU-Qing QU Qun Zheng Uday K. Roy							
7. PERFORMING ORGANIZATION NAME(S) AND ADDRESS(ES) Computational Mechanics Laboratory Department of Civil Engineering, University of Arkansas Fayetteville, AR 72701				8. PERFORMING ORGANIZATION REPORT NUMBER			
9. SPONSORING / MONITORING AGENCY NAME(S) AND ADDRESS(ES) AFOSR/NM 110 Duncan Avenue, Suite B115 Bolling AFB DC 20332-8050				10. SPONSORING / MONITORING AGENCY REPORT NUMBER			
11. SUPPLEMENTARY NOTES The views, opinions and/or findings contained in this report are those of the author(s) and should not be construed as an official Department of the Army position, policy or decision, unless so designated by other documentation.							
12 a. DISTRIBUTION / AVAILABILITY STATEMENT Approved for public release; distribution unlimited.				AIR FORCE OFFICE OF SCIENTIFIC RESEARCH (AFOSR) NOTICE OF TRANSMITTAL DTIC. THIS TECHNICAL REPORT HAS BEEN REVIEWED AND IS APPROVED FOR PUBLIC RELEASE UARF 100-12. DISTRIBUTION IS UNLIMITED.			
13. ABSTRACT (Maximum 200 words) <p>With the resurgent interest in flight vehicles such as the High-Speed Civil Transport (HSCT), the X-33 Advanced Technology Demonstrator, the Reusable Launch Vehicle (RLV), the Joint Strike Fighter (JSF) and the X-38 Spacecraft using a lifting-body concept that will operate at supersonic/hypersonic Mach numbers, the need for panel flutter analysis has received broad acknowledgement. The linear and nonlinear analysis of the panel flutter has been studied extensive during the past two decades. However, most of the researches on this area are concentrated on the structural side, i.e., panel or plate. In these researches, the approximate theories, such as quasi-steady piston theory, full linearized (inviscid) potential flow theory, etc., are used to estimate the aerodynamic pressure. This kind of linear aerodynamics may not be adequate to predict the dynamic characteristics of the fluid and structure because the fluid flow is strongly nonlinear at the transonic and supersonic speeds. As we know, the high-fidelity equations, such as Euler or Navier-Stokes equations, can predict the flow characteristics more accurately. One of the important reasons that the high-fidelity equations have not been used to predict the aerodynamic loads is that the corresponding numerical simulation is very computationally expensive. With the fast development of the computer techniques, the full analysis of the nonlinear panel flutter coupled with the Euler or Navier-Stokes flow equations becomes possible.</p>							
14. SUBJECT TERMS Nonlinear Aeroelastic Deforming Meshes				15. NUMBER OF PAGES 173		16. PRICE CODE	
17. SECURITY CLASSIFICATION OR REPORT UNCLASSIFIED				18. SECURITY CLASSIFICATION ON THIS PAGE UNCLASSIFIED		19. SECURITY CLASSIFICATION OF ABSTRACT UNCLASSIFIED	
20. LIMITATION OF ABSTRACT UL							

**PREDICTING THE NONLINEAR RESPONSE OF
AEROSPACE STRUCTURES USING AEROELASTIC
NS SOLUTIONS ON DEFORMING MESHES**

(Final Report for 04/01/98-03/31/01, DOD/EPSCOR)

(Grant No.: F49620-98-1-0396)

(November 2001)



R. PANNEER SELVAM

ZU-QING QU

Qun Zheng

Uday K. Roy

Computational Mechanics Laboratory

Department of Civil Engineering

University of Arkansas at Fayetteville

Content

Preface	iii
0 Introduction	1
0.1 Importance of Current Panel Flutter Analysis	1
0.2 Description of Current Panel Flutter Analysis	2
0.3 Organization of this Report	3
References	5

PART I: COMPUTATIONAL STRUCTURAL DYNAMICS

1 Nonlinear Plate Analysis Using Total Lagrangian Formulations	7
1.1 Introduction	7
1.2 Finite Element Formulation of Large Deflection Plates	9
1.3 DKT Triangular Element	13
1.4 Static Nonlinear Problems of Large Deflection	16
1.5 Dynamic Nonlinear Problems of Large Deflection	20
1.6 Non-Dimensional Form of FEM Formulations	23
1.7 Summary	28
References	28
2 Nonlinear Plate Analysis Using Co-Rotational Formulations	37
2.1 Introduction	37
2.2 Nonlinear Static Analysis of Plates	38
2.3 Nonlinear Dynamic Analysis of Plates	46
2.4 Summary	52
2.5 Appendix	53
References	63

PART II: COMPUTATIONAL FLUID DYNAMICS

3 Moving Grid and Deforming Mesh	65
3.1 Introduction	65
3.2 Description and Evaluation of Different Algorithms	66
3.3 Theory of the Deforming Mesh	78
3.4 Numerical Simulations	82
3.5 Summary	82
References	83
4 Computations of Navier-Stokes Equations Using Finite Volume Method	97
4.1 Introduction	97
4.2 Governing Equations	97
4.3 Numerical Procedures	102
4.4 Boundary Conditions Implementation	109
4.5 Computational Results and Discussions	111
References	112
PART III: FLUID - STRUCTURE INTERACTION	
5 Three Dimensional Aeroelastic Solver for Nonlinear Panel Flutter	121
5.1 Nomenclature	121
5.2 Introduction	123
5.3 Aerodynamic Theories	125
5.4 Governing Equations of Thin Plate	131
5.5 Numerical Procedure	133
5.6 Results and Discussions	138
5.7 Summary	162
References	163
Conclusions	167

Preface

Panel flutter, an aeroelastic stability structural problem, has been a research topic for more than three decades. When a flight vehicle flies at a supersonic speed in the air, some skin panels may experience high level vibrations and fail due to the aerodynamic pressure on the vehicle surface. This aeroelastically induced, self-excited motion has been described as panel flutter. In the early stage of this research, before 1960s, it was usually assumed that the phenomena could be adequately understood in terms of linear models and inviscid aerodynamics and that the questions of self-excited stability and response to external disturbances could be readily separated. Later, from the late of 1960s and early 1970s, it has been found that these assumptions are invalidated most frequently for the aeroelastic behavior of plates and shells. Great progress has been made in understanding the effects of nonlinearities, viscous flow, and complex relation between the stability and response since then. Most recently, the smart material and structural technique has been implemented into this area to suppress the flutter of panels.

However, most of the researches on this area are concentrated on the structural side, i.e., panel or plate. In these researches, the approximate theories, such as quasi-steady piston theory, full linearized (inviscid) potential flow theory, etc., are used to estimate the aerodynamic pressure. This kind of linear aerodynamics may not be adequate to predict the dynamic characteristics of the fluid and structure because the fluid flow is strongly nonlinear at the transonic and supersonic speeds. As we know, the high-fidelity equations, such as Euler or Navier-Stokes equations, can predict the flow characteristics more accurately. One of the important reasons that the high-fidelity equations have not been used to predict the aerodynamic loads is that the corresponding numerical simulation is very computational expensive. With the fast development of the computer techniques, the full analysis of the nonlinear panel flutter coupled with the Euler or Navier-Stokes flow equations becomes possible.

The Air Force Office of Scientific Research (AFOSR), Department of Defense (DOD), sponsored a grant (F49620-98-1-0396) through the University of Arkansas at Fayetteville during the period of April 1st 1998 and March 31st 2001. The development of an aeroelastic solver which combined the Computational Structural Dynamics (CSD) and the Computational Fluid Dynamic (CFD) was required in this grant. Such a code is able to predict the change in shape or position of a structure due to a calculated fluid pressure exerted on it, and able to model the flow of fluid around the structure. As

required, the aeroelastic solver has been developed. Some important and useful results have been proposed.

This report sets out to explain the principles used in the aeroelastic solver. In the structural side, two formulations, total Lagrangian and co-rotational formulations, for the nonlinear analysis of the thin plate are discussed in detail. In the fluid side, the finite volume method has been used to solve the Euler and Navier-Stokes equations. To accurately model the problems with moving and deforming boundaries, the deforming mesh schemes are provided and discussed to make the fluid grid conform to the changing shape of the boundary. The numerical simulation of the aeroelastic solver is provided using a specific panel. Several issues of the panel flutter are surveyed at the end of this report.

We would like to express our special thanks to the AFOSR, DOD, for their sponsorship of this research. Thanks also go out to Dr. R. E. Gordnier and Dr. M. R. Visbal at the Air Force Research Laboratory for their help during the research. We also would like to record our appreciation of many helpful information and comments made by the graduate students, Jerry Scott R. Prescott, Yangki Jung, Douglas Benton, in this laboratory. Finally, our wives and children are certainly not to be omitted from our acknowledgement.

R. Panneer Selvam Zu-Qing Qu

Fayetteville, Arkansas, USA

November 2001

CHAPTER 0

INTRODUCTION

- 0.1 Importance of Current Panel Flutter Analysis
 - 0.2 Description of Current Panel Flutter Analysis
 - 0.3 Organization of this Report
-

0.1 Importance of Current Panel Flutter Analysis

With the resurgent interest in flight vehicles such as the High-Speed Civil Transport (HSCT), the X-33 Advanced Technology Demonstrator, the Reusable Launch Vehicle (RLV), the Joint Strike Fighter (JSF) and the X-38 Spacecraft using a lifting-body concept that will operate at supersonic/hypersonic Mach numbers, the need for panel flutter analysis has received broad acknowledgement¹.

The linear and nonlinear analysis of the panel flutter has been studied extensive during the past two decades¹⁻⁶. However, most of the researches on this area are concentrated on the structural side, i.e., panel or plate. In these researches, the approximate theories, such as quasi-steady piston theory^{7,8}, full linearized (inviscid) potential flow theory^{9,10}, etc., are used to estimate the aerodynamic pressure. This kind of linear aerodynamics may not be adequate to predict the dynamic characteristics of the fluid and structure because the fluid flow is strongly nonlinear at the transonic and supersonic speeds. As we know, the high-fidelity equations, such as Euler or Navier-Stokes equations, can predict the flow characteristics more accurately. One of the important reasons that the high-fidelity equations have not been used to predict the aerodynamic loads is that the corresponding numerical simulation is very computationally expensive. With the fast development of the computer techniques, the full analysis of the nonlinear panel flutter coupled with the Euler or Navier-Stokes flow equations becomes possible.

0.2 Description of Current Panel Flutter Analysis

Panel flutter in the supersonic flow falls in the category of self-excited or self-sustained oscillations. Historically, flutter and other problems involving a fluid and a structure were predicted using wind tunnels. This type of testing required building small test models, which are expensive and time consuming. In addition to physical models being costly, testing facilities such as wind tunnels capable of producing air speed beyond the speed of sound are very rare. However, within the past couple of decades, advances in computer technology has greatly lowered the time and cost of design by enabling us to model complex engineering problems on computer rather than building costly physical test models. Through computer modeling it is possible for engineers to predict the motion of complex shapes in a fluid field and correct failures and other problems of a design before the first prototype is built.

The aerospace industry was among the first to use and further develop computer modeling to predict all types of phenomenon, several of these are dynamic loads, moments, fluid pressures, shock waves, and turbulence. Initially, computer modeling of aircraft was separated into two fields, Computational Structural Dynamics (CSD) and Computational Fluid Dynamics (CFD). In CSD a structure is analyzed by assuming a fluid pressure for a given air speed as the structural load. Then apply it to the structure to obtain the displacements and stress. For CFD the flow of fluid is analyzed around an immobile, infinitely stiff structure.

As technology progressed to produce faster aircraft so did the need to understand the nature of fluid and its interaction with a structure and more importantly to predict it. Highly maneuverable aircraft such as fighters can experience very complex fluid flow such as vortices, flow separation, shock waves, flutter, and other high speed, nonlinear flow phenomenon.

Such problems create the need to combine CFD and CSD. The unity of these two programs is known as an aeroelastic code. Such a code is able to predict the change in shape or position of a structure due to a calculated fluid pressure exerted on it, and able to model the flow of fluid around the structure. However, neither CFD nor CSD has been perfected to give exact, computationally efficient results. Any errors produced in the structural calculations are carried over to the fluid calculations and vice versa via the fluid structure interaction.

Fluid structure interaction is the exchange of information or data from one medium to the other. This takes place where the boundary of the fluid meets the boundary of the structure. The computational result of one medium becomes the initial boundary conditions of the other. In a physical problem the effect of one particle of fluid on a structure will change the motion of the structure and the

fluid will react to that change. In nature this process happens almost instantaneously. To accurately model this behavior the equations of motion for the fluid, structure, and the fluid-structure interaction have to be solved simultaneously. An integrate algorithm in which the fluid and structure are modeled as a single dynamic system¹¹ may satisfy this requirement. This, however, requires the development of an entirely new solver. One commonly used scheme is that the effects of one medium on the other is delayed or lagged in time and the results of one medium can be used to calculate the results of the other. The amount of lag or time step size affects the accuracy of the results. To reduce this error the Newton-type subiteration¹² may be used.

Another obstacle to be overcome in the fluid-structure interaction is the coordinate system that describes the motion of a fluid or a structure (The computational grid of the fluid or the structure represents the coordinate system). There are two types of coordinate systems, the Euler and the Lagrangian. Generally, the motion of a fluid is described by the Euler coordinate system, where the coordinate system does not move with the material particles in time. The motion of a structure is described by the Lagrangian coordinate system, where the coordinate system moves with the material particles in time. When dealing with a structure that is moving within a fluid, the fluid grid must be updated at each time step to conform to the new position of the structure. To solve this issue two things must be taken into account, how to modify the fluid equations to allow for movement and still get accurate results and, how to create a grid to conform to the new shape of the structure.

Small amplitude linear structural theory indicates that there is a critical dynamic pressure above which the panel motion becomes unstable and grows exponentially with time. In reality, however, geometrically nonlinear effect is present due to vibration with large amplitudes. The panel not only bends but also stretches with in-plane tensile stresses. Such in-plane tensile stresses provide a stabilizing effect that restrains the panel motion to bound limit cycle oscillations with increasing amplitude as the dynamic pressure increases. The skin panels of the flight vehicle can thus withstand velocities beyond those predicted based on the small amplitude linear structural theory. For a more thorough understanding and more realistic assessment of the panel flutter problems, the geometrically nonlinear effect due to the large amplitude oscillations should be considered.

0.3 Organization of this Report

Geometric nonlinearity is increasingly being considered in structural analysis, especially for those structures that undergo large displacement with very little actual staining occurring. There are many

works on the way in which the geometrically non-linear problems may be formulated. Three main methods have been currently employed, namely, the Total Lagrangian (TL) formulation, the Updated Lagrangian (UL) formulation and the Co-Rotational (CR) formulation. Each of these formulation has its inherent drawbacks, merits and advocates. The details of the pros and cons of the formulations were surveyed using a cantilever beam in our laboratory¹³. Due to the slow convergence of the UL formulation, the TL and CR formulations will be discussed in this report.

The large deflection of thin plates, which considers the coupling effect between the flexure and the in-plane deformation, is investigated in Chapter 1 by using the finite element method. The TL formulation in which the original undeformed configuration is taken as the reference configuration is to be used. Based on the von-Karman nonlinear strain-displacement relation, the dynamic equations of large deflection plates are derived at first. The formulation of Discrete Kirchhoff Theory (DKT) for triangular elements is then presented for the discretization of the thin plate. An iterative method between the equations of the flexure and membrane is used to solve the nonlinear equations at each time step. To make the method efficient, a relaxation factor was also used. The Newmark- β method is used to approximate in time. Several numerical examples are also included in this chapter to demonstrate the efficiency of the method for nonlinear dynamic problems.

The CR formulation makes use of both the original configuration and the current deformed configuration to formulate the system matrices. Although restricted to small rotation between iterations, it exhibits good rate of convergence and, thereby, reduces the computation time. In Chapter 2, CR formulation for static and dynamic analysis of plate structures using DKT triangular elements is presented. A number of numerical examples are presented to fully test the capabilities of this formulation. The CR formulation code developed in this study can be used for more understanding and realistic assessment of the panel flutter problems.

As mentioned above, the fluid equations are usually derived using the Eulerian motion description and the structural equations derived using the Lagrangian description. To accurately model problems with moving and deforming boundaries requires that the fluid grid conform to the changing shape of the boundary. To accommodate the movement of the fluid grid either a new grid must be generated at each time step (dynamic regridding) or the differential equations for the fluid must be modified to allow the movement of the existing fluid grid (ALE, Corotational, Space-Time). Once a method is found for modifying the fluid equations to allow for grid movement a method must be chosen to move or update the fluid grid to the new position of the structure. In Chapter 3, different methods used to modify the fluid equations to allow the movement of a structure within the fluid domain are described. For the ALE method, various methods used to update or move the fluid grid to conform to a changing

structural boundary are also described and evaluated. The details of the implementation of the Trans-Finite Interpolation scheme for the deforming mesh is provided in this chapter. Numerical simulation is also included to show the features of this scheme.

In the fluid side of the fluid-structure interaction, the fluid dynamic computation must have the fidelity to capture the relevant flow features and provide accurate aerodynamic loads on the structure in developing a perfect fluid-structure interaction solver in computational aeroelasticity. A finite volume method is used in Chapter 4 to establish computational solvers for Euler equation and Navier-Stokes equation.

A numerical simulation of the three-dimensional nonlinear panel flutter at supersonic flow is performed using the high-fidelity flow equations - Euler equations in Chapter 5. These flow equations are solved using the Beam-Warming, alternate-direction, implicit scheme. The governing equations of the thin panel are based on the von-Karman large deflection plate theory. Since the finite difference method is much more efficient than the finite element method for a simple structure, the former is used to discretize these governing equations in space and Newmark- β integration scheme is applied to solve them in time domain. The Newton-like subiteration is implemented to eliminate the lagging errors associated with the exchange of the pressure and deformations between the fluid and panel at their interface. A simply supported square panel is considered at this time. The results at the supersonic flow are compared with those from the aerodynamic approximations, such as potential flow theory and quasi-steady supersonic theory. The flutter frequency and the effects of the panel thickness are also discussed in this chapter.

Reference:

¹Mei, C., Abdel-Motagaly, K., and Chen, R., "Review of Nonlinear Panel Flutter at Supersonic and Hypersonic Speeds," *Applied Mechanics Review*, Vol.52, No.10, 1999, pp.321-332.

²Dowell, E. H., *Aerodynamic of Plates and Shells*, Noordhoff International Publishing, Leyden, Netherlands, 1975.

³Dowell, E. H., "Panel Flutter: A Review of the Aeroelastic Stability of Plates and Shells," *AIAA Journal*, Vol.8, No.3, 1970, pp.385-399.

⁴Yang, T. Y., and Sung, S.H., "Finite Element Panel Flutter under Three Dimensional Supersonic Unsteady Potential Flow," *AIAA Journal*, Vol.15, No.12, 1977, pp.1677-1683.

⁵Bismarck-Nasr, M. N., "Finite Element Analysis of Aeroelasticity of Plates and Shells," *Applied Mechanics Reviews*, Vol.45, No.12, Part 1, 1992, pp.461-482.

⁶Bismarck-Nasr, M. N., "Finite Elements in Aeroelasticity of Plates and Shells," *Applied Mechanics Reviews*, Vol.49, No.10, Part 2, 1996, pp.s17-s24.

⁷Ashley, H., and Zartarian, G., "Piston Theory – a New Aerodynamic Tool for Aeroelastician," *Journal of Aeronautical Science*, Vol.23, No., 1956, pp.1109-1118.

⁸Dowell, E. H., "Nonlinear Oscillations of a Fluttering Plate," *AIAA Journal*, Vol.4, No.7, 1966, pp.1267-1275.

⁹Cunningham, H. J., "Flutter Analysis of Flat Rectangular Panels Based on Three Dimensional Supersonic Potential Flow," *AIAA Journal*, Vol.1, No.8, 1963, pp.1795-1801.

¹⁰Dowell, E. H., "Nonlinear Oscillations of a Fluttering Plate II," *AIAA Journal*, Vol.5, No.10, 1967, pp.1856-1862.

¹¹Bendiksen, O. O., and Davis, G. A., "Nonlinear Traveling Wave Flutter of Plates in Transonic Flow," 1995, AIAA Paper 95-1486.

¹²Selvam, R. P., Visbal, M. R., and Morton, S. A., "Computation of Nonlinear Viscous Panel Flutter Using a Fully Implicit Aeroelastic Solver," AIAA Paper 98-1844, April 1998.

¹³Jung, Y., Geometric Nonlinear Finite Element Analysis, Master Thesis, Department of Civil Engineering, the University of Arkansas, May 2000.

CHAPTER 1

NONLINEAR PLATE ANALYSIS USING TOTAL LAGRANGIAN FORMULATIONS

- 1.1 Introduction
 - 1.2 Finite Element Formulation of Large Deflection Plates
 - 1.3 DKT Triangular Element
 - 1.4 Static Nonlinear Problems of Large Deflection
 - 1.5 Dynamic Nonlinear Problems of Large Deflection
 - 1.6 Non-Dimensional Form of FEM Formulations
 - 1.7 Summary
-

1.1 Introduction

Panel flutter, an aeroelastic structural problem, has been a research topic for the past three decades and has recently received great interest ¹⁻⁴. When a vehicle flies at a supersonic speed in the air, some skin panels may experience high level vibrations and fail due to the aerodynamic pressure on the vehicle surface. This aeroelastically induced, self-excited motion has been described as panel flutter. Experiments showed that there are critical dynamic pressures in panel flutter. Below these critical pressures the panel has a random oscillation with small amplitude which is a small fraction of the panel thickness. The predominant frequency components are observed to be near the lower panel natural frequencies. Basically, the panel is undergoing a linear oscillation. These critical dynamic pressures are also called the flutter boundary. Beyond this boundary, the amplitude of the panel oscillation grows rapidly to the order of the panel thickness. For this case, the responses predicted using the small deflection linear theory are no longer applicable, and, therefore, nonlinear theory taking account the effects of large amplitude should be applied.

The analytical solution of the vibrations of large deflection thin plates was surveyed by many researchers more than 20 years ago. Most of the studies, however, have been concerned with circular

or rectangular plates due to the difficulty of the mathematical treatment. With the increased use of the plate in many optimum- or minimum-weight designed built-up structures, many numerical methods, such as finite difference method⁵, the finite element method⁶⁻⁸, finite strips method^{9,10}, finite element – transfer matrix method¹¹ and so on, were used to discretize the plates in physical space.

The nine-parameter bending plate element is a simple element that is widely used in engineering. Many such triangular elements have been developed. They include the element BCIZ¹², discrete Kirchhoff element DKT¹³, natural formulation element TRUNC¹⁴, free formulation element T_{3A}¹⁵, hybrid stress element HSM^{16,17}, etc. Recently, a set of three good triangular elements¹⁸ and a refined direct stiffness method (RDSM)¹⁹ have been proposed.

The formulation of elements based on the discrete Kirchhoff theory for thin bending plates is obtained by considering a theory of plates including transverse shear deformation. In this case, the independent quantities are the deflection and rotations and only C⁰ continuity requirements need to be satisfied. The transverse shear energy is neglected altogether and the Kirchhoff hypothesis introduced in a discrete way along the edges of the element to relate the relations to the transverse displacements.

Batoz^{20,21} studied the DKT element and concluded that it is one of the efficient, cost effective and reliable elements of its class for static bending. The convergence properties of the DKT element do not deteriorate with an increase in the element aspect ratio and which is not so far for other elements. Ratoz²¹ also presented the stiffness matrix of the DKT element in explicitly form in local coordinate system. This means that the stiffness matrix is to be transformed to a global coordinate system before assembly. A simple algorithm was proposed by Jeyachandrabose and Kirkhope²² to directly obtain the stiffness matrix in the global coordinates. The relationship of a series of elements based on Reissner-Mindlin assumptions and using discrete (collocation type) constraints was discussed by Zienkiewicz and Taylor et al²³. Most recently many researchers^{24,25} have been trying to improve the accuracy and efficiency of the DKT triangular and rectangular elements.

In this report, the large deflection of thin plates, which considers the coupling effect between the flexure and the in-plane deformation, is investigated by using finite element method. Based on the von-Karman nonlinear strain-displacement relation and the DKT of triangular elements, the dynamic equations of large deflection plates are derived using the finite element method. The Newmark- β method is used to solve the dynamic equations of equilibrium in time domain. Several numerical examples are also included to demonstrate the efficiency of the method for nonlinear dynamic problems.

1.2 Finite Element Formulation of Large Deflection Plates

1.2.1 Assumptions

The following assumptions will be used during the derivation of the finite element formulation of the large deflection plates:

- Isotropic material obeys Hook's Law (small strain);
- Thin plate ($a/t > 20$), and $\sigma_z = 0$;
- Inplane inertia, rotatory inertia and transverse shear deformation effects are negligible;
- Von Karman large deflection strain-displacement relations are valid. The displacements are not infinitesimal (linear problem), but also not excessively large (change in geometry, very large deflection problem);
- Material is linear elastic, isotropic.

1.2.2 Displacement Functions

The finite element method assumes that the displacement solution is a node displacement vector \mathbf{W} . For a plate structure, the displacement vector consists of flexure and membrane displacement vectors \mathbf{W}_f and \mathbf{W}_m , i.e.

$$\mathbf{W} = \begin{Bmatrix} \mathbf{W}_f \\ \mathbf{W}_m \end{Bmatrix} \quad (1-1)$$

Relatively, the element displacement vector can be expressed as

$$\mathbf{w} = \begin{Bmatrix} \mathbf{w}_f \\ \mathbf{w}_m \end{Bmatrix} \quad (1-2)$$

The displacements at any point on the element could be expressed in terms of element nodal displacements as

$$\mathbf{w} = \mathbf{C}_w \mathbf{w}_f \quad (1-3-a)$$

$$\mathbf{u} = \mathbf{C}_u \mathbf{w}_m \quad (1-3-b)$$

$$\mathbf{v} = \mathbf{C}_v \mathbf{w}_m \quad (1-3-c)$$

where, the \mathbf{C}_w , and \mathbf{C}_u and \mathbf{C}_v are the row vectors of interpolation functions.

1.2.3 Nonlinear Strain-Displacement Relation (von Karman)

Considering small inplane strain and large lateral displacement, the total strain vector is given by

$$\boldsymbol{e} = \boldsymbol{e}_m + \boldsymbol{e}_\theta \quad (1-4)$$

where the membrane strain vector \boldsymbol{e}_m consists of two parts:

$$\boldsymbol{e}_m = \boldsymbol{e}_m + \boldsymbol{e}_\theta \quad (1-5)$$

The linear membrane strain vector \boldsymbol{e}_m is related to the displacements as

$$\boldsymbol{e}_m = \begin{Bmatrix} u_{,x} \\ v_{,y} \\ u_{,y} + v_{,x} \end{Bmatrix} \quad (1-6)$$

Here a comma represents differentiation. The nonlinear stretching strain vector, \boldsymbol{e}_θ , induced from large lateral deflection by the von Karman strain-displacement relation is given as

$$\boldsymbol{e}_\theta = \begin{Bmatrix} \frac{1}{2} w_{,x}^2 \\ \frac{1}{2} w_{,y}^2 \\ w_{,x} w_{,y} \end{Bmatrix} \quad (1-7)$$

The vector of bending curvatures $\boldsymbol{\gamma}$ in equation (1-4) is expressed as

$$\boldsymbol{\gamma} = - \begin{Bmatrix} w_{,xx} \\ w_{,yy} \\ 2w_{,xy} \end{Bmatrix} \quad (1-8)$$

By using the finite element displacement functions, equation (1-3), the membrane strain and curvature vectors can be expressed in terms of the element nodal displacements. The linear membrane strains from equations (1-3-b), (1-3-c) and (1-6) are given by

$$\boldsymbol{e}_m = \begin{Bmatrix} \frac{\partial}{\partial x} \mathbf{C}_u \\ \frac{\partial}{\partial y} \mathbf{C}_v \\ \frac{\partial}{\partial y} \mathbf{C}_u + \frac{\partial}{\partial x} \mathbf{C}_v \end{Bmatrix} \quad \boldsymbol{w}_m = \mathbf{C}_m \boldsymbol{w}_m \quad (1-9)$$

The nonlinear membrane strains from equations (1-3-a) and (1-7) are expressed as

$$\mathbf{e}_\theta = \frac{1}{2} \begin{bmatrix} w_{,x} & 0 \\ 0 & w_{,y} \\ w_{,y} & w_{,x} \end{bmatrix} \begin{Bmatrix} w_{,x} \\ w_{,y} \end{Bmatrix} = \frac{1}{2} ?\theta = \frac{1}{2} ? \begin{Bmatrix} \frac{\partial}{\partial x} \mathbf{C}_w \\ \frac{\partial}{\partial y} \mathbf{C}_w \end{Bmatrix} \mathbf{w}_f = \frac{1}{2} ?\mathbf{C}_\theta \mathbf{w}_f \quad (1-10)$$

where the slope matrix and vector are given by

$$? = \begin{bmatrix} w_{,x} & 0 \\ 0 & w_{,y} \\ w_{,y} & w_{,x} \end{bmatrix}, \quad \theta = \begin{Bmatrix} w_{,x} \\ w_{,y} \end{Bmatrix} \quad (1-11)$$

and the curvatures from equations (1-3-a) and (1-8) are expressed as

$$? = \begin{bmatrix} -\frac{\partial^2}{\partial x^2} \mathbf{C}_w \\ -\frac{\partial^2}{\partial y^2} \mathbf{C}_w \\ -\frac{\partial^2}{\partial xy} \mathbf{C}_w \end{bmatrix} \mathbf{w}_f = \mathbf{C}_f \mathbf{w}_f \quad (1-12)$$

1.2.4 Relations of Stress and Strain

The general stress-strain relation for a plane stress ($\sigma_z = 0$) is given by

$$\mathbf{s} = \begin{Bmatrix} \sigma_x \\ \sigma_y \\ \tau_{xy} \end{Bmatrix} = \mathbf{E}\mathbf{e} \quad (1-13)$$

where the strain vector is given by equation (1-4) and the elastic coefficient matrix is

$$\mathbf{E} = \frac{E}{1-\nu^2} \begin{bmatrix} 1 & \nu & 0 \\ \nu & 1 & 0 \\ 0 & 0 & \frac{1-\nu}{2} \end{bmatrix} \quad (1-14)$$

The membrane or inplane force vector \mathbf{N} and moment vector \mathbf{M} are defined as

$$(\mathbf{N}, \mathbf{M}) = \int_{-h/2}^{h/2} (1, z) \mathbf{\sigma} dz = (\mathbf{A}\mathbf{e}, \mathbf{D}\mathbf{e}) \quad (1-15)$$

where \mathbf{A} and \mathbf{D} are symmetric matrix of material properties; h is the thickness of the plate. For an isotropic plate of uniform thickness, they are given by

$$\mathbf{A} = \frac{Eh}{1-\nu^2} \begin{bmatrix} 1 & \nu & 0 \\ \nu & 1 & 0 \\ 0 & 0 & \frac{1-\nu}{2} \end{bmatrix}, \quad \mathbf{D} = \frac{Eh^3}{12(1-\nu^2)} \begin{bmatrix} 1 & \nu & 0 \\ \nu & 1 & 0 \\ 0 & 0 & \frac{1-\nu}{2} \end{bmatrix} \quad (1-16)$$

1.2.5 Equations of Motion

According to the principle of virtual work, the total work done by internal and external forces (including inertia force) on an infinitesimal virtual displacement is zero, that is,

$$\delta W = \delta W_{\text{int}} - \delta W_{\text{ext}} = 0 \quad (1-17)$$

where, the internal and external work are given by

$$\delta W_{\text{int}} = \int_V \delta \mathbf{e}^T \mathbf{s} dV, \quad \delta W_{\text{ext}} = \int_V \delta \mathbf{w}^T \mathbf{f}_{\text{ext}} dV \quad (1-18)$$

Substituting all the corresponding equations into equations (1-17) and (1-18), the element equilibrium can be reached as (not including damping here)

$$\begin{bmatrix} \mathbf{m}_{ff} & 0 \\ 0 & \mathbf{m}_{mm} \end{bmatrix} \begin{bmatrix} \ddot{\mathbf{w}}_f \\ \ddot{\mathbf{w}}_m \end{bmatrix} + \begin{bmatrix} \mathbf{k}_{ff} & \mathbf{k}_{fm} \\ \mathbf{k}_{mf} & \mathbf{k}_{mm} \end{bmatrix} \begin{bmatrix} \mathbf{w}_f \\ \mathbf{w}_m \end{bmatrix} = \begin{bmatrix} \mathbf{f}_f \\ \mathbf{f}_m \end{bmatrix} \quad (1-19)$$

where \mathbf{m}_{ff} and \mathbf{m}_{mm} are the mass matrices of flexure and membrane, respectively. They are defined as

$$\mathbf{m}_{ff} = \rho_s h \int_s \mathbf{C}_w^T \mathbf{C}_w ds, \quad \mathbf{m}_{mm} = \rho_s h \int_s \mathbf{C}_{uv}^T \mathbf{C}_{uv} ds \quad (1-20)$$

and

$$\begin{aligned} \mathbf{k}_{fm} &= \mathbf{k}_{fm}^1 = \frac{1}{2} \int_s \mathbf{C}_\theta^T \mathbf{?}^T \mathbf{A} \mathbf{C}_m ds, \quad \mathbf{k}_{mf} = \mathbf{k}_{mf}^1 = \frac{1}{2} \int_s \mathbf{C}_m^T \mathbf{A} \mathbf{?} \mathbf{C}_\theta ds \\ \mathbf{k}_{ff} &= \mathbf{k}_{ff}^0 + \mathbf{k}_{ff}^1 + \mathbf{k}_{ff}^2 \end{aligned} \quad (1-21)$$

\mathbf{k}_{ff}^0 , \mathbf{k}_{ff}^1 and \mathbf{k}_{ff}^2 are the linear, the first order nonlinear and the second order nonlinear parts of the stiffness matrix. They are defined as

$$\mathbf{k}_{ff}^0 = \int_s \mathbf{C}_f^T \mathbf{D} \mathbf{C}_f ds, \quad \mathbf{k}_{ff}^1 = \frac{1}{2} \int_s \mathbf{C}_\theta^T \mathbf{N}_m \mathbf{C}_\theta ds, \quad \mathbf{k}_{ff}^2 = \frac{1}{2} \int_s \mathbf{C}_\theta^T \mathbf{?}^T \mathbf{A} \mathbf{?} \mathbf{C}_\theta ds \quad (1-22)$$

and mid-surface force matrix

$$\mathbf{N}_m = \begin{bmatrix} N_{mx} & N_{mxy} \\ N_{mxy} & N_{my} \end{bmatrix} \quad (1-23)$$

is constructed from^{1,26}

$$N_m = \begin{bmatrix} N_{mx} \\ N_{my} \\ N_{mxy} \end{bmatrix} = \mathbf{AC}_m w_m \quad (1-24)$$

The stiffness matrix pertaining to membrane is given by

$$\mathbf{k}_{mm} = \int_s \mathbf{C}_m^T \mathbf{A} \mathbf{C}_m ds \quad (1-25)$$

1.3 DKT Triangular Element

In the following, the DKT element shown in Figure 1.1 is adopted from Batoz et al²⁰, Jeyachandrabose et al²² and Xue²⁶ without modification. DKT element defines element shape functions due to slopes as²⁰

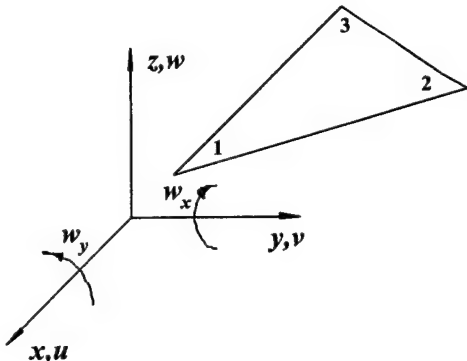


Figure 1.1 DKT triangular element

$$\frac{\partial w}{\partial x} = \mathbf{H}_x(\xi, \eta) w_f, \quad \frac{\partial w}{\partial y} = \mathbf{H}_y(\xi, \eta) w_f \quad (1-26)$$

where ξ and η are area coordinates and the displacement vector w_f is expressed as

$$\mathbf{w}_f = [w_1, w_{x1}, w_{y1}, w_2, w_{x2}, w_{y2}, w_3, w_{x3}, w_{y3}]^T \quad (1-27)$$

The nine components of shape function vectors, \mathbf{H}_x and \mathbf{H}_y , are given by

$$H_{x1} = -1.5 a_6 N_6 - a_5 N_5 \quad (1-28-a)$$

$$H_{x2} = N_1 - C_5 N_5 - C_6 N_6 \quad (1-28-b)$$

$$H_{x3} = -b_5 N_5 + b_6 N_6 \quad (1-28-c)$$

$$H_{y1} = -1.5 d_6 N_6 - d_5 N_5 \quad (1-28-d)$$

$$H_{y2} = -b_5 N_5 + b_6 N_6 \quad (1-28-e)$$

$$H_{y3} = N_1 - e_5 N_5 - e_6 N_6 \quad (1-28-f)$$

The functions H_{x4} , H_{x5} , H_{x6} , H_{y4} , H_{y5} and H_{y6} are obtained from the above expressions by replacing N_1 by N_2 and indices 6 and 5 by 4 and 6, respectively. The functions H_{x7} , H_{x8} , H_{x9} , H_{y7} , H_{y8} and H_{y9} are, respectively, obtained by replacing N_1 by N_3 and indices 6 and 5 by 5 and 4.

The shape functions are given by

$$N_1 = 2(1-\xi-\eta) \left(\frac{1}{2} - \xi - \eta \right) \quad (1-29-a)$$

$$N_2 = \xi \ 2\xi - 1 \quad (1-29-b)$$

$$N_3 = \eta \ 2\eta - 1 \quad (1-29-c)$$

$$N_4 = 4\xi\eta \quad (1-29-d)$$

$$N_5 = 4\eta \ 1 - \xi - \eta \quad (1-29-e)$$

$$N_6 = 4\xi \ 1 - \xi - \eta \quad (1-29-f)$$

and the coefficients are given by

$$a_k = -x_{ij}/l_{ij}^2 \quad (1-30-a)$$

$$b_k = \frac{3}{4}x_{ij}y_{ij}/l_{ij}^2 \quad (1-30-b)$$

$$c_k = \left(\frac{1}{4}x_{ij}^2 - \frac{1}{2}y_{ij}^2 \right)/l_{ij}^2 \quad (1-30-c)$$

$$d_k = -y_{ij}/l_{ij}^2 \quad (1-30-d)$$

$$e_k = \left(\frac{1}{4}y_{ij}^2 - \frac{1}{2}x_{ij}^2 \right)/l_{ij}^2 \quad (1-30-e)$$

$$l_{ij}^2 = x_{ij}^2 + y_{ij}^2 \quad (1-30-f)$$

where $k = 4, 5, 6$ for the sides $i = 23, 31, 12$ respectively, and

$$x_{ij} = x_i - x_j, \quad y_{ij} = y_i - y_j \quad (1-31)$$

According to equation (1-10), the slope transformation matrix \mathbf{C}_θ can be found as

$$\mathbf{C}_\theta = \begin{bmatrix} \mathbf{H}_x \\ \mathbf{H}_y \end{bmatrix} \quad (1-32)$$

The curvature transformation matrix \mathbf{C}_f can be derived as

$$\mathbf{C}_f = \frac{1}{2A} \begin{bmatrix} y_{31}\mathbf{H}_{x,\xi} + y_{12}\mathbf{H}_{x,\eta} \\ -x_{31}\mathbf{H}_{y,\xi} - x_{12}\mathbf{H}_{y,\eta} \\ -x_{31}\mathbf{H}_{x,\xi} - x_{12}\mathbf{H}_{x,\eta} + y_{31}\mathbf{H}_{y,\xi} + y_{12}\mathbf{H}_{y,\eta} \end{bmatrix} \quad (1-33)$$

where A is the area of an element

$$2A = x_{31}y_{12} - x_{12}y_{31} \quad (1-34)$$

The matrix $\mathbf{H}_{x,\xi}$, $\mathbf{H}_{x,\eta}$, $\mathbf{H}_{y,\xi}$ and $\mathbf{H}_{y,\eta}$ are given by

$$\mathbf{H}_{x,\xi}^T = \begin{bmatrix} p_6(1-2\xi) + \eta(p_5 - p_6) \\ 4 - 6(\xi + \eta) - r_6(1-2\xi) + \eta(r_5 + r_6) \\ q_6(1-2\xi) - \eta(q_5 + q_6) \\ -p_6(1-2\xi) + \eta(p_4 + p_6) \\ 2 - 6\xi - r_6(1-2\xi) - \eta(r_4 - r_6) \\ q_6(1-2\xi) - \eta(q_6 - q_4) \\ -\eta(p_5 + p_4) \\ \eta(r_5 - r_4) \\ \eta(q_4 - q_5) \end{bmatrix}, \quad \mathbf{H}_{y,\xi}^T = \begin{bmatrix} t_6(1-2\xi) + \eta(t_5 - t_6) \\ q_6(1-2\xi) - \eta(q_5 + q_6) \\ 1 + r_6(1-2\xi) - \eta(r_5 + r_6) \\ -t_6(1-2\xi) + \eta(t_4 + t_6) \\ q_6(1-2\xi) + \eta(q_4 - q_6) \\ -1 + r_6(1-2\xi) + \eta(r_4 - r_6) \\ -\eta(t_4 + t_5) \\ \eta(q_4 - q_5) \\ \eta(r_4 - r_5) \end{bmatrix} \quad (1-35-a)$$

$$\mathbf{H}_{x,\xi}^T = \begin{bmatrix} -p_5(1-2\eta) - \xi(p_6 - p_5) \\ 4 - 6(\xi + \eta) - r_5(1-2\eta) + \xi(r_5 + r_6) \\ q_5(1-2\eta) - \xi(q_5 + q_6) \\ \xi(p_4 + p_6) \\ \xi(r_6 - r_4) \\ \xi(q_4 - q_6) \\ p_5(1-2\eta) - \xi(p_4 + p_5) \\ 2 - 6\eta - r_5(1-2\eta) - \xi(r_4 - r_5) \\ q_5(1-2\eta) + \xi(q_4 - q_5) \end{bmatrix}, \quad \mathbf{H}_{y,\xi}^T = \begin{bmatrix} -t_5(1-2\eta) - \xi(t_6 - t_5) \\ q_5(1-2\eta) - \xi(q_5 + q_6) \\ 1 + r_5(1-2\eta) - \xi(r_5 + r_6) \\ \xi(t_4 + t_6) \\ \xi(q_4 - q_6) \\ \xi(r_4 - r_6) \\ t_5(1-2\eta) - \xi(t_4 + t_5) \\ q_5(1-2\eta) + \xi(q_4 - q_5) \\ -1 + r_5(1-2\eta) + \xi(r_4 - r_5) \end{bmatrix} \quad (1-35-b)$$

where,

$$p_k = -6x_{ij}/l_{ij}^2, \quad t_k = -6y_{ij}/l_{ij}^2, \quad q_k = 3x_{ij}y_{ij}/l_{ij}^2, \quad r_k = 3y_{ij}^2/l_{ij}^2 \quad (1-36)$$

$k = 4, 5, 6$ for $i = 23, 31, 12$ respectively.

To develop the mass matrix of flexure and membrane the following displacement functions are used

$$w = \mathbf{C}_w \mathbf{w}_f = \begin{bmatrix} L_1^2(1+2L_2+2L_3) + 2L_1L_2L_3 \\ L_1^2(x_{31}L_3 - x_{12}L_2) + \frac{1}{2}L_1L_2L_3(x_{31} - x_{12}) \\ L_1^2(y_{31}L_3 - y_{12}L_2) + \frac{1}{2}L_1L_2L_3(y_{31} - y_{12}) \\ L_2^2(1+2L_3+2L_1) + 2L_1L_2L_3 \\ L_2^2(x_{12}L_1 - x_{23}L_3) + \frac{1}{2}L_1L_2L_3(x_{12} - x_{23}) \\ L_2^2(y_{12}L_1 - y_{23}L_3) + \frac{1}{2}L_1L_2L_3(y_{12} - y_{23}) \\ L_3^2(1+2L_1+2L_2) + 2L_1L_2L_3 \\ L_3^2(x_{23}L_2 - x_{31}L_1) + \frac{1}{2}L_1L_2L_3(x_{23} - x_{31}) \\ L_3^2(y_{23}L_2 - y_{31}L_1) + \frac{1}{2}L_1L_2L_3(y_{23} - y_{31}) \end{bmatrix}^T \begin{bmatrix} w_1 \\ w_{x1} \\ w_{y1} \\ w_2 \\ w_{2x} \\ w_{2y} \\ w_3 \\ w_{3x} \\ w_{3y} \end{bmatrix} \quad (1-37)$$

The membrane displacement functions are linear functions of the nodal displacements, i.e.,

$$\begin{bmatrix} u \\ v \end{bmatrix} = \begin{bmatrix} L_1 & 0 & L_2 & 0 & L_3 & 0 \\ 0 & L_1 & 0 & L_2 & 0 & L_3 \end{bmatrix} \begin{bmatrix} u_1 \\ v_1 \\ u_2 \\ v_2 \\ u_1 \\ v_3 \end{bmatrix} = \mathbf{C}_{uv} \mathbf{w}_m \quad (1-38)$$

Introducing equation (1-38) into equations (1-6) and (1-9), one has

$$\mathbf{C}_m = \frac{1}{2A} \begin{bmatrix} y_{23} & y_{31} & y_{12} & 0 & 0 & 0 \\ 0 & 0 & 0 & x_{32} & x_{13} & x_{21} \\ x_{32} & x_{13} & x_{21} & y_{23} & y_{31} & y_{12} \end{bmatrix} \quad (1-39)$$

1.4 Statically Nonlinear Problems of Large Deflection

1.4.1 Scheme for solving nonlinear static equations

The structural static equation is given by

$$\begin{bmatrix} \mathbf{K}_{ff} & \mathbf{K}_{fm} \\ \mathbf{K}_{mf} & \mathbf{K}_{mm} \end{bmatrix} \begin{Bmatrix} \mathbf{W}_f \\ \mathbf{W}_m \end{Bmatrix} = \begin{Bmatrix} \mathbf{F}_f \\ \mathbf{F}_m \end{Bmatrix} \quad (1-40)$$

Equation (1-40) is equivalent to the following two equations

$$\mathbf{K}_{ff}\mathbf{W}_f = \mathbf{F}_f - \mathbf{K}_{fm}\mathbf{W}_m \quad (1-41-a)$$

$$\mathbf{K}_{mm}\mathbf{W}_m = \mathbf{F}_m - \mathbf{K}_{mf}\mathbf{W}_f \quad (1-41-b)$$

Hence, the iterative equations are given by

$$\begin{cases} \mathbf{K}_{ff}^{(i)} \mathbf{W}_f^{(i-1)} - \mathbf{W}_f^{(i)} = \mathbf{F}_f - \mathbf{K}_{fm}^{(i)} \mathbf{W}_f^{(i-1)} - \mathbf{W}_m^{(i-1)} \\ \bar{\mathbf{W}}_f^{(i)} = R_f \mathbf{W}_f^{(i)} + (1 - R_f) \mathbf{W}_f^{(i-1)} \\ \mathbf{K}_{mm} \mathbf{W}_m^{(i)} = \mathbf{F}_m - \mathbf{K}_{mf}^{(i+1)} (\bar{\mathbf{W}}_f^{(i)}) \bar{\mathbf{W}}_f^{(i)} \\ \bar{\mathbf{W}}_m^{(i)} = R_m \mathbf{W}_m^{(i)} + (1 - R_m) \mathbf{W}_m^{(i-1)} \end{cases} \quad (i=1,2,\dots) \quad (1-42)$$

and

$$\mathbf{W}_f^{(0)} = \mathbf{0}, \quad \mathbf{W}_m^{(0)} = \mathbf{0} \quad (1-43)$$

where, R_f and R_m are relaxation factors for the flexure and membrane.

The scheme for solving the nonlinear static problem is listed as below.

1. Select constants for iteration;
2. Formulate the load vectors \mathbf{F}_f and \mathbf{F}_m ;
3. Initialize the displacement vectors \mathbf{W}_f and \mathbf{W}_m ;
4. Calculate the stiffness matrix of membrane \mathbf{K}_{mm} and then factorize it;
5. For i th iteration:
 - 5.1. Calculate the stiffness matrix $\mathbf{K}_{ff}^{(i)}$ and general force vector $\mathbf{K}_{fm}^{(i)}\mathbf{W}_m^{(i-1)}$
 - 5.2 Solve the first equation of equation (1-42) to obtain $\mathbf{W}_f^{(i)}$;
 - 5.3 Check convergence for flexure;
 - 5.4 Construct new flexure displacement vector $\bar{\mathbf{W}}_f^{(i)}$ by using R_f ;
 - 5.5 Calculate the general force vector $\mathbf{K}_{mf}^{(i+1)}\bar{\mathbf{W}}_f^{(i)}$;
 - 5.6 Solve the third equation of equation (1-42) to obtain $\mathbf{W}_m^{(i)}$;
 - 5.7 Check convergence for membrane;
 - 5.8 Construct new membrane displacement vector $\bar{\mathbf{W}}_m^{(i)}$ by using R_m ;
 - 5.9 If the displacements of flexure or membrane are not convergent, go back to 5.1;

6. Output results.

1.4.2 Results and Discussions

1.4.2.1 Accuracy of the Program

Example I

A clamped squared plate subjected to a uniform distributed load is considered. The length of the sides is 7.62m. The thickness is 0.0762m. Modulus elasticity and possion ratio are $E = 2.0685 \times 10^{11} \text{ N/m}^2$ and 0.316 respectively. This example has become a “standard” used by many authors²⁷⁻³¹ to check the GNL (Geometric Nonlinear) thin plate formulations. The analytical thin plate solution is given by Levy³² who solved von Karman’s equations using a double Fouries series. This solution is quoted as having a possible error of less than 2%³⁰. The plate is divided into 200 triangular elements and 121 nodes. The error tolerances are 10^{-5} and $R_f = 0.7$. The results are shown in Table 1.1. $Q = (qa^4)/(Et^4)$ is a non-dimensional uniformed distributed load. The third column, shown in Table 1.1, was obtained from Wood²⁹ by using the Irons-Razzaque non-conforming triangular thin plate element. The results in Columns 4 and 5 are based on Mindlin’s plate theory. Obviously, the results of present method are acceptable.

Table 1.1. Comparison of central deflections from different methods (clamped plate)

Load (Q)	Exact	Wood	Pica, et al	Rao, et al	Present
17.79	0.237	0.2387	0.2351	0.2346	0.2383
38.3	0.471	0.4717	0.4673	0.4660	0.4636
63.4	0.695	0.6916	0.6887	0.6862	0.6791
95	0.912	0.9008	0.9003	0.8987	0.8721
134.9	1.121	1.1025	1.1041	1.1025	1.0677
184	1.323	1.2961	1.2990	1.2979	1.2595
245	1.521	1.4879	1.4913	1.4890	1.4539
318	1.714	1.6744	1.6774	1.6750	1.6475
402	1.902	1.8529	1.8682	1.8526	1.8365

Example II

The program is checked again by using a simply supported square plate with immovable inplane edges. The other parameters are identical to the above example. The results are listed in Table 1.2. The

results in the second column were obtained by Rushton³³ who used a finite difference dynamic relation approach based on thin Kirchhoff plate. There is a little difference between these results.

Table 1.2. Comparison of central deflections from different methods (simply supported)

Load (Q)	Rushton	Pica, et al	Present
9.16	0.335	0.3478	0.3296
36.6	0.818	0.8184	0.7625
146.5	1.47	1.4655	1.4168
586	2.40	2.3927	2.4520
2344	3.83	3.8124	4.1733
9377	6.07	6.0521	7.1272

1.4.2.2 Effects of R_f on the convergence

Example I

In this analysis, a simply supported square plate subjected to an uniformed distributed load is considered. The length of the sides is 10m. The thickness is 0.1m. Modulus elasticity and possion ratio are $E = 2.0 \times 10^{11}$ N/m² and 0.3 respectively. The plate is divided into 200 triangular elements and 121 nodes. The iterations and central deflections for different R_f are listed in Table 1.3. The error tolerances are 0.01. Obviously, R_f should be close to 1 for linear problems, while it is much smaller for nonlinear problems.

Table 1.3. Iterations and central deflections for different R_f

Pressure (Pa)	Deflection of Linear	$R_f = 1.0$		$R_f = 0.7$		$R_f = 0.4$	
		Iter.	Nonlinear	Iter.	Nonlinear	Iter.	Nonlinear
200	.440689e-03	1	.440673e-03	5	.440673e-03	10	.440673e-03
2000	.440689e-02	1	.439068e-03	5	.439089e-02	9	.439114e-02
20000	.440689e-01	7	.355715e-01	2	.356139e-01	7	.356482e-01
100000	.220345e+00	-	-	15	.896526e-01	3	.900227e-01
200000	.440689e+00	-	-	-	-	4	.122599e+00
2000000	.440689e+01	-	-	-	-	11	.304909e+00

Example II

The example II in section 1.4.2.1 is considered again to check the convergence of the iteration. The iterations for different cases are listed in Table 1.4. The results show that it is very difficult to find

a single optimal R_f for different load cases. For higher nonlinearity, lower R_f is needed as shown in Table 1.4.

Table 1.4. Iterations for different methods (simply supported plate)

Load (Q)	$R_f = 0.5$	$R_f = 0.2$	$R_f = 0.05$
9.16	12	38	169
36.6	11	34	148
146.5	16	34	150
586	31	38	159
2344	-	52	158
9377	-	-	201

1.5 Dynamic Nonlinear Problems of Large Deflection

1.5.1 Scheme for solving the nonlinear dynamic equation

The classical Newmark- β method³⁴ is used to approximate in time. For convenience, the damping is not considered. The dynamic equations of the large deflection problem without damping can be written in matrix form as

$$\begin{bmatrix} \mathbf{M}_{ff} & \mathbf{0} \\ \mathbf{0} & \mathbf{M}_{mm} \end{bmatrix} \begin{bmatrix} \ddot{\mathbf{W}}_f \\ \ddot{\mathbf{W}}_m \end{bmatrix} + \begin{bmatrix} \mathbf{K}_{ff} & \mathbf{K}_{fm} \\ \mathbf{K}_{mf} & \mathbf{K}_{mm} \end{bmatrix} \begin{bmatrix} \mathbf{W}_f \\ \mathbf{W}_m \end{bmatrix} = \begin{bmatrix} \mathbf{F}_f \\ \mathbf{F}_m \end{bmatrix} \quad (1-44)$$

According to the Newmark method, the effective stiffness matrix at time $t + \Delta t$ is

$${}^{t+\Delta t} \hat{\mathbf{K}} = {}^{t+\Delta t} \mathbf{K} + a_0 {}^{t+\Delta t} \mathbf{M} \quad (1-45)$$

Substituting equation (1-44) into equation (1-45), one has

$${}^{t+\Delta t} \begin{bmatrix} \hat{\mathbf{K}}_{ff} & \hat{\mathbf{K}}_{fm} \\ \hat{\mathbf{K}}_{mf} & \hat{\mathbf{K}}_{mm} \end{bmatrix} = {}^{t+\Delta t} \begin{bmatrix} \mathbf{K}_{ff} & \mathbf{K}_{fm} \\ \mathbf{K}_{mf} & \mathbf{K}_{mm} \end{bmatrix} + a_0 {}^{t+\Delta t} \begin{bmatrix} \mathbf{M}_{ff} & \mathbf{0} \\ \mathbf{0} & \mathbf{M}_{mm} \end{bmatrix} \quad (1-46)$$

Because \mathbf{M}_{ff} , \mathbf{M}_{mm} and \mathbf{K}_{mm} are constant matrices, we have

$$\begin{cases} {}^{t+\Delta t} \hat{\mathbf{K}}_{ff} = {}^{t+\Delta t} \mathbf{K}_{ff} + a_0 \mathbf{M}_{ff} \\ {}^{t+\Delta t} \hat{\mathbf{K}}_{fm} = {}^{t+\Delta t} \mathbf{K}_{fm} \\ {}^{t+\Delta t} \hat{\mathbf{K}}_{mf} = {}^{t+\Delta t} \mathbf{K}_{mf} \\ {}^{t+\Delta t} \hat{\mathbf{K}}_{mm} = \mathbf{K}_{mm} + a_0 \mathbf{M}_{mm} \end{cases} \quad (1-47)$$

According to the Newmark method, the effective load vector is given by

$${}^{t+\Delta t} \hat{\mathbf{F}} = {}^{t+\Delta t} \mathbf{F} + \mathbf{M} (a_0' \mathbf{W} + a_2' \dot{\mathbf{W}} + a_3' \ddot{\mathbf{W}}) \quad (1-48)$$

which can be rewritten in partitioned form as

$$\begin{Bmatrix} {}^{t+\Delta t} \hat{\mathbf{F}}_f \\ {}^{t+\Delta t} \hat{\mathbf{F}}_m \end{Bmatrix} = \begin{Bmatrix} {}^{t+\Delta t} \mathbf{F}_f \\ {}^{t+\Delta t} \mathbf{F}_m \end{Bmatrix} + \begin{bmatrix} \mathbf{M}_{ff} & \mathbf{0} \\ \mathbf{0} & \mathbf{M}_{mm} \end{bmatrix} \begin{Bmatrix} a_0' \mathbf{W}_f \\ a_2' \mathbf{W}_m \end{Bmatrix} + a_3' \begin{Bmatrix} \dot{\mathbf{W}}_f \\ \dot{\mathbf{W}}_m \end{Bmatrix} + a_3' \begin{Bmatrix} \ddot{\mathbf{W}}_f \\ \ddot{\mathbf{W}}_m \end{Bmatrix} \quad (1-49)$$

Hence, the effective load vectors of flexure and membrane are given by

$${}^{t+\Delta t} \mathbf{F}_f = {}^{t+\Delta t} \mathbf{F}_f + \mathbf{M}_{ff} a_0' \mathbf{W}_f + a_2' \dot{\mathbf{W}}_f + a_3' \ddot{\mathbf{W}}_f \quad (1-50a)$$

$${}^{t+\Delta t} \mathbf{F}_m = {}^{t+\Delta t} \mathbf{F}_m + \mathbf{M}_{mm} a_0' \mathbf{W}_m + a_2' \dot{\mathbf{W}}_m + a_3' \ddot{\mathbf{W}}_m \quad (1-50b)$$

The final equations to be solved are given by

$$\begin{bmatrix} \hat{\mathbf{K}}_{ff} & \hat{\mathbf{K}}_{fm} \\ \hat{\mathbf{K}}_{mf} & \hat{\mathbf{K}}_{mm} \end{bmatrix} {}^{t+\Delta t} \begin{Bmatrix} \mathbf{W}_f \\ \mathbf{W}_m \end{Bmatrix} = {}^{t+\Delta t} \begin{Bmatrix} \hat{\mathbf{F}}_f \\ \hat{\mathbf{F}}_m \end{Bmatrix} \quad (1-51)$$

According to the assumption, one has $\mathbf{M}_{mm} = \mathbf{0}$. Therefore, the iterative equations for effective equations are given by

$$\begin{cases} {}^{t+\Delta t} \hat{\mathbf{K}}_{ff} {}^{t+\Delta t} \mathbf{W}_f^{(i)} - {}^{t+\Delta t} \mathbf{W}_f^{(i-1)} = {}^{t+\Delta t} \hat{\mathbf{F}}_f - {}^{t+\Delta t} \mathbf{K}_{fm}^{(i)} {}^{t+\Delta t} \mathbf{W}_f^{(i-1)} - {}^{t+\Delta t} \mathbf{W}_m^{(i-1)} \\ {}^{t+\Delta t} \overline{\mathbf{W}}_f^{(i)} = R_f {}^{t+\Delta t} \mathbf{W}_f^{(i)} + (1 - R_f) {}^{t+\Delta t} \mathbf{W}_f^{(i-1)} \\ {}^{t+\Delta t} \mathbf{K}_{mm} {}^{t+\Delta t} \mathbf{W}_m^{(i)} = {}^{t+\Delta t} \mathbf{F}_m - {}^{t+\Delta t} \mathbf{K}_{mf}^{(i+1)} \left({}^{t+\Delta t} \overline{\mathbf{W}}_f^{(i)} \right) {}^{t+\Delta t} \overline{\mathbf{W}}_f^{(i)} \\ {}^{t+\Delta t} \overline{\mathbf{W}}_m^{(i)} = R_m {}^{t+\Delta t} \mathbf{W}_m^{(i)} + (1 - R_m) {}^{t+\Delta t} \mathbf{W}_m^{(i-1)} \end{cases} \quad (i = 1, 2, \dots) \quad (1-52)$$

The scheme for solving the nonlinear dynamic problem is listed as below.

1. Select constants for Newmark- β method and the static iteration;
2. Calculate integration constants for Newmark- β method;
3. Initialize structural data and evaluate index vectors for diagonals in the structural matrices of flexure and membrane;
4. Initialize the displacement, velocity and acceleration vectors;
5. Evaluate and factorize the stiffness matrix of membrane \mathbf{K}_{mm} ;
6. Evaluate the mass matrix of flexure \mathbf{M}_{ff} ;
7. Calculate the dynamic responses step by step (Newmark- β loop):
 - 7.1 Formulate external force vectors \mathbf{F}_f and \mathbf{F}_m ;
 - 7.2 Evaluate effective loads at time $t + \Delta t$ for flexure;

7.3 Initialize displacement vectors;

7.4 For the i th iteration of nonlinear effective static problem:

7.4.1 Calculate stiffness matrix ${}^{t+\Delta t} \mathbf{K}_{ff}^{(i)}$ and general force vector ${}^{t+\Delta t} \mathbf{K}_{fm}^{(i)} {}^{t+\Delta t} \mathbf{W}_m^{(i-1)}$ of flexure;

7.4.2 Calculate effective stiffness matrix ${}^{t+\Delta t} \mathbf{K}_{ff}^{(i)}$ for flexure;

7.4.3 Solve the first equation of equation (1-52) to obtain ${}^{t+\Delta t} \mathbf{W}_f^{(i)}$;

7.4.4 Check convergence for flexure;

7.4.5 Construct new flexure displacement vector ${}^{t+\Delta t} \overline{\mathbf{W}}_f^{(i)}$ by using R_f ;

7.4.6 Calculate general force vector ${}^{t+\Delta t} \mathbf{K}_{mf}^{(i+1)} {}^{t+\Delta t} \overline{\mathbf{W}}_f^{(i)}$;

7.4.7 Solve the third equation of equation (1-52) to obtain ${}^{t+\Delta t} \mathbf{W}_m^{(i)}$;

7.4.8 Check convergence for membrane;

7.4.9 Construct new membrane displacement vector ${}^{t+\Delta t} \overline{\mathbf{W}}_m^{(i)}$ by using R_m ;

7.4.10 If the displacements of flexure or membrane are not convergent, go back to 7.4.1;

8. Output results.

1.5.2 Numerical Examples

1.5.2.1 Example I

A simply supported square steel plate with immovable inplane edges is considered. The length of the sides is 1.0m. The thickness is 0.01m. Modulus elasticity and possion ratio are $E=2.0E11N/m^2$ and 0.3 respectively. The plate is divided into 200 triangular elements and 121 nodes. Assume a concentrated load, $P = 10 \sin 2\omega t$ N, acts on the center of the plate. The central responses for different time step sizes (0.0004, 0.0002, and 0.0001) and error tolerances (10^{-2} , 10^{-4} , and 10^{-6}) are drawn in Figure 1.2 respectively. The iterations for these three cases are 5, 8, and 12 respectively. The results show that the error tolerance has much effect on the accuracy of the responses. When the error tolerance is large the responses change with the time step size. For this problem, the error tolerance can be set 10^{-6} .

1.5.2.2. Example II

The plate used in example I is considered again. Assume the concentrated load is $P = 5 \sin \omega t$ kN. The central responses of the plate for $\omega = 3$ rad/s, $\omega = 100$ rad/s and $\omega = 200$ rad/s are drawn in Figure 1.3 respectively. The error tolerance is 2×10^{-7} . A and B denote the responses

obtained from the nonlinear and linear theories respectively. For the nonlinear problems, 19 to 23, 13 to 14, and 13 to 14 iterations are required in the three cases respectively.

1.5.2.3 Example III

Another simply supported square aluminum plate with immovable inplane edges³⁵ is considered. The length of the sides is 0.8m. The thickness is 0.025m. Modulus elasticity and possion ratio are $E=6.9e10\text{N/m}^2$ and 0.33 respectively. A moving load, $P=1000kN$, travels at constant velocity $v=153.7\text{m/s}$ in the y -direction along the centerline. The plate is divided into 200 triangular elements and 121 nodes. $R_f = 0.7$ is used here. The responses at the center of the plate for linear and nonlinear are given in Figure 1.4. Again, A and B denote the responses obtained from the nonlinear and linear theories, respectively. In this figure, the error tolerance is 2×10^{-7} and the iterations are 13 to 14 for the nonlinear case.

1.6 Non-Dimensional Form of FEM Formulations

The finite element formulations defined above are dimensional. As we know, dimensionless parameters are usually used in the fluid equations. To make them compatible, these FEM formulations are to be non-dimensionalized with respect to the length of the plate and other parameters from fluid. The dimensionless dynamic equations of equilibrium using finite element method may be obtained by non-dimensionalizing either the partial differential equations of nonlinear plate or the integration form of the finite element formulations. The details of the former will be shown in Section 5.4. The non-dimensional form of the latter is to be provided in the following.

Assume the dimensionless parameters are given by

$$\begin{cases} \tilde{u} = \frac{u}{l}, \quad \tilde{v} = \frac{v}{l}, \quad \tilde{w} = \frac{w}{l}, \quad \tilde{x} = \frac{x}{l}, \quad \tilde{y} = \frac{y}{l}, \quad \tilde{z} = \frac{z}{l} \\ \tilde{w}_x = w_x, \quad \tilde{w}_y = w_y \\ \tilde{t} = \frac{tV_\infty}{l}, \quad \tilde{p} = \frac{p}{\rho_a V_\infty^2} \end{cases} \quad (1-53)$$

where l is the length of the plate; V_∞ is the velocity of the air in the far field; ρ_a denotes the mass density of air; p is the air pressure acting on the plate. With this assumption, the relation of the membrane displacement vectors between the dimensional form and dimensionless form is given by

$$w_m = \tilde{w}_m l \quad (1-54)$$

For the triangular element used above, the dimensionless membrane and flexural displacement vectors are defined as

$$\tilde{\mathbf{w}}_m = \begin{bmatrix} \tilde{u}_1 & \tilde{v}_1 & \tilde{u}_2 & \tilde{v}_2 & \tilde{u}_3 & \tilde{v}_3 \end{bmatrix}^T \quad (1-55)$$

$$\tilde{\mathbf{w}}_f = \begin{bmatrix} \tilde{w}_1 & w_{x1}, w_{y1}, \tilde{w}_2, w_{x2}, w_{y2}, \tilde{w}_3, w_{x3}, w_{y3} \end{bmatrix}^T \quad (1-56)$$

Clearly, the dimensionless flexural displacement vector does not have the simple relation, as shown in equation (1-54), with its dimensional form. To simplify the derivation, defined the flexural displacement vector as

$$\mathbf{w}_f = \begin{bmatrix} w_1, l w_{x1}, l w_{y1}, w_2, l w_{x2}, l w_{y2}, w_3, l w_{x3}, l w_{y3} \end{bmatrix}^T \quad (1-57)$$

Now, we have the relation

$$\mathbf{w}_f = \tilde{\mathbf{w}}_f l \quad (1-58)$$

Using the definition in equation (1-57), the following relations of the interpolation functions or other parameters between the dimensional form and the dimensionless form may be obtained from equations (1-3), (1-9), (1-11), (1-10), and (1-12) respectively, that is,

$$C_w = \tilde{C}_w \quad (1-59)$$

$$C_u = \tilde{C}_u, \quad C_v = \tilde{C}_v \quad (1-60)$$

$$C_m = \tilde{C}_m / l \quad (1-61)$$

$$\theta = \tilde{\theta} \quad (1-62)$$

$$C_\theta = \tilde{C}_\theta / l \quad (1-63)$$

$$C_f = \tilde{C}_f / l^2 \quad (1-64)$$

Introducing equations (1-59) through (1-64) into equations (1-20), (1-21), (1-22), and (1-25) leads to

$$\mathbf{m}_{ff} = \rho_s h l^2 \int_{\tilde{s}} \tilde{\mathbf{C}}_w^T \tilde{\mathbf{C}}_w ds = \rho_s h l^2 \tilde{\mathbf{m}}_{ff}, \quad \mathbf{m}_{mm} = \rho_s h l^2 \int_{\tilde{s}} \tilde{\mathbf{C}}_{uv}^T \tilde{\mathbf{C}}_{uv} ds = \rho_s h l^2 \tilde{\mathbf{m}}_{mm} \quad (1-65)$$

$$\mathbf{k}_{fm} = \mathbf{k}_{fm}^1 = D_m \frac{1}{2} \int_{\tilde{s}} \tilde{\mathbf{C}}_\theta^T \tilde{\mathbf{?}}^T \tilde{\mathbf{D}} \tilde{\mathbf{C}}_m ds = D_m \tilde{\mathbf{k}}_{fm}, \quad \mathbf{k}_{mf} = \mathbf{k}_{mf}^1 = \mathbf{k}_{fm}^T \quad (1-66)$$

$$\mathbf{k}_{ff}^0 = \frac{D_f}{l^2} \int_{\tilde{s}} \tilde{\mathbf{C}}_f^T \tilde{\mathbf{D}} \tilde{\mathbf{C}}_f ds = \frac{D_f}{l^2} \tilde{\mathbf{k}}_{ff}^0 \quad (1-67)$$

$$\mathbf{k}_{ff}^1 = D_m \frac{1}{2} \int_{\tilde{s}} \tilde{\mathbf{C}}_\theta^T \tilde{\mathbf{N}}_m \tilde{\mathbf{C}}_\theta ds = D_m \tilde{\mathbf{k}}_{ff}^1 \quad (1-68)$$

$$\mathbf{k}_{ff}^2 = D_m \frac{1}{2} \int_{\tilde{s}} \tilde{\mathbf{C}}_\theta^T \tilde{\mathbf{?}}^T \tilde{\mathbf{D}} \tilde{\mathbf{?}} \tilde{\mathbf{C}}_\theta ds = D_m \tilde{\mathbf{k}}_{ff}^2 \quad (1-69)$$

$$\mathbf{k}_{mm} = D_m \int_s \tilde{\mathbf{C}}_m^T \tilde{\mathbf{D}} \tilde{\mathbf{C}}_m ds = D_m \mathbf{k}_{mm} \quad (1-70)$$

where,

$$\tilde{\mathbf{D}} = \begin{bmatrix} 1 & v & 0 \\ v & 1 & 0 \\ 0 & 0 & \frac{1-v}{2} \end{bmatrix} \quad (1-71)$$

$$D_m = \frac{Eh}{1-v^2}, \quad D_f = \frac{Eh^3}{12(1-v^2)} \quad (1-72)$$

$$\tilde{\mathbf{N}}_m = \begin{bmatrix} \tilde{N}_{mx} & \tilde{N}_{mxy} \\ \tilde{N}_{mxy} & \tilde{N}_{my} \end{bmatrix} \quad (1-73)$$

$$\tilde{\mathbf{N}}_m = \begin{bmatrix} \tilde{N}_{mx} \\ \tilde{N}_{my} \\ \tilde{N}_{mxy} \end{bmatrix} = \tilde{\mathbf{D}} \tilde{\mathbf{C}}_m \tilde{\mathbf{w}}_m \quad (1-74)$$

Using equation (1-53), the dimensionless acceleration and force vectors are given by

$$\ddot{\mathbf{w}}_f = \frac{V_\infty^2}{l} \tilde{\mathbf{w}}_f, \quad \ddot{\mathbf{w}}_m = \frac{V_\infty^2}{l} \tilde{\mathbf{w}}_m \quad (1-75)$$

$$f = ps = \rho_a V_\infty^2 l^2 \tilde{p} \tilde{s} = \rho_a V_\infty^2 l^2 \tilde{f} \quad (1-76)$$

Remember, the vector $\ddot{\mathbf{w}}_f$ in equation (1-75) is corresponding to the displacement vector in equation (1-57). Inserting equations (1-65) through (1-70), (1-75), and (1-76) into equation (1-19) results in

$$\rho_s h l V_\infty^2 \begin{bmatrix} \tilde{\mathbf{m}}_{ff} & \mathbf{0} \\ \mathbf{0} & \tilde{\mathbf{m}}_{mm} \end{bmatrix} \begin{Bmatrix} \tilde{\mathbf{w}}_f \\ \tilde{\mathbf{w}}_m \end{Bmatrix} + \left(\frac{D_f}{l} \begin{bmatrix} \tilde{\mathbf{k}}_{ff}^0 & \mathbf{0} \\ \mathbf{0} & \mathbf{0} \end{bmatrix} + D_m l \begin{bmatrix} \tilde{\mathbf{k}}_{ff}^1 + \tilde{\mathbf{k}}_{ff}^2 & \tilde{\mathbf{k}}_{fm} \\ \tilde{\mathbf{k}}_{mf} & \tilde{\mathbf{k}}_{mm} \end{bmatrix} \right) \begin{Bmatrix} \tilde{\mathbf{w}}_f \\ \tilde{\mathbf{w}}_m \end{Bmatrix} = \rho_a V_\infty^2 l^2 \begin{Bmatrix} \tilde{f}_f \\ \tilde{f}_m \end{Bmatrix} \quad (1-77)$$

Dividing both hand sides of equation (1-77) by $\rho_s h l V_\infty^2$ yields

$$\begin{bmatrix} \tilde{\mathbf{m}}_{ff} & \mathbf{0} \\ \mathbf{0} & \tilde{\mathbf{m}}_{mm} \end{bmatrix} \begin{Bmatrix} \tilde{\mathbf{w}}_f \\ \tilde{\mathbf{w}}_m \end{Bmatrix} + \left(\frac{\mu_s}{\lambda} \begin{bmatrix} \tilde{\mathbf{k}}_{ff}^0 & \mathbf{0} \\ \mathbf{0} & \mathbf{0} \end{bmatrix} + t_{nl} \mu_s \begin{bmatrix} \tilde{\mathbf{k}}_{ff}^1 + \tilde{\mathbf{k}}_{ff}^2 & \tilde{\mathbf{k}}_{fm} \\ \tilde{\mathbf{k}}_{mf} & \tilde{\mathbf{k}}_{mm} \end{bmatrix} \right) \begin{Bmatrix} \tilde{\mathbf{w}}_f \\ \tilde{\mathbf{w}}_m \end{Bmatrix} = \mu_s \begin{Bmatrix} \tilde{f}_f \\ \tilde{f}_m \end{Bmatrix} \quad (1-78)$$

in which the dimensionless dynamic pressure λ , mass ratio μ_s , and internal force coefficient t_{nl} are defined as

$$\lambda = \frac{\rho_a V_\infty^2 l^3}{D_f}, \quad \mu_s = \frac{\rho_a l}{\rho_s h}, \quad t_{nl} = \frac{12}{\lambda} \left(\frac{l}{h} \right)^2 \quad (1-79)$$

Equation (1-78) is the dynamic equilibrium of an element in non-dimensional form.

Because the flexural displacement vector used here is different from that used in the triangular element in Section 1.3, the functions pertaining to this flexural displacement should be different from those defined in Section 1.3. The former may be obtained simply by dividing the items pertaining to the rotational degrees of freedom in the latter by the length l , namely,

- Flexural displacement functions:

$$\hat{\mathbf{C}}_w = \begin{bmatrix} L_1^2(1+2L_2+2L_3) + 2L_1L_2L_3 \\ L_1^2(\tilde{x}_{31}L_3 - \tilde{x}_{12}L_2) + \frac{1}{2}L_1L_2L_3(\tilde{x}_{31} - \tilde{x}_{12}) \\ L_1^2(\tilde{y}_{31}L_3 - \tilde{y}_{12}L_2) + \frac{1}{2}L_1L_2L_3(\tilde{y}_{31} - \tilde{y}_{12}) \\ L_2^2(1+2L_3+2L_1) + 2L_1L_2L_3 \\ L_2^2(\tilde{x}_{12}L_1 - \tilde{x}_{23}L_3) + \frac{1}{2}L_1L_2L_3(\tilde{x}_{12} - \tilde{x}_{23}) \\ L_2^2(\tilde{y}_{12}L_1 - \tilde{y}_{23}L_3) + \frac{1}{2}L_1L_2L_3(\tilde{y}_{12} - \tilde{y}_{23}) \\ L_3^2(1+2L_1+2L_2) + 2L_1L_2L_3 \\ L_3^2(\tilde{x}_{23}L_2 - \tilde{x}_{31}L_1) + \frac{1}{2}L_1L_2L_3(\tilde{x}_{23} - \tilde{x}_{31}) \\ L_3^2(\tilde{y}_{23}L_2 - \tilde{y}_{31}L_1) + \frac{1}{2}L_1L_2L_3(\tilde{y}_{23} - \tilde{y}_{31}) \end{bmatrix}^T \quad (1-80)$$

- Slope transformation matrix:

$$\hat{\mathbf{C}}_\theta = \begin{bmatrix} \hat{\mathbf{H}}_x \\ \hat{\mathbf{H}}_y \end{bmatrix} \quad (1-81)$$

in which $\hat{\mathbf{H}}_x$ and \mathbf{H}_y are the shape function vectors. Their components have the same forms as those shown in equation (1-28) while the coefficients b_k , c_k , and e_k are given by

$$b_k = \frac{3}{4l} x_{ij} y_{ij} / l_{ij}^2 \quad (1-82a)$$

$$c_k = \left(\frac{1}{4l} x_{ij}^2 - \frac{1}{2l} y_{ij}^2 \right) / l_{ij}^2 \quad (1-82b)$$

$$e_k = \left(\frac{1}{4l} y_{ij}^2 - \frac{1}{2l} x_{ij}^2 \right) / l_{ij}^2 \quad (1-82c)$$

- Curvature transformation matrix has the same form of that in equation (1-33) except the coefficients q_k and r_k in equation (1-36) which are given by

$$q_k = \frac{3}{l} x_{ij} y_{ij} / l_{ij}^2, \quad r_k = \frac{3}{l} y_{ij}^2 / l_{ij}^2 \quad (1-83)$$

Finally, the dimensionless forms of these functions may be obtained by using the relations in equations (1-59) through (1-64). They are listed in the following for reference.

- Flexural displacement functions:

$$\tilde{\mathbf{C}}_w = \begin{bmatrix} L_1^2(1+2L_2+2L_3) + 2L_1L_2L_3 \\ L_1^2(\tilde{x}_{31}L_3 - \tilde{x}_{12}L_2) + \frac{1}{2}L_1L_2L_3(\tilde{x}_{31} - \tilde{x}_{12}) \\ L_1^2(\tilde{y}_{31}L_3 - \tilde{y}_{12}L_2) + \frac{1}{2}L_1L_2L_3(\tilde{y}_{31} - \tilde{y}_{12}) \\ L_2^2(1+2L_3+2L_1) + 2L_1L_2L_3 \\ L_2^2(\tilde{x}_{12}L_1 - \tilde{x}_{23}L_3) + \frac{1}{2}L_1L_2L_3(\tilde{x}_{12} - \tilde{x}_{23}) \\ L_2^2(\tilde{y}_{12}L_1 - \tilde{y}_{23}L_3) + \frac{1}{2}L_1L_2L_3(\tilde{y}_{12} - \tilde{y}_{23}) \\ L_3^2(1+2L_1+2L_2) + 2L_1L_2L_3 \\ L_3^2(\tilde{x}_{23}L_2 - \tilde{x}_{31}L_1) + \frac{1}{2}L_1L_2L_3(\tilde{x}_{23} - \tilde{x}_{31}) \\ L_3^2(\tilde{y}_{23}L_2 - \tilde{y}_{31}L_1) + \frac{1}{2}L_1L_2L_3(\tilde{y}_{23} - \tilde{y}_{31}) \end{bmatrix}^T \quad (a)$$

- Membrane displacement functions:

$$\tilde{\mathbf{C}}_{uv} = \begin{bmatrix} L_1 & 0 & L_2 & 0 & L_3 & 0 \\ 0 & L_1 & 0 & L_2 & 0 & L_3 \end{bmatrix} \quad (b)$$

- Membrane strain coefficients:

$$\tilde{\mathbf{C}}_m = \frac{1}{2A} \begin{bmatrix} \tilde{y}_{23} & \tilde{y}_{31} & \tilde{y}_{12} & 0 & 0 & 0 \\ 0 & 0 & 0 & \tilde{x}_{32} & \tilde{x}_{13} & \tilde{x}_{21} \\ \tilde{x}_{32} & \tilde{x}_{13} & \tilde{x}_{21} & \tilde{y}_{23} & \tilde{y}_{31} & \tilde{y}_{12} \end{bmatrix} \quad (c)$$

- Slope transformation matrix:

$$\tilde{\mathbf{C}}_\theta = \begin{bmatrix} \tilde{\mathbf{H}}_x \\ \tilde{\mathbf{H}}_y \end{bmatrix} \quad (d)$$

where $\tilde{\mathbf{H}}_x$ and $\tilde{\mathbf{H}}_y$ are the dimensionless shape function vectors. Their components have the same forms as those shown in equation (1-28) while the all the variables on the right hand sides of equations (1-30) should be their non-dimensional forms.

- Curvature transformation:

$$\tilde{\mathbf{C}}_f = \frac{1}{2A} \begin{bmatrix} \tilde{y}_{31}\tilde{\mathbf{H}}_{x,\xi} + \tilde{y}_{12}\tilde{\mathbf{H}}_{x,\eta} \\ -\tilde{x}_{31}\tilde{\mathbf{H}}_{y,\xi} - \tilde{x}_{12}\tilde{\mathbf{H}}_{y,\eta} \\ -\tilde{x}_{31}\tilde{\mathbf{H}}_{x,\xi} - \tilde{x}_{12}\tilde{\mathbf{H}}_{x,\eta} + \tilde{y}_{31}\tilde{\mathbf{H}}_{y,\xi} + \tilde{y}_{12}\tilde{\mathbf{H}}_{y,\eta} \end{bmatrix} \quad (e)$$

The dimensionless derivatives of the shape function vectors have the same forms as those expressed in equation (1-35) except the definitions in equation (1-36). In the new definitions, the dimensional variables in equations (1-36) are replaced by the dimensionless variables shown in equation (1-53).

1.7 Summary

The large deflection of thin plates, which considers the coupling effect between the flexure and the in-plane deformation, was investigated by using finite element method. Based on the von-Karman nonlinear strain-displacement relation, the dynamic equations of large deflection plates were derived at first. The Formulation of Discrete Kirchhoff Theory (DKT) for triangular elements was then presented for the discretization of the thin plate. An iterative method between the equations of the flexure and the membrane was used to solve the static nonlinear problem. To make the method efficient, a relaxation factor was used in this method. The Newmark- β method was applied to solve the dynamic equations in time domain. Several numerical examples were included to demonstrate the efficiency of the method for the nonlinear dynamic problem. The following conclusions can be drawn from the theory and the results of the examples:

1. The results from the present program are acceptable by comparing with other typical results.
2. The relaxation factor is very important for the convergence of the iterative method. If improper relaxation factor is selected, the iteration may not converge.
3. R_f should be close to 1 for linear problems, while it is close to zero for nonlinear problems.
4. The error tolerance has much effect on the accuracy of the responses. When the error tolerance is large the responses change with the time step size.

References:

¹Gray, Jr. C. E., "Large Amplitude Finite Element Flutter Analysis of Composite Panels in Hypersonic Flow," Ph.D. Thesis, Engineering Mechanics, Old Dominion University, USA, 1991.

²Xue, D. Y. and Mei, C., "Finite Element Nonlinear Panel Flutter with Arbitrary Temperatures in Supersonic Flow," *AIAA Journal*, Vol.31, No.1, 1993, pp.154-162.

³Selvam, R. P., Visbal, M. R. and Morton, S. A., "Computation of Nonlinear Viscous Panel Flutter Using a Fully-Implicit Aeroelastic Solver," *Proceedings of the 39th AIAA/ASME/ASCE/AHC/ASC Structures, Structural Dynamics, and Materials Conference and Exhibit*, AIAA, Reston, VA, USA, 1998, pp.1263-1272.

⁴Radu, U. "Higher Finite Element Model in Nonlinear Panel Flutter Analysis," *Proceedings of the 39th AIAA/ASME/ASCE/AHC/ASC Structures, Structural Dynamics, and Materials Conference and Exhibit*, AIAA, Reston, VA, USA, 1998, pp.1252-1262.

⁵Szilard, R., "Theory and Analysis of Plates: Classical and Numerical Methods," Englewood Cliffs, NJ: Prentice-Hall, 1973.

⁶Mei, C., and Decha-Umphai, K., "A Finite Element Method for Nonlinear Forced Vibration of Rectangular Plates," *AIAA Journal*, Vol.23, No.7, 1985, pp.1104-1110.

⁷Soh, A.-K., Soh, C.-K., and Hoon, K.-H., "Development of a Simplified Plate Element for Large Deflection Elastic-Plastic Finite Element Analysis," *Computers and Structures*, Vol.61, No.1, 1996, pp.183-188.

⁸Shi, Y., Lee, R., and Mei, C., "Finite Element Method for Nonlinear Free Vibrations of Composite Plates," *AIAA Journal*, Vol.35, No.1, 1997, pp.159-166.

⁹Kong, J., and Cheung, Y. K., "Application of the Spline Finite Strip to the Analysis of Shear-Deformable Plates," *Computers and Structures*, Vol.46, No.6, 1993, pp.985-988.

¹⁰Kong, J., and Cheung, Y. K., "A Reduction Method for the Analysis of Non-Linear Forced Vibration of Plates," *Journal of Sound and Vibration*, Vol.184, No.4, 1995, pp.611-626.

¹¹Chen, Y., "Geometrically Non-Linear Dynamic Analysis of Plates by an Improved Finite Element – Transfer Matrix Method on a Microcomputer," *Structural Engineering and Mechanics*, Vol.2, No.4, 1994, pp.395-402.

¹²Bazeley, G. P., Cheung, Y. K., Irons, B. M., and Zienkiewicz, O. C., "Triangular Elements in Bending Conforming and Non-Conforming Solution," *Proceedings of the Conference on Matrix Methods in Structural Mechanics, Air Force Ins. Tech., Wright-Patterson, OH, USA*, 1965, pp.547-576.

¹³Stricklin, J. A., Haisler, W. E., Tisdale, P. R., and Gunderson, R., "A Rapidly Converging Triangular Plate Element," *AIAA Journal*, Vol.7, No.1, 1969, pp.180-181.

¹⁴Argyris, J. H., Hease, M., and Mlejnek, H. P., "On an Unconventional but Natural Formulation of a Stiffness Matrix," *Computer Methods in Applied Mechanics and Engineering*, Vol.22, No.1, 1980, pp.1-22.

¹⁵Felippa, C. A., and Bergan, P. G., "A Triangular Bending Element Based on Energy-Orthogonal Free Formulation," *Computer Methods in Applied Mechanics and Engineering*, Vol.61, No.1, 1987, pp.129-160.

¹⁶Allwood, R. J., and Cornes, G. M., "A Polygonal Finite Element for Plate Bending Problems Using the Assumed Stress Approach," *International Journal for Numerical Methods in Engineering*, Vol.1, No.1, 1969, pp.135-149.

¹⁷Neale, B. K., Henshell, R. D., and Edwards, G., "Hybrid Plate Bending Elements," *Journal of Sound and Vibration*, Vol.23, No.1, 1972, pp.101-112.

¹⁸Long, Z. F., "Generalized Conforming Triangular Elements for Plate Bending," *Communications in Numerical Methods in Engineering*, Vol.9, No.1, 1993, pp.53-63.

¹⁹Cheung, Y. K., and Chen, W. J., "Refined Nine-Parameter Triangular Thin Plate Bending Element by Using Refined Direct Stiffness Method," *International Journal for Numerical Methods in Engineering*, Vol.38, No.2, 1995, pp.283-298.

²⁰Batoz, J. -L., Bathe, K. J., and Ho, L.- W., "A Study of Three-Node Triangular Plate Bending Elements," *International Journal for Numerical Methods in Engineering*, Vol.15, No.12, 1980, pp.1771-1812.

²¹Batoz, J. L., "An Explicit Formulation for an Efficient Triangular Plate-Bending Element," *International Journal for Numerical Methods in Engineering*, Vol.18, No.7, 1982, pp.1077-1089.

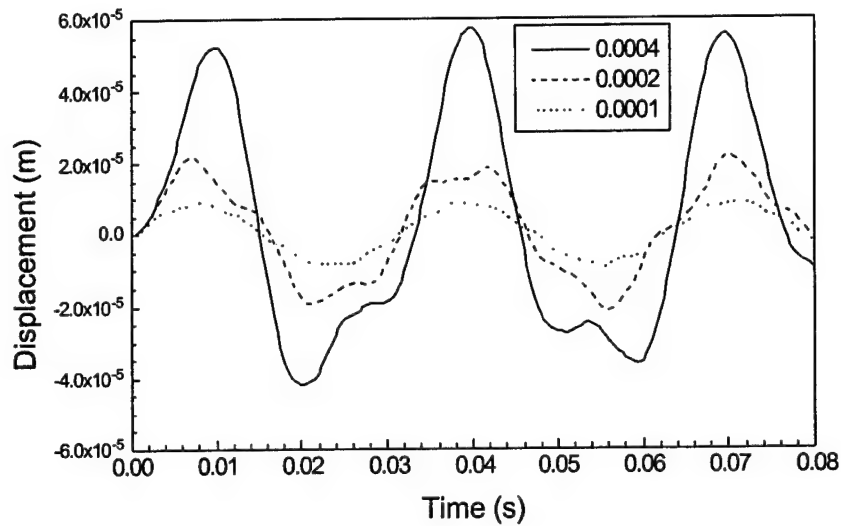
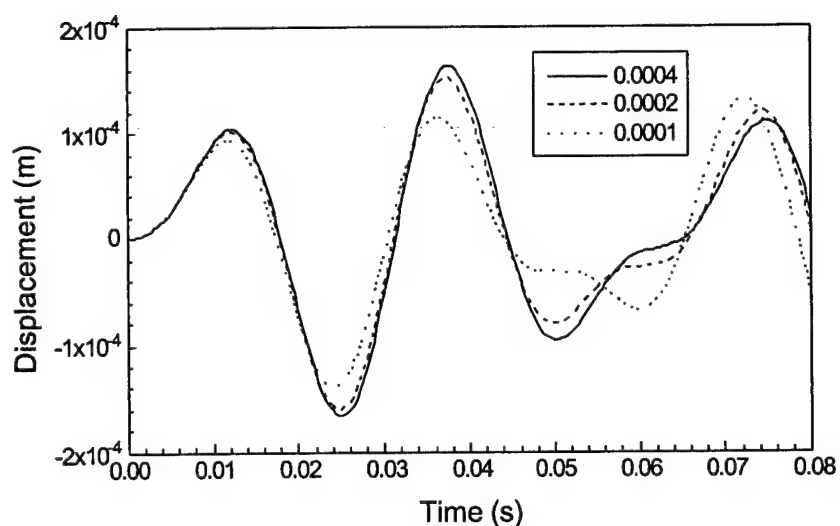
²²Jeyachandrabose, C., and Kirkhope, J., "An Alternative Explicit Formulation for the DKT Plate-Bending Element," *International Journal for Numerical Methods in Engineering*, Vol.21, No. , 1985, pp.1289-1293.

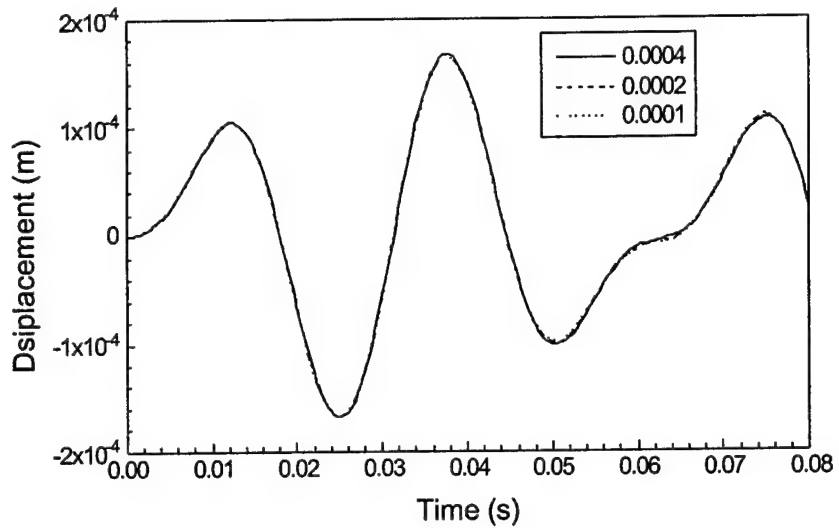
²³Zienkiewicz, O. C., Taylor, R. L., Papadopoulos, P., and Onate, E., "Plate Bending Elements with Discrete Constraints New Triangular Elements," *Computers and Structures Frontiers in Computational Mechanics*, Vol.35, No.4, 1990, pp.505-522.

²⁴Zhao, Z., "General Method to Improve Discrete Kirchhoff Thin Plate Bending Elements," *Journal of Dalian University of Technology*, Vol.34, No.2, 1994, pp.189-192.

²⁵Chen, W., and Cheung, Y. K., "Refined Triangular Discrete Kirchhoff Plate Element for Thin Plate Bending, Vibration and Buckling Analysis," *International Journal for Numerical Methods in Engineering*, Vol.41, No.8, 1998, pp.1507-1525.

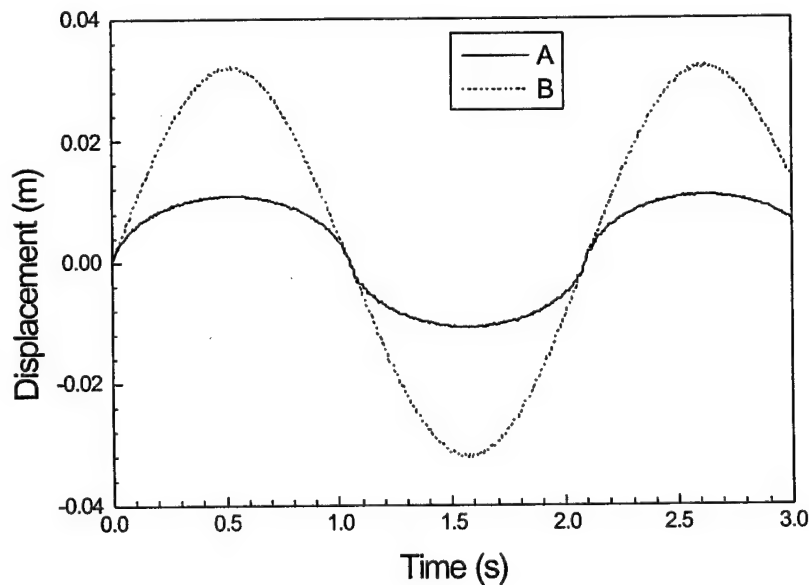
- ²⁶Xue, D. Y., "Finite Element Frequency Domain Solution of Nonlinear Panel Flutter with Temperature Effects and Fatigue Life Analysis," Ph.D. Thesis, Engineering Mechanics, Old Dominion University, USA, 1991.
- ²⁷Murray, D. W., and Wilson, E. L., "Finite Element Large Deflection Analysis of Plates," *ASCE*, Vol.95(EM1), 1969, pp.143-165.
- ²⁸Bergan, P. G., and Clough, R. W., "Large Deflection Analysis of Plates and Shallow Shells Using the Finite Element Method," *International Journal for Numerical Methods in Engineering*, Vol.5, No. , 1973, pp.543-556.
- ²⁹Wood, R. D., "The Application of Finite Element Methods to Geometrically Nonlinear Structural Analysis," University of Wales, Swansea, U.K., C/Ph/20/73, 1973.
- ³⁰Pica, A., Wood, R. D., and Hinton, E., "Finite Element Analysis of Geometrically Nonlinear Plate Behavior Using a Midlin Formulation," *Computers and Structures*, Vol.11, No.3, 1980, pp.203-215.
- ³¹Rao, D. V., Sheikh, A. H., and Mukhopadhyay, M., "Finite Element Large Displacement Analysis of Stiffened Plates," *Computers and Structures*, Vol.47, No.6, 1993, pp.987-993.
- ³²Levy, S., "Square Plate with Clamped Edges Under Normal Pressure Producing Large Deflection," *NASA Technical Note*, 847, 1942.
- ³³Rushton, K. R., "Large Deflexion of Plates with Initial Curvature," *International Journal of Mechanic Science*, Vol.12, No. , 1970, pp.1037-1051.
- ³⁴Bathe, K. J., "Finite Element Procedures," Englewood Cliffs, N. J., Prentice-Hall, 1996.
- ³⁵Weaver, Jr. W., and Johnson, P. R., "Structural Dynamics by Finite Element," Prentice-Hall Inc., Englewood Cliffs, NJ, USA, 1987.

1.2(a) Error tolerance is 10^{-2} 1.2(b) Error tolerance is 10^{-4}



2(c) Error tolerance is 10^{-6}

Figure 1.2. Central responses for different time step sizes and error tolerances



1.3 (a) $\omega = 3 \text{ rad/s}$

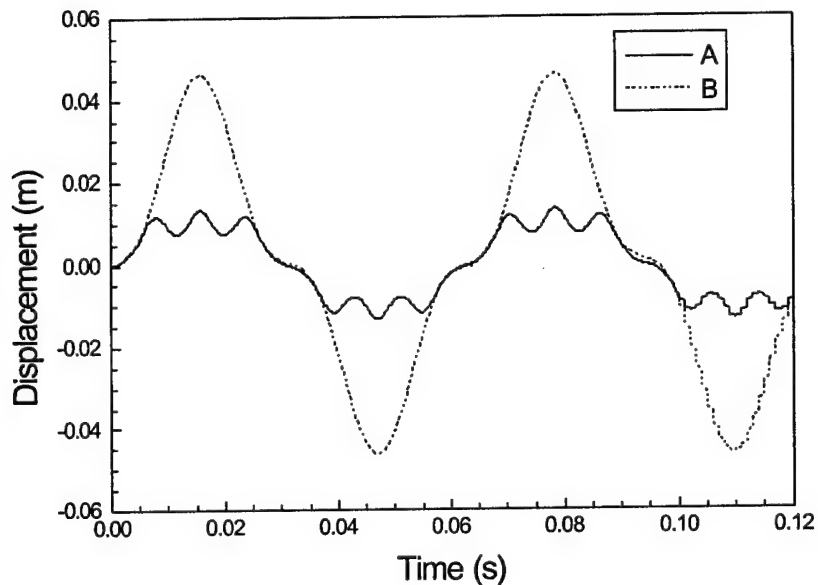
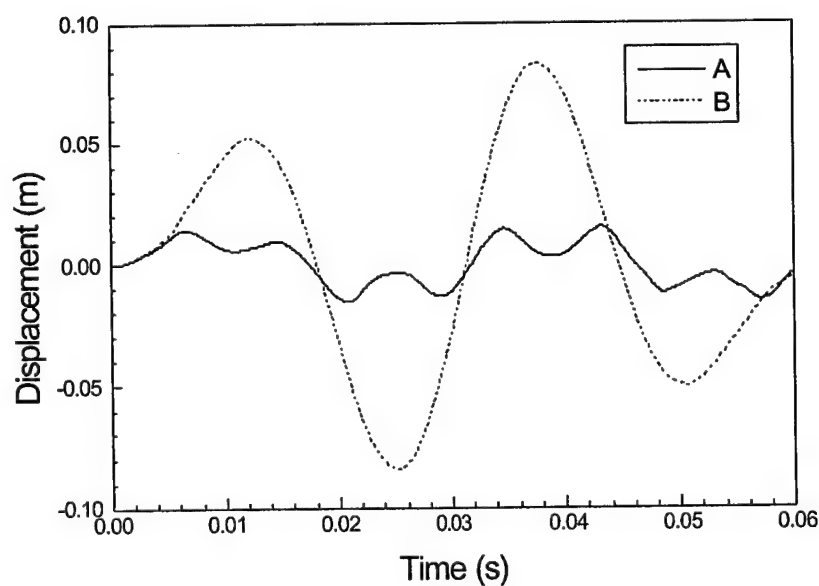
1.3 (b) $\omega=100\text{rad/s}$ 1.3 (c) $\omega=200\text{rad/s}$

Figure 1.3. Central responses for different cases

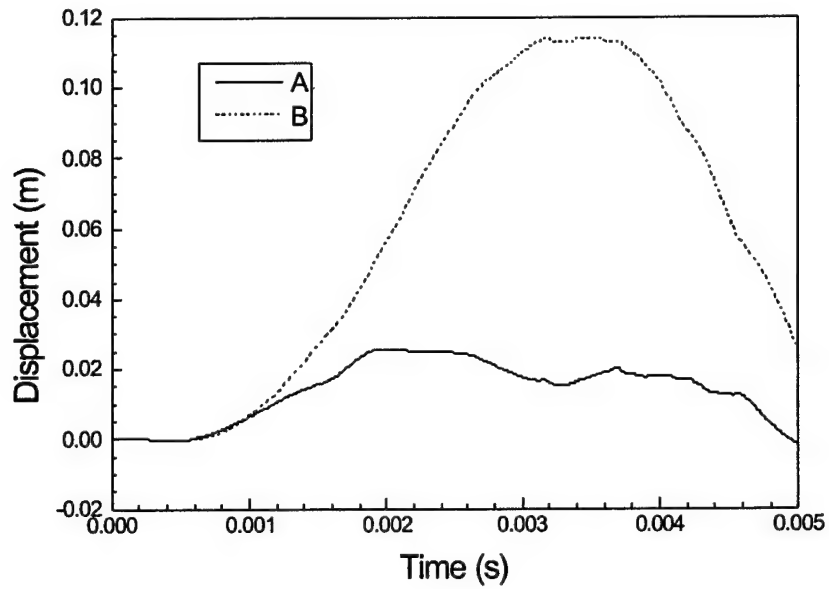


Figure 1.4. Translational responses at the center of plate

CHAPTER 2

NONLINEAR PLATE ANALYSIS USING COROTATIONAL FORMULATIONS

2.1 Introduction

2.2 Nonlinear Static Analysis of Plates

2.3 Nonlinear Dynamic Analysis of Plates

2.4 Summary

2.5 Appendix

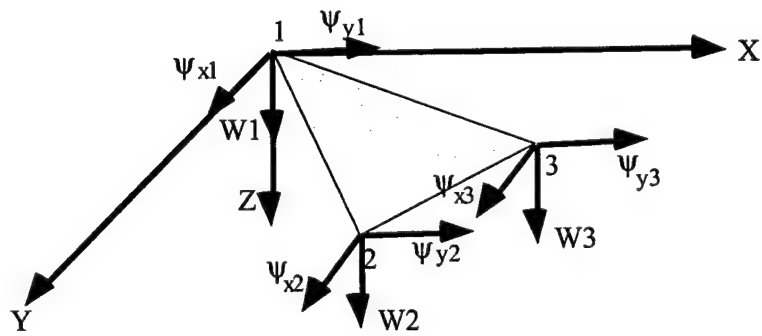
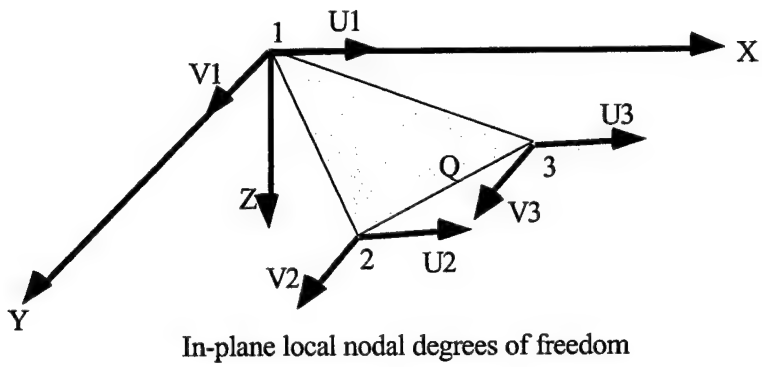
2.1 Introduction

Geometric non-linearity is increasingly being considered in structural analysis especially for those structures that undergo large displacement with very little actual staining occurring, such as beams and plates. There are many works on the way in which the geometrically nonlinear problems may be formulated. Three main methods are currently employed, the Total Lagrangian (TL) formulation, the Updated Lagrangian (UL) formulation, and the Co-Rotational (CR) formulation. Each of these formulation has its inherent drawbacks, merits and advocates. The TL formulation in which the original undeformed configuration is taken as the reference configuration is only really effective for relatively small rotation. The UL formulation where the configuration at the end of the last iteration is used as the reference configuration can be path dependent and can also show very slow convergence. The CR formulation which makes use of both the original configuration and the current deformed configuration to formulate the system matrices, although restricted to small rotation between iterations^{1,2}, exhibits good rate of convergence and thereby reducing the computation time. In this work, the CR formulation for static and dynamic analysis of plate structures using DKT triangular elements is presented. A number of numerical examples are presented that fully test the capabilities of the formulation. The CR formulation code developed in this study can be used for more understanding and realistic assessment of the panel flutter problems.

2.2 Nonlinear Static Analysis of Plates

2.2.1 Elements in the Analysis

Large deflection plate problem generally involves the coupling of in-plane and out-of-plane effects. In-plane deformation associated with the constant strain triangle with six degrees of freedom, two at each node, and out-of-plane deformation associated with the DKT triangle with nine degrees of freedom, three at each node, are shown in Figure 2.1. Local displacement has, in total, fifteen degrees of freedom, five at each node, of the triangular element. Local and global degrees of freedom are represented by D and d , respectively. Symbolically, they are given by



Out-of-plane local nodal degrees of freedom

Figure 2.1 Degrees of freedom (in-plane and out-of-plane)

$$D = U_1 \ V_1 \ W_1 \ \psi_{x1} \ \psi_{y1} \ U_2 \ V_2 \ W_2 \ \psi_{x2} \ \psi_{y2} \ U_3 \ V_3 \ W_3 \ \psi_{x3} \ \psi_{y3}^T \quad (2.1)$$

and

$$d = u_1 \ v_1 \ w_1 \ \theta_{x1} \ \theta_{y1} \ u_2 \ v_2 \ w_2 \ \theta_{x2} \ \theta_{y2} \ u_3 \ v_3 \ w_3 \ \theta_{x3} \ \theta_{y3}^T \quad (2.2)$$

For plane stress: $[u] = u_1 \ u_2 \ u_3^T, [v] = v_1 \ v_2 \ v_3^T,$

For bending: $[w] = w_1 \ \theta_{x1} \ \theta_{y1} \ w_2 \ \theta_{x2} \ \theta_{y2} \ w_3 \ \theta_{x3} \ \theta_{y3}^T,$

Where $\theta_{x1} = \tan^{-1}\left(\frac{\partial w_1}{\partial y}\right)$ and $\theta_{y1} = -\tan^{-1}\left(\frac{\partial w_1}{\partial x}\right)$ and so on.

2.2.2 General Procedures of Large Deflection Analysis of Plates

1. Generate the element stiffness matrix K_p (6×6) for plane stress condition (appendix-2) and K_B (9×9) for plate bending (Appendix-3) and assemble them to find the element stiffness matrix K_e (15×15) in local co-ordinates. It is obvious that the element stiffness matrix in global coordinates would be the same as K_e ;
2. Assemble all the element stiffness matrices to obtain global structure stiffness matrix K . The equilibrium equation in global coordinates is $[K] d = r$ where d is the vector of nodal displacement components and $[r]$ is the vector of externally applied nodal forces. Solve the equilibrium equation to obtain the global displacement vector d ;
3. Compute the element stiffness matrix K_e^{new} in its current local configuration and establish the transformation matrix $[T]$ (15×15) as derived in Appendix-1;
4. Determine the local displacement vector D from global displacement vector d . Local displacements are defined as the displacement of the nodal points of the deformed element from the nodes of an undeformed *reference element* (1" - 2" - 3") located in the $X^d - Y^d$ plane as shown in Figure 2.2;
5. Compute the local resisting force $Q = K_e [D]$;

6. Transform the resisting force \mathbf{Q} and stiffness matrix \mathbf{K}_e to global orientation by $[\mathbf{T}]^T \mathbf{Q}$ and $[\mathbf{T}]^T \mathbf{K}_e [\mathbf{T}]$, respectively, and assemble them to obtain \mathbf{q} and \mathbf{K} in global coordinates;
7. Compute the increments in global displacement $\Delta\mathbf{d}$ by solving the incremental equilibrium equation $[\mathbf{K}] \Delta\mathbf{d} = [\Delta\mathbf{r}]$, where $[\Delta\mathbf{r}] = [\mathbf{r} - \mathbf{q}]$;
8. Determine the new estimate of global displacement $[\mathbf{d}_{\text{new}}] = [\mathbf{d}] + [\Delta\mathbf{d}]$ and repeat steps 3 through 7 until $\Delta\mathbf{r}$ becomes arbitrarily small;
9. Apply a new load increment and follow the steps 3 through 8 until equilibrium is established for the new load increment.

2.2.3 Coordinate System

Coordinate systems before and after deformation of the triangular element used in the analysis are shown in Figure 2.2.

1. x, y, z : the global coordinate system before deformation. Plate element initially lies completely on $x-y$ plane. Hence, x_i, y_i is the global coordinates of any point on the element before deformation. The global coordinates of nodes 1, 2 and 3 are x_1, y_1 , x_2, y_2 and x_3, y_3 , respectively, with z -coordinate of each node being zero.
2. X, Y : Local coordinates of any point on the element before deformation. The local coordinates of nodes 1, 2 and 3 are X_1, Y_1 , X_2, Y_2 and X_3, Y_3 , respectively.

$$X_i, Y_i = x_i, y_i - x_1, y_1$$

3. x^d, y^d, z^d : Global coordinates of any point on the element after deformation. The global coordinates of nodes 1, 2 and 3 of the deformed element are (x_1^d, y_1^d, z_1^d) , (x_2^d, y_2^d, z_2^d) and x_3^d, y_3^d, z_3^d , respectively.

$$x_i^d, y_i^d, z_i^d = (x_i, y_i, 0) + u_i, v_i, w_i$$

4. X^d, Y^d, Z^d : Local coordinates of any point on the element after deformation. The local coordinates of nodes 1, 2, and 3 are X_1^d, Y_1^d, Z_1^d , X_2^d, Y_2^d, Z_2^d and X_3^d, Y_3^d, Z_3^d , respectively.

5. X^u, Y^u : Local coordinates of any point on the undeformed *reference element* whose first node coincides with the first node of the deformed element. Z^u -coordinate of the undeformed reference element ($1''-2''-3''$) is zero as it completely lies on X^d-Y^d plane.

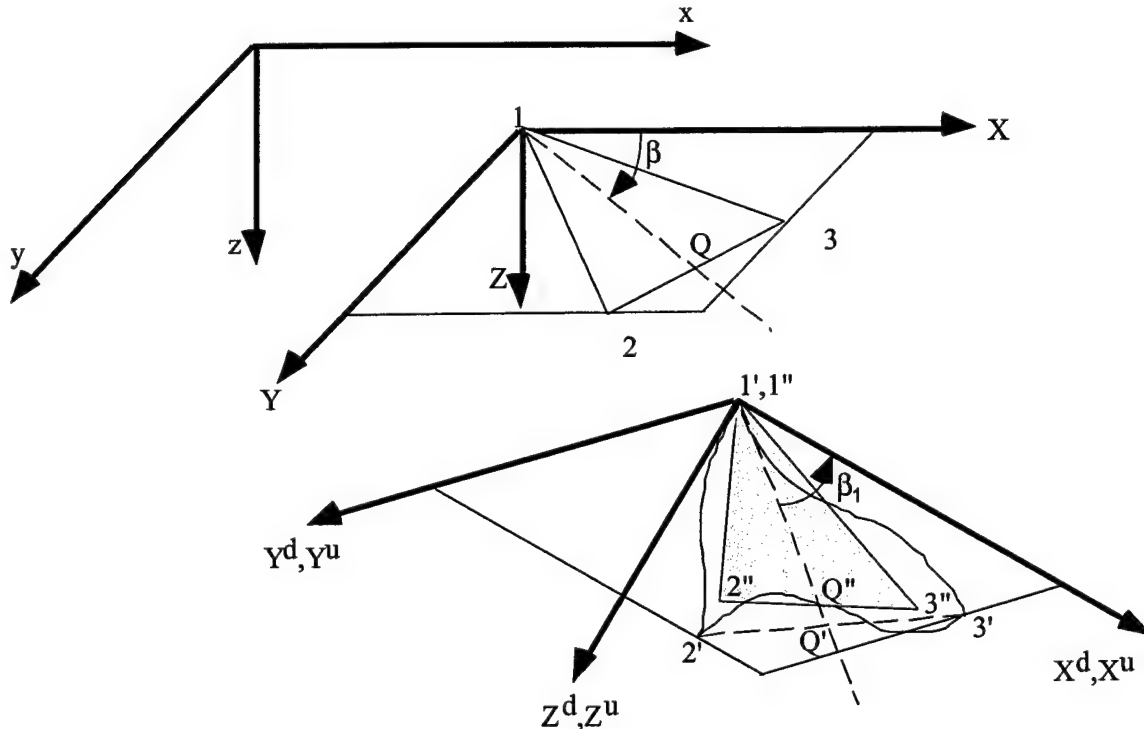


Figure 2.2 Coordinate systems before and after deformation

2.2.4 Determination of local displacement D from global displacement d

1. Compute global coordinates after deformation (x_1^d, y_1^d, z_1^d) , (x_2^d, y_2^d, z_2^d) and (x_3^d, y_3^d, z_3^d) from the global displacement vector

$d = u_1 \ v_1 \ w_1 \ \theta_{x1} \ \theta_{y1} \ u_2 \ v_2 \ w_2 \ \theta_{x2} \ \theta_{y2} \ u_3 \ v_3 \ w_3 \ \theta_{x3} \ \theta_{y3}$ T obtained in step-2 of Art. 1.2 and the input global coordinates x, y, z before deformation. The relationship stands for

$$x_i^d, y_i^d, z_i^d = (x_i, y_i, 0) + u_i, v_i, w_i$$

2. Rearrange the displacement vector d as

$$[\mathbf{d}_a] = \left[\underbrace{\mathbf{u}_1 \ \mathbf{u}_2 \ \mathbf{u}_3 \ \mathbf{v}_1 \ \mathbf{v}_2 \ \mathbf{v}_3 \ \mathbf{w}_1 \ \mathbf{w}_2 \ \mathbf{w}_3}_{\text{Translational components of displacement}} \ \underbrace{\theta_{x1} \ \theta_{y1} \ \theta_{x2} \ \theta_{y2} \ \theta_{x3} \ \theta_{y3}}_{\text{Rotational components of displacement}} \right]^T;$$

3. Compute the new coordinate transformation matrix T_t from equation A2.8 as described in Appendix-1 and determine the local co-ordinates of $2''(X_2^u, Y_2^u)$, $3''(X_3^u, Y_3^u)$;
4. Determine the translational components of the nodal displacements in local coordinates as

$$\begin{bmatrix} U \\ V \\ W \end{bmatrix}_i = \begin{bmatrix} a_{11} & a_{12} & a_{13} \\ a_{21} & a_{22} & a_{23} \\ a_{31} & a_{32} & a_{33} \end{bmatrix} \begin{bmatrix} u \\ v \\ w \end{bmatrix}$$

in which $\begin{bmatrix} u \\ v \\ w \end{bmatrix} = \begin{bmatrix} u - u_1 + 1 - a_{11} X_i^u & -a_{21} Y_i^u \\ v - v_1 & -a_{12} X_i^u + (1 - a_{22}) Y_i^u \\ w - w_1 & -a_{13} X_i^u & -a_{23} Y_i^u \end{bmatrix}$

5. Compute rotational components of nodal displacement in the local coordinate system

$$\Psi_{Xi} = -\tan \frac{\partial W_i}{\partial Y^d}; \Psi_{Yi} = \tan \frac{\partial W_i}{\partial X^d}$$

$$\begin{aligned} \text{in which, } \frac{\partial W_i}{\partial X^d} &= \frac{\left(a_{11} X_X^u + a_{21} Y_X^u + a_{11} U_{XE} + a_{21} V_{XE} \right) \left(a_{31} + a_{33} \frac{\partial w_i}{\partial x^d} \right)}{1 - a_{31} \left(a_{31} + a_{33} \frac{\partial w_i}{\partial x^d} \right) - a_{32} \left(a_{32} + a_{33} \frac{\partial w_i}{\partial y^d} \right)} \text{ and} \\ \frac{\partial W_i}{\partial Y^d} &= \frac{\left(a_{12} X_X^u + a_{22} Y_X^u + a_{12} U_{XE} + a_{22} V_{XE} \right) \left(a_{32} + a_{33} \frac{\partial w_i}{\partial y^d} \right)}{1 - a_{31} \left(a_{31} + a_{33} \frac{\partial w_i}{\partial x^d} \right) - a_{32} \left(a_{32} + a_{33} \frac{\partial w_i}{\partial y^d} \right)} \end{aligned}$$

where, $\frac{\partial w_i}{x^d} = \tan^{-1}(\theta_{y_i}) ; \frac{\partial w_i}{\partial y^d} = -\tan^{-1}(\theta_{x_i})$

$$X_x^u = \frac{\partial X^u}{\partial X^d} = \frac{1 + \frac{\partial V_i}{\partial Y^u}}{\left(1 + \frac{\partial U_i}{\partial X^u}\right)\left(1 + \frac{\partial V_i}{\partial Y^u}\right) - \frac{\partial U_i}{\partial Y^u} \frac{\partial V_i}{\partial X^u}} \text{ and}$$

$$Y_x^u = \frac{\partial Y^u}{\partial X^d} = \frac{-\frac{\partial V_i}{\partial Y^u}}{\left(1 + \frac{\partial U_i}{\partial X^u}\right)\left(1 + \frac{\partial V_i}{\partial Y^u}\right) - \frac{\partial U_i}{\partial Y^u} \frac{\partial V_i}{\partial X^u}}$$

Similar values for $X_Y^u = \frac{\partial X^u}{Y^d}$ and $Y_Y^u = \frac{\partial Y^u}{Y^d}$ can be computed as

$$X_Y^u = \frac{\partial X^u}{\partial Y^d} = \frac{-\frac{\partial U_i}{\partial Y^u}}{\left(1 + \frac{\partial U_i}{\partial X^u}\right)\left(1 + \frac{\partial V_i}{\partial Y^u}\right) - \frac{\partial U_i}{\partial Y^u} \frac{\partial V_i}{\partial X^u}}$$

$$Y_Y^u = \frac{\partial Y^u}{\partial Y^d} = \frac{1 + \frac{\partial U_i}{\partial X^d}}{\left(1 + \frac{\partial U_i}{\partial X^d}\right)\left(1 + \frac{\partial V_i}{\partial Y^d}\right) - \frac{\partial U_i}{\partial Y^d} \frac{\partial V_i}{\partial X^d}}$$

Now, $U_{XE} = \frac{\partial U_i}{\partial X^u} \left(\frac{\partial X^u}{\partial X^d} \right) + \frac{\partial U_i}{\partial Y^u} \left(\frac{\partial Y^u}{\partial X^d} \right), V_{XE} = \frac{\partial V_i}{\partial X^u} \left(\frac{\partial X^u}{\partial X^d} \right) + \frac{\partial V_i}{\partial Y^u} \left(\frac{\partial Y^u}{\partial X^d} \right)$,

$U_{YE} = \frac{\partial U_i}{\partial Y^u} \left(\frac{\partial Y^u}{\partial Y^d} \right) + \frac{\partial U_i}{\partial X^u} \left(\frac{\partial X^u}{\partial Y^d} \right), V_{YE} = \frac{\partial V_i}{\partial Y^u} \left(\frac{\partial Y^u}{\partial Y^d} \right) + \frac{\partial V_i}{\partial X^u} \left(\frac{\partial X^u}{\partial Y^d} \right)$ can easily be computed.

From equations A2.10 and A2.11 (Appendix-2), it can be seen that the values of $\frac{U_i}{\partial X^u}, \frac{\partial U_i}{Y^u}, \frac{\partial V_i}{X^u}$,

$\frac{\partial V_i}{Y^u}$ are all constants and they are,

$$\frac{\partial U_i}{X^u} = \alpha_2 = \frac{1}{2\Delta} [(y_2 - y_3)U_1 + (y_3 - y_1)U_2 + (y_1 - y_2)U_3]$$

$$\frac{\partial U_i}{Y^u} = \alpha_3 = \frac{1}{2\Delta} [(x_3 - y_2)U_1 + (x_1 - x_3)U_2 + (x_2 - x_1)U_3]$$

$$\frac{\partial V_i}{X^u} = \beta_2 = \frac{1}{2\Delta} [(y_2 - y_3)V_1 + (y_3 - y_1)V_2 + (y_1 - y_2)V_3]$$

$$\frac{\partial V_i}{Y^u} = \beta_3 = \frac{1}{2\Delta} [(x_3 - y_2)V_1 + (x_1 - x_3)V_2 + (x_2 - x_1)V_3]$$

6. Rearrange the D_a^{-T} to corner order to have D^{-T} .

2.2.5 Results and Discussion

Example 1

A clamped square plate subjected to a uniformly distributed load q is considered. The plate is of $7620 \text{ mm} \times 7620 \text{ mm}$ having a thickness of 76.2 mm . Modulus of elasticity (E) and Poisson's ratio (ν) are $2.0685 \times 10^5 \text{ N/mm}^2$ and 0.316 , respectively. This example has also been used by Selvam and Qu³. The analytical thin plate solution is given by Levy⁴ who solved von Karman's equations using double fourier series.

The plate is divided into 288 triangular elements. The number of nodes was 169. The error tolerance was 10^{-4} . The results are shown in Table 2.1 where $Q = qa^4/Et^4$ is a non-dimensional uniformly distributed load. It can be observed that the present analysis estimates the results well.

Example 2

The program is checked by using a simply supported square plate with immovable inplane edges. The other parameters are identical to Example 1. The results are listed in Table 2.2. The program was checked for linear analysis using a concentrated load P equal to 10^5 N at the center of the plate. The result is checked against the standard solution ($\delta_{\max} = \alpha Pa^2/D = 7.9495 \text{ mm}$) as derived by Timoshenko⁵. The maximum deflection was found to be 7.9324 mm with an estimated error of 0.2%.

Table 2.1 Comparison of the ratios of central deflections to thickness
for different methods (clamped plate)

Q	D_{max}/t						% Error
	Exact	Wood	Pica, et al	Rao, et al	Selvam, et al	Present	
17.79	0.237	0.2387	0.2351	0.2346	0.2383	0.2391	0.886
38.30	0.471	0.4717	0.4673	0.4660	0.4636	0.4748	0.807
63.40	0.695	0.6916	0.6887	0.6862	0.6791	0.6990	0.576
95.00	0.912	0.9008	0.9003	0.8987	0.8721	0.9131	0.121
134.90	1.121	1.1025	1.1041	1.1025	1.0677	1.1193	0.152
184.00	1.323	1.2961	1.2990	1.2979	1.2595	1.3168	0.469
245.00	1.521	1.4879	1.4913	1.4890	1.4539	1.5106	0.684
318.00	1.714	1.6744	1.6774	1.6750	1.6475	1.7006	0.782
402.00	1.902	1.8529	1.8682	1.8526	1.8365	1.8802	1.146

Table 2.2 Comparison of the ratios of central deflections to thickness
for different methods (Simply supported)

Q	D_{max}/t			
	Russton	Pica, et al	Selvam et al	Present
9.16	0.3350	0.3478	0.3296	0.3424
36.60	0.8180	0.8184	0.7625	0.8073
146.50	1.4700	1.4655	1.4168	1.4471
586.00	2.4000	2.3927	2.4520	2.3706
2344.00	3.8300	3.8124	4.1733	3.7836
9377.00	6.0700	6.0521	7.1272	6.0273

The computation in each loading was obtained by using a single load increment i.e. the load for which the solution is sought is applied in full at a time and the iteration was performed within this load until the difference of the applied full load and the resisting forces becomes minimum(of the order of 10^{-4}). The computation can also be performed by using as many load steps as desired without using the full load at a time. But the number of iterations is much less for the former case. As we are interested in the central deflection of the plate, the computation was performed with the error tolerance based on the difference of the central deflection in consecutive two iterations. It was observed that the solution begins to diverge at a load equal to and greater than $Q=586$ ($D_{max}/t=2.314$) for which the problem becomes highly non-linear. For convergence of the solution for higher loads, a relaxation factor (R_f) of 0.3 was used. After a few trial computations it was found that the result begins to diverge

for a load when D_{max}/t becomes approximately equal to 1.90 and an introduction of relaxation factor is then needed for the convergence of the solution.

Example 3

In this case, a simply supported square plate of size and thickness equal to 16 inch and 0.1 inch, respectively was used. In the computation, the modulus of elasticity (E) and Poisson's ratio (v) were taken as 30×10^6 psi, 0.316, respectively. This example was used by Murray⁶. The central deflection was carried out for $q=15$ psi in 5 increments and the results are shown in Table 2.3 along with the results read from the graph produced by Murray. For higher loads the deflection was computed and the results are shown in Table 2.4.

Table 2.3 Comparison of the ratios of central deflections
to thickness (Simply supported)

q,psi	D_{max}/t	
	Analysis	Murray (read from graph)
3	1.0499	1.05
6	1.3868	1.38
9	1.6122	1.60
12	1.7875	1.78
15	1.9335	1.92

Table 2.4 Central deflection of the plate

q,psi	20	40	60	80	100	120	140
D_{max}/t	2.1362	2.7044	3.0990	3.4129	3.6774	3.9088	4.1152

2.3 Nonlinear Dynamic Analysis of Plates

2.3.1 Formulation of Nonlinear Dynamic Equations

Newmark implicit time integration scheme is employed to calculate the nonlinear dynamic response. For convenience, the damping is not considered in the present calculation although the inclusion of damping will not affect the formulation. The dynamic equations for the large deflection problems without damping can be written in matrix form as:

$$\begin{bmatrix} M_B & 0 \\ 0 & M_P \end{bmatrix} \begin{bmatrix} \ddot{D}_B \\ \ddot{D}_P \end{bmatrix} + \begin{bmatrix} K_B & 0 \\ 0 & K_P \end{bmatrix} \begin{bmatrix} D_B \\ D_P \end{bmatrix} = \begin{bmatrix} F_B \\ F_P \end{bmatrix} \quad (2.3)$$

where the subscripts B and P represents the characteristics associated with the bending and in-plane nodal displacements, respectively. Equation (2.2) can be written in general form as

$$M\ddot{D} + KD = F \quad (2.4)$$

If the thickness of an element is t and that is assumed to be constant within the element, the consistent mass matrix can be computed from the following equation:

$$M_e = \rho t \iint N^T N dx dy \quad (2.5)$$

The following displacement functions are used to develop the mass matrix for flexure⁷

$$N^T = \begin{bmatrix} L_1 + L_1^2 L_2 + L_1^2 L_3 - L_1 L_2^2 - L_1 L_3^2 \\ b_2 \left(L_1^2 L_3 + \frac{1}{2} L_1 L_2 L_3 \right) - b_3 \left(L_1^2 L_2 + \frac{1}{2} L_1 L_2 L_3 \right) \\ c_2 \left(L_1^2 L_3 + \frac{1}{2} L_1 L_2 L_3 \right) - c_3 \left(L_1^2 L_2 + \frac{1}{2} L_1 L_2 L_3 \right) \\ L_2 + L_2^2 L_3 + L_2^2 L_1 - L_2 L_3^2 - L_2 L_1^2 \\ b_3 \left(L_2^2 L_1 + \frac{1}{2} L_1 L_2 L_3 \right) - b_1 \left(L_2^2 L_3 + \frac{1}{2} L_1 L_2 L_3 \right) \\ c_3 \left(L_2^2 L_1 + \frac{1}{2} L_1 L_2 L_3 \right) - c_1 \left(L_2^2 L_3 + \frac{1}{2} L_1 L_2 L_3 \right) \\ L_3 + L_3^2 L_1 + L_3^2 L_2 - L_3 L_1^2 - L_3 L_2^2 \\ b_1 \left(L_3^2 L_2 + \frac{1}{2} L_1 L_2 L_3 \right) - b_2 \left(L_3^2 L_1 + \frac{1}{2} L_1 L_2 L_3 \right) \\ c_1 \left(L_3^2 L_2 + \frac{1}{2} L_1 L_2 L_3 \right) - c_2 \left(L_3^2 L_1 + \frac{1}{2} L_1 L_2 L_3 \right) \end{bmatrix} \quad (2.6)$$

The mass matrix for flexure has been computed numerically following the procedures given by Anderson⁸ and that for membrane can be determined explicitly and is given by Zienkiewicz⁷. The formulation of stiffness matrix has been described in the static part.

Employing Newmark's assumptions

$${}^{t+\Delta t}\dot{D} = {}^t\dot{D} + [1 - \delta] {}^t\ddot{D} + \delta {}^{t+\Delta t}\ddot{D} \Delta t \quad (2.7)$$

$${}^{t+\Delta t}D = {}^tD + {}^t\dot{D} \Delta t + \left[\left(\frac{1}{2} - \alpha \right) {}^t\ddot{D} + \alpha {}^{t+\Delta t}\ddot{D} \right] \Delta t^2 \quad (2.8)$$

The equilibrium equation at time $t + \Delta t$

$$M^{t+\Delta t} \ddot{D} + K^{t+\Delta t} D = {}^{t+\Delta t} F \quad (2.9)$$

Expression for ${}^{t+\Delta t} \ddot{D}$ can be obtained by solving equation (2.8) for ${}^{t+\Delta t} \ddot{D}$ in terms of the unknown displacement ${}^{t+\Delta t} D$ and then substituting for ${}^{t+\Delta t} \ddot{D}$ into equation (2.7), expression for the velocity ${}^{t+\Delta t} \dot{D}$ can be obtained. These are as follow:

$${}^{t+\Delta t} \ddot{D} = a_0 {}^{t+\Delta t} D - a_2 {}^t D - a_3 {}^t \dot{D} = a_0 {}^{t+\Delta t} D - {}^t Q \quad (2.10)$$

$${}^{t+\Delta t} \dot{D} = {}^t \dot{D} + a_6 {}^t \ddot{D} + a_7 {}^{t+\Delta t} \ddot{D} = a_7 {}^{t+\Delta t} \ddot{D} + {}^t R \quad (2.11)$$

where ${}^t Q = [a_0 {}^t D + a_2 {}^t \dot{D} + a_3 {}^t \ddot{D}]$ and $R = [{}^t \dot{D} + a_6 {}^t \ddot{D}]$. Expression for the unknown displacement ${}^{t+\Delta t} D$ can be obtained by substituting equation (2.10) into equation (2.9) as

$$a_0 M + K {}^{t+\Delta t} D = {}^{t+\Delta t} \hat{F} \quad (2.12)$$

Where the effective load vector, ${}^{t+\Delta t} \hat{F}$ at time $t + \Delta t$ is given by

$${}^{t+\Delta t} \hat{F} = {}^{t+\Delta t} F + M a_0 {}^t D + a_2 {}^t \dot{D} + a_3 {}^t \ddot{D} = {}^{t+\Delta t} R + M {}^t Q \quad (2.13)$$

2.3.2 Iteration schemes

Using implicit time integration, the equilibrium of the system at time $t + \Delta t$ is considered. This requires in nonlinear analysis that iteration be performed. Neglecting the effects of damping matrix and using the modified Newton-Raphson iteration, the governing equilibrium equations are:

$${}^{t+\Delta t} M^n {}^{t+\Delta t} \ddot{D}^n + {}^{t+\Delta t} K^n \Delta D^n = {}^{t+\Delta t} F - {}^{t+\Delta t} P^{n-1} \quad (2.14)$$

and

$${}^{t+\Delta t} D^n = {}^{t+\Delta t} D^{n-1} + \Delta D^n \quad (2.15)$$

where ${}^{t+\Delta t} P^{n-1}$ is the static resisting force. Using the expression of acceleration at time $t + \Delta t$, ${}^{t+\Delta t} \ddot{D}$ in equation (2.10), equation (2.15) can be written as

$${}^{t+\Delta t} \ddot{D}^n = a_0 {}^{t+\Delta t} D^{n-1} - {}^t Q + a_0 \Delta D^n \quad (2.16)$$

and the velocity

$${}^{t+\Delta t} \dot{D}^n = a_7 {}^{t+\Delta t} \ddot{D}^n + {}^t R \quad (2.17)$$

Substituting equation (2.16) in equation (2.14), the final expression for the incremental displacement ΔD^n can be obtained as

$$a_0^{t+\Delta t} M^n + a_1^{t+\Delta t} K^n \Delta D^n = a_0^{t+\Delta t} F - a_1^{t+\Delta t} P^{n-1} - a_2^{t+\Delta t} M^n a_0^{t+\Delta t} D^{n-1} - a_3^{t+\Delta t} Q \quad (2.18)$$

2.3.3 Steps of Computing Nonlinear Dynamic Response

1. Compute: Stiffness matrix, K, Mass matrix, M, Damping matrix, C;
2. Set initial conditions at time, Displacement, D_0 and Velocity, \dot{D}_0 ;
3. Compute initial accelerations, \ddot{D}_0 , $\ddot{D}_0 = M^{-1} [F_0 - C\dot{D}_0 - K D_0]$;
4. Select: Time step, Δt and Parameters, α and γ . Calculate Integration constants $a_0, a_1, a_2, a_3, a_4, a_5, a_6$, and a_7 ;
5. Form effective stiffness matrix \hat{K} , $\hat{K} = K + a_0 M + a_1 C$ and factorize it $\hat{K} = LUL^T$;
6. Calculate effective loads at time $t + \Delta t$, $\hat{F} = a_0 F + M' Q + C' S$, where,
 $'Q = [a_0 'D + a_2 'D + a_3 'D]$ and $'S = [a_1 'D + a_4 'D + a_5 'D]$;
7. Solve for displacement at time $t + \Delta t$, $\hat{D} = (LUL^T)^{t+\Delta t} F$;
8. Calculate acceleration and velocity at time $t + \Delta t$, $\hat{D} = a_0^{t+\Delta t} D - a_1^{t+\Delta t} Q$ and
 $\hat{\dot{D}} = a_7^{t+\Delta t} \ddot{D} + R$;
9. Now for the n-th iteration at this instant of time, $t + \Delta t$:
 - (a) Transform the displacement \hat{D} into local co-ordinates (\hat{d}), establish local element stiffness (k) and element mass (m) matrices. Compute local balancing elastic forces, and transform and assemble it to global axis ($\sum T^T \hat{k} \hat{d}$). Compute the global mass matrix (M) from $\sum T^T m T$ and global stiffness matrix K from $\sum T^T k T$;
 - (b) Calculate the unbalanced forces at time, $t + \Delta t$ at the n-th iteration as
 $\Delta F^n = a_0^{t+\Delta t} F - \sum T^T k \hat{d} - a_1^{t+\Delta t} M^{n-1} \hat{D}^{n-1}$
 $\Delta F^n = a_0^{t+\Delta t} F - \sum T^T k \hat{d} - a_1^{t+\Delta t} M^{n-1} a_0^{t+\Delta t} D^{n-1} - a_3^{t+\Delta t} Q$;
 - (c) Compute the effective stiffness as $\hat{K}^n = a_0^{t+\Delta t} K^{n-1} + a_1^{t+\Delta t} M^{n-1}$;
 - (d) Solve for incremental displacement $\Delta D^n = \hat{K}^n \Delta F^n$;
 - (e) Update displacement, acceleration, and velocity by
 $D^n = D^{n-1} + \Delta D^n$, $\dot{D}^n = a_0^{t+\Delta t} D^{n-1} - Q + a_0 \Delta D^n$ and $\ddot{D}^n = a_0^{t+\Delta t} \ddot{D}^{n-1} + R$, respectively;

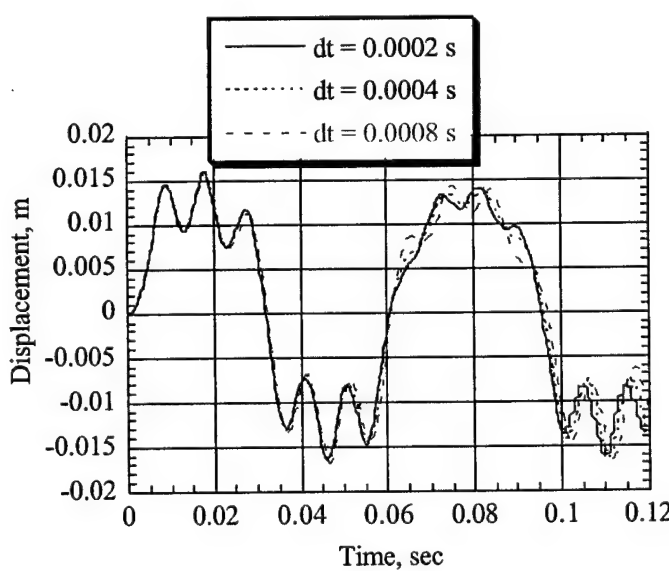
- (f) Continue from 9(a) to 9(e) until the both or either of the following two criteria has been met
 (i) an error limit based on unbalanced forces i.e. $\frac{\| \Delta F^n \|}{\| F^n \|} < \text{specified limit}$, (ii) an error limit based on displacement, i.e. $\frac{\| \Delta D^n \|}{\| D^n \|} < \text{specified limit}$.

2.3.4 Results

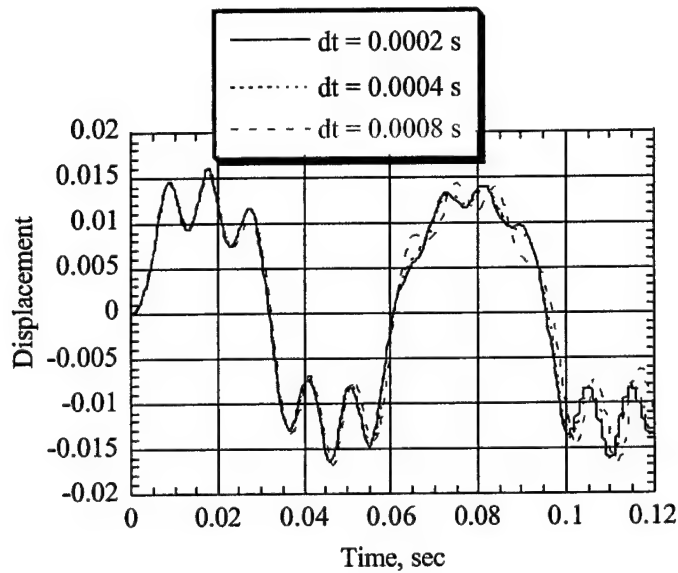
Example 1:

A simply supported square steel plate is considered. The length of the side and thickness are respectively, 1.0 m and 0.01 m. The modulus of elasticity and the Poisson's ratio are $2.0 \times 10^{11} \text{ N/m}^2$ and 0.3, respectively. A concentrated load $P = 50000 \sin \omega t \text{ N}$ is assumed to be acting on the center of the plate and the central responses were computed for $\omega = 3 \text{ rad/s}$, 100 rad/s and 200 rad/s .

Figure 2.3 shows the central responses at different time steps with different error levels at a forcing frequency of 100 rad/s . Figure 2.4 shows the linear and nonlinear central responses at different frequencies. At low frequencies (3 rad/s) the nonlinear responses are similar to results presented in the report of Selvam and Qu, but at higher frequencies (100 rad/s and 200 rad/s) the response does not match exactly with the report especially at later times.



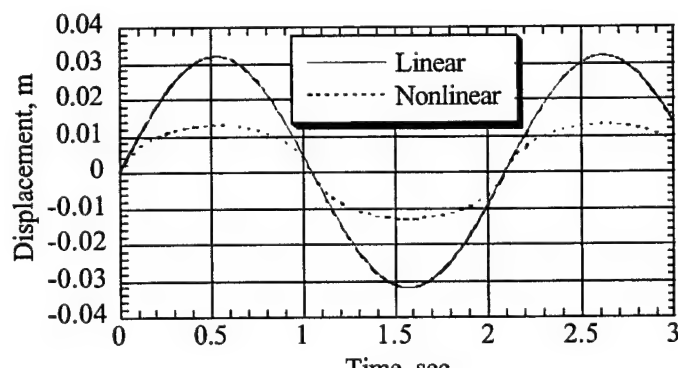
(a)



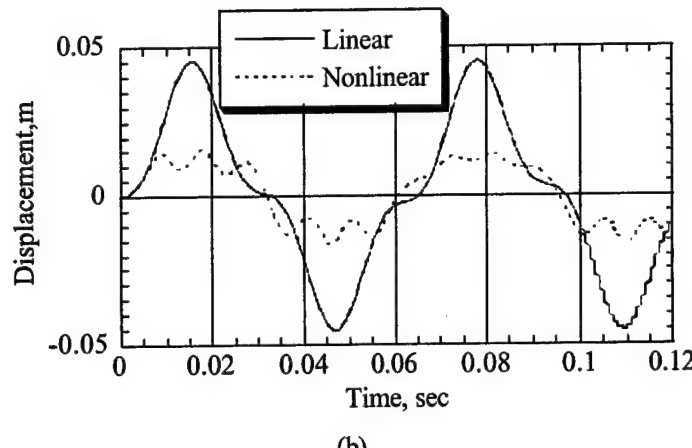
(b)

Figure 2.3 Central responses of the plate at $\omega=3 \text{ rad/s}$ at different time steps with an error level of

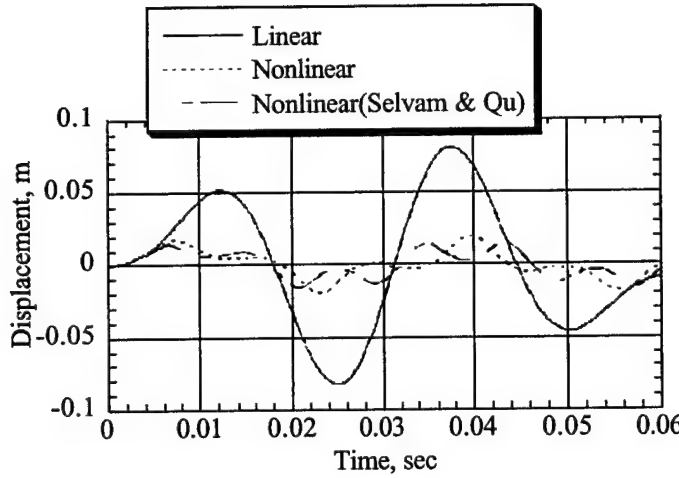
(a) 10^{-5} and (b) 10^{-7}



(a)



(b)



(c)

Figure 2.4 Central responses of the plate at (a) $\omega=3 \text{ rad/s}$, (b) $\omega=100 \text{ rad/s}$, (c) $\omega=200 \text{ rad/s}$

2.4 Summary

A Co-Rotational formulation for static and dynamic analysis of geometrically non-linear plates is presented using DKT triangular elements. A number of numerical examples are provided and the results are compared with other methods of computation. The computation in each loading was obtained by using a single load increment i.e. the load for which the solution is sought is applied in full at a time and the iteration was performed within this load until the difference of the applied full

load and the resisting forces becomes minimum. The computation can also be performed by using as many load steps as desired without using the full load at a time. But the number of iterations was found to be much less for the former case. For proper convergence at higher load levels a relaxation factor has been introduced. For static analysis this formulation produces the closest results of all the methods to the exact solution. There are some discrepancies in responses between the present method and other methods in dynamics analysis of plates which needs to be investigated in future.

2.5 Appendix

2.5.1 Determination of Rotational Transformation Matrix

1. Determine the local co-ordinates of the undeformed triangular element $(X_1, Y_1), (X_2, Y_2)$ and X_3, Y_3 from the input global co-ordinates and determine the co-ordinates of Q

$$X_q, Y_q = \left(\frac{X_2 + X_3}{2}, \frac{Y_2 + Y_3}{2} \right) \quad (\text{A2.1})$$

and the angle

$$\beta = \tan^{-1} \left(\frac{Y_2 + Y_3}{X_2 + X_3} \right) \quad (\text{A2.2})$$

2. Define local co-ordinate system by identifying the X^d - Y^d plane by passing through all the three displaced nodes 1', 2', and 3'. Determine the co-ordinates of Q' as

$$x_q^d, y_q^d, z_q^d = \left(\frac{x_2^d + x_3^d}{2}, \frac{y_2^d + y_3^d}{2}, \frac{z_2^d + z_3^d}{2} \right) \quad (\text{A2.3})$$

3. The undeformed element is so placed on the displaced X^d - Y^d plane that the first node of the undeformed element coincides with the first node of the deformed element (origin of X^d - Y^d - Z^d coordinate system), i.e. $(X_1^d, Y_1^d) = 0,0$. (X_2^d, Y_2^d) and X_3^d, Y_3^d can be obtained by coordinate transformation Establish the vector

$$V_{rQ'} = V_{Q^d} = x_q^d - x_1^d \quad y_q^d - y_1^d \quad z_q^d - z_1^d = V_{Qx} \quad V_{Qy} \quad V_{Qz}$$

$$\text{Similarly vector } V_{1'2'} = \{x_2^d - x_1^d \quad y_2^d - y_1^d \quad z_2^d - z_1^d\}$$

A vector V_{Z^d} in the direction Z^d is given by the cross product $V_{Z^d} = V_{rQ'} \times V_{1'2'}$

$$\vec{V}_{Z^d} = \left\{ \begin{array}{l} y_q^d - y_1^d \quad z_2^d - z_1^d \quad -y_2^d - y_1^d \quad z_q^d - z_1^d \\ (z_q^d - z_1^d)(x_2^d - x_1^d) - (x_q^d - x_1^d)(z_2^d - z_1^d) \\ (x_q^d - x_1^d)(y_2^d - y_1^d) - (x_2^d - x_1^d)(y_q^d - y_1^d) \end{array} \right\}$$

$$\text{Or, } V_{Z^d} = V_{zx} \quad V_{zy} \quad V_{zz}$$

4. Now the vector perpendicular to $Z^d - 1' - Q'$ plane is given by $V_{R^d} = V_{Z^d} \times V_{1'Q'}$

$$V_{R^d} = V_{zy}V_{Qz} - V_{zz}V_{Qy} \quad V_{zz}V_{Qx} - V_{zx}V_{Qz} \quad V_{zx}V_{Qy} - V_{zy}V_{Qx}$$

5. Determine the magnitudes of the vectors V_{Q^d} , V_{Z^d} and V_{R^d} as

$$\begin{aligned} R_{Q^d} &= \sqrt{V_{Qx}^2 + V_{Qy}^2 + V_{Qz}^2} \\ R_{Z^d} &= \sqrt{V_{zx}^2 + V_{zy}^2 + V_{zz}^2} \\ R_{R^d} &= \sqrt{V_{Rx}^2 + V_{Ry}^2 + V_{Rz}^2} \end{aligned} \tag{A2.4}$$

6. Let (l_1, m_1, n_1) denotes the direction cosines of the vectors V_{Q^d} . Similarly l_2, m_2, n_2 and l_3, m_3, n_3 are the direction cosines of the vectors V_{Z^d} and V_{R^d} respectively. The direction cosines are given by

$$\begin{aligned} l_1 &= \frac{V_{Qx}}{R_{Q^d}}, \quad m_1 = \frac{V_{Qy}}{R_{Q^d}}, \quad n_1 = \frac{V_{Qz}}{R_{Q^d}} \\ l_2 &= \frac{V_{Rx}}{R_{R^d}}, \quad m_2 = \frac{V_{Ry}}{R_{R^d}}, \quad n_2 = \frac{V_{Rz}}{R_{R^d}} \\ l_3 &= \frac{V_{zx}}{R_{Z^d}}, \quad m_3 = \frac{V_{zy}}{R_{Z^d}}, \quad n_3 = \frac{V_{zz}}{R_{Z^d}} \end{aligned} \tag{A2.5}$$

The direction cosines of the new co-ordinate system are given in matrix form as

$$\begin{bmatrix} Q^d \\ R^d \\ Z^d \end{bmatrix} = \begin{bmatrix} l_1 & m_1 & n_1 \\ l_2 & m_2 & n_2 \\ l_3 & m_3 & n_3 \end{bmatrix} \begin{bmatrix} x' \\ y' \\ z' \end{bmatrix} \tag{A2.6}$$

7. Now rotate the coordinate system around Z^d by the angle β , and determine the transformation matrix $\underbrace{T_t}_{3 \times 3}$ from

$$\begin{bmatrix} X^d \\ Y^d \\ Z^d \end{bmatrix} = \begin{bmatrix} \cos\beta & \sin\beta & 0 \\ -\sin\beta & \cos\beta & 0 \\ 0 & 0 & 1 \end{bmatrix} \underbrace{\begin{bmatrix} l_1 & m_1 & n_1 \\ l_2 & m_2 & n_2 \\ l_3 & m_3 & n_3 \end{bmatrix}}_{T_t} \begin{bmatrix} x' \\ y' \\ z' \end{bmatrix} \quad (A2.7)$$

The elements of the transformation matrix is given by a_{ij} as

$$[T_t] = \begin{bmatrix} a_{11} & a_{12} & a_{13} \\ a_{21} & a_{22} & a_{23} \\ a_{31} & a_{32} & a_{33} \end{bmatrix} \quad (A2.8)$$

8. There are five degrees of freedom at each node of the element; three translational components and two rotational components. Hence the complete transformation matrix of the element would be

$$[T] = \begin{bmatrix} T_C & 0 & 0 \\ 0 & T_C & 0 \\ 0 & 0 & T_C \end{bmatrix} \quad (A2.9)$$

$$\text{where } [T_C] = \begin{bmatrix} a_{11} & a_{12} & a_{13} & 0 & 0 \\ a_{21} & a_{22} & a_{23} & 0 & 0 \\ a_{31} & a_{32} & a_{33} & 0 & 0 \\ 0 & 0 & 0 & a_{11} & a_{12} \\ 0 & 0 & 0 & a_{21} & a_{22} \end{bmatrix}$$

Steps in getting the transformation matrix $\underbrace{T}_{15 \times 15}$:

1. Determine the local coordinates of Q from equation (A2.1);
2. Compute the angle β (location of the median of the element from the local x-axis) for each element from equation (A2.2);
3. Compute the directions cosines of the new coordinate systems from equation (A2.5);
4. Compute the elements of the trasformation matrix for three translational components of displacement from equation (A2.7);
5. Determine the complete 15×15 transformation matrix T form equation (A2.9).

2.5.2 Derivation of Stiffness Matrix for Plane Stress Condition

Element displacement is represented in terms of nodal displacement as

$$u^e = \alpha_1 + \alpha_2 x + \alpha_3 y \text{ or, } u^e = 1 \quad x \quad y \quad \alpha_1 \quad \alpha_2 \quad \alpha_3^T \quad (\text{A2.10})$$

Similary,

$$v^e = \beta_1 + \beta_2 x + \beta_3 y \text{ or, } v^e = 1 \quad x \quad y \quad \beta_1 \quad \beta_2 \quad \beta_3^T \quad (\text{A2.11})$$

Local coordinates of nodes 1, 2 and 3 are (x_1, y_1) , (x_2, y_2) and (x_3, y_3) , respectively. From equation (A2.1), we have

$$u_1 = \alpha_1 + \alpha_2 x_1 + \alpha_3 y_1$$

$$u_2 = \alpha_1 + \alpha_2 x_2 + \alpha_3 y_2$$

$$u_3 = \alpha_1 + \alpha_2 x_3 + \alpha_3 y_3$$

which can be written in matrix form as

$$\begin{bmatrix} u_1 \\ u_2 \\ u_3 \end{bmatrix} = \begin{bmatrix} 1 & x_1 & y_1 \\ 1 & x_2 & y_2 \\ 1 & x_3 & y_3 \end{bmatrix} \begin{bmatrix} \alpha_1 \\ \alpha_2 \\ \alpha_3 \end{bmatrix} \quad (\text{A2.12})$$

or,

$$\begin{bmatrix} \alpha_1 \\ \alpha_2 \\ \alpha_3 \end{bmatrix} = \begin{bmatrix} 1 & x_1 & y_1 \\ 1 & x_2 & y_2 \\ 1 & x_3 & y_3 \end{bmatrix}^{-1} \begin{bmatrix} u_1 \\ u_2 \\ u_3 \end{bmatrix} \quad (\text{A2.13})$$

The coefficient matrix can be obtained as

$$\begin{bmatrix} \alpha_1 \\ \alpha_2 \\ \alpha_3 \end{bmatrix} = [A]^{-1} \begin{bmatrix} u_1 \\ u_2 \\ u_3 \end{bmatrix}$$

or

$$\begin{bmatrix} \alpha_1 \\ \alpha_2 \\ \alpha_3 \end{bmatrix} = \frac{1}{|A|} \begin{bmatrix} x_2 y_3 - y_2 x_3 & x_3 y_1 - x_1 y_3 & x_1 y_2 - x_2 y_1 \\ y_2 - y_3 & y_3 - y_1 & y_1 - y_2 \\ x_3 - x_2 & x_1 - x_3 & x_2 - x_1 \end{bmatrix} \begin{bmatrix} u_1 \\ u_2 \\ u_3 \end{bmatrix}$$

where,

$$\begin{aligned} |A| &= \begin{vmatrix} 1 & x_1 & y_1 \\ 1 & x_2 & y_2 \\ 1 & x_3 & y_3 \end{vmatrix} \\ &= (x_2 y_3 - x_3 y_2) - (x_1 y_3 - x_3 y_1) + (x_1 y_2 - x_2 y_1) \\ &= 2 \times \text{area of the triangle} = 2\Delta \end{aligned}$$

Hence equation (A2.10) can be expressed in terms of nodal co-ordinates and nodal displacement components as

$$\mathbf{u}^e = [1 \quad x \quad y] \frac{1}{|A|} \begin{bmatrix} x_2y_3 - y_2x_3 & x_3y_1 - x_1y_3 & x_1y_2 - x_2y_1 \\ y_2 - y_3 & y_3 - y_1 & y_1 - y_2 \\ x_3 - x_2 & x_1 - x_3 & x_2 - x_1 \end{bmatrix} \begin{bmatrix} u_1 \\ u_2 \\ u_3 \end{bmatrix}$$

$$\mathbf{u}^e = N_1(x,y) \quad N_2(x,y) \quad N_3(x,y) \quad u_1 \quad u_2 \quad u_3^T$$

or, $\mathbf{u}^e = \mathbf{N} \mathbf{x}, \mathbf{y} \quad [\mathbf{u}] \quad (\text{A2.14})$

$$\begin{bmatrix} \mathbf{u}^e \\ \mathbf{v}^e \end{bmatrix} = \begin{bmatrix} N_1(x,y) & N_2(x,y) & N_3(x,y) & 0 & 0 & 0 \\ 0 & 0 & 0 & N_1(x,y) & N_2(x,y) & N_3(x,y) \end{bmatrix} \begin{bmatrix} u_1 \\ u_2 \\ u_3 \\ v_1 \\ v_2 \\ v_3 \end{bmatrix}$$

$$\begin{bmatrix} \mathbf{u} \\ \mathbf{v} \end{bmatrix}^e = \begin{bmatrix} N_1(x,y) & 0 & N_2(x,y) & 0 & N_3(x,y) & 0 \\ 0 & N_1(x,y) & 0 & N_2(x,y) & 0 & N_3(x,y) \end{bmatrix} \begin{bmatrix} u_1 \\ v_1 \\ u_2 \\ v_2 \\ u_3 \\ v_3 \end{bmatrix} \quad (\text{A2.15})$$

$$\boldsymbol{\epsilon}_p = \begin{bmatrix} \epsilon_x \\ \epsilon_y \\ \epsilon_{xy} \end{bmatrix} = \begin{bmatrix} \frac{\partial}{\partial x} & 0 \\ 0 & \frac{\partial}{\partial y} \\ \frac{\partial}{\partial y} & \frac{\partial}{\partial x} \end{bmatrix} \begin{bmatrix} \mathbf{u} \\ \mathbf{v} \end{bmatrix}^e$$

Strain-displacement relationship:

$$\boldsymbol{\epsilon}_p = \mathbf{B}_p \mathbf{a}_p \quad (\text{A2.16})$$

where $\left[\mathbf{B}_p \right] = \frac{1}{|A|} \begin{bmatrix} y_2 - y_3 & 0 & y_3 - y_1 & 0 & y_1 - y_2 & 0 \\ 0 & x_3 - x_2 & 0 & x_1 - x_3 & 0 & x_2 - x_1 \\ x_3 - x_2 & y_2 - y_3 & x_1 - x_3 & y_3 - y_1 & x_2 - x_1 & y_1 - y_2 \end{bmatrix}$ and

$$\begin{aligned} K_p &= \int_A [B_p]^T D B_p t dA \\ &= [B_p]^T D [B_p] t \Delta \end{aligned} \quad (A2.17)$$

For plane stress condition, the elasticity matrix is given by

$$D = \frac{E}{1-\nu^2} \begin{bmatrix} 1 & \nu & 0 \\ \nu & 1 & 0 \\ 0 & 0 & \frac{1-\nu}{2} \end{bmatrix}, \quad D = \begin{bmatrix} d_{11} & d_{12} & 0 \\ d_{21} & d_{22} & 0 \\ 0 & 0 & d_{33} \end{bmatrix} \quad (A2.18)$$

Note: The elements of the stiffness matrix for plain strain condition are given in Reference 2, pp.69.

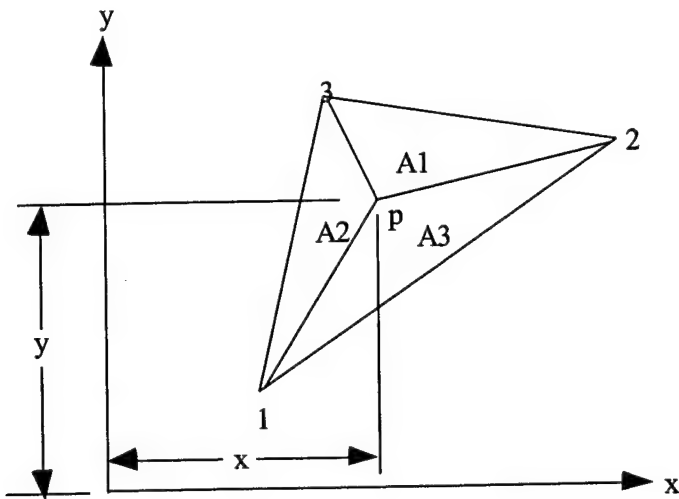
2.5.3 Derivation of Stiffness Matrix for Plate Bending

In choosing a function for the lateral displacement w , the polynomial must include nine unknown constants e.g.

$$w = \alpha_1 + \alpha_2 x + \alpha_3 y + \alpha_4 x^2 + \alpha_5 y^2 + \alpha_6 xy + \alpha_7 x^3 + \alpha_8 x^2 y + \alpha_9 y^3$$

Comparing this to a full cubic polynomial, it may be noted that one term has been omitted, namely xy^2 term. Many researchers have tried several methods to overcome this difficulty. For example the ten terms of the full cubic expression can be retained in the expression for w , two of the coefficients being specified to be equal, e.g. $\alpha_8 = \alpha_9$. However, if this is done, the $[A]$ matrix in the expression A2.4 becomes singular for certain orientation of triangular element, e.g. when two sides of the isosceles triangles are parallel to x and y -axes.

Derivation of element stiffness matrix using area coordinates



The position of P is uniquely defined by the area of three small triangles namely A_1 , A_2 and A_3 . Denoting the area of the triangular element by Δ , the area co-ordinates (L_1 , L_2 and L_3) of P are defined as:

$$L_1 = \frac{A_1}{\Delta}, L_2 = \frac{A_2}{\Delta} \text{ and } L_3 = \frac{A_3}{\Delta} \quad (\text{A2.19})$$

Here, $L_1 + L_2 + L_3 = 1$ and $A_1 + A_2 + A_3 = \Delta$. The area of each triangle can be expressed in terms of nodal co-ordinates

$$\Delta = \frac{1}{2} \det \begin{vmatrix} 1 & x_1 & y_1 \\ 1 & x_2 & y_2 \\ 1 & x_3 & y_3 \end{vmatrix}$$

That is, $\Delta = \frac{1}{2} [x_2 y_3 - y_2 x_3 + x_1 y_2 - y_1 x_2 + x_3 y_1 - y_3 x_1]$. Similarly,

$$A_1 = \frac{1}{2} [x_2 y_3 - y_2 x_3 + x_1 y_2 - y_1 x_2 + x_3 y_1 - y_3 x_1] \quad (\text{A2.20})$$

Let,

$$a_1 = x_2 y_3 - y_2 x_3, b_1 = y_2 - y_3 \text{ and } c_1 = x_3 - x_2 \quad (\text{A2.21})$$

Equation (A2.20) stands for

$$A_1 = \frac{1}{2} [a_1 + b_1 x + c_1 y],$$

Substituting the value of A_1 in equation (A2.19), we get

$$L_1 = \frac{a_1 + b_1 x + c_1 y}{2\Delta}, \text{ and similarly}$$

$$L_2 = \frac{a_2 + b_2 x + c_2 y}{2\Delta} \text{ and } L_3 = \frac{a_3 + b_3 x + c_3 y}{2\Delta} \quad (\text{A2.22})$$

where

$$a_2 = x_3 y_1 - y_3 x_1, b_2 = y_3 - y_1, c_2 = x_1 - x_3$$

$$a_3 = x_1 y_2 - y_1 x_2, b_3 = y_1 - y_2, c_3 = x_2 - x_1$$

Total displacement in the element=rigid body movement (no curvature)+simply supported case
(No nodal translation)

$$w = w^{rb} + w^{ss} \quad (\text{A2.23})$$

Since no curvatures as set up in the case of rigid body movement case, the lateral displacement must be linear function of x and y

$$w^{rb} = w_1 L_1 + w_2 L_2 + w_3 L_3 \quad (\text{A2.24})$$

Considering simply supported case, the element has only two rotational degrees of freedom at each node, i.e. θ_x and θ_y . The element displacement vector may be written as:

$$\begin{bmatrix} D^{ss} \end{bmatrix} = \begin{bmatrix} \theta_{x1}^{ss} & \theta_{y1}^{ss} & \theta_{x2}^{ss} & \theta_{y2}^{ss} & \theta_{x3}^{ss} & \theta_{y3}^{ss} \end{bmatrix}^T \quad (\text{A2.25})$$

The corresponding force vector F^{ss} contains six terms and the stiffness matrix K^{ss} is then a 6X6 matrix.

$$\theta_x^{ss} = -\frac{\partial w^{ss}}{\partial y} \text{ and } \theta_y^{ss} = \frac{\partial w^{ss}}{\partial x}$$

Substituting for w^{ss} from equation (A2.23)

$$\theta_x^{ss} = \theta_x + \frac{\partial w^{rb}}{\partial y} \text{ and } \theta_y^{ss} = \theta_y - \frac{\partial w^{rb}}{\partial x} \quad (\text{A2.26})$$

Substituting the expression assumed for w^{rb} in equation (A2.24) into equation (A2.26), the slopes at a point in the simply supported case can be expressed in terms of total slopes at that point and the lateral displacement as follows:

$$\theta_x^{ss} = \theta_x + \frac{1}{\Delta} (w_1 c_1 + w_2 c_2 + w_3 c_3)$$

$$\theta_y^{ss} = \theta_y - \frac{1}{\Delta} (w_1 b_1 + w_2 b_2 + w_3 b_3) \quad (\text{A2.27})$$

The slopes can be determined at each node. For example at node 1,

$$\theta_{x1}^{ss} = \theta_{x1} + \frac{1}{\Delta} (w_1 c_1 + w_2 c_2 + w_3 c_3)$$

$$\theta_{y1}^{ss} = \theta_{y1} - \frac{1}{\Delta} (w_1 b_1 + w_2 b_2 + w_3 b_3)$$

Similar expression can be obtained for other two nodes and the complete relationship between the nodal rotations of the simply supported element and those of the complete element may be written in matrix form as

$$[D^{ess}] = \begin{bmatrix} \theta_{x1}^{ss} \\ \theta_{y1}^{ss} \\ \theta_{x2}^{ss} \\ \theta_{y2}^{ss} \\ \theta_{x3}^{ss} \\ \theta_{y3}^{ss} \end{bmatrix} = \frac{1}{2\Delta} \begin{bmatrix} c_1 & 2\Delta & 0 & c_2 & 0 & 0 & c_3 & 0 & 0 \\ -b_1 & 0 & 2\Delta & -b_2 & 0 & 0 & -b_3 & 0 & 0 \\ c_1 & 0 & 0 & c_2 & 2\Delta & 0 & c_3 & 0 & 0 \\ -b_1 & 0 & 0 & -b_2 & 0 & 2\Delta & -b_3 & 0 & 0 \\ c_1 & 0 & 0 & c_2 & 0 & 0 & c_3 & 2\Delta & 0 \\ -b_1 & 0 & 0 & -b_2 & 0 & 0 & -b_3 & 0 & 2\Delta \end{bmatrix} \begin{bmatrix} w_1 \\ \theta_{x1} \\ \theta_{y1} \\ w_2 \\ \theta_{x2} \\ \theta_{y2} \\ w_3 \\ \theta_{x3} \\ \theta_{y3} \end{bmatrix} \quad (A2.28)$$

This can be summarized as:

$$D^{ess} = [T] D^e \quad (A2.29)$$

From the principle of virtual displacement

$$D^{ess T} F^{ess} = D^e T F^e \quad (A2.30)$$

From equations (A2.29) and (A2.30),

$$F^e = [T]^T F^{ess} \quad (A2.31)$$

Again,

$$F^{ess} = K^{ess} D^{ess} \quad (A2.32)$$

From equations (A2.32) and (A2.29), it can be shown that

$$K_B = K^e = T^T K^{ess} T \quad (A2.33)$$

Derivation of Stiffness Matrix for Simply Supported Element

Lateral displacement at a point on the simply supported element in terms of the nodal displacement is chosen as follows:

$$w^{ss} = N_{x1}\theta_{x1}^{ss} + N_{y1}\theta_{y1}^{ss} + N_{x2}\theta_{x2}^{ss} + N_{y2}\theta_{y2}^{ss} + N_{x3}\theta_{x3}^{ss} + N_{y3}\theta_{y3}^{ss} \quad (A2.34)$$

Each individual N_x and N_y term in the expression represents the shape function. The slopes θ_x^{ss} and θ_y^{ss} at each point are obtained from $\theta_x^{ss} = \frac{\partial w^{ss}}{\partial y}$ and $\theta_y^{ss} = -\frac{\partial w^{ss}}{\partial x}$

$$\begin{aligned} \theta_x^{ss} &= \frac{\partial N_{x1}}{\partial y} \theta_{x1}^{ss} + \frac{N_{y1}}{\partial y} \theta_{y1}^{ss} + \frac{\partial N_{x2}}{\partial y} \theta_{x2}^{ss} + \frac{N_{y2}}{\partial y} \theta_{y2}^{ss} + \frac{\partial N_{x3}}{\partial y} \theta_{x3}^{ss} + \frac{N_{y3}}{\partial y} \theta_{y3}^{ss} \\ \theta_y^{ss} &= -\left[\frac{\partial N_{x1}}{\partial x} \theta_{x1}^{ss} + \frac{\partial N_{y1}}{\partial x} \theta_{y1}^{ss} + \frac{\partial N_{x2}}{\partial x} \theta_{x2}^{ss} + \frac{\partial N_{y2}}{\partial x} \theta_{y2}^{ss} + \frac{\partial N_{x3}}{\partial x} \theta_{x3}^{ss} + \frac{\partial N_{y3}}{\partial x} \theta_{y3}^{ss} \right] \end{aligned}$$

The individual shape functions must be chosen so that they satisfy boundary conditions at the nodes of the simply supported element and constant strain criterion.

$$\begin{aligned} N_{x1} &= b_3 \left(L_1^2 L_2 + \frac{1}{2} L_1 L_2 L_3 \right) - b_2 \left(L_1^2 L_3 + \frac{1}{2} L_1 L_2 L_3 \right) \\ N_{y1} &= c_3 \left(L_1^2 L_2 + \frac{1}{2} L_1 L_2 L_3 \right) - c_2 \left(L_1^2 L_3 + \frac{1}{2} L_1 L_2 L_3 \right) \end{aligned} \quad (A2.35)$$

The expression for other shape functions can be obtained by changing the subscripts in cyclic order.

$$\begin{aligned} N_{x2} &= b_1 \left(L_2^2 L_3 + \frac{1}{2} L_1 L_2 L_3 \right) - b_3 \left(L_2^2 L_1 + \frac{1}{2} L_1 L_2 L_3 \right) \\ N_{y2} &= c_1 \left(L_2^2 L_3 + \frac{1}{2} L_1 L_2 L_3 \right) - c_3 \left(L_2^2 L_1 + \frac{1}{2} L_1 L_2 L_3 \right) \\ N_{x3} &= b_2 \left(L_3^2 L_1 + \frac{1}{2} L_1 L_2 L_3 \right) - b_1 \left(L_3^2 L_2 + \frac{1}{2} L_1 L_2 L_3 \right) \\ N_{y3} &= c_2 \left(L_3^2 L_1 + \frac{1}{2} L_1 L_2 L_3 \right) - c_1 \left(L_3^2 L_2 + \frac{1}{2} L_1 L_2 L_3 \right) \end{aligned}$$

The curvatures set up in the simply supported element may now be related to nodal displacements as follows:

$$[\epsilon^{ss}(x, y)] = \left[-\frac{\partial^2 w^{ss}}{\partial x^2} \quad -\frac{\partial^2 w^{ss}}{\partial y^2} \quad 2 \frac{\partial^2 w^{ss}}{\partial x \partial y} \right]^T$$

$$\epsilon^{ss} \ x, y = B^{ss} \ D^{ss}$$

where the matrix B^{ss} 3X6 matrix and can readily be determined by substituting the expression for w^{ss} from equation (A2.34).

$$[B^{ss}] = \begin{bmatrix} -\frac{\partial^2 N_{x1}}{\partial x^2} & -\frac{\partial^2 N_{y1}}{\partial x^2} & -\frac{\partial^2 N_{x2}}{\partial x^2} & -\frac{\partial^2 N_{y2}}{\partial x^2} & -\frac{\partial^2 N_{x3}}{\partial x^2} & -\frac{\partial^2 N_{y3}}{\partial x^2} \\ -\frac{\partial^2 N_{x1}}{\partial y^2} & -\frac{\partial^2 N_{y1}}{\partial y^2} & -\frac{\partial^2 N_{x2}}{\partial y^2} & -\frac{\partial^2 N_{y2}}{\partial y^2} & -\frac{\partial^2 N_{x3}}{\partial y^2} & -\frac{\partial^2 N_{y3}}{\partial y^2} \\ 2\frac{\partial^2 N_{x1}}{\partial x \partial y} & 2\frac{\partial^2 N_{y1}}{\partial x \partial y} & 2\frac{\partial^2 N_{x2}}{\partial x \partial y} & 2\frac{\partial^2 N_{y2}}{\partial x \partial y} & 2\frac{\partial^2 N_{x3}}{\partial x \partial y} & 2\frac{\partial^2 N_{y3}}{\partial x \partial y} \end{bmatrix} \quad (A2.36)$$

Finally the stiffness matrix for the simply supported element can be obtained from

$$K^{ss} = \iint B^{ss}^T E B^{ss} t dx dy \quad (A2.37)$$

where K^{ss} is a 6×6 matrix. Having thus found the stiffness matrix for the simply supported element, the stiffness for the actual element K^e can be obtained from equation (A2.33).

Steps in deriving the element stiffness matrix for plate bending:

1. Determine the local coordinates of elements using the transformation matrix as described in appendix A-1;
2. Compute the values of a_i , b_i and c_i from equation (A2.21) and determine the area coordinate values L_1 , L_2 and L_3 ;
3. Compute the values of shape functions N_{x1} , N_{y1} etc. from equation (A2.35);
4. Establish the B^{ss} matrix in equation (A2.36);
5. Evaluate the product $B^{ss}^T E B^{ss}$;
6. Integrate this product as in equation (A2.37) to get the stiffness matrix for the simply supported element $[K^{ess}]$;
7. Evaluate T matrix as given in equation (A2.28);
8. Evaluate the required element stiffness matrix K_B from equation (A2.33);

In this computation a closed form DKT element⁹ is used for bending.

References:

¹Argyris, J. H., and Dune, P. C., "On the Application of Natural Mode Technique to Small Stain Large Displacement Problems," World Congress on Finite Element Methods in Structural Mechanics, Bournemouth, 1975.

²Cook, R. D. Concepts and Applications of Finite Element Analysis, John Wiley and Sons, 2nd Edition, 1981.

³Selvam, R. P., and Qu, Z. Q., "Predicting the Nonlinear Response of Aerospace Structures Using Aeroelastic NS Solutions on Deforming Meshes," Project Report, 1999.

⁴Levy, S., "Square Plate with Clamped Edges Under Normal Pressures producing Large Deflection," Nasa Technical Note 847, 1942.

⁵Timoshenko, S., and Woinowsky-Krieger, S., Theory of Plates and Shells, McGraw-Hill Book Company, Inc., 1959.

⁶Murray, D. W., Large Deflection Analysis of Plates, Ph.D. Thesis, University of California, Berkeley, 1967.

⁷Zienkiewicz, O. C, The Finite Element Method, McGraw-Hill Publishing Company Limited, Third Edition, 1977.

⁸Anderson, R. G., Irons, B. M., and Zienkiewicz, O. C., "Vibration and Stability of Plates using Finite Elements," *International Journal of Solids and Structures*, Vol.4, 1968, pp.1031-1055.

⁹Cook, R. D., Malkus, D. S., Plesha, M. E., Concepts and Applications of Finite Element Analysis, John Wiley and Sons, 1989.

CHAPTER 3

MOVING GRID AND DEFORMING MESH

- 3.1 Introduction
 - 3.2 Description and Evaluation of Different Algorithms
 - 3.3 Theory of the Deforming Mesh
 - 3.4 Numerical Simulations
 - 3.5 Summary
-

3.1 Introduction

As we know, fluid equations are derived using the Eulerian motion description (stationary grid with respect to time) and the structural equations derived using the Lagrangian description (grid moves with the displacement of the physical medium). To accurately model problems with moving and deforming boundaries, such as in aeroelastic analysis, requires that the fluid grid conform to the changing shape of the boundary. To accommodate the movement of the fluid grid in an aeroelastic code either a new grid must be generated at each time step (dynamic regridding) or the differential equations for the fluid must be modified to allow the movement of the existing fluid grid (ALE, Corotational, Space-Time). Once a method is found for modifying the fluid equations to allow for grid movement a method must be chosen to move or update the fluid grid to the new position of the structure.

Grids are usually moved or updated with the same constraints used in the programs used to create the initial grid. Such constraints control the size of the grid cells, their distribution, and the orthogonality of the cell intersections and boundaries. The goal of any grid updating or moving method is to maintain a desirable grid throughout the duration of the program. If at any point the grid fails to meet the required level of quality a new grid must be generated that meets the desired quality. Generating a new grid or regridding requires the incorporation of a grid generation program into the aeroelastic solver and the interpolation of the values from the old grid to the new grid. This process

takes time and can introduce errors due to the interpolation process. However, such a program is often needed for aeroelastic problems with large deflections and deformation.

Ideally, a grid would be moved in such a way that would maintain grid quality under large deflection and deformation, introduce minimal errors, and be computationally efficient. Just like any other numerical method you have to give in one of these areas to get in another. One way to increase computational efficiency was addressed by Donea¹ in that since the computational domain or the boundary of the fluid grid usually extends relatively far away from the structure and its movement, only the portions of the fluid grid near the structure, are required to be moved to accommodate deflection and deformation. The less grid points that are moved at each time step, the more efficient the code will be². However, grid quality may suffer if the area allowed to move is not large enough to allow a smooth transition from the fixed points and the displaced structure.

In this chapter the different methods used to modify the fluid equations to allow the movement of a structure within the fluid domain are described. For the ALE method, various methods used to update or move the fluid grid to conform to a changing structural boundary are also described and evaluated. The details of the implementation of the Trans-Finite Interpolation scheme for the deforming mesh is provided. Numerical simulation is also included to show the features of this scheme.

3.2 Description and Evaluation of Different Algorithms

3.2.1 Dynamic Regridding

The dynamic regridding method is implemented by simply forming a new grid at each time step to conform to the shape of the structure³. The method can be summarized by:

- Create an initial fluid grid.
- Calculate the fluid pressure on the structure.
- Calculate the structural response.
- Generate a new grid around the new position of the structure.
- Obtain the values of the flow variables for each grid point of the new grid by interpolating the values of the flow variables from nearby grid points of the old grid.

The new grid needed at each time step can either be generated manually (i.e. a person with a grid generation program) or by an automatic grid generation program incorporated into the aeroelastic program. A simple aeroelastic analysis can require several thousand time steps. This makes it

impossible to generate the grid manually. Programs with the grids generated automatically require a very robust generation program to ensure grid quality since the grids generated automatically cannot be viewed for quality and errors during the execution of the program.

Compared to newer methods for moving boundaries, dynamic regridding is inefficient due to the amount of time needed to generate new grids. The method also introduces greater errors due to the interpolation of data from the old grid to the new.

3.2.2 Corotational method

Among the different methods developed to allow solvers to handle moving fluid grids is the corotational method. Farhat and Lin⁴ described the equation of motion of the fluid in moving frames of reference, which are attached to specific nodes of the structure. The result is an implicit generation of a structure attached corotational fluid grid. Using this scheme the grid does not need to be updated for rigid body motion. Instead of recalculating the new position of the grid points, the entire coordinate axis system is moved or rotated in physical space as seen in Figure 3.1.

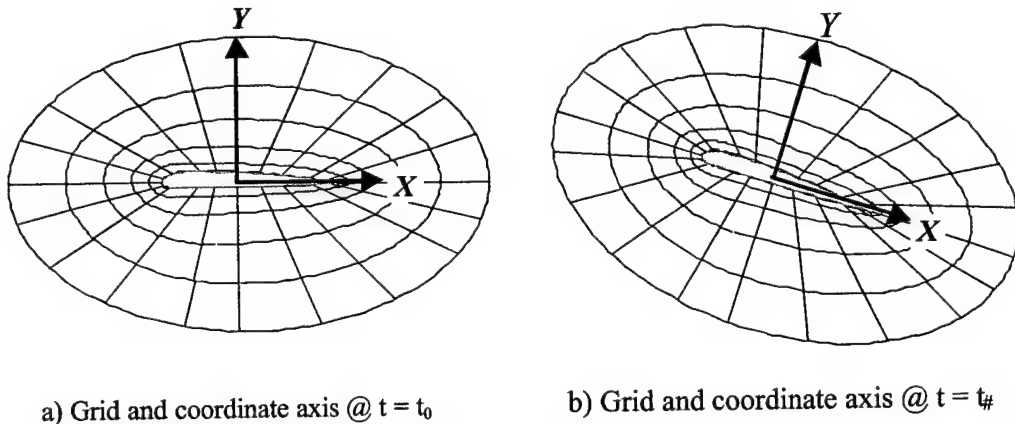


Figure 3.1 Moving frame of reference

The result of this procedure is that the coordinates of the individual grid points do not have to be recalculated at every time step. The grid is moved in the physical domain but remains stationary in the computational domain⁵. The fluid equations are modified by adding terms that describe the grid and axis movement on the right hand side of the equations. This method was originally designed for rigid body motion, but it can be modified to account for small structural deformations. Lin described ways

to implement the corotational approach to flexible configurations by implementing different Jacobian updating schemes.

The attraction of this method is its ability to move the entire coordinate system with the movement of the structure. No updating is needed, so the same grid can be used for all time steps. The downside of this method is the difficulty in applying the unusually large amount of terms added to the fluid equations to account for movement. If small structural deflections are to be accounted for even more terms are added.

3.2.3 Arbitrary Lagrangian Eulerian method

A method presented by Hirt, Amsden, and Cook⁶, called the Arbitrary Lagrangian Eulerian method or ALE for short, suggests a way of modifying the fluid equation in a way that would reflect Eulerian, Lagrangian or an arbitrary combination of the two descriptions of motion. This method, originally developed for finite difference equations, was later modified for use with finite elements¹.

The ALE method takes advantage of the good properties in the Lagrangian and Eulerian systems by allowing a specified region of the fluid grid to move to conform to structural displacements. Yet allow the outer regions of the grid to remain motionless. Figure 3.2 shows the location of the ALE

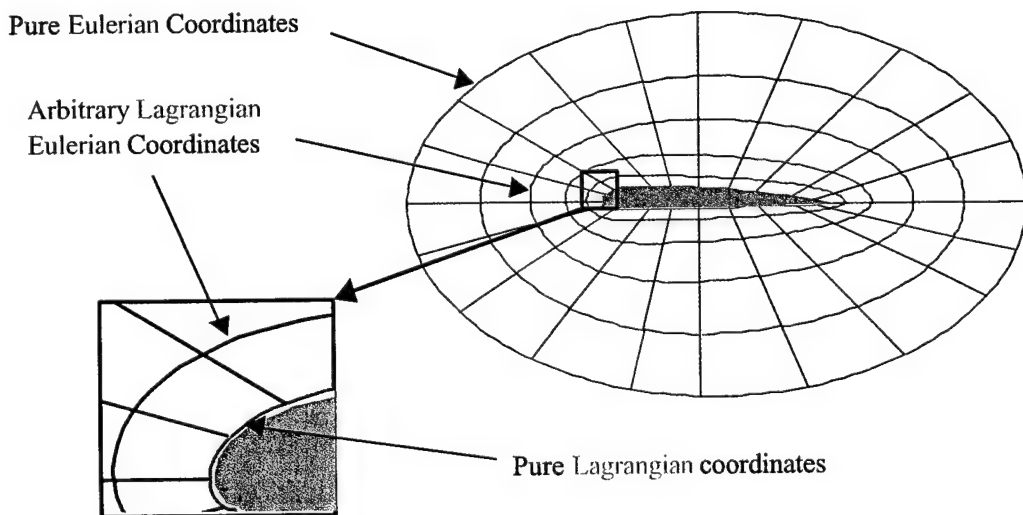


Figure 3.2 Body conforming grid with ALE region

portion of the fluid grid. In this figure the different descriptions of motion that correspond to a specific

grid region are shown. The blue shows the Eulerian coordinates, the green is Lagrangian, and the red is the ALE.

In this method the equations for the structure and the outer fluid region remain unchanged with Lagrangian and Eulerian descriptions respectively. For the ALE portion of the fluid grid the convective flux terms of the fluid equations are modified to account for the change in velocity of the moving grid. This is done by taking into account the fluid grid velocity and subtracting it from the calculated fluid velocity at each node. The equation reprinted below is an example of the ALE form of the momentum equation. The highlighted portion of the equation shows the grid velocity V_j being

$$U_{i,j} + \boxed{(U_j - V_j)U_{i,j}} = -\left(\frac{p}{\rho}\right)_j + [V(U_{i,j} + U_{j,i})]_j$$

subtracted from the fluid velocity U_j . The grid velocity is calculated by taking the change in position of the grid with respect to time from one time step to the next. This velocity will vary depending on the location within the ALE grid. At the surface of the structure the grid velocity will be equal to the velocity of the structure and decrease with distance from the structure until it is equal to zero at the outer edge of the ALE grid as seen in Figure 3.3. The result is a modified fluid equation that represents

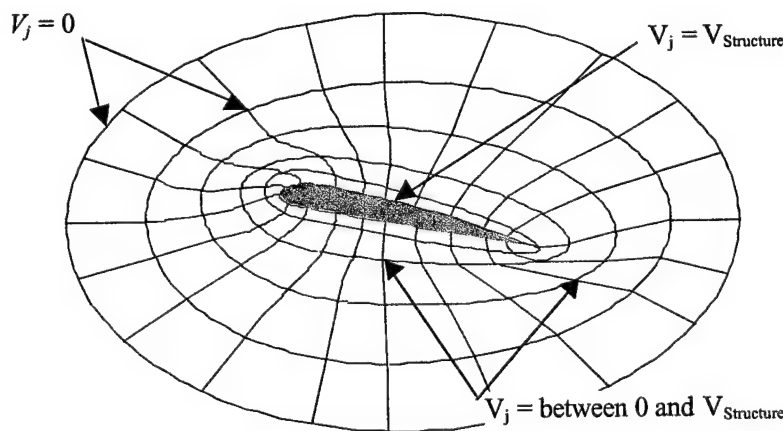


Figure 3.3 Grid velocities for ALE method

pure Lagrangian motion at the structure surface, pure Eulerian motion description at the outer edge of the ALE grid, and a mix between Lagrangian and Eulerian motions descriptions in between.

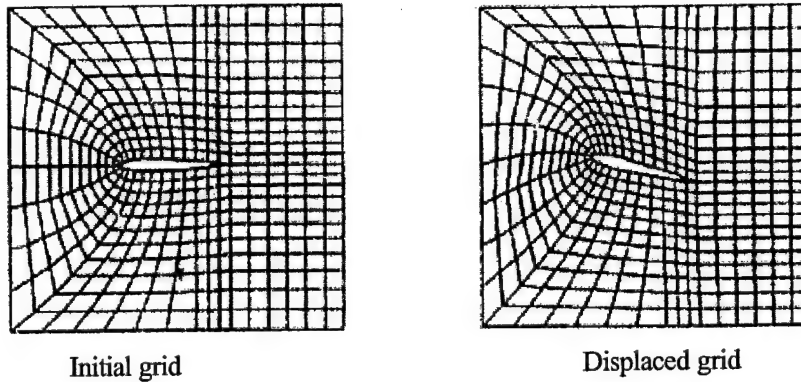
The ALE method is one of the most widely used methods for problems involving moving structures. One advantage to this method is the ability to specify how much of the fluid grid is allowed to move. Limiting the size of the ALE region, limits the amount of grid that needs to be updated to correspond to the new position. This saves computational time and assures grid quality for the unmoved portion of the grid. The method can handle rigid body problems as well as problems involving structural deflection. Unlike the corotational method, the ALE method is also suitable for problems where the outer perimeter of the fluid grid is not allowed to move due to a boundary condition. However the method does have a disadvantage.

The disadvantage of the ALE method is that it requires that the fluid grid be updated after each time step to correspond to the new position of a structure. The quality and efficiency of the ALE approach are dependent on the grid updating procedure used. If an updating procedure used fails to maintain grid quality, then the grid must be regenerated, which is computationally expensive. Therefore a grid updating procedure should be chosen carefully. Several grid updating procedures include the Trans-Finite Interpolation (TFI), a Cubic Blending, a dynamic mesh, and a rigid grid method are discussed below.

3.2.3.1 Trans-Finite Interpolation (TFI)

A commonly used method for grid generation, called Trans-Finite Interpolation (TFI), was used by Guruswamy⁷. In this paper Guruswamy developed an algebraic method using TFI for aeroelastic configuration adaptive grids. TFI controls grid quality by connecting grid lines perpendicular to the structure and distributing the nodes exponentially away from the structure to the outer boundary. The outer boundary is also located a significant distance away from the moving structure. The outer portions of the grid are restrained from moving by shearing the grid along the outer boundary. Grid lines are prevented from overlapping by preserving the arc-length distribution between nodes, and by using a simple linear distribution of translational displacement.

At each time step the deformed shape of the structure is calculated by the displacement vector $\{d\} = [\Phi]\{q\}$, where $[\Phi]$ is the modal matrix and $\{q\}$ is the generalized displacement vector. The new positions of the grid points are calculated using the positions of the grid points from previous time steps. This is achieved using a first order backward difference scheme. The grid points are distributed along the grid lines in the radial direction using a spacing function. An example of this updating scheme can be seen in Figure 3.4.


 Figure 3.4 An example of the TFI updating scheme⁸

Shankar and Ide⁹, Gaitonde and Fiddes⁸, and Gaitonde, Jones, and Fiddes¹⁰ used a general structured grid method based on TFI for rapid grid generation at each time step. Selvam, Visbal, and Morton¹¹ used TFI method to update grid points in an aeroelastic solver for non-linear panel flutter. The advantages of the TFI method is that it is efficient and relatively simple to apply. A disadvantage is that mesh orthogonality at deforming surfaces cannot be guaranteed with TFI during moderate deflections¹². Orthogonality at the surface is desired for simulations with a high Reynolds number and viscous flow. In some cases TFI can limit solution accuracy and stability.

3.2.3.2 Cubic Blending

Another algebraic method was developed by Melville, Morton, and Rizzetta¹². This method is similar to TFI in that it is based on redefining the grid lines normal to the surface but it assures grid orthogonality near a deforming surface for deflections and rotations. This method also allows the option of fixing the outer region so the grid overlap connectivity remains unchanged. The name cubic blending comes from the procedure used to combine an old grid and a calculated reference grid together to form a new grid.

The procedure for this method starts by solving the fluid equations and transferring the pressure to the structure. Then after the structural equations have been solved and the structure is moved, the new grid is calculated by first calculating the transition and rotation of each surface node by the equations:

$$\text{Translational displacements: } \Delta x = x_{i,1} - x_{i,1} \quad \Delta y = y_{i,1} - y_{i,1}$$

$$\text{Rotational displacements: } \cos \theta_i = \frac{s \cdot s'}{|s||s'|} \quad \sin \theta_i = \frac{s \times s' \cdot \hat{e}_z}{|s||s'|}$$

Where: s is the original surface vector from $i-1$ to $i+1$

s' is the displaced surface vector

Then, according to the displacement of the surface node, the normal grid line is moved as a rigid body to form a displaced grid line, which serves as a reference grid line. These referenced grid lines are defined by the equations:

$$x_{i,j}^{REF} = x_{i,1} + \Delta x_i + (x_{i,j} - x_{i,1})\cos\theta_i - (y_{i,j} - y_{i,1})\sin\theta_i$$

$$y_{i,j}^{REF} = y_{i,1} + \Delta y_i + (x_{i,j} - x_{i,1})\sin\theta_i - (y_{i,j} - y_{i,1})\cos\theta_i$$

Blending the old grid line and the reference grid line together forms the new grid line. Morton suggest blending the grid lines in arc-length space rather than in computational space by using the arc-length equation:

$$s_{i,j} = \sum_{k=2}^j \sqrt{(x_{i,k} - x_{i,k-1})^2 + (y_{i,k} - y_{i,k-1})^2}$$

Where the arc-length of the starting node is $s_{i,1} = 0$. Cubic blending with a zero slope at the end points ensures wall orthogonality is maintained, and that there is a smooth grid translation in the outer regions of the grid. The blending equation is:

$$b_{i,j} = 3\left(\frac{s_{i,j}}{s_{i,j \max}}\right)^2 - 2\left(\frac{s_{i,j}}{s_{i,j \max}}\right)^3$$

The variable j_{\max} is the last node along each normal line that is allowed to deflect. The new grid can now be formed by applying the blending function to the reference grid and the old grid by the equations:

$$x'_{i,j} = b_{i,j} * x_{i,j} + (1 - b_{i,j}) * x_{i,j}^{REF}$$

$$y'_{i,j} = b_{i,j} * y_{i,j} + (1 - b_{i,j}) * y_{i,j}^{REF}$$

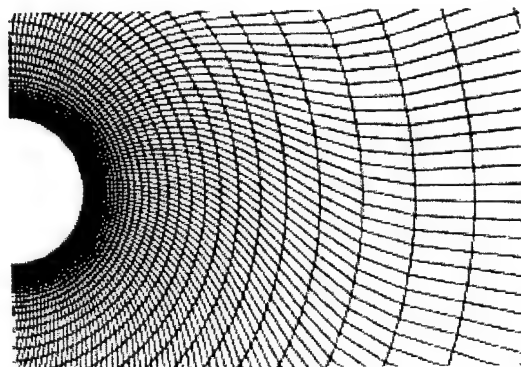


Figure 3.5 Displaced grid on a circular cylinder using the cubic blending method¹².

The advantage of this method is that, unlike TFI, cubic blending allows the grid lines to intersect perpendicular to the structure and the outer boundary. By doing this the quality of the grid can be maintained under larger deflections. The method is also applied in a relatively simple manner. One disadvantage is that cubic blending may require more grid points to be allocated to move than TFI. This is done to ensure grid quality.

3.2.3.3 Dynamic mesh

A unique way of updating the fluid grid was developed by Batina¹³ for an unstructured mesh. This method uses the ALE method in that it allows the outer regions to be held fixed and a region to be specified where the fluid grid is allowed to move and deform to conform to the deflected or deformed structure. In this method Batina models each edge of a triangular element in the fluid grid by a spring, where the spring stiffness is the inverse of the length of the edge of the element and calculated by the equation $k_m = 1 / (x_j - x_i)^2 + (y_j - y_i)^2^{\frac{1}{2}}$. Figure 3.6 shows an example of a triangular element modeled as a spring. An example of a network of triangular springs can be seen in figure 3.7. In this figure the blue indicates the stationary Eulerian grid points, and the red the ALE grid points.

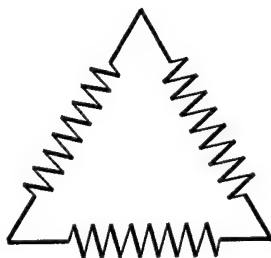


Figure 3.6 Element modeled as a spring system

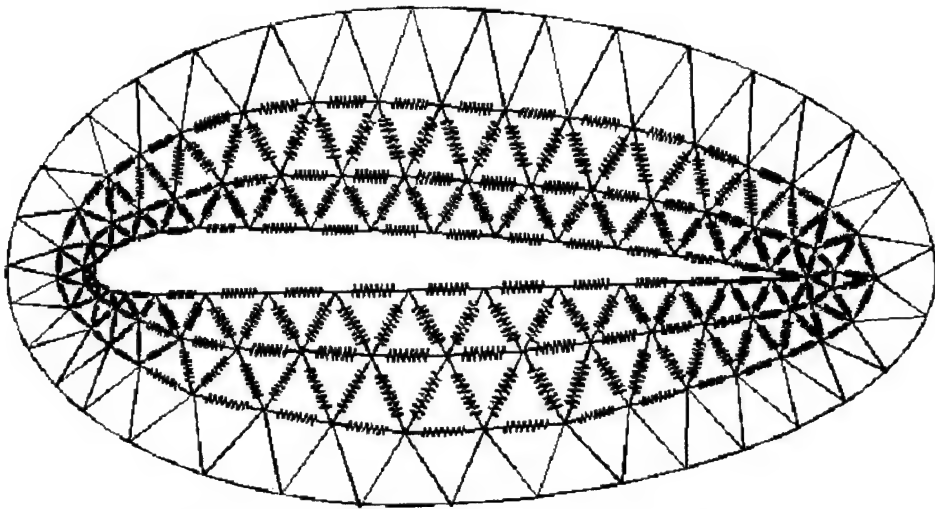


Figure 3.7 Illustration of a fictitious spring system about an airfoil.

The procedure for this method starts by solving the fluid equations and transferring the pressure to the structure. Then, the structural displacement is calculated and the structure is moved. The new mesh is found using a predictor-corrector procedure. At each time step when the structure deflects, the grid points on the outer boundaries are held fixed and the grid points on the body are prescribed by the structural deflection. Moving the nodes along the structure to their new location causes tension forces in the network of the springs. Summing these forces at each point in the x and y direction, gives static equilibrium equations. These equations are then solved for the nodal displacements, δ_{x_i} and δ_{y_i} . The nodal displacements are predicted by a linear extrapolation of displacements from two previous time steps.

$$\text{Nodal displacements: } \tilde{\delta}_{x_i} = 2\delta_{x_i}^n - \delta_{x_i}^{n-1} \quad \tilde{\delta}_{y_i} = 2\delta_{y_i}^n - \delta_{y_i}^{n-1}$$

These displacements are then corrected using Jacobi iterations of the static equilibrium equations.

$$\delta_{x_i}^{n+1} = \frac{\sum k_m \tilde{\delta}_{x_m}}{\sum k_m} \quad \delta_{y_i}^{n+1} = \frac{\sum k_m \tilde{\delta}_{y_m}}{\sum k_m}$$

Then summing for all the edges of triangles that have node (i) as an endpoint.

Finally the new locations of the interior nodes are calculated by.

$$x_i^{n+1} = x_i^n + \delta_{x_i}^{n+1} \quad y_i^{n+1} = y_i^n + \delta_{y_i}^{n+1}$$

Batina¹³ states that the predictor-corrector procedure is more efficient than performing Jacobi iterations alone. This is due to a fewer number of iterations required to achieve acceptable

convergence. Figure 3.8, taken from Batina's paper, shows the movement of the grid using the dynamic mesh method.

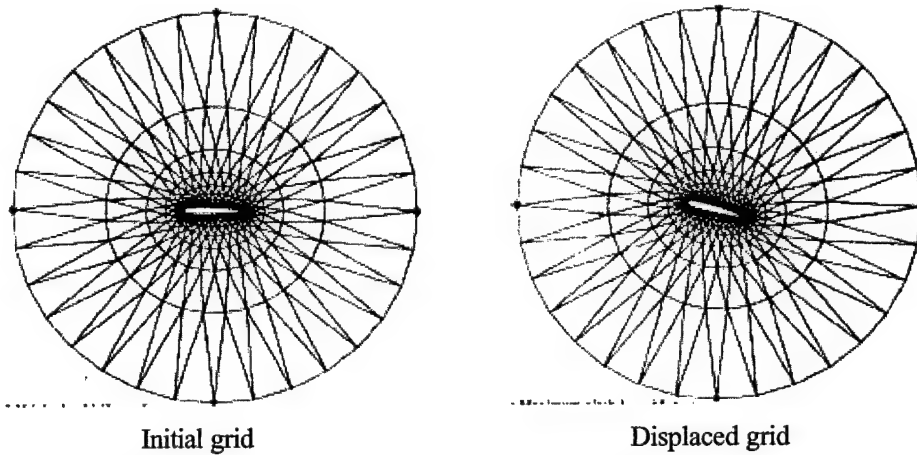


Figure 3.8 Illustration of the dynamic mesh method about a pitching airfoil¹³.

This concept was later expanded for 3-D unstructured meshes by Batina¹⁴. In this method the mesh is modeled by tetrahedrons with springs on the sides as shown in Figure 3.9.

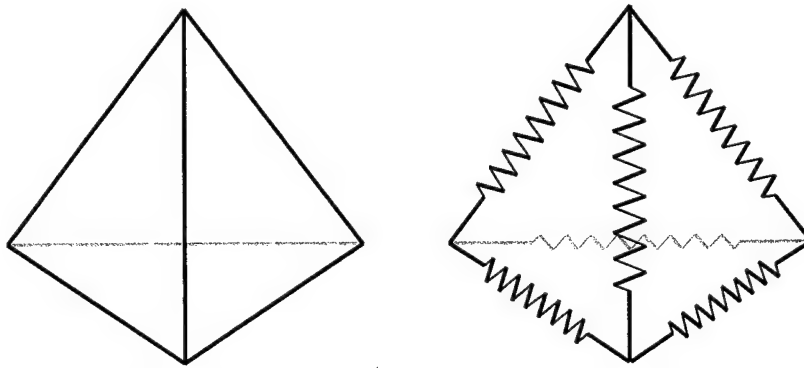


Figure 3.9 Tetrahedral element and the spring equivalent.

Robinson, Batina, and Yang¹⁵ modified the dynamic mesh to work with structured hexahedral grids (Figure 3.10). In this version additional springs were added to the diagonal of each cell face to control cell shearing. A factor was also added to the equation for the spring stiffness for the ability to control the spring stiffness of the cells near the wing to prevent distortion.

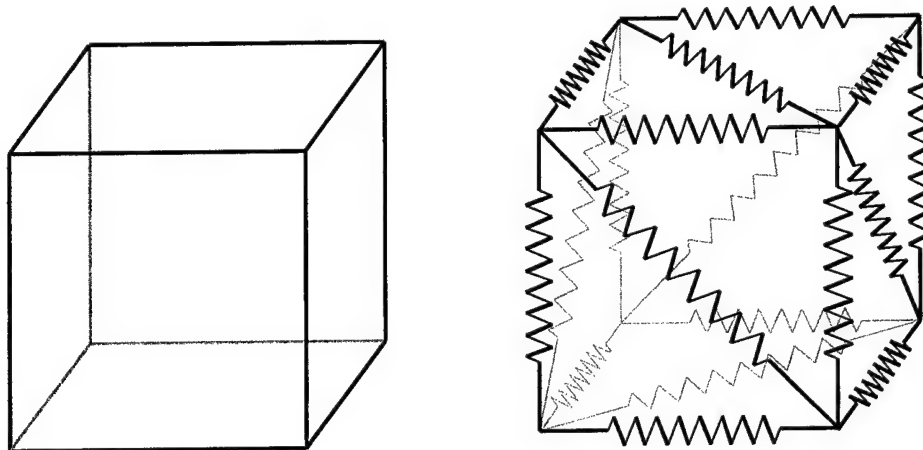


Figure 3.10 Hexahedral element and spring equivalent.

Singh, Newman, and Baysal² used the dynamic mesh algorithm with the factor for spring stiffness control proposed by Robinson, Batina, and Yang¹⁵ on a 2-D unstructured system. In this paper the number of elements available to adapt to the structure were limited in order to reduce storage and decrease CPU time. The authors call this the adaptive window procedure. Figure 3.11 shows an example of this method.

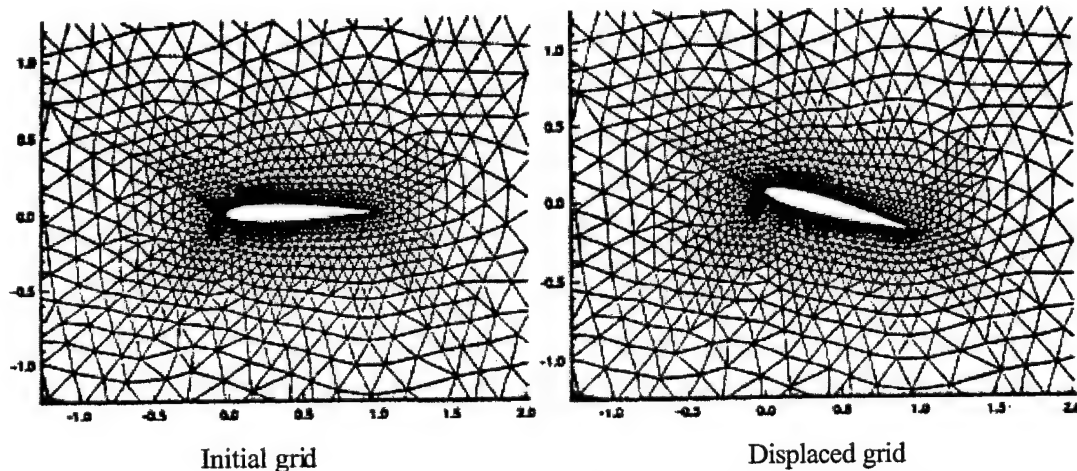


Figure 3.11 Unstructured dynamic mesh about a pitching airfoil²

Lesoinne and Farhat¹⁶ further modified the dynamic mesh by adding fictitious damping and mass to the spring elements to create a moving system known as a pseudo structural system. The authors of this paper also developed a method for analyzing the stability of the dynamic mesh algorithm. They

found that it could destabilize the fluid-structure interaction by introducing artificial instabilities. Farhat¹⁷ added to the pseudo-structural system by placing torsional springs at the vertex of the tetrahedron to prevent a vertex from interpenetrating the facet of a tetrahedron as seen in Figure 3.12.

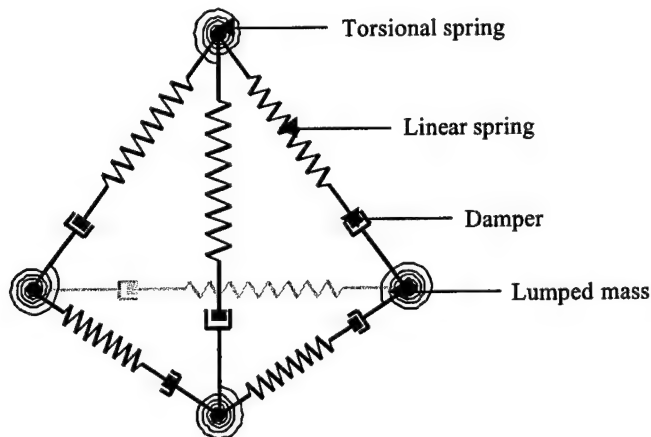


Figure 3.12 Pseudo-structural tetrahedron

An advantage of the dynamic mesh method is the ability to specify the spring stiffness near the structure. This gives it the ability to handle large deflections and still maintain grid quality. One of the disadvantages is that the method is not as efficient as some of the other grid updating schemes. This is due to the predictor corrector procedure and the Jacobi iterations. The method also becomes more difficult to apply and less efficient as extra springs are added to the network to control cell shearing as discussed in Robinson, Batina, and Yang¹⁵. And the addition of the torsional springs to control interpenetration as discussed by Farhat¹⁷.

3.2.3.4 Rigid grid method

Tamura et al¹⁸ used an updating procedure implementing ALE by making the structural and the fluid grids attached, and move in a rigid fashion. This method is similar to the corotational approach⁴ in that the fluid grid is attached to a structure undergoing rigid body motion and the entire fluid-structure system moves together. What makes this method different is that the coordinate axis is fixed in space and does not move with the computational grid as seen in Figure 4-13.

The same method is used by Selvam, Govindaswamy, and Bosch¹⁹ to model the incompressible flow of air around a bridge deck section to determine the critical velocities of the structure. Kandil and Chung²⁰ used this method to model the compressible flow of air around an airfoil.

In this method the entire fluid grid is rotated about an origin in a rigid fashion to correspond to the changing position of the structure. The new grid is found by simply rotating the old grid in a rigid fashion the same amount of angular displacement that the structure was moved. Since the entire fluid

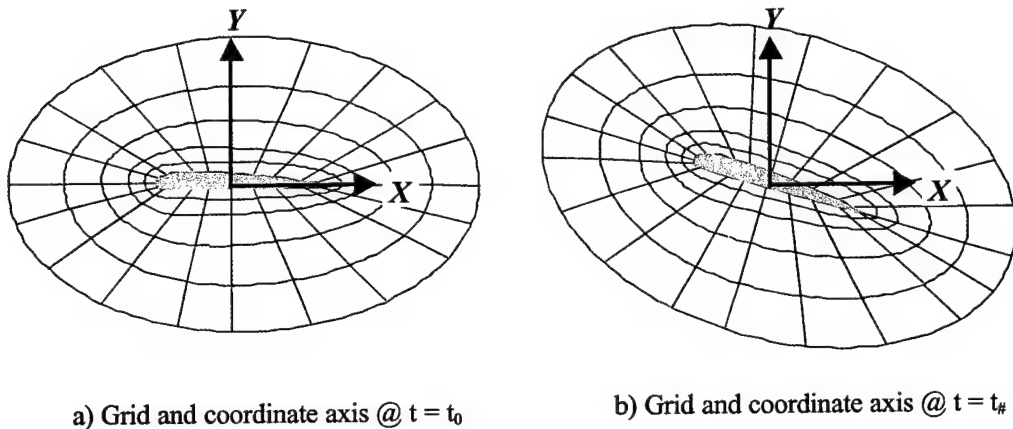


Figure 3.13 Movement of a rigid grid

grid is moved there are no fixed regions (pure Euler coordinates), therefore the whole fluid grid is considered ALE

The advantage of this method is that the same grid is used throughout the entire process. Since the grid is moved in a rigid fashion the element areas and sizes do not change from time step to time step. Therefore, grid quality is assured for every time step. The method is also easy to apply due to the grid displacement being the same as the structural displacement. No numerical methods have to be introduced to predict the new position of the grid making the method computationally efficient. The disadvantage that the outer boundary must be free to rotate and cannot be fixed to an outer boundary.

3.3 Theory of the Deforming Mesh

A grid deformation method^{12,21} which is suitable for aeroelastic simulations on overset grids is used in the following. This strategy is similar to TFI in that it is algebraic approach based on redefining the normal grid lines. However, unlike TFI, this method maintains the grid quality of the initial mesh near deforming surfaces under arbitrary, moderate deflections and rotations. In addition, a

specified region in the far-field may be held fixed so that the grid overlap regions, and their connectivities, remain unchanged.

3.3.1. Calculation of the Translations and Rotations

Given an original (starting) grid and perturbed surface (assumed to be at $k=1$ here), the translation and rotation of each surface node can be computed from the deflected aerodynamic surface.

Defining the coordinates of the original and perturbed nodes at $i, j, k (=)$ as

$$\mathbf{X}_o^1 = [x_{ij1}^o, y_{ij1}^o, z_{ij1}^o]^T, \quad \mathbf{X}_p^1 = [x_{ij1}^p, y_{ij1}^p, z_{ij1}^p]^T \quad (3.1)$$

where the superscript “1” and/or subscripts “o”, “p” denote $k = 1$, original and present respectively.

The translational displacements are given by

$$\Delta\mathbf{X}^1 = \mathbf{X}_p^1 - \mathbf{X}_o^1 \quad (3.2)$$

The calculation of the rotational displacements is a little complex. It can be found by forming an orthonormal basis for the original surface position and the perturbed surface at that node. The following four steps are used to calculate the orthonormal basis.

(1) Define and normalize surface vectors. Suppose the given node is 1 shown in Figure 3.14. The two surface vectors \mathbf{a} and \mathbf{b} are defined as

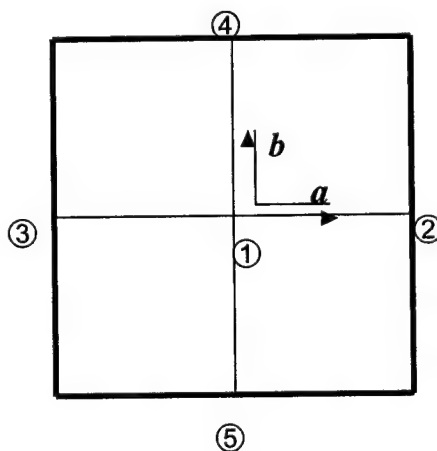


Figure 3.14. Definition of the surface vectors

$$\mathbf{a} = \mathbf{X}_2^1 - \mathbf{X}_3^1, \quad \mathbf{b} = \mathbf{X}_4^1 - \mathbf{X}_5^1 \quad (3.3)$$

where the subscript “2”, “3”, “4”, and “5” denote the nodes 2, 3, 4, and 5 respectively. The two surface vectors can be normalized as

$$\mathbf{a}^0 = \frac{\mathbf{a}}{\|\mathbf{a}\|}, \quad \mathbf{b}^0 = \frac{\mathbf{b}}{\|\mathbf{b}\|} \quad (3.4)$$

If the present surface node (i) is a boundary node, the nodes 2, 3, 4, and 5 defined as follows:

(a) set incremental numbers of nodes 2, 3, 4, and 5 are zeros, i.e.,

$$i_k = 0, \quad j_k = 0, \quad (k = 2,3,4,5)$$

(b) Set

$$\begin{cases} i_2 = 1, & i \neq ie \\ i_3 = -1, & i \neq is \\ j_4 = 1, & j \neq je \\ j_5 = -1, & s \neq js \end{cases}$$

where ie , i , je , and js denote the ending node and starting node in the i and s directions

(c) The actual nodal number of 1 through 5 are given by

$$i + i_k, \quad j + j_k, \quad (k = 1,2,3,4,5)$$

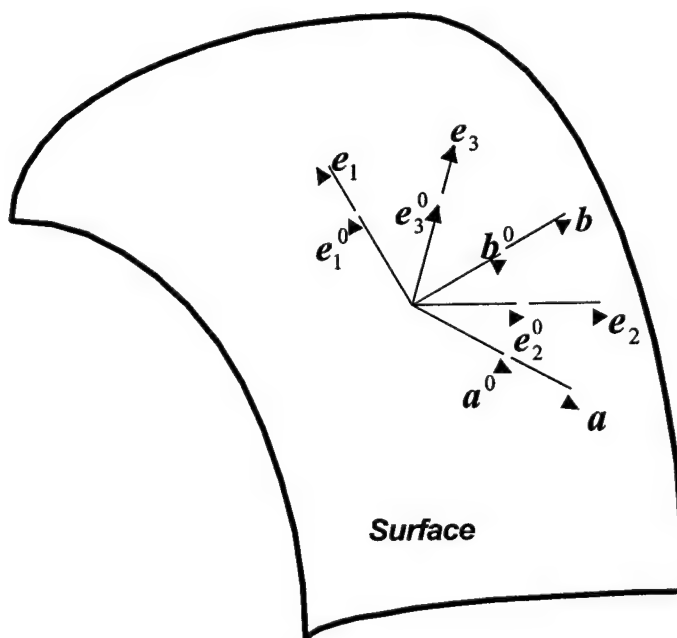


Figure 3.15. Basis on the given surface

(2) Form and unitize the surface vectors. As shown in Figure 3.15, the summation and unitized vectors of the two surface vectors are expressed as

$$\mathbf{e}_2 = \mathbf{a}^0 + \mathbf{b}^0 \quad (3.5)$$

$$\mathbf{e}_2^0 = \frac{\mathbf{e}_2}{\|\mathbf{e}_2\|} \quad (3.6)$$

(3) Form and unitize the surface normal vector. The normal vector of the surface is the cross-product of the two surface vectors \mathbf{a}^0 and \mathbf{b}^0 which are shown in Figure.

$$\mathbf{e}_1 = \mathbf{a}^0 \times \mathbf{b}^0 \quad (3.7)$$

$$\mathbf{e}_1^0 = \frac{\mathbf{e}_1}{\|\mathbf{e}_1\|} \quad (3.8)$$

(4) Form the third vector for the basis

$$\mathbf{e}_3^0 = \mathbf{e}_1^0 \times \mathbf{e}_2^0 \quad (3.9)$$

The orthonormal basis for the original and perturbed surfaces are given by

$$\mathbf{E}_o = [\mathbf{e}_1^0 \quad \mathbf{e}_2^0 \quad \mathbf{e}_3^0], \quad \mathbf{E}_p = [\mathbf{e}_1^0 \quad \mathbf{e}_2^0 \quad \mathbf{e}_3^0]_p \quad (3.10)$$

Actually, \mathbf{E}_o and \mathbf{E}_p are 3×3 matrices. The corresponding surface rotation matrix can be defined as

$$\mathbf{R} = \mathbf{E}_p \cdot \mathbf{E}_o \quad (3.11)$$

3.3.2. Update a Given Grid Line (Blending)

Each normal grid line is moved in a rigid-body way according to the displacement of the surface node to form a reference, displaced grid line defined by

$$\mathbf{X}_r = \mathbf{X}_o^1 + \Delta \mathbf{X}^1 + \mathbf{R} (\mathbf{X}_o^k - \mathbf{X}_o^1) \quad (3.12)$$

The subscript “ r ” denotes reference. The new grid line is constructed by blending the reference grid line and the old grid line. The blending choice is arbitrary but is best done in arc-length space rather than in computational space. The arc-length for each node is defined

$$s_k = \sum_{l=2}^k |\mathbf{X}^l - \mathbf{X}^{l-1}| \quad (3.13)$$

where $s_1 = 0$.

A cubic blending with zero slope at the end points and that the grid transitions smoothly in the far-field. This can be written as

$$b_k = 3\left(\frac{s_k}{s_{k_{\max}}}\right)^2 - 2\left(\frac{s_k}{s_{k_{\max}}}\right)^3 \quad (3.14)$$

where k_{\max} represents the last node along each normal line that is allowed to deflect. Finally, the new position of each grid point can be calculated by applying the blending function to the reference, displaced grid and the original grid:

$$\mathbf{X}_{new}^k = b_k \mathbf{X}_o^k + 1 - b_k \mathbf{X}_r^k, \quad (k=1,2,\dots) \quad (3.15)$$

3.4 Numerical Simulations

A simply supported square plate is considered. The side lengths and thickness are non-dimensionalized to the length of the side. The detailed information of the plate will be discussed in Chapter 5. The plate is discretized as 50×50 elements. Possion ratio is 0.3. $\mu = \frac{\rho_\infty l}{\rho_s t} = 0.1$.

$\lambda = \frac{\rho_\infty u_\infty^2 l^3}{D} = 60$. The initial translational velocities on all the nodes are 0.01. The grid coordinates

of the fluid in the Z direction are $0.02 \times IZ$, where IZ is the integer from KS to KE. The other parameters are IE=JE=51, IS=JS=KE=1, NSF=1, NFF=3, and IDEFM=3. Two cases, KE=10 and 40 are considered. The moved grids for the two cases are shown in Figures 3.16, 3.17, and 3.18 respectively.

One disadvantage of the grid deformation approach is the grid will overlap when the deformation is a little large and the deformed grid in the boundary is not usually satisfied.

3.5 Summary

Different methods used to modify the fluid equations to allow the movement of a structure within the fluid domain are described in this chapter. For the ALE method, various methods used to update or move the fluid grid to conform to a changing structural boundary are also described and evaluated. After that, a gird deformation method which is suitable for aeroelastic simulations on overset grids is presented. This strategy is similar to TFI in that it is algebraic approach based on redefining the

normal grid lines. However, unlike TFI, this method maintains the grid quality of the initial mesh near deforming surfaces under arbitrary, moderate deflections and rotations. In addition, a specified region in the far-field may be held fixed so that the grid overlap regions, and their connectivities, remain unchanged. Numerical simulation shows that this scheme may be used for the deforming mesh of the panel flutter.

Reference:

- ¹Donea, J., "Arbitrary Lagrangian-Eulerian Finite Element Methods," *Computational Methods for Transient Analysis*, Chapter 10, Elsevier Science Publisher B.V., 1983, pp. 473-516.
- ²Singh, K. P., Newman, J. C., and Baysal, O., "Dynamic Unstructured Method for Flows Past Multiple Objects in Relative Motion," *AIAA Journal*, Vol. 33, No. 4, 1995, pp. 641-649.
- ³De Sampaio, P. A., Lyra, P. R., Morgan, K., and Weatherill, N. P., 'Petrov-Galerkin Solutions of the Incompressible Navier-Stokes Equations in Primitive Variables With Adaptive Remeshing,' *Computer Methods in Applied Mechanics and Engineering*, Vol.106, No., 1993, pp. 143-178.
- ⁴Farhat, C., and Lin, T.Y., "Transient Aeroelastic Computations Using Multiple Moving Frames of Reference," *AIAA Paper*, 1990, 90-3053-CP.
- ⁵Lin, T. Y., "A Multiple Frames of Reference Approach to Aeroelastic Computations: Application to Airfoil Flutter Analysis," Ph.D. Thesis, Aerospace Engineering Sciences, University of Colorado, 1990.
- ⁶Hirt, C. W., Amsden, A. A., and Cook, J. L., "An Arbitrary Lagrangian-Eulerian Computing Method for All flow Speeds," *Journal of Computational Physics*, Vol. 14, No., 1974, pp. 227-253.
- ⁷Guruswamy G. P., "Navier-Stokes Computations on Swept-Tapered Wings, Including Flexibility," *Journal of Aircraft*, Vol. 29, No. 4, 1992, pp. 588-597.
- ⁸Gaitonde, A. L., Fiddes, S. P., "A three-dimensional moving mesh method for the calculation of unsteady transonic flows," *The Aeronautical Journal*, Vol.99, No.984, 1995, pp. 150-160.
- ⁹Shankar, V., Ide, H., "Aeroelastic Computations of Flexible Configurations," *Computers and Structures*, Vol. 30, No. 1/2, 1988, pp. 15-28.
- ¹⁰Gaitonde, A. L., Jones, D. P., Fiddes, S. P., "A 2D Navier-Stokes method for unsteady compressible flow calculations on moving meshes," *The Aeronautical Journal*, 1998, pp. 89-97.
- ¹¹Selvam, R. P., Visbal, M. R., Morton, S. A., "Computation of Nonlinear Viscous Panel Flutter Using a Fully-Implicit Aeroelastic Solver," *AIAA Paper*, 1998, 98-1844.

¹²Melville, R. B., Morton, S. A., Rizzetta, D. P., "Implementation of a Fully-Implicit, Aeroelastic Navier-Stokes Solver," *AIAA Paper*, 1997, 97-2039.

¹³Batina, J. T., "Unsteady Euler Airfoil Solutions Using Unstructured Dynamic Meshes," *AIAA Journal*, Vol. 28, No. 8, 1990, pp. 1381-1388.

¹⁴Batina, J. T., "Unsteady Euler Algorithm with Unstructured Dynamic Mesh for Complex-Aircraft Aerodynamic Analysis," *AIAA Journal*, Vol. 29, No.3, 1991, pp. 327- 333.

¹⁵Robinson, B. A., Batina, J. T., Yang, H. T. Y., "Aeroelastic Analysis of Wings Using the Euler Equations with a Deforming Mesh," *Journal of Aircraft*, Vol. 28, No. 11, 1991, pp. 781-788.

¹⁶Lesoinne, M., Farhat, C., "Stability Analysis of Dynamic Meshes for Transient Aeroelastic Computations," *AIAA Paper*, 1993, 93-3325-CP.

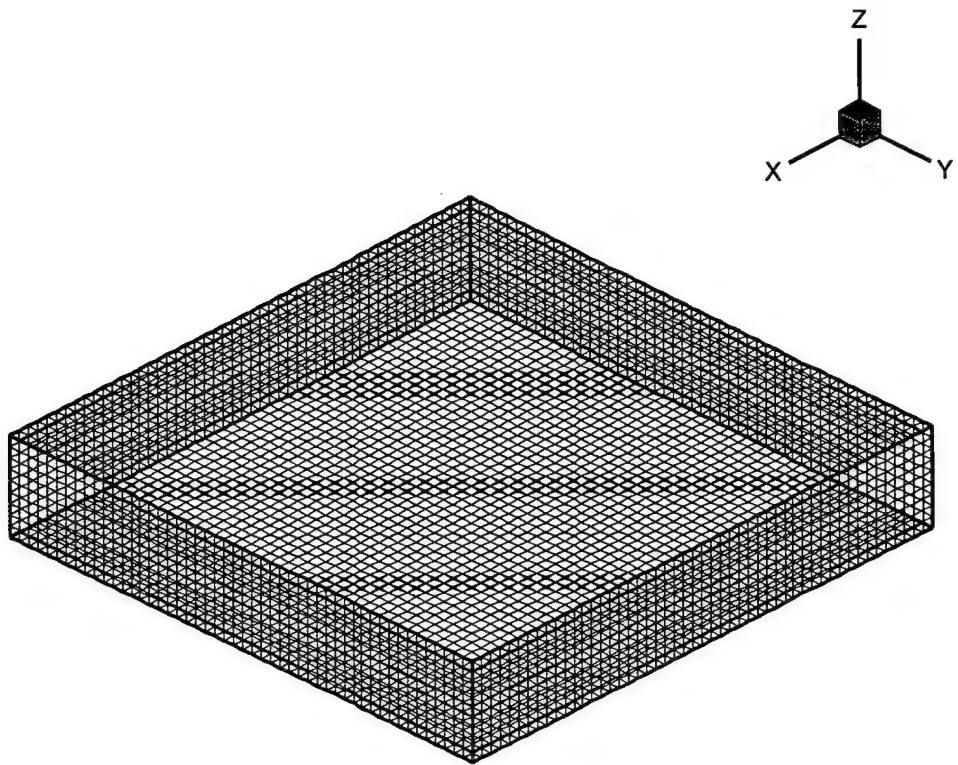
¹⁷Farhat, C., "High performance Simulation of Coupled Nonlinear Transient Aeroelastic Problems," *AGARD Report*, 1995, R-807, pp. 8.1-8.79.

¹⁸Tamura, T., Itoh, Y., Wada, A., Kuwahara, K., "Numerical Study of Pressure Fluctuations on a Rectangular Cylinder in Aerodynamic Oscillation", *Journal of Wind Engineering and Industrial Aerodynamics*, Vol. 54/55, 1995, pp. 239-250.

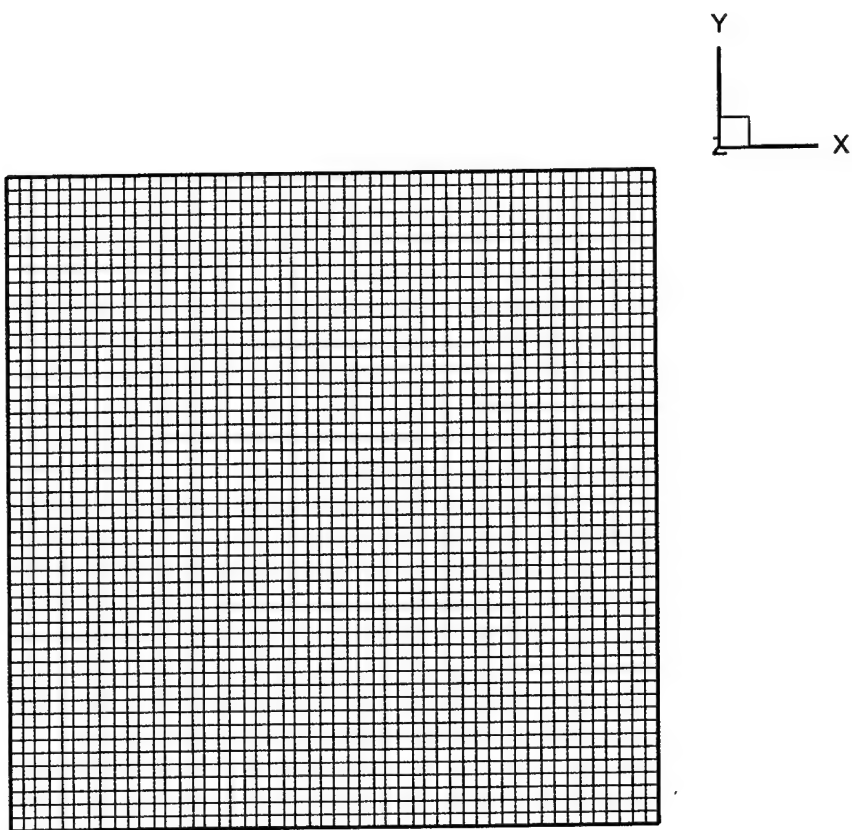
¹⁹Selvam, R. P., Govindasamy, S., Bosch, H., "Aeroelastic Analysis of Bridges Using FEM and Moving Grids," 3^d International Symposium on Computational Wind Engineering, University of Birmingham, UK, September 4-7, 2000.

²⁰Kandil, O., A., Chung, H. A., "Unsteady Vortex-Dominated Flows Around Maneuvering Wings Over a Wide Range of Mach Numbers," *AIAA paper*, 1988, 88-0317.

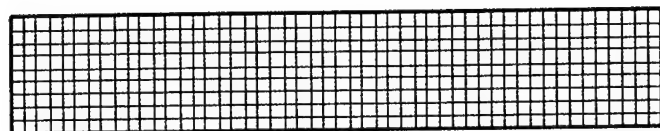
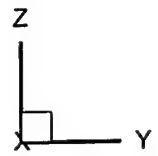
²¹Morton, S. A., Melville, R. B., and Visbal, M.R., "Accuracy and Coupling Issues of Aeroelastic Navier-Stokes Solutions on Deforming Meshes," *Journal of Aircraft*, Vol.35, No.5, 1998, pp.798-805.



(a)

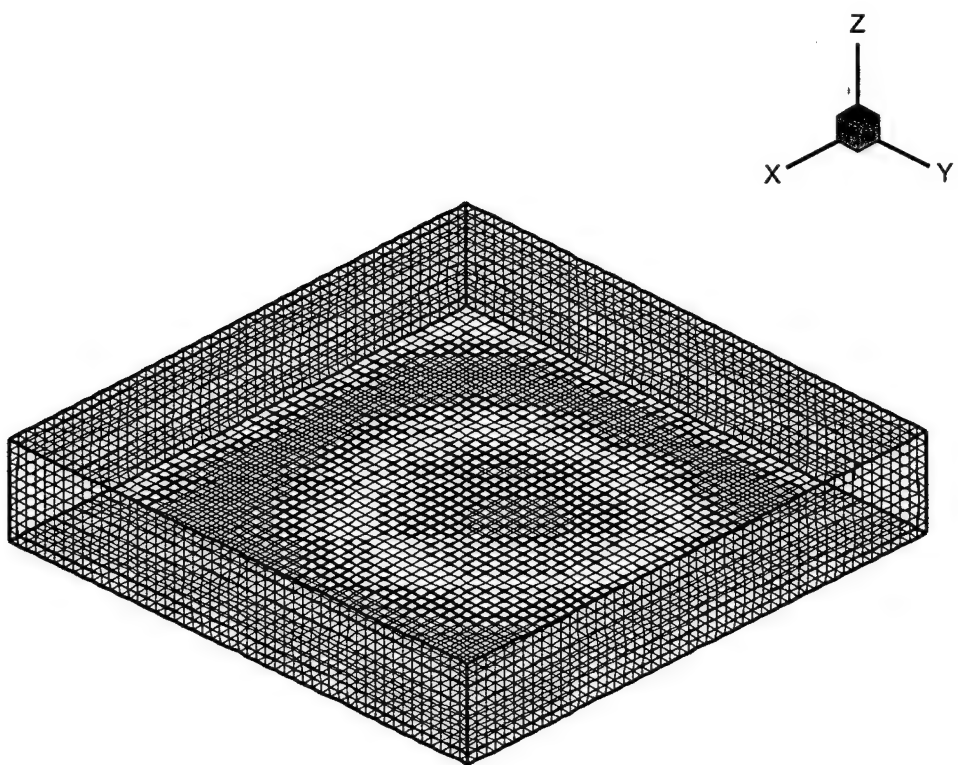


(b)

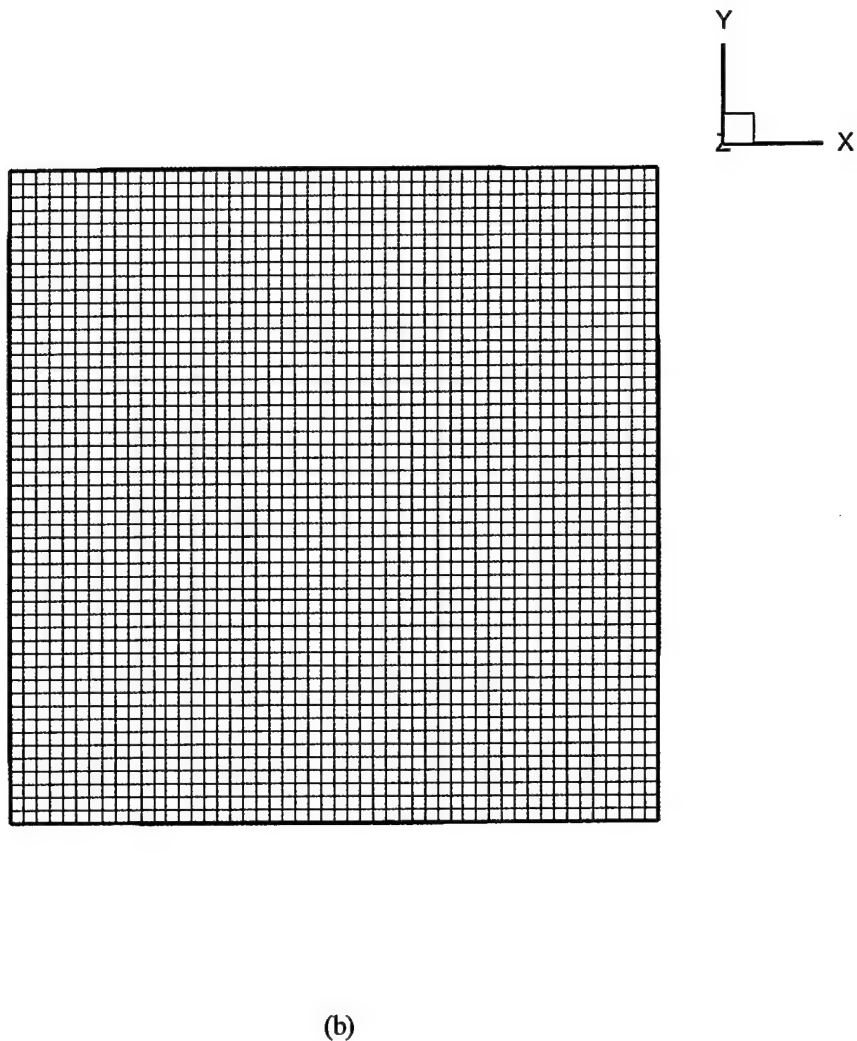


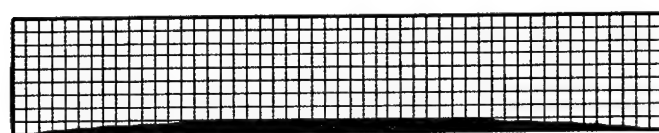
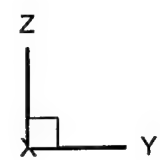
(c)

Figure 3.16. The original grid of the fluid for case 1: (a) in 3-D coordinates;
(b) in X-Y coordinate plane; (c) in Y-Z and X-Z coordinate planes.



(a)





(c)

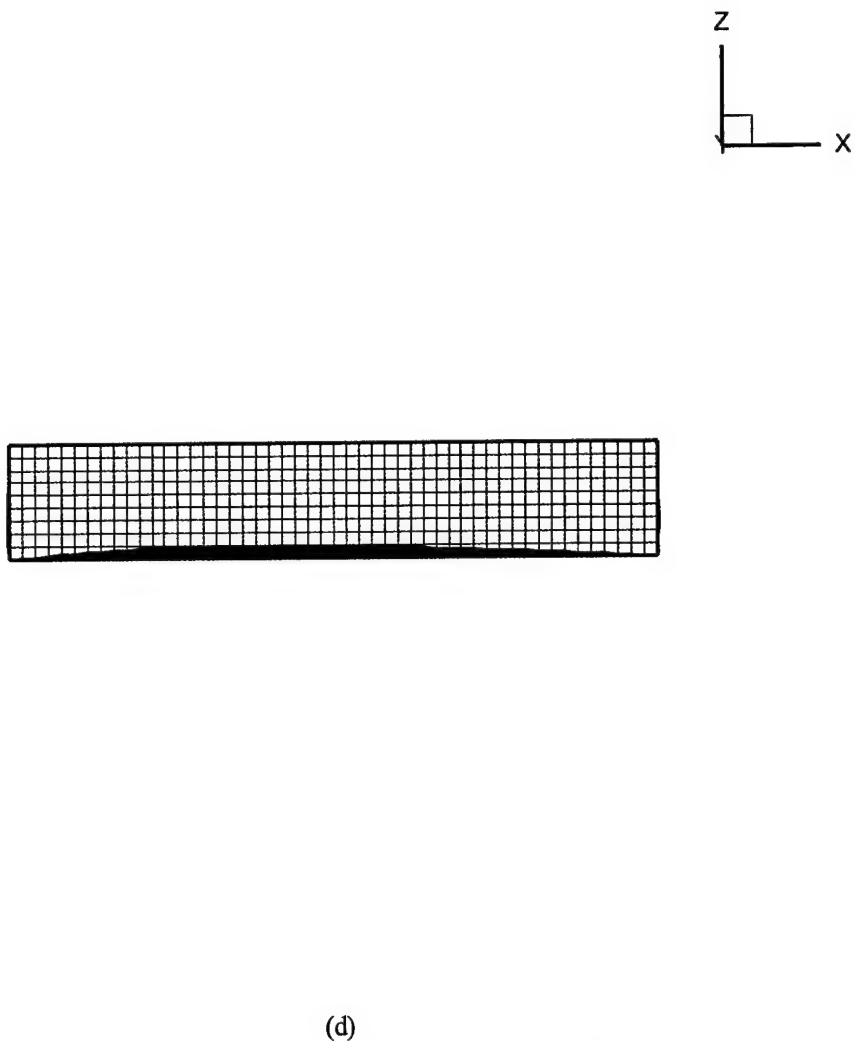
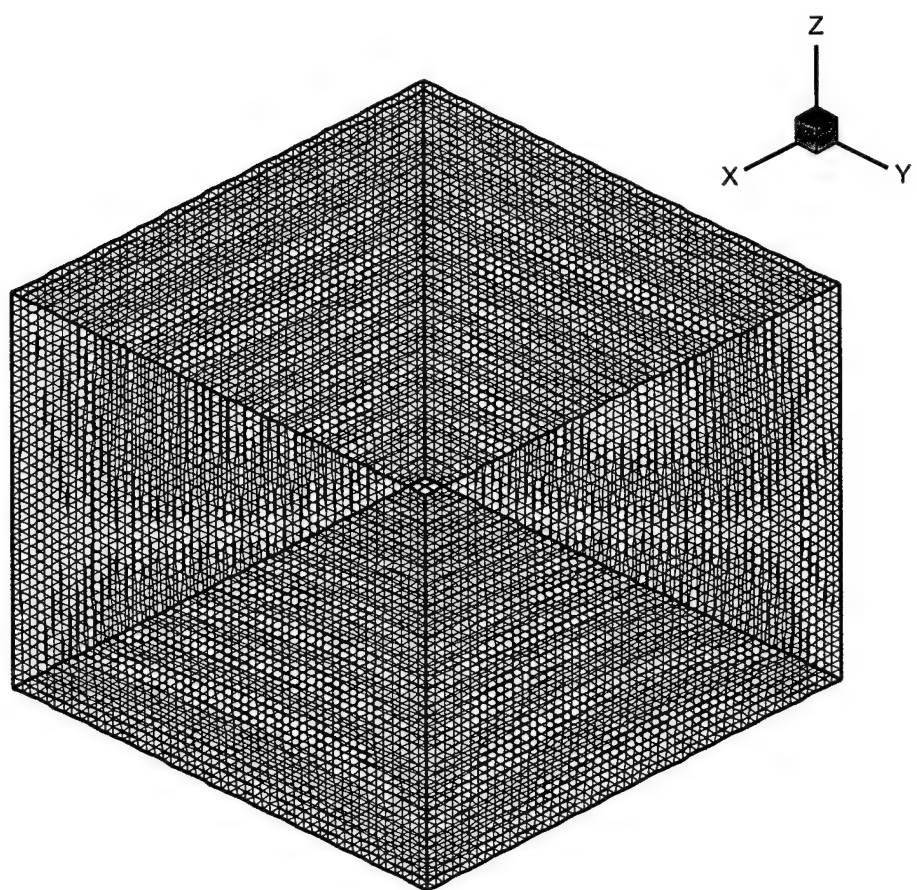
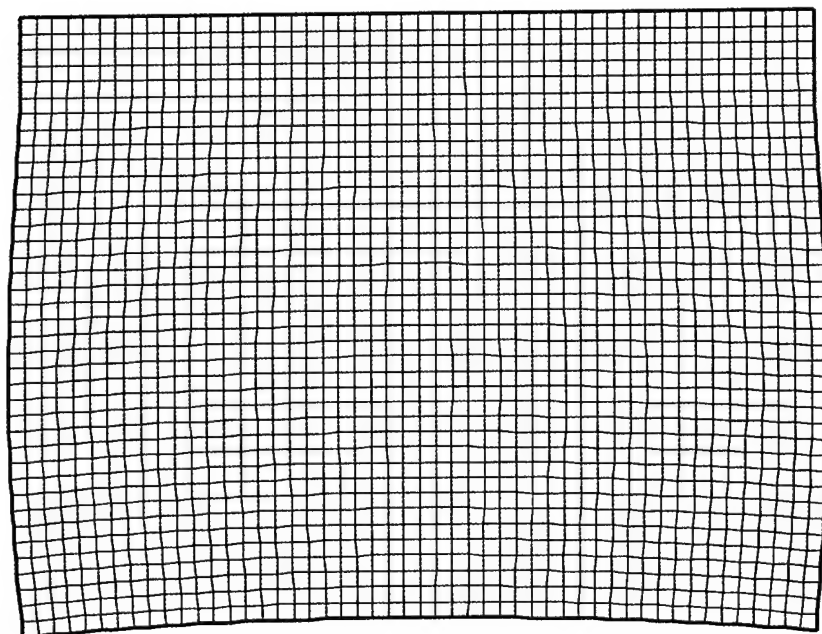
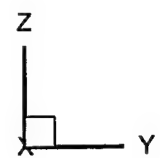


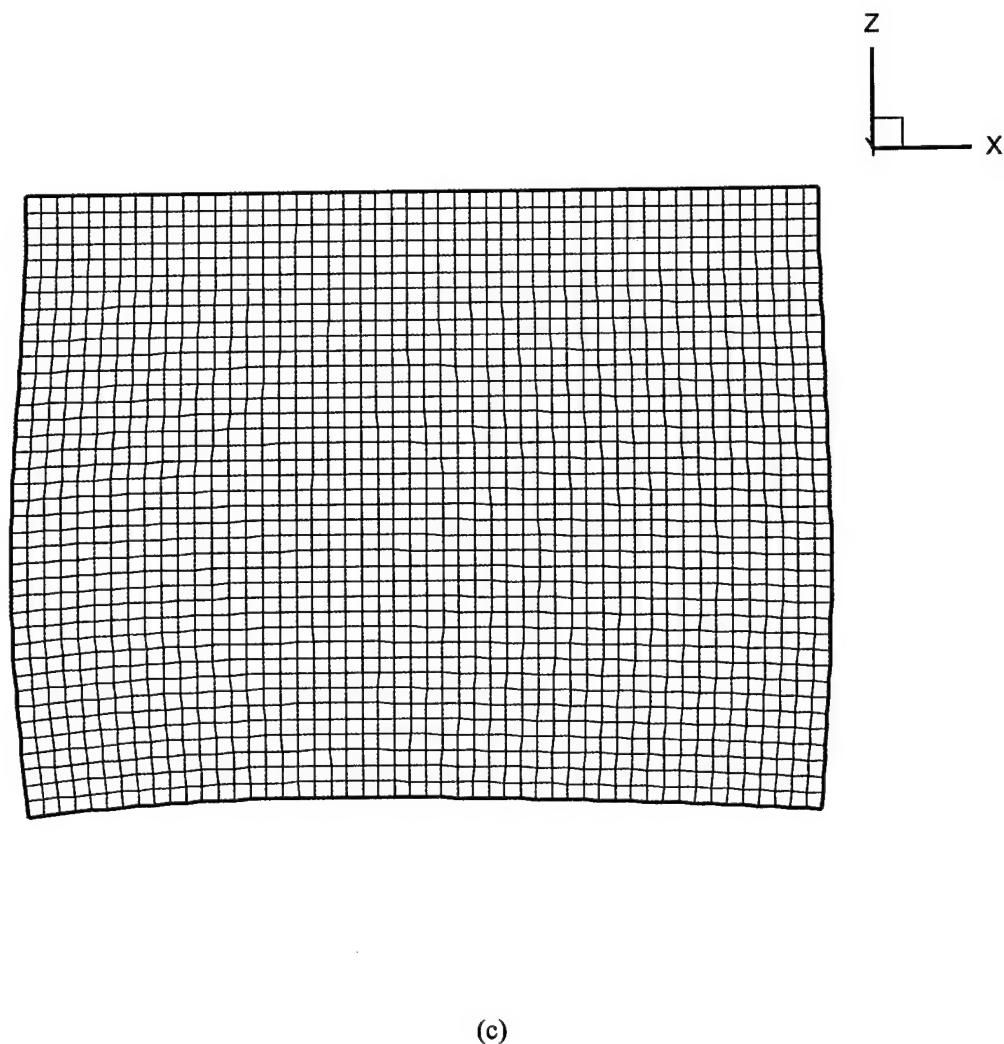
Figure 3.17. The deformed grid of the fluid for case 1: (a) in 3-D coordinates; (b) in X-Y coordinate plane; (c) in Y-Z coordinate plane; (d) in X-Z coordinate plane.



(a)



(b)



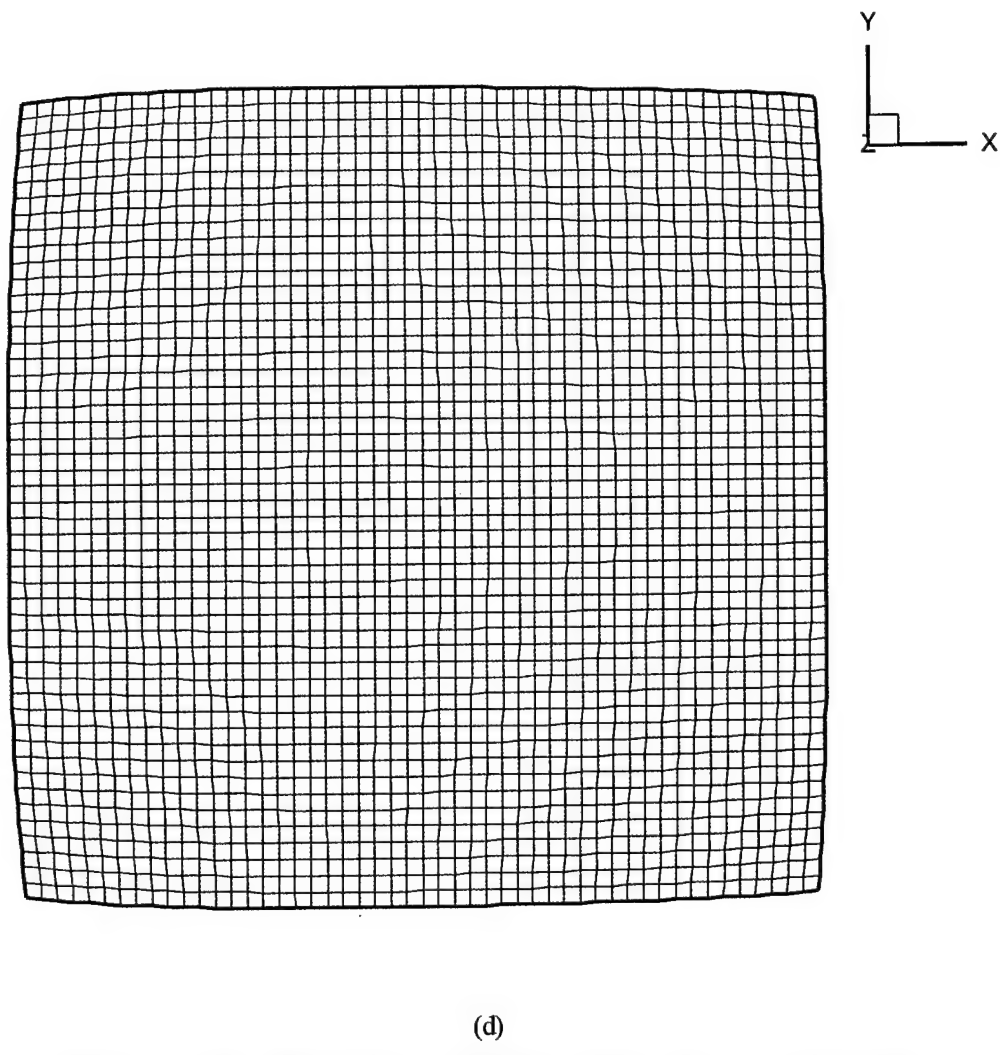


Figure 3.18. The deformed grid of the fluid for case 2: (a) in 3-D coordinates;
(b) in Y-Z coordinate plane for $I=25$; (c) in X-Z coordinate plane for $J=25$;
(d) in X-Y coordinate plane for $K=20$.

CHAPTER 4

COMPUTATIONS OF NAVIER-STOKES EQUATIONS USING FINITE VOLUME METHOD

- 4.1 Introduction
 - 4.2 Governing Equations
 - 4.3 Numerical Procedures
 - 4.4 Boundary Conditions Implementation
 - 4.5 Computational Results and Discussions
-

4.1 Introduction

The fluid dynamic computation must have the fidelity to capture the relevant flow features and provide accurate aerodynamic loads on the structure in developing a perfect fluid-structure interaction solver, or say in computational aeroelasticity. In the following sections, a finite volume method is used to establish computational solvers for Euler equation and Navier-Stokes equation.

4.2 Governing Equations

4.2.1 Governing Equation in Cartesian Coordinates:

4.2.1.1 Non-Viscous Flow

The governing equations of non-viscous fluid flow are Euler equations and the corresponding continuity, energy equations. In Cartesian coordinate, they are given by

$$\frac{U}{\partial t} + \frac{F}{\partial x} + \frac{G}{\partial y} = 0 \quad (4-1)$$

$$U = \begin{bmatrix} \rho \\ \rho u \\ \rho v \\ \rho E \end{bmatrix}, F = \begin{bmatrix} \rho u \\ \rho u^2 + p \\ \rho uv \\ (E + p)u \end{bmatrix}, G = \begin{bmatrix} \rho v \\ \rho uv \\ \rho v^2 + p \\ (E + p)v \end{bmatrix} \quad (4-2)$$

The conservative components of the above equations are given by

$$\frac{\partial}{\partial t} + \frac{(\rho u)}{\partial x} + \frac{(\rho v)}{\partial y} = 0 \quad (4-3)$$

$$\frac{(\rho u)}{\partial t} + \frac{(\rho uu)}{\partial x} + \frac{(\rho uv)}{\partial y} = -\frac{p}{\partial x} \quad (4-4)$$

$$\frac{(\rho v)}{\partial t} + \frac{(\rho uv)}{\partial x} + \frac{(\rho vv)}{\partial y} = -\frac{p}{\partial y} \quad (4-5)$$

$$\frac{(\rho E)}{\partial t} + \frac{[(\rho E + p)u]}{\partial x} + \frac{(\rho E + p)v)}{\partial y} = 0 \quad (4-6)$$

where,

$$E = e + \frac{1}{2}(u^2 + v^2) \quad (4-7)$$

and the state equation is defined as

$$p = (\gamma - 1)[\rho E - \frac{1}{2}\rho(u^2 + v^2)] \quad (4-8)$$

4.2.1.2 Viscous Flow

The governing equations of viscous fluid flow are Navier-Stokes equation and the corresponding continuity, energy equations. They are given by

$$\frac{U}{\partial t} + \frac{F}{\partial x} + \frac{G}{\partial y} = 0 \quad (4-9)$$

$$U = \begin{bmatrix} \rho \\ \rho u \\ \rho v \\ \rho E \end{bmatrix}, F = \begin{bmatrix} \rho u \\ \rho u^2 + p - \tau_{xx} \\ \rho uv - \tau_{xy} \\ (E + p)u - u\tau_{xx} - v\tau_{xy} + q_x \end{bmatrix}, G = \begin{bmatrix} \rho v \\ \rho uv - \tau_{xy} \\ \rho v^2 + p - \tau_{yy} \\ (E + p)v - u\tau_{xy} - v\tau_{yy} + q_y \end{bmatrix} \quad (4-10)$$

The conservative components of the above equation are given by

$$\frac{\rho}{\partial t} + \frac{(\rho u)}{\partial x} + \frac{(\rho v)}{\partial y} = 0 \quad (4-11)$$

$$\frac{\partial(\rho u)}{\partial t} + \frac{\partial(\rho uu)}{\partial x} + \frac{\partial(\rho uv)}{\partial y} = -\frac{\partial p}{\partial x} + \frac{\partial \tau_{xx}}{\partial x} + \frac{\partial \tau_{yx}}{\partial y} \quad (4-12)$$

$$\frac{\partial(\rho v)}{\partial t} + \frac{\partial(\rho uv)}{\partial x} + \frac{\partial(\rho vv)}{\partial y} = -\frac{\partial p}{\partial y} + \frac{\partial \tau_{xy}}{\partial x} + \frac{\partial \tau_{yy}}{\partial y} \quad (4-13)$$

$$\frac{\partial(\rho E)}{\partial t} + \frac{\partial[(\rho E + p)u]}{\partial x} + \frac{\partial(\rho E + p)v}{\partial y} = \frac{\partial(u\tau_{xx} + v\tau_{xy} - q_x)}{\partial x} + \frac{\partial(u\tau_{yx} + v\tau_{yy} - q_y)}{\partial y} \quad (4-14)$$

where, according to the Stokes hypothesis,

$$\tau_{xx} = \mu[2\frac{u}{\partial x} + \lambda(\frac{u}{\partial x} + \frac{v}{\partial y})] \quad (4-15)$$

$$\tau_{xy} = \mu(\frac{u}{\partial y} + \frac{v}{\partial x}) \quad (4-16)$$

$$\tau_{yy} = \mu[2\frac{v}{\partial y} + \lambda(\frac{u}{\partial x} + \frac{v}{\partial y})] \quad (4-17)$$

and λ is second viscosity, for gases it can be take $\lambda = -\frac{2}{3}\mu$. The momentum equations are given by

$$\frac{(\rho u)}{\partial t} + \frac{(\rho uu)}{\partial x} + \frac{(\rho uv)}{\partial y} = -\frac{p}{\partial x} + \frac{\partial}{\partial x}[\mu(2\frac{u}{\partial x} - \frac{2}{3}(\frac{u}{\partial x} + \frac{v}{\partial y}))] + \frac{\partial}{\partial y}[\mu(\frac{u}{\partial y} + \frac{v}{\partial x})] \quad (4-18)$$

$$\frac{(\rho v)}{\partial t} + \frac{(\rho uv)}{\partial x} + \frac{(\rho vv)}{\partial y} = -\frac{p}{\partial y} + \frac{\partial}{\partial y}[\mu(\frac{u}{\partial y} + \frac{v}{\partial x})] + \frac{\partial}{\partial x}[\mu(2\frac{v}{\partial y} - \frac{2}{3}(\frac{u}{\partial x} + \frac{v}{\partial y}))] \quad (4-19)$$

For convenience, casting the governing equation (4-9) in nondimensional form. If L is the characteristic length, and other characteristic quantities are taken to be freestream values denoted by subscript ∞ , we may define the dimensionless variables, denoted by an asterisk, as

$$\begin{aligned} x^* &= \frac{x}{L}, & y^* &= \frac{y}{L}, & t^* &= \frac{t}{V_\infty} \\ u^* &= \frac{u}{L}, & v^* &= \frac{v}{L}, & \mu^* &= \frac{\mu}{L} \\ \rho^* &= \frac{\rho}{\rho_\infty V_\infty}, & p^* &= \frac{p}{\rho_\infty V_\infty^2}, & T^* &= \frac{T}{T_\infty}, & e^* &= \frac{e}{V_\infty^2} \end{aligned} \quad (4-20)$$

This nondimensionalized procedure is applied to the compressible Navier-Stokes equation (4-9), the following dimensionless equation are obtained as

$$\frac{\partial U^*}{\partial t^*} + \frac{\partial F^*}{\partial x^*} + \frac{\partial G^*}{\partial y^*} = 0 \quad (4-21)$$

Where U^*, F^*, G^* are the vectors given by equation (4-10), except that each term is dimensionless, denoted by an asterisk, and the dimensionless total energy per unit volume is given by

$$E^* = e^* + \frac{u^* + v^*}{\rho} \quad (4-22)$$

The components of the shear stress tensor and the heat flux vector in dimensionless form are expressed as

$$\begin{aligned} \tau_{xx}^* &= \frac{\mu^*}{Re} \left(\frac{4}{3} \frac{\partial u^*}{\partial x^*} - \frac{2}{3} \frac{\partial v^*}{\partial y^*} \right) \\ \tau_{xy}^* &= \frac{\mu^*}{Re} \left(\frac{\partial u^*}{\partial y^*} + \frac{\partial v^*}{\partial x^*} \right) \\ \tau_{yy}^* &= \frac{\mu^*}{Re} \left(\frac{4}{3} \frac{\partial v^*}{\partial y^*} - \frac{2}{3} \frac{\partial u^*}{\partial x^*} \right) \\ q_x^* &= - \frac{\mu^*}{(\gamma - 1) M_\infty^2 Re Pr} \frac{\partial T^*}{\partial x^*} \\ q_y^* &= - \frac{\mu^*}{(\gamma - 1) M_\infty^2 Re Pr} \frac{\partial T^*}{\partial y^*} \end{aligned} \quad (4-23)$$

where M_∞ , Re , Pr are the freestream Mach number, Reynolds number and Prandlt number respectively, given by

$$Re = \frac{\rho_\infty V_\infty L}{\mu_\infty} , \quad M_\infty = \frac{V_\infty}{\sqrt{\gamma R T_\infty}} , \quad Pr = \frac{C_p \mu}{k} \quad (4-24)$$

μ^* is dimensionless viscosity. It can be taken as constant ($=1.0$) if the temperature variation is not very large, or be calculated from Sutherland's law

$$\mu^* = (T^*)^{1.5} \frac{(1+C_1)}{(T^* + C_1)} \quad (4-25)$$

Where T^* is dimensionless temperature, constant $C_1 = \frac{110}{T_\infty}$. Here T_∞ is freestream temperature ($^{\circ}\text{K}$).

The perfect gas equation of state become

$$p^* = \frac{\rho^* T^*}{\gamma M_\infty^2} , \quad e^* = \frac{\rho T^*}{\gamma(\gamma - 1) M_\infty^2} \quad (4-26)$$

4.2.2 Governing Equation in Non-orthogonal Coordinates:

4.2.2.1 Non-Viscous Flow

From the Cartesian equations, we can get the governing equations in non-orthogonal coordinates:

Continue equation:

$$\frac{\rho}{\partial t} + \frac{(\rho u)}{\partial \xi} \xi_x + \frac{(\rho u)}{\partial \eta} \eta_x + \frac{(\rho v)}{\partial \xi} \xi_y + \frac{(\rho v)}{\partial \eta} \eta_y = 0 \quad (4-27)$$

Because $\frac{(\rho u)_\xi \xi_x}{J} = \left[\frac{(\rho u) \xi_x}{J} \right]_\xi - (\rho u) \left(\frac{\xi_x}{J} \right)_\xi = \left[\frac{(\rho u) \xi_x}{J} \right]_\xi - (\rho u) (\eta_\eta)_\xi = \left[\frac{(\rho u) \xi_x}{J} \right]_\xi$, one has

$$\frac{\partial}{\partial t} \left(\frac{\rho}{J} \right) + \frac{\partial}{\partial \xi} \left[\frac{(\rho u) \xi_x + (\rho v) \xi_y}{J} \right] + \frac{\partial}{\partial \eta} \left[\frac{(\rho u) \eta_x + (\rho v) \eta_y}{J} \right] = 0 \quad (4-28)$$

$$\frac{\partial}{\partial t} \left(\frac{\rho}{J} \right) + \frac{\partial}{\partial \xi} \left(\frac{\rho U}{J} \right) + \frac{\partial}{\partial \eta} \left(\frac{\rho V}{J} \right) = 0 \quad (4-29)$$

Momentum equations:

$$\frac{\partial(\rho u)}{\partial t} + \frac{\partial(\rho u^2 + p)}{\partial \xi} \xi_x + \frac{\partial(\rho u^2 + p)}{\partial \eta} \eta_x + \frac{\partial(\rho uv)}{\partial \xi} \xi_y + \frac{\partial(\rho uv)}{\partial \eta} \eta_y = 0 \quad (4-30)$$

then we have,

$$\frac{\partial}{\partial t} \left(\frac{\rho u}{J} \right) + \frac{\partial}{\partial \xi} \left(\frac{\rho u U + \xi_x p}{J} \right) + \frac{\partial}{\partial \eta} \left(\frac{\rho u V + \eta_x p}{J} \right) = 0 \quad (4-31)$$

$$\frac{\partial}{\partial t} \left(\frac{\rho v}{J} \right) + \frac{\partial}{\partial \xi} \left(\frac{\rho v U + \xi_y p}{J} \right) + \frac{\partial}{\partial \eta} \left(\frac{\rho v V + \eta_y p}{J} \right) = 0 \quad (4-32)$$

4.2.2.2 Viscous Flow

Momentum equations:

$$\begin{aligned} & \frac{\partial}{\partial t} \left(\frac{\rho u}{J} \right) + \frac{\partial}{\partial \xi} \left\{ [\rho u U + \left(\frac{4}{3} (\mu \xi_x)_x + (\mu \xi_y)_y \right) u + \left(-\frac{2}{3} (\mu \xi_x)_y + (\mu \xi_y)_x \right) v + \xi_x p] / J \right\} \\ & + \frac{\partial}{\partial \eta} \left\{ [\rho u V + \left(\frac{4}{3} (\mu \eta_x)_x + (\mu \eta_y)_y \right) u + \left(-\frac{2}{3} (\mu \eta_x)_y + (\mu \eta_y)_x \right) v + \eta_x p] / J \right\} \\ & = \frac{\partial}{\partial \xi} \left(\frac{\partial}{\partial \xi} \left[\left(\frac{4}{3} \xi_x^2 + \xi_y^2 \right) \mu u + \frac{1}{3} \mu \xi_x \xi_y v \right] / J \right) + \frac{\partial}{\partial \eta} \left(\frac{\partial}{\partial \xi} \left[2 \left(\frac{4}{3} \xi_x \eta_x + \xi_y \eta_y \right) \mu u + \frac{1}{3} \mu (\xi_x \eta_y + \xi_y \eta_x) v \right] / J \right) \\ & + \frac{\partial}{\partial \eta} \left(\frac{\partial}{\partial \eta} \left[\left(\frac{4}{3} \eta_x^2 + \eta_y^2 \right) \mu u + \frac{1}{3} \mu \eta_x \eta_y v \right] / J \right) \end{aligned} \quad (4-33)$$

$$\begin{aligned}
 & \frac{\partial}{\partial t} \left(\frac{\rho v}{J} \right) + \frac{\partial}{\partial \xi} \left\{ [\rho v U + ((\mu \xi_x)_y - \frac{2}{3} (\mu \xi_y)_x) u + ((\mu \xi_x)_x + \frac{4}{3} (\mu \xi_y)_y) v + \xi_y p] / J \right\} \\
 & + \frac{\partial}{\partial \eta} \left\{ [\rho v V + ((\mu \eta_x)_y - \frac{2}{3} (\mu \eta_y)_x) u + (\frac{4}{3} (\mu \eta_y)_y + (\mu \eta_x)_x) v + \eta_y p] / J \right\} \\
 & = \frac{\partial}{\partial \xi} \left(\frac{\partial}{\partial \xi} \left[\left(\frac{4}{3} \xi_y^2 + \xi_x^2 \right) \mu v + \frac{1}{3} \mu \xi_x \xi_y u \right] / J \right) + \frac{\partial}{\partial \eta} \left(\frac{\partial}{\partial \xi} \left[2 \left(\frac{4}{3} \xi_y \eta_y + \xi_x \eta_x \right) \mu v + \frac{1}{3} \mu (\xi_x \eta_y + \xi_y \eta_x) u \right] / J \right) \\
 & + \frac{\partial}{\partial \eta} \left(\frac{\partial}{\partial \eta} \left[\left(\frac{4}{3} \eta_y^2 + \eta_x^2 \right) \mu v + \frac{1}{3} \mu \eta_x \eta_y u \right] / J \right)
 \end{aligned} \tag{4-34}$$

Energy equation:

$$\frac{\partial}{\partial t} \left(\frac{\rho E}{J} \right) + \frac{\partial}{\partial \xi} \left\{ [(\rho E + p) U] / J \right\} + \frac{\partial}{\partial \eta} \left\{ [(\rho E + p) V] / J \right\} = \frac{\partial}{\partial \xi} \left[\frac{(u \tau_{xx} + v \tau_{xy} - q_x)}{J} \right] + \frac{\partial}{\partial \eta} \left[\frac{(u \tau_{yx} + v \tau_{yy} - q_y)}{J} \right] \tag{4-35}$$

4.3 Numerical Procedures

4.3.1 Finite Volume Method

The Governing equations (Navier-Stokes) are discretized in control volume:

4.3.1.1 Continuity equation:

$$\frac{\Delta x \Delta y}{\Delta t} (\rho_{i,j}^{n+1} - \rho_{i,j}^n) + [(\rho u)_{i+\frac{1}{2},j}^{n+1} - (\rho u)_{i-\frac{1}{2},j}^{n+1}] \Delta y + [(\rho v)_{i,j+\frac{1}{2}}^{n+1} - (\rho v)_{i,j-\frac{1}{2}}^{n+1}] \Delta x = 0 \tag{4-36}$$

x-direction momentum equation:

$$\begin{aligned}
 & \frac{\Delta x \Delta y}{\Delta t} [(\rho u)_{i,j}^{n+1} - (\rho u)_{i,j}^n] + [(\rho uu)_{i+\frac{1}{2},j}^{n+1} - (\rho uu)_{i-\frac{1}{2},j}^{n+1}] \Delta y + [(\rho uv)_{i,j+\frac{1}{2}}^{n+1} - (\rho uv)_{i,j-\frac{1}{2}}^{n+1}] \Delta x \\
 & = (p_{i,j}^{n+1} - p_{i+1,j}^{n+1}) \Delta y + [(\mu \frac{\partial u}{\partial x})_{i+\frac{1}{2},j}^{n+1} - (\mu \frac{\partial u}{\partial x})_{i-\frac{1}{2},j}^{n+1}] \Delta y + [(\mu \frac{\partial u}{\partial y})_{i,j+\frac{1}{2}}^{n+1} - (\mu \frac{\partial u}{\partial y})_{i,j-\frac{1}{2}}^{n+1}] \Delta x + Sa
 \end{aligned} \tag{4-37}$$

We denote the node (i,j) as P and its neighbor nodes $(i+1,j)$, $(i-1,j)$, $(i,j+1)$ and $(i,j-1)$ as E, W, N, S respectively, and the surfaces which locate at $(i + \frac{1}{2}, j)$, $(i - \frac{1}{2}, j)$, $(i, j + \frac{1}{2})$, $(i, j - \frac{1}{2})$ between these nodes as e, w, n, s etc.. as shown in Figure 4.1.

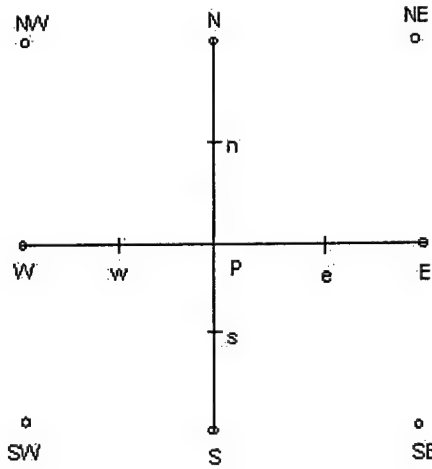


Figure 4.1 Diagram of points used for discretization

The discrete continuity equation is given by

$$\frac{\rho_p^{n+1} - \rho_p^n}{\Delta t} \Delta x \Delta y + [(\rho u)_e - (\rho u)_w] \Delta y + [(\rho u)_n - (\rho u)_s] \Delta x = 0 \quad (4-38)$$

Here, upwind scheme is applied to the convection terms, for example,

$$F_e \phi_e = \phi_p \max(F_e, 0) - \phi_E \max(-F_e, 0) \quad (4-39)$$

where F_e is flux across the control surface e . Therefore, we have

$$\begin{aligned} & \frac{\rho_p^{n+1}}{\Delta t} \Delta x \Delta y - \frac{\rho_p^n}{\Delta t} \Delta x \Delta y + \max(F_e, 0) \rho_p^{n+1} - \max(-F_e, 0) \rho_E^{n+1} - \max(F_w, 0) \rho_W^{n+1} + \max(-F_w, 0) \rho_p^{n+1} \\ & + \max(F_n, 0) \rho_P^{n+1} - \max(-F_n, 0) \rho_N^{n+1} - \max(F_s, 0) \rho_S^{n+1} + \max(-F_s, 0) \rho_P^{n+1} = 0 \end{aligned} \quad (4-40)$$

The discretization equation is written as

$$a_p \rho_p^{n+1} = a_E \rho_E^{n+1} + a_W \rho_W^{n+1} + a_N \rho_N^{n+1} + a_S \rho_S^{n+1} + b_\rho \quad (4-41)$$

where, the coefficients, source term and flux are respectively

$$a_p = \max(F_e, 0) + \max(-F_w, 0) + \max(F_n, 0) + \max(-F_s, 0) + \frac{\Delta x \Delta y}{\Delta t}$$

$$a_E = \max(-F_e, 0), \quad a_W = \max(-F_w, 0), \quad a_N = \max(-F_n, 0), \quad a_S = \max(-F_s, 0)$$

$$b_\rho = \rho_p^n \frac{\Delta x \Delta y}{\Delta t}$$

$$F_e = u_e (\Delta y)_e, \quad F_w = u_w (\Delta y)_w, \quad F_n = u_n (\Delta x)_n, \quad F_s = u_s (\Delta x)_s$$

(4-42)

The x -direction momentum equation is rewritten as

$$\begin{aligned} \frac{(\rho u)_P^{n+1} - (\rho u)_P^n}{\Delta t} \Delta x \Delta y + [(\rho uu)_e - (\rho uu)_w] \Delta y + [(\rho uv)_n - (\rho uv)_s] \Delta x &= -[p_e(\Delta y)_e - p_w(\Delta y)_w] + \\ &[\frac{\mu_e}{Re} (\frac{\partial u}{\partial x})_e - \frac{\mu_w}{Re} (\frac{\partial u}{\partial x})_w] \Delta y + [\frac{\mu_n}{Re} (\frac{\partial u}{\partial y})_n - \frac{\mu_s}{Re} (\frac{\partial u}{\partial y})_s] \Delta x + \\ &\frac{1}{3} [\frac{\mu_e}{Re} (\frac{\partial u}{\partial x})_e - \frac{\mu_w}{Re} (\frac{\partial u}{\partial x})_w] \Delta y + \frac{1}{3} [\frac{\mu_n}{Re} (\frac{\partial v}{\partial x})_n - \frac{\mu_s}{Re} (\frac{\partial v}{\partial x})_s] \Delta x \end{aligned} \quad (4-43)$$

Upwind scheme is used for the convection term, and central scheme is used for diffusive terms, then

$$\begin{aligned} \frac{(\rho u)_P^{n+1}}{\Delta t} \Delta x \Delta y - \frac{(\rho u)_P^n}{\Delta t} \Delta x \Delta y + \max(F_e, 0)(\rho u)_P^{n+1} - \max(-F_e, 0)(\rho u)_E^{n+1} - \max(F_w, 0)(\rho u)_W^{n+1} \\ + \max(-F_w, 0)(\rho u)_P^{n+1} + \max(F_n, 0)(\rho u)_P^{n+1} - \max(-F_n, 0)(\rho u)_N^{n+1} - \max(F_s, 0)(\rho u)_S^{n+1} \\ + \max(-F_s, 0)(\rho u)_P^{n+1} = -[p_e(\Delta y)_e - p_w(\Delta y)_w] + \\ \frac{\mu_e \Delta y}{\rho_e Re(\delta x)_e} [(\rho u)_E - (\rho u)_P] - \frac{\mu_w \Delta y}{\rho_w Re(\delta x)_w} [(\rho u)_P - (\rho u)_W] + \\ \frac{\mu_n \Delta y}{\rho_n Re(\delta x)_n} [(\rho u)_N - (\rho u)_P] - \frac{\mu_s \Delta y}{\rho_s Re(\delta x)_s} [(\rho u)_P - (\rho u)_S] + \\ \frac{\mu_e \Delta y}{3 \rho_e Re(\delta x)_e} [(\rho u)_E - (\rho u)_P] - \frac{\mu_w \Delta y}{3 \rho_w Re(\delta x)_w} [(\rho u)_P - (\rho u)_W] + \\ \frac{\mu_n \Delta y}{\rho_n Re(\delta x)_n} [(\rho v)_{ne} - (\rho v)_{nw}] - \frac{\mu_s \Delta y}{\rho_s Re(\delta x)_s} [(\rho v)_{se} - (\rho v)_{sw}] \end{aligned} \quad (4-44)$$

Then, the x-direction momentum equation in discrete form is

$$a_P (\rho u)_P^{n+1} = a_E (\rho u)_E^{n+1} + a_W (\rho u)_W^{n+1} + a_N (\rho u)_N^{n+1} + a_S (\rho u)_S^{n+1} + b_u \quad (4-45)$$

where the coefficients are respectively

$$\begin{aligned} a_E &= \frac{\mu_e \Delta y}{\rho_e Re(\delta x)_e} + \max(-F_e, 0) = D_e + \max(-F_e, 0) \\ a_W &= \frac{\mu_w \Delta y}{\rho_w Re(\delta x)_w} + \max(F_w, 0) = D_w + \max(F_w, 0) \\ a_N &= \frac{\mu_n \Delta y}{\rho_n Re(\delta x)_n} + \max(-F_n, 0) = D_n + \max(-F_n, 0) \\ a_S &= \frac{\mu_s \Delta y}{\rho_s Re(\delta x)_s} + \max(F_s, 0) = D_s + \max(F_s, 0) \end{aligned}$$

$$a_p = D_e + \max(F_e, 0) + D_w + \max(-F_w, 0) + D_n + \max(F_n, 0) + D_s + \max(-F_s, 0) + \frac{\Delta x \Delta y}{\Delta t} \quad (4-46)$$

Source term

$$b_u = (\rho u)_p^n \frac{\Delta x \Delta y}{\Delta} - [p_e(\Delta y)_e - p_w(\Delta y)_w] + b' \quad (4-47)$$

Where b' is given by

$$\begin{aligned} b' = & \frac{\mu_e \Delta y}{3 \rho_e \operatorname{Re}(\delta x)_e} [(\rho u)_E - (\rho u)_p] - \frac{\mu_w \Delta y}{3 \rho_w \operatorname{Re}(\delta x)_w} [(\rho u)_p - (\rho u)_w] + \\ & \frac{\mu_n \Delta y}{\rho_n \operatorname{Re}(\delta x)_n} [(\rho v)_{ne} - (\rho v)_{nw}] - \frac{\mu_s \Delta y}{\rho_s \operatorname{Re}(\delta x)_s} [(\rho v)_{se} - (\rho v)_{sw}] \end{aligned} \quad (4-48)$$

The iteration equation is

$$(\rho u)_p^{n+1} = (\rho u)_p^n - \alpha * res / a_p \quad (4-49)$$

where the residual is given by

$$res = a_p(\rho u)_p^{n+1} - a_E(\rho u)_E^{n+1} + a_w(\rho u)_w^{n+1} + a_N(\rho u)_N^{n+1} + a_S(\rho u)_S^{n+1} + b_u \quad (4-50)$$

y-direction momentum equation:

Similarly, y-direction momentum equation is discretized as:

$$a_p(\rho v)_p^{n+1} = a_E(\rho v)_E^{n+1} + a_w(\rho v)_w^{n+1} + a_N(\rho v)_N^{n+1} + a_S(\rho v)_S^{n+1} + b_v \quad (4-51)$$

Its coefficients are all the same as that in x-direction equation, but the source term is

$$b_v = (\rho v)_p^n \frac{\Delta x \Delta y}{\Delta} - [p_n(\Delta x)_n - p_s(\Delta x)_s] + b'' \quad (4-52)$$

where,

$$\begin{aligned} b'' = & \frac{\mu_n \Delta x}{3 \rho_n \operatorname{Re}(\delta y)_n} [(\rho v)_N - (\rho v)_p] - \frac{\mu_s \Delta x}{3 \rho_s \operatorname{Re}(\delta y)_s} [(\rho v)_p - (\rho v)_s] + \\ & \frac{\mu_e \Delta y}{\rho_e \operatorname{Re}(\delta y)_e} [(\rho u)_{en} - (\rho u)_{es}] - \frac{\mu_w \Delta y}{\rho_w \operatorname{Re}(\delta y)_w} [(\rho u)_{wn} - (\rho u)_{ws}] \end{aligned} \quad (4-53)$$

4.3.1.2 Energy equation:

The energy equation is

$$\begin{aligned} \frac{\partial(\rho E)}{\partial t} + \frac{\partial(\rho u E)}{\partial x} + \frac{\partial(\rho v E)}{\partial y} = & - \left[\frac{\partial(pu)}{\partial x} + \frac{\partial(pv)}{\partial y} \right] + \frac{\partial}{\partial x}(u\tau_{xx} + v\tau_{xy}) + \frac{\partial}{\partial y}(u\tau_{yx} + v\tau_{yy}) + \\ & \frac{\mu}{(\gamma - 1)M_\infty^2 \operatorname{Re} \operatorname{Pr}} \left[\frac{\partial}{\partial x} \left(\frac{\partial T}{\partial x} \right) + \frac{\partial}{\partial y} \left(\frac{\partial T}{\partial y} \right) \right] \end{aligned}$$

(4-54)

For convenience of discretization, rewrite the energy equation as

$$\begin{aligned} \frac{\partial(\rho E)}{\partial t} + \frac{\partial(\rho u E)}{\partial x} + \frac{\partial(\rho v E)}{\partial y} = & -\left[\frac{\partial(pu)}{\partial x} + \frac{\partial(pv)}{\partial y}\right] + \frac{\partial}{\partial x}(u\tau_{xx} + v\tau_{xy}) + \frac{\partial}{\partial y}(u\tau_{yx} + v\tau_{yy}) + \\ & \frac{\mu\gamma}{Re Pr} \left\{ \frac{\partial}{\partial x} \left[\frac{\partial}{\partial x} \left(\frac{T}{\gamma(\gamma-1)M_\infty^2} + \frac{u^2 + v^2}{2} \right) \right] + \frac{\partial}{\partial y} \left[\frac{\partial}{\partial y} \left(\frac{T}{\gamma(\gamma-1)M_\infty^2} + \frac{u^2 + v^2}{2} \right) \right] \right\} - \\ & \frac{\mu\gamma}{Re Pr} \left\{ \frac{\partial}{\partial x} \left[\frac{\partial}{\partial x} \left(\frac{u^2 + v^2}{2} \right) \right] + \frac{\partial}{\partial y} \left[\frac{\partial}{\partial y} \left(\frac{u^2 + v^2}{2} \right) \right] \right\} \end{aligned} \quad (4-55)$$

Because specific energy $E = \left(\frac{T}{\gamma(\gamma-1)M_\infty^2} + \frac{u^2 + v^2}{2} \right)$, the above equation is

$$\begin{aligned} \frac{\partial(\rho E)}{\partial t} + \frac{\partial(\rho u E)}{\partial x} + \frac{\partial(\rho v E)}{\partial y} = & -\left[\frac{\partial(pu)}{\partial x} + \frac{\partial(pv)}{\partial y}\right] + \frac{\partial}{\partial x}(u\tau_{xx} + v\tau_{xy}) + \frac{\partial}{\partial y}(u\tau_{yx} + v\tau_{yy}) + \\ & \frac{\mu\gamma}{Re Pr} \left[\frac{\partial}{\partial x} \left(\frac{\partial E}{\partial x} \right) + \frac{\partial}{\partial y} \left(\frac{\partial E}{\partial y} \right) \right] - \frac{\mu\gamma}{Re Pr} \left\{ \frac{\partial}{\partial x} \left[\frac{\partial}{\partial x} \left(\frac{u^2 + v^2}{2} \right) \right] + \frac{\partial}{\partial y} \left[\frac{\partial}{\partial y} \left(\frac{u^2 + v^2}{2} \right) \right] \right\} \end{aligned} \quad (4-56)$$

we can discrete the energy equation in the same way as momentum equation,

$$a_p (\rho E)_P^{n+1} = a_E (\rho E)_E^{n+1} + a_w (\rho E)_W^{n+1} + a_n (\rho E)_N^{n+1} + a_s (\rho E)_S^{n+1} + b_E \quad (4-57)$$

where the diffusion conductance in the coefficients are respectively

$$\begin{aligned} D_e &= \frac{\mu_e \gamma \Delta y}{\rho_e Re Pr(\delta x)_e}, \quad D_w = \frac{\mu_w \gamma \Delta y}{\rho_w Re Pr(\delta x)_w} \\ D_n &= \frac{\mu_n \gamma \Delta y}{\rho_n Re Pr(\delta x)_n}, \quad D_s = \frac{\mu_s \gamma \Delta y}{\rho_s Re Pr(\delta x)_s} \end{aligned} \quad (4-58)$$

Source term b_E is

$$\begin{aligned} b_E = & \left\{ -\left[\frac{\partial(pu)}{\partial x} + \frac{\partial(pv)}{\partial y}\right] + \frac{\partial}{\partial x}(u\tau_{xx} + v\tau_{xy}) + \frac{\partial}{\partial y}(u\tau_{yx} + v\tau_{yy}) \right. \\ & \left. - \frac{\mu\gamma}{Re Pr} \left\{ \frac{\partial}{\partial x} \left[\frac{\partial}{\partial x} \left(\frac{u^2 + v^2}{2} \right) \right] + \frac{\partial}{\partial y} \left[\frac{\partial}{\partial y} \left(\frac{u^2 + v^2}{2} \right) \right] \right\} \right\} \Delta x \Delta y + (\rho E)_P^n \frac{\Delta x \Delta y}{\Delta t} \end{aligned} \quad (4-59)$$

$$b_E = b_E^1 + b_E^{21} + b_E^{22} + b_E^{23} + b_E^3 \quad (4-60)$$

$$b_E^1 = -\left[\frac{(pu)}{\partial x} + \frac{(pv)}{\partial y}\right] \Delta x \Delta y = -[p_e F_e - p_w F_w + p_n F_n - p_s F_s] \quad (4-61)$$

$$b_E^2 = \left[\frac{\partial}{\partial x} (u\tau_{xx} + v\tau_{xy}) + \frac{\partial}{\partial y} (u\tau_{yx} + v\tau_{yy}) \right] \Delta x \Delta y \quad (4-62)$$

$$\begin{aligned} b_E^{21} &= \left[\frac{\partial}{\partial x} (u\tau_{xx} + v\tau_{xy}) \right] \Delta x \Delta y \\ &= \frac{\mu u_e \Delta y}{Re} \left(\frac{4}{3} \frac{\partial u}{\partial x} - \frac{2}{3} \frac{\partial v}{\partial y} \right)_e - \frac{\mu u_w \Delta y}{Re} \left(\frac{4}{3} \frac{\partial u}{\partial x} - \frac{2}{3} \frac{\partial v}{\partial y} \right)_w + \frac{\mu v_e \Delta y}{Re} \left(\frac{\partial u}{\partial y} + \frac{\partial v}{\partial x} \right)_e - \frac{\mu v_w \Delta y}{Re} \left(\frac{\partial u}{\partial y} + \frac{\partial v}{\partial x} \right)_w \\ &= \frac{\mu u_e \Delta y}{Re} \left[\frac{4}{3} \frac{1}{(\delta x)_e} (u_E - u_P) - \frac{2}{3} \frac{1}{(\delta y)_e} (v_{en} - v_{es}) \right] - \frac{\mu u_w \Delta y}{Re} \left[\frac{4}{3} \frac{1}{(\delta x)_w} (u_P - u_W) - \frac{2}{3} \frac{1}{(\delta y)_w} (v_{wn} - v_{ws}) \right] \\ &\quad + \frac{\mu v_e \Delta y}{Re} \left[\frac{1}{(\delta y)_e} (u_{en} - u_{es}) - \frac{1}{(\delta x)_e} (v_E - v_P) \right] - \frac{\mu v_w \Delta y}{Re} \left[\frac{1}{(\delta y)_w} (u_{wn} - u_{ws}) - \frac{1}{(\delta x)_w} (v_P - v_W) \right] \end{aligned} \quad (4-63)$$

$$\begin{aligned} b_E^{22} &= \left[\frac{\partial}{\partial y} (u\tau_{xy} + v\tau_{yy}) \right] \Delta x \Delta y \\ &= \frac{\mu u_n \Delta x}{Re} \left(\frac{\partial u}{\partial y} + \frac{\partial v}{\partial x} \right)_n - \frac{\mu u_s \Delta x}{Re} \left(\frac{\partial u}{\partial y} + \frac{\partial v}{\partial x} \right)_s + \frac{\mu v_n \Delta x}{Re} \left(\frac{4}{3} \frac{\partial v}{\partial y} - \frac{2}{3} \frac{\partial u}{\partial x} \right)_n - \frac{\mu u_s \Delta x}{Re} \left(\frac{4}{3} \frac{\partial v}{\partial y} - \frac{2}{3} \frac{\partial u}{\partial x} \right)_s \\ &= \frac{\mu u_n \Delta x}{Re} \left[\frac{1}{(\delta y)_n} (u_N - u_P) - \frac{1}{(\delta x)_n} (v_{ne} - v_{nw}) \right] - \frac{\mu u_s \Delta x}{Re} \left[\frac{1}{(\delta y)_s} (u_P - u_S) - \frac{1}{(\delta x)_s} (v_{se} - v_{sw}) \right] \\ &\quad + \frac{\mu v_n \Delta x}{Re} \left[\frac{4}{3} \frac{1}{(\delta y)_n} (v_N - v_P) - \frac{2}{3} \frac{1}{(\delta x)_n} (u_{ne} - u_{nw}) \right] - \frac{\mu u_s \Delta x}{Re} \left[\frac{4}{3} \frac{1}{(\delta y)_s} (v_P - v_S) - \frac{2}{3} \frac{1}{(\delta x)_s} (u_{se} - u_{sw}) \right] \end{aligned} \quad (4-64)$$

$$\begin{aligned} b_E^{23} &= \frac{\mu \gamma}{Re Pr} \left\{ \frac{\partial}{\partial x} \left[\frac{\partial}{\partial x} \left(\frac{u^2 + v^2}{2} \right) \right] + \frac{\partial}{\partial y} \left[\frac{\partial}{\partial y} \left(\frac{u^2 + v^2}{2} \right) \right] \right\} \Delta x \Delta y \\ &= \frac{\mu \gamma}{Re Pr} \frac{\Delta y}{(\delta x)_e} \left[\frac{u_E^2 + v_E^2}{2} - \frac{u_P^2 + v_P^2}{2} \right] - \frac{\mu \gamma}{Re Pr} \frac{\Delta y}{(\delta x)_w} \left[\frac{u_P^2 + v_P^2}{2} - \frac{u_W^2 + v_W^2}{2} \right] \\ &\quad + \frac{\mu \gamma}{Re Pr} \frac{\Delta x}{(\delta y)_n} \left[\frac{u_N^2 + v_N^2}{2} - \frac{u_P^2 + v_P^2}{2} \right] - \frac{\mu \gamma}{Re Pr} \frac{\Delta x}{(\delta x)_s} \left[\frac{u_P^2 + v_P^2}{2} - \frac{u_S^2 + v_S^2}{2} \right] \end{aligned} \quad (4-65)$$

$$b_E^3 = (\rho E)_P^n \frac{\Delta x \Delta y}{\Delta} \quad (4-66)$$

In the above discrete equations, the terms are calculated as following:

$$\Delta x = 0.5(x_E - x_W), \quad \Delta y = 0.5(y_N - y_S),$$

$$(\Delta y)_e = 0.5(\frac{y_N - y_S}{2} + \frac{y_{NE} - y_{SE}}{2}), \quad (\Delta y)_w = 0.5(\frac{y_N - y_S}{2} + \frac{y_{NW} - y_{SW}}{2})$$

$$(\Delta x)_n = 0.5(\frac{x_E - x_W}{2} + \frac{x_{EN} - x_{WN}}{2}), \quad (\Delta x)_s = 0.5(\frac{x_E - x_W}{2} + \frac{x_{ES} - x_{WS}}{2})$$

$$(\delta x)_e = x_E - x_P, \quad (\delta x)_w = x_P - x_W, \quad (\delta y)_n = y_N - y_P, \quad (\delta y)_s = y_P - y_S$$

$$\begin{aligned}
 (\delta x)_n &= (\Delta x)_n, (\delta x)_s = (\Delta x)_s, (\delta y)_e = (\Delta y)_e, (\delta y)_w = (\Delta y)_w \\
 (\Delta x)_e &= 0.5\left(\frac{x_N - x_S}{x_{NE} - x_{SE}} + \frac{x_{NE} - x_{SE}}{x_N - x_S}\right), (\Delta x)_w = 0.5\left(\frac{x_N - x_S}{x_{NW} - x_{SW}} + \frac{x_{NW} - x_{SW}}{x_N - x_S}\right) \\
 (\Delta y)_n &= 0.5\left(\frac{y_E - y_W}{y_{EN} - y_{WN}} + \frac{y_{EN} - y_{WN}}{y_E - y_W}\right), (\Delta x)_s = 0.5\left(\frac{y_E - y_W}{y_{ES} - y_{WS}} + \frac{y_{ES} - y_{WS}}{y_E - y_W}\right) \\
 \phi_e &= 0.5(\phi_E + \phi_P), \phi_w = 0.5(\phi_P + \phi_W), \phi_n = 0.5(\phi_N + \phi_P), \phi_s = 0.5(\phi_P + \phi_S) \\
 (\phi)_{ne} &= 0.5\left(\frac{\phi_N + \phi_P}{\phi_{NE} + \phi_E} + \frac{\phi_{NE} + \phi_E}{\phi_N + \phi_P}\right), (\phi)_{nw} = 0.5\left(\frac{\phi_N + \phi_P}{\phi_{NW} + \phi_W} + \frac{\phi_{NW} + \phi_W}{\phi_N + \phi_P}\right) \\
 (\phi)_{se} &= 0.5\left(\frac{\phi_S + \phi_P}{\phi_{SE} + \phi_E} + \frac{\phi_{SE} + \phi_E}{\phi_S + \phi_P}\right), (\phi)_{sw} = 0.5\left(\frac{\phi_S + \phi_P}{\phi_{SW} + \phi_W} + \frac{\phi_{SW} + \phi_W}{\phi_S + \phi_P}\right) \\
 (\phi)_{en} &= 0.5\left(\frac{\phi_E + \phi_P}{\phi_{EN} + \phi_N} + \frac{\phi_{EN} + \phi_N}{\phi_E + \phi_P}\right), (\phi)_{es} = 0.5\left(\frac{\phi_E + \phi_P}{\phi_{ES} + \phi_S} + \frac{\phi_{ES} + \phi_S}{\phi_E + \phi_P}\right) \\
 (\phi)_{wn} &= 0.5\left(\frac{\phi_W + \phi_P}{\phi_{WN} + \phi_N} + \frac{\phi_{WN} + \phi_N}{\phi_W + \phi_P}\right), (\phi)_{ws} = 0.5\left(\frac{\phi_W + \phi_P}{\phi_{WS} + \phi_S} + \frac{\phi_{WS} + \phi_S}{\phi_W + \phi_P}\right)
 \end{aligned} \tag{4-67}$$

4.3.2 QUICK Scheme

The accuracy of upwind scheme is only first-order in terms of Taylor series truncation error. The use of upwind quantities ensures that the schemes are stable and obey the transportiveness requirement but the first-order accuracy makes them prone to numerical diffusion errors. Such errors can be minimized by employing higher order discretisation.

The quadratic upwind interpolation for convective kinetics (QUICK) scheme uses a three-point upstream-weighted quadratic interpolation for cell face values. The face value of ϕ is obtained from a quadratic function passing through two bracketing nodes (on each side of the face) and a node on the upstream side. The Hayase QUICK scheme can be summarized as follows:

$$\begin{aligned}
 \phi_w &= \phi_W + \frac{1}{3}(3\phi_P - 2\phi_W - \phi_{WW}) && \text{for } F_w > 0 \\
 \phi_e &= \phi_P + \frac{1}{3}(3\phi_E - 2\phi_P - \phi_W) && \text{for } F_e > 0 \\
 \phi_w &= \phi_P + \frac{1}{3}(3\phi_W - 2\phi_P - \phi_E) && \text{for } F_w < 0 \\
 \phi_e &= \phi_E + \frac{1}{3}(3\phi_P - 2\phi_E - \phi_{EE}) && \text{for } F_e < 0
 \end{aligned}$$

$$\begin{aligned}
 \phi_s &= \phi_s + \frac{1}{3} (3\phi_p - 2\phi_s - \phi_{ss}) && \text{for } F_s > 0 \\
 \phi_n &= \phi_p + \frac{1}{3} (3\phi_N - 2\phi_p - \phi_s) && \text{for } F_n > 0 \\
 \phi_s &= \phi_p + \frac{1}{3} (3\phi_s - 2\phi_p - \phi_N) && \text{for } F_s < 0 \\
 \phi_n &= \phi_N + \frac{1}{3} (3\phi_p - 2\phi_N - \phi_{NN}) && \text{for } F_n < 0
 \end{aligned} \tag{4-68}$$

The QUICK scheme has greater formal accuracy and retains the upwind weighted characteristics. The resultant false diffusion is small and solutions achieved with coarse grids are considerably more accurate than those of the upwind or hybrid schemes. The QUICK scheme can, however, give (minor) undershoots and overshoots as is evident in computational results (Figure 4.5).

4.4 Boundary Conditions Implementation

4.4.1 Inlet

For the non-dimensional equations, at inlet the following conditions are given by

$$\begin{aligned}
 u &= 1.0 ; v = 0.0 ; \rho = ; p = p_\infty ; T = T_\infty \\
 p &= \frac{1}{\gamma M_\infty^2} ; E = \frac{1}{\gamma(\gamma-1)M_\infty^2} + \frac{1}{2}
 \end{aligned} \tag{4-69}$$

4.4.2 Onlet

In flow direction, gradients of variables are zero, which is:

$$\frac{\phi}{l} = 0 \tag{4-70}$$

4.4.3 Solid Wall

4.4.3.1 Euler equation boundary conditions

The basis is impermeable boundary condition:

$$V_n = 0 \tag{4-71}$$

If the coordinates are non-orthogonal, we have,

$$\begin{aligned}
 V_n &= V \cdot n \\
 &= V_\xi n_\xi + V_\eta n_\eta + V_\zeta n_\zeta + V_\xi n_\eta (\bar{e}_\xi \cdot \bar{e}_\eta) + V_\xi n_\zeta (\bar{e}_\xi \cdot \bar{e}_\zeta) + V_\eta n_\xi (\bar{e}_\eta \cdot \bar{e}_\xi) + V_\eta n_\zeta (\bar{e}_\eta \cdot \bar{e}_\zeta) \\
 &\quad + V_\zeta n_\xi (\bar{e}_\zeta \cdot \bar{e}_\xi) + V_\zeta n_\eta (\bar{e}_\zeta \cdot \bar{e}_\eta) \\
 &= V_\xi n_\xi + V_\eta n_\eta + V_\zeta n_\zeta \\
 &\quad + (V_\xi n_\eta + V_\eta n_\xi) [\cos(\xi, \eta)] + (V_\xi n_\zeta + V_\zeta n_\xi) [\cos(\xi, \zeta)] + (V_\eta n_\zeta + V_\zeta n_\eta) [\cos(\eta, \zeta)] \\
 &= V_\zeta n_\zeta + V_\xi n_\zeta [\cos(\xi, \zeta)] + V_\eta n_\zeta [\cos(\eta, \zeta)]
 \end{aligned} \tag{4-72}$$

Here, n is the surface normal direction, $n = n_\xi e_\xi + n_\eta e_\eta + n_\zeta e_\zeta$. ξ, η Coordinates are on the solid surface.

For two-dimensional flow problem, the above equation can be write as:

$$V_n = V_\eta n_\eta + V_\xi n_\eta [\cos(\xi, \eta)] \tag{4-73}$$

Here the η coordinate is on the solid surface.

Planar wall:

The ξ, η components of velocity V_ξ, V_η and other parameters are extended to boundary by linear interpolation or symmetry techniques are used. V_ζ is obtained with the above equation. For example, when symmetry techniques are used, the boundary conditions are as follows:

$$p_{-1} = p_{+1}, \rho_{-1} = \rho_{+1} \tag{4-74}$$

$$(V_\tau)_{-1} = (V_\tau)_{+1} \rightarrow \begin{cases} (V_\xi)_{-1} = (V_\xi)_{+1} \\ (V_\eta)_{-1} = (V_\eta)_{+1} \end{cases} \tag{4-75}$$

$$\begin{aligned}
 (V_n)_{-1} &= -(V_n)_{+1} \rightarrow \\
 \{V_\zeta n_\zeta + V_\xi n_\zeta [\cos(\xi, \zeta)] + V_\eta n_\zeta [\cos(\eta, \zeta)]\}_{-1} &= -\{V_\zeta n_\zeta + V_\xi n_\zeta [\cos(\xi, \zeta)] + V_\eta n_\zeta [\cos(\eta, \zeta)]\}_{+1}
 \end{aligned} \tag{4-76}$$

Here point -1 is the imaginary point outside the boundary.

Curvature wall:

For Curvature wall, the pressure boundary condition should be corrected with the following equation:

$$(\frac{\partial p}{\partial n})_{wall} = -\rho \frac{|V|^2}{R} \tag{4-77}$$

Here R is radius of curvature. Then the pressure condition is corrected as:

$$p_{-1} = p_{+1} - \rho \frac{|V|^2}{R} \Delta n_{+1} \quad (4-78)$$

Here Δn_1 represent the distance between points 1 and -1 . The density boundary condition is:

$$\rho_{-1} = \rho_{+1} \left(\frac{p_{-1}}{p_{+1}} \right)^{\frac{1}{\gamma}} \quad (4-79)$$

4.4.3.2 Navier-Stokes Equation Boundary Conditions

On the solid wall boundary, the viscous flow no-slip conditions are applied.

$$u = 0, v = 0 \quad (4-80)$$

The temperature boundary condition is adiabatic wall condition or given the freestream temperature T_∞

$$\frac{T}{T_\infty} = 0 \text{ or } T = T_\infty \quad (4-81)$$

4.5 Computational Results and Discussions

The two numerical methods, Euler solver and Navier-Stokes solver, described in the previous section were combined into a single code in such a way that we could readily select between one method and the other in solving a specified flow problem.

The problem of the flow in a channel with a circular arc “bump” was chosen to evaluate the code for subsonic, transonic, and supersonic steady state modeling. This particular problem is well suited for code development and testing. The geometry and the grids are easy to generate accurately and the problem symmetry and geometrical simplicity aid the interpretation of the results. Two circular arc bump thickness-to-chord ratios were used: 10% for subsonic and transonic modeling, 4% for the supersonic model. To the upper and lower boundaries of the channel, the solid wall boundary conditions were applied. The inflow boundary is on the left side.

Figure 1 is the computational geometry for the flow model. Figure 2 shows isomach lines of the steady flow solution for an upstream Mach number, $M_\infty = 0.5$, obtained using the Euler solver. The isomach lines distributions are nearly symmetry. That is the verification of correctness of the computational code. The contour is not smooth enough, that may be result from the hyperbolic characteristics of Euler equation and the first-order boundary condition implementation. Improving the boundary conditions to second-order or adopting finer grids can make it better. Figure 3 shows the

channel upper and lower surfaces Mach number distribution for the same test case. A little asymmetry is due to the influence of the sharp leading and trailing edge. Figure 4 and 5 present the contour of Mach number and the surface Mach number distribution of the transonic flow solution for the same 10% thick arc bump for $M_{\infty} = 0.675$ using the Euler solver.

The computational code can simulate the sharp shock profile very well that appears on the bump, except that there is a small spurious oscillating. That is the dispersion introduced by QUICK scheme along with its improvement in accuracy. Figure 6 and 7 present results for the supersonic flow in a channel with a 4% thick arc bump for $M_{\infty} = 1.65$ obtained with Euler code. The shock wave, their reflection and interaction can be simulated pretty well. The quality is improved when the grids get finer. Figure 8 and 9 show the contour of Mach number and near surface Mach number distribution of subsonic flow solution for the 10% thick arc bump for upstream Mach number $M_{\infty} = 0.5$ using Navier-Stokes equations.

The Mach number contour is asymmetry, not as that of results of Euler solver. The reason is that viscous boundary layer developing along the surface and that the boundary separation near the trailing edge of the bump (Fig.8). The boundary layer and its separation also change the flow passage in non-viscous sense, therefore, the Mach number increases and the flow pattern is not symmetry anymore. Figure 10 and 11 present the results for transonic flow in the channel for the same test case with $M_{\infty} = 0.675$ using Navier-Stokes equation.

The shock wave is a little smeared because of the physical viscosity, and at the same time the spurious oscillating does not appear also due to the physical viscosity. There is a shock and boundary interaction downstream of the bump. The boundary layer and its interaction with the shock affect the flow field in the channel. Figure 12-15 shows supersonic flow over a flat plate with 0% thickness for upstream Mach $M_{\infty} = 1.8$ using Navier-Stokes equation. The upper boundary is free stream.

A shock wave appears in the middle of the plate, its action with the boundary layer generates an expansion shock downstream of it. The two shocks dominate the flow field pattern over the flat plate.

References:

¹Selvam, R. P., "Computation of Nonlinear Viscous Panel Flattening Using a Fully-Implicit Aeroelastic Solver," AIAA Paper, 1998, 98-1184.

²Eidelman, S., "Application of the Godunov Method and Its Second-order Extension to the Cascade Flow Modeling," *AIAA Journal*, Vol.22, No.11, 1998, pp.1609-1613.

³Versteeg, H. K., and Malalasekera, W., "An Introduction to Computational Fluid dynamics," The Finite Volume Method. Longman, 1995.

⁴Liu, S. L., and Zheng, Q., "Computational Fluid Dynamics," HRBEU Press, 1998.

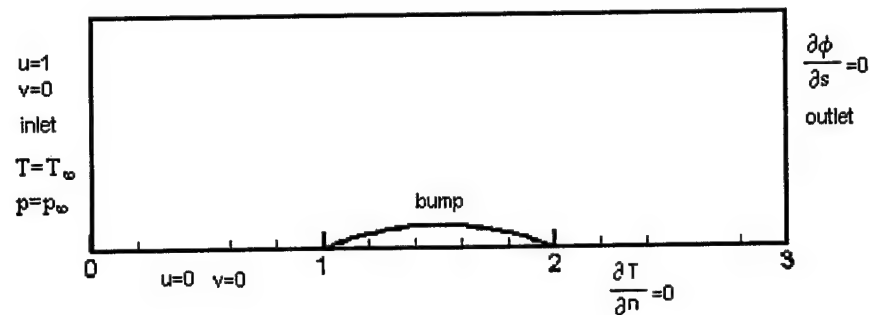


Figure 4.2 The computational geometry of flow over a bump

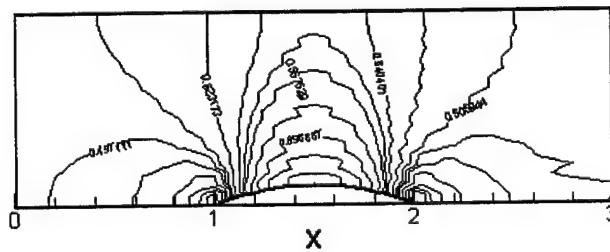


Figure 4.3 Contour of Mach number of flow over a bump

(Inflow Mach number $M_\infty = 0.5$, Euler solution)

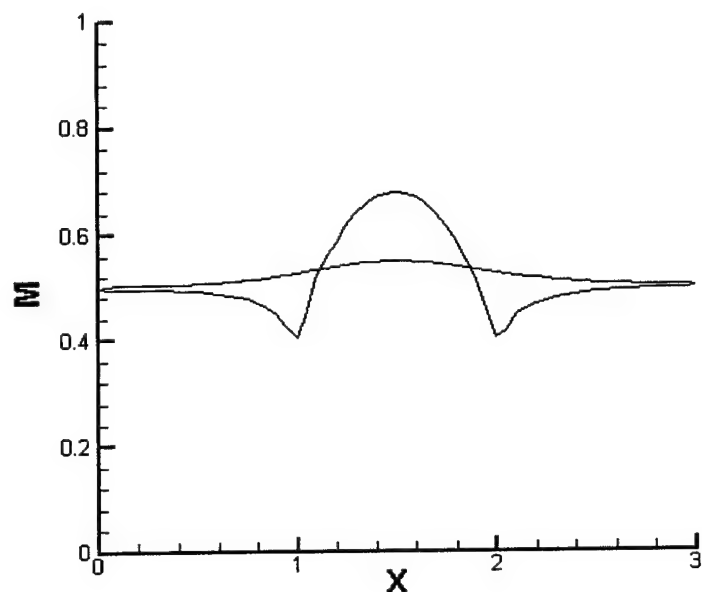


Figure 4.4 Mach number distribution on the upper and lower surface
(Inflow Mach number $M_{\infty} = 0.5$, Euler solution)

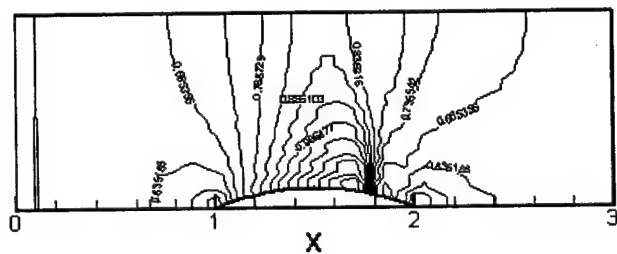


Figure 4.5 Contour of Mach number of flow over a bump
(Inflow Mach number $M_{\infty} = 0.675$, Euler solution)

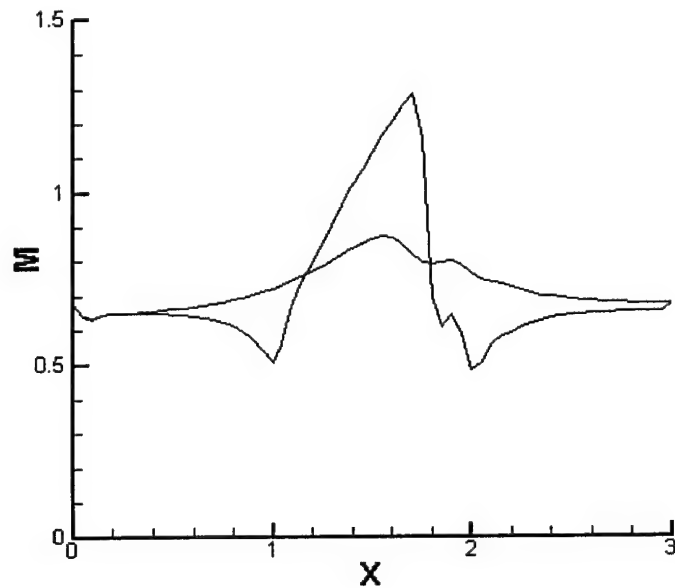


Figure 4.6 Mach number distribution on the upper and lower surface
(Inflow Mach number $M_{\infty} = 0.675$, Euler solution)

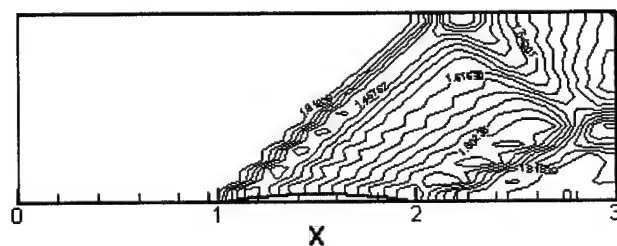


Figure 4.7 Contour of Mach number of flow over a bump
(Inflow Mach number $M_{\infty} = 1.65$, Euler solution)

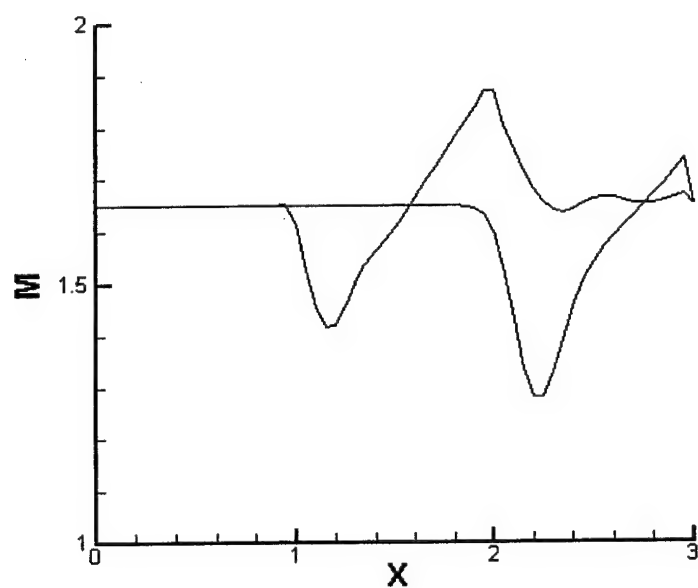


Figure 4.8 Mach number distribution on the upper and lower surface
(Inflow Mach number $M_{\infty} = 1.65$, Euler solution)

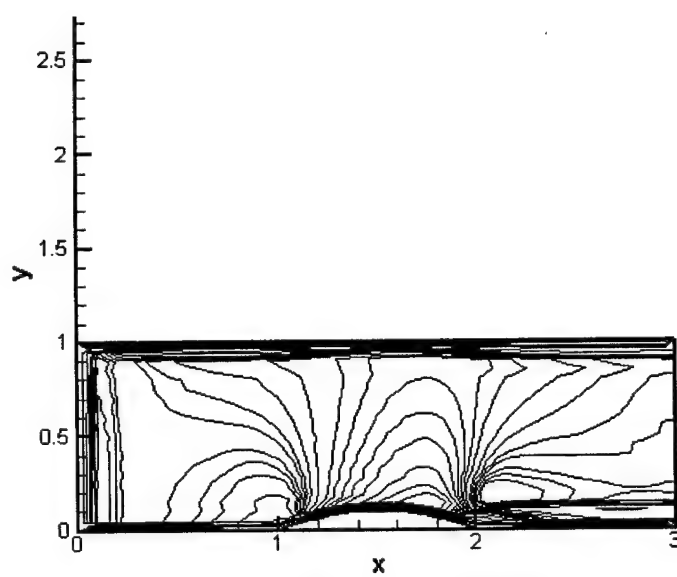


Figure 4.9 Contour of Mach number of flow over a bump
(Inflow Mach number $M_{\infty} = 0.5$, Navier-Stokes solution)

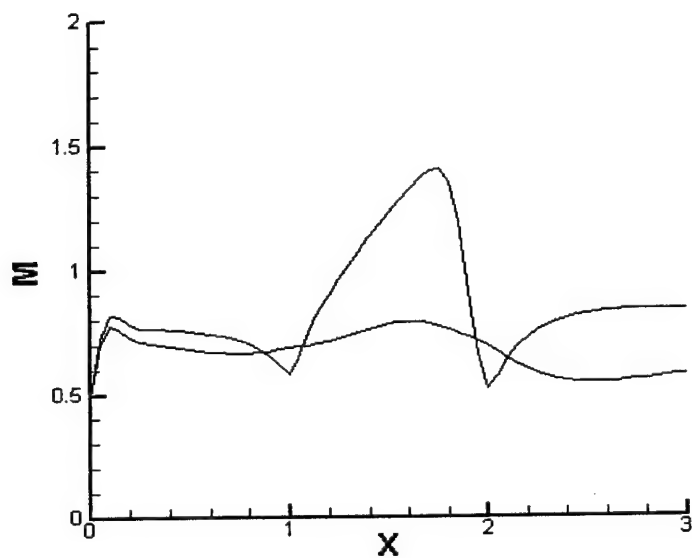


Figure 4.10 Mach number distribution near the upper and lower surface
(Inflow Mach number $M_{\infty} = 0.5$, Navier-Stokes solution)

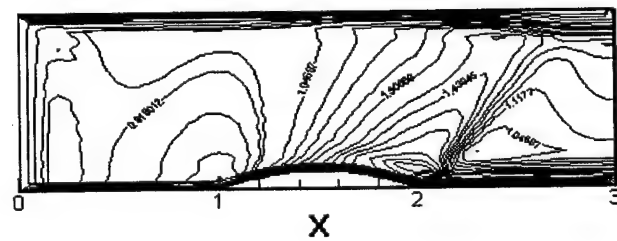


Figure 4.11 Contour of Mach number of flow over a bump
(Inflow Mach number $M_{\infty} = 0.675$, Navier-Stokes solution)

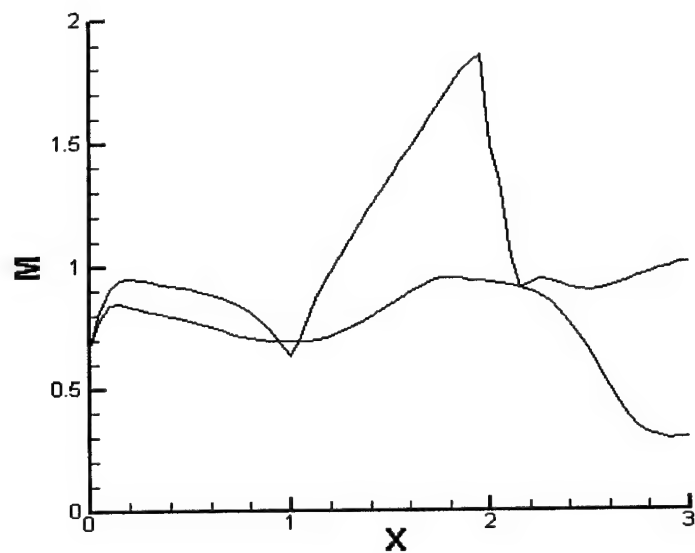


Figure 4.12 Mach number distribution near the upper and lower surface
(Inflow Mach number $M_{\infty} = 0.675$, Navier-Stokes solution)

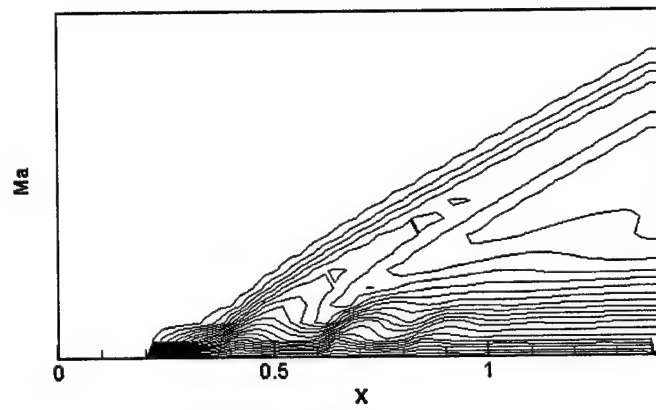


Figure 4.13 Mach number contour of flow over flat plate (Inflow Mach number $M_{\infty} = 3.0$)

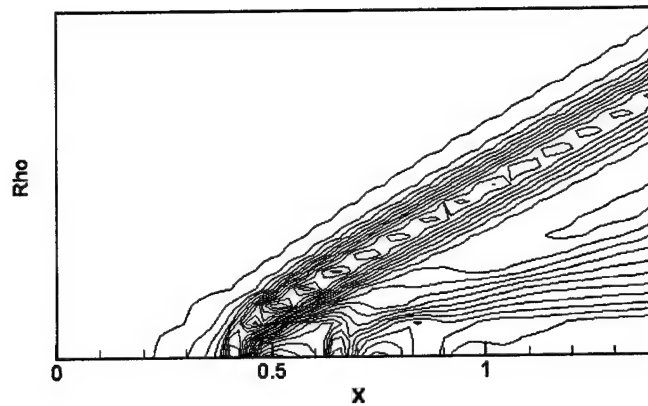


Figure 4.14 Density contour of flow over flat plate (Inflow mach number $M_{\infty} = 3.0$)

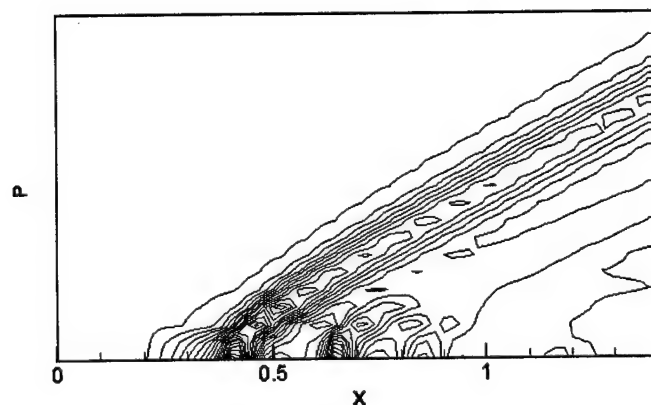


Figure 4.15 Pressure contour of flow over flat plate (Inflow mach number $M_{\infty} = 3.0$)

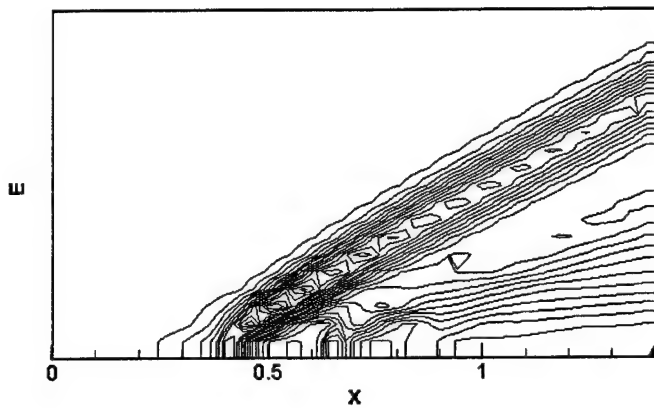


Figure 4.16 Energy contour of flow over flat plate (Inflow mach number $M_{\infty} = 3.0$)

CHAPTER 5

THREE DIMENSIONAL AEROELASTIC SOLVER FOR NONLINEAR PANEL FLUTTER

- 5.1 Nomenclature
 - 5.2 Introduction
 - 5.3 Aerodynamic Theories
 - 5.4 Governing Equations of Thin Plate
 - 5.5 Numerical Procedure
 - 5.6 Results and Discussions
 - 5.7 Summary
-

5.1 Nomenclature

- B = membrane rigidity of plate defined in equation (5-33);
- \hat{c} = speed of sound in air;
- D = bending rigidity of plate defined in equation (5-33);
- E = total specific energy per unit volume defined in equation (5-22);
- E_s = elastic modulus of plate;
- h = thickness of plate;
- H_{GCL} = GCL source vector term;
- J = Jacobian of the transformation;
- \hat{l} = side length of plate; characteristic length;
- M_∞ = free-stream Mach number;
- = dimensionless air pressure;
- P_r = Prandtl number, 0.73 for standard air;

CHAPTER 5: Three Dimensional Aeroelastic Solver for Nonlinear Panel Flutter

- Δ = aerodynamic pressure, positive in the direction opposite to w ;
- $\Delta\hat{p}^M$ = aerodynamic pressure due to plate motion;
- $\Delta\hat{p}^E$ = "external" aerodynamic pressure independent of plate motion, e.g. turbulent pressure fluctuations;
- Re_l = Reynolds number, $\hat{\rho}_a \hat{V}_\infty l / \hat{\mu}_\infty$;
- = dimensionless time;
- t_{nl} = nonlinear internal force coefficient defined in equation (5-38);
- T = dimensionless static temperature;
- w = dimensionless deformations of the plate in x z directions;
- w = dimensional deformations of the plate in x y z directions;
- u = dimensionless displacement vector of the plate in x direction: $u = u_1, u_2, \dots, u_n$;
- V = velocity, $V = v_x i + v_y j + v_z k$;
- V_∞ = free-stream velocity;
- v_x, v_y, v_z = three components of the velocity;
- v = dimensionless displacement vector of the plate in z direction: $v = v_1, v_2, \dots, v_n$;
- w = dimensionless displacement vector of the plate in z direction: $w = w_1, w_2, \dots, w_n$;
- x y z = dimensionless Cartesian coordinates;
- α β δ = constants for Newmark- β integration method;
- δ_{ij} = Kronecker delta function;
- ϕ = velocity potential function;
- γ = ratio of specific heat, 1.4 for perfect gas;
- λ = dimensionless dynamic pressure defined in equation (5-38);
- μ = molecular viscosity coefficient;
- μ_s = mass ratio defined in equation (5-38);
- ρ_a = dimensionless mass density of air;
- ρ_s = dimensionless mass density of plate;
- ν = Poisson's ratio;

τ = time in computational space;
 $\xi \eta \zeta$ = Coordinates in the computational space;

Subscripts:

a = air;
 b = boundary;
 s = structure (plate);
 v = viscous;
 ∞ = free-stream value;

Overhead:

$\hat{\cdot}$ = denote the dimensional parameter

5.2 Introduction

An important goal of computational aeroelasticity is to impact the design process with simulations of full aircraft configurations. In developing a fluid-structure interaction solver, three sets of governing equations, as well as their coupling, must be considered. These are the fluid dynamic, structural dynamic, and fluid-structure interface equations. The fluid dynamic equations must have the fidelity to capture the relevant flow features and provide accurate loads on the structure. The structural dynamic equations must in turn be capable of modeling the structural deformation properties under a given time-varying load. Since, in general, the aerodynamic and the structural discretizations are not identical, accurate and stable structural interface equations must be established to transfer the aerodynamic loads to the structure and the structural deformations to the aerodynamic mesh.

When considered independently, high-fidelity fluid dynamic and structural dynamic solution algorithms have become mature for flows or structural members exhibiting nonlinearities. However, application of these solvers in a time accurate, multidisciplinary environment requires further study in order to elucidate various issues arising in the coupling of these high-fidelity solvers.

Historically, researchers interested in dynamic aeroelastic computations have taken well-validated, implicit Navier-Stokes algorithms developed to solve complex flows over three dimensional, rigid bodies, and extended them to include aeroelastic effects. The most common practice is to simply lag the effects of moving/deforming structures by one time step^{1,2} allowing current algorithms to be used

in updating the aerodynamic variables. Bendiksen and Hwang³ pointed out that when took this approach unknown phrase and integration errors were introduced leading in some cases to incorrect prediction of the stability behavior of the fluid structure interaction system. To overcome this problem Bendiksen and Davis⁴ took the alternate approach to develop a new tightly integrated algorithm in which the fluid and structures are modeled as a single dynamical system. Although this approach has been shown to eliminate the lagging errors, it requires the development of an entirely new solver. This would entail large additional investments by the aircraft industry for developing and validating new flow solvers, and would result as well in the loss of the significant user experience already accumulated with existing aerodynamic and structural tools.

An attractive alternative method for eliminating these phrase and integration errors, while utilizing existing fluid dynamic and structure dynamic algorithms, is implementing Newton-like subiterations^{5,6}. Subiterations can eliminate the errors from the linearization and factorization, as well as from the lagging boundary conditions and turbulence models. The added computational cost of subiterations is typically an additional solution vector storage, and each subiteration is equivalent in workload to a time step of the baseline algorithm. The result is a fully implicit coupling between the fluid and structures without having to develop a completely new tightly coupled solver.

Morton, Melville, Visbal^f applied this approach to an elastically mounted cylinder in a uniform crossflow. The subiteration methodology was shown to reduce the structural coupling errors and allowed higher order accurate time integration scheme to be used with relatively minor changes to the baseline aerodynamic solver. The overall workload of the algorithm was improved by a factor of ten over traditional first order lagged approaches due to demonstrated second order, coupled, temporal integration. The structural dynamics solver was comprised two linear, second order differential equations describing motion in the horizontal and vertical axes and were integrated in time with the same method used in the aerodynamic code. The fluid-structural interface equations were trivial for this simple model. Melville, Morton, and Rizzetta⁷ also have used this technique to couple a three dimensional Navier-Stokes code with a general, linear second-order structural model. This solver has been applied successfully to the problems of transonic wing flutter⁸, tail-buffet⁹, and limit-cycle oscillations¹⁰.

In order to identify pertinent issues related to coupling nonlinear structural dynamic and aerodynamic equations, a model problem that is geometrically simple, has reasonable computational requirements, yet requires high-fidelity fluid and structural solvers is desired. One such model problem is nonlinear panel flutter.

Only a few computational studies have recently been considered the nonlinear flow effects in panel flutter. Davis and Bendiksen¹¹, Davis¹², Bendiksen and Davis⁴ have employed an improved modeling of the aerodynamics by tightly coupling the Euler equations with a nonlinear finite element model for two-dimensional, Transonic panel flutter problems. Selvam, Visbal, and Morton¹³ extended the subiteration methodology to more complex structural models including nonlinear effects and requiring the coupling of different time-integration schemes for the fluid and the structure. In addition, they provided some insight into the effects of viscosity on thin panel flutter in the transonic regime. Gordnier and Visbal¹⁴ extended the preliminary work of Selvam, Visbal and Morton for two-dimensional panel flutter. Viscous effect on the flutter dynamic pressure for supersonic and subsonic flow was discussed. Additionally, some computations were performed for inviscid, three-dimensional panel flutter.

Several commonly used approximate aerodynamic theories, linearized potential flow theory, quasi-steady supersonic theory, first order piston theory and full three order piston theory, are first listed in Section 3 for comparison purposes. The valid range of Mach number is provided for each theory. The unsteady, compressible, three-dimensional Euler equations are also provided in this section to predict the aerodynamic pressure acting on the panel due to its deformation. To reduce the interaction error between the fluid and structure, the expression for the Geometric Conservation Law (GCL) is discussed. In Section 4, the governing equations based on the von Karman large deflection theory are provided. All these governing equations are nondimensionalized by the appropriate combination of freestream density, velocity and the length of panel. In Section 5, the Beam-Warming, alternate-direction, implicit scheme is listed to solve the flow equations. The finite difference method and the Newmark- β integration scheme are used to solve the governing equations of nonlinear panel. The Newton-like subiteration is also implemented in this section to eliminate the lagging errors associated with the exchange of the pressure and deformations between the fluid and panel at their interface. The nonlinear panel flutter under Euler flow is simulated for a square panel in Section 6. The amplitudes of the Limit Cycle Oscillation (LCO) are compared with those obtained from full linearized potential flow theory and quasi-steady linear piston theory. The flutter frequencies are also discussed and compared with their natural frequencies.

5.3 Aerodynamic Theories

5.3.1 Approximate Aerodynamic Theories

Normally the aerodynamic pressure may be considered as the sum of two parts, one given by the pressure fluctuations on the plate in the absence of any plate motion, e.g., due to turbulent boundary layer fluctuations, and the other due to the plate motion itself¹⁵. The superposition of these two contributions to form the total aerodynamic pressure implies that the plate motion and the consequent portion of the aerodynamic pressure are sufficiently small so that the turbulent pressure fluctuations themselves are not substantially modified. Hence,

$$\Delta\hat{p} = \Delta\hat{p}^M + \Delta\hat{p}^E \quad (5-1)$$

$\Delta\hat{p}^E$ is taken as prescribed from experiment or separate analysis while $\Delta\hat{p}^M$ may be related to the deformation of the plate. The full expression of the $\Delta\hat{p}^M$ was defined by Dowell¹⁵.

As disclosed by the survey papers, a vast quantity of literature exists on panel flutter using approximate aerodynamic theories without considering the effect of $\Delta\hat{p}^E$. Several frequently used theories are listed in the following. Their valid ranges of Mach number were summarized by Mei¹⁶.

5.3.1.1 Linearized Potential Flow Theory

For air flow with Mach number close to one and less than five ($1 < M_\infty < 5$), the full linearized inviscid potential theory aerodynamics is usually employed¹⁷. The aerodynamic pressure loading is given by

$$\hat{p} - \hat{p}_\infty = -\hat{\rho}_a \left(\frac{\partial \phi}{\partial \hat{t}} + \hat{V}_\infty \frac{\partial \phi}{\partial \hat{x}} \right) \quad (5-2)$$

where the velocity potential function ϕ must satisfy

$$\nabla^2 \phi - \frac{1}{c^2} \left(\frac{\partial}{\partial \hat{t}} + \frac{\partial}{\partial \hat{x}} \right)^2 \phi = 0 \quad (5-3)$$

subject to the boundary conditions

$$\left. \frac{\partial \phi}{\partial \hat{z}} \right|_{\hat{z}=0} = \begin{cases} \frac{\partial \hat{w}}{\partial \hat{t}} + \hat{V}_\infty \frac{\partial \hat{w}}{\partial \hat{x}} & \text{on plate} \\ 0 & \text{off plate} \end{cases} \quad (5-4)$$

5.3.1.2 Quasi-Steady Supersonic Theory

The aerodynamic theory employed for most part of the panel flutter at higher supersonic Mach number ($M_\infty > 1.6$) is the quasi-steady first order piston aerodynamic theory by Ashley and Zartarian¹⁸. The aerodynamic pressure as given in this theory is given by

$$\hat{p} - \hat{p}_\infty = \frac{2\hat{q}_a}{\beta} \left(\frac{\partial \hat{w}}{\partial \hat{x}} + \frac{M_\infty^2 - 2}{M_\infty^2 - 1} \frac{1}{\hat{V}_\infty} \frac{\partial \hat{w}}{\partial \hat{t}} \right) \quad (5-5)$$

where $\hat{q}_a = \hat{\rho}_a \hat{V}_\infty^2 / 2$ is the free stream dynamic pressure; $\beta = \sqrt{M_\infty^2 - 1}$. If the aerodynamic damping is neglected in Equation (5-5), the quasi-static Ackeret aerodynamic theory, also known as the static strip theory, is simplified to

$$\hat{p} - \hat{p}_\infty = \frac{2\hat{q}_a}{\beta} \frac{\hat{w}}{\partial \hat{x}} \quad (5-6)$$

5.3.1.3 First Order Piston Aerodynamic Theory

The simplified formula of the aerodynamic pressure within the first order piston theory has the expression^{15,19}

$$\hat{p} - \hat{p}_\infty = \frac{2\hat{q}_a}{M_\infty} \left(\frac{\partial \hat{w}}{\partial \hat{x}} + \frac{1}{\hat{V}_\infty} \frac{\partial \hat{w}}{\partial \hat{t}} \right) \quad (5-7)$$

This approximation is usually used for the supersonic and hypersonic flow ($2.5 < M_\infty < 5$ by Krause and Dinkler²⁰, or $\sqrt{2} < M_\infty < 5$ by Mei¹⁶).

5.3.1.4 Full Third Order Piston Aerodynamic Theory

In the hypersonic regime ($M_\infty > 5$), the unsteady full third-order piston theory aerodynamics¹⁸ is used to develop the aerodynamic pressure given by

$$\hat{p} - \hat{p}_\infty = \frac{2\hat{q}_a}{M_\infty} \left[\frac{\partial \hat{w}}{\partial \hat{x}} + \frac{1}{\hat{V}_\infty} \frac{\partial \hat{w}}{\partial \hat{t}} + \frac{(\gamma+1)M_\infty}{4} \left(\frac{\partial \hat{w}}{\partial \hat{x}} + \frac{1}{\hat{V}_\infty} \frac{\partial \hat{w}}{\partial \hat{t}} \right)^2 + \frac{(\gamma+1)M_\infty^2}{12} \left(\frac{\partial \hat{w}}{\partial \hat{x}} + \frac{1}{\hat{V}_\infty} \frac{\partial \hat{w}}{\partial \hat{t}} \right)^3 \right] \quad (5-8)$$

where γ is the ratio of specific heat.

5.3.2 Aerodynamic Theory Based on Navier-Stokes Equations

The aerodynamic governing equations are the unsteady, compressible, three-dimensional Navier-Stokes equations written in nondimensional, strong-conservation law form employing a general time dependent transformation

$$\begin{cases} \xi = \xi(x, y, z, t) \\ \eta = \eta(x, y, z, t) \\ \zeta = \zeta(x, y, z, t) \\ \tau = t \end{cases} \quad (5-9)$$

The resulting system of governing equations is repressed as

$$\frac{\partial \tilde{\mathbf{U}}}{\partial t} + \frac{\partial}{\partial \xi} \left(\tilde{\mathbf{F}} - \frac{1}{Re_l} \tilde{\mathbf{F}}_v \right) + \frac{\partial}{\partial \eta} \left(\tilde{\mathbf{G}} - \frac{1}{Re_l} \tilde{\mathbf{G}}_v \right) + \frac{\partial}{\partial \zeta} \left(\tilde{\mathbf{H}} - \frac{1}{Re_l} \tilde{\mathbf{H}}_v \right) = \mathbf{H}_{GCL} \quad (5-10)$$

The source vector term, \mathbf{H}_{GCL} , defined as

$$\mathbf{H}_{GCL} = \mathbf{U} \left[\frac{\partial J^{-1}}{\partial \tau} + \left(\frac{\xi_{,\tau}}{J} \right)_{,\xi} + \left(\frac{\eta_{,\tau}}{J} \right)_{,\eta} + \left(\frac{\zeta_{,\tau}}{J} \right)_{,\zeta} \right] \quad (5-11)$$

is applied in order to account for errors associated with the GCL and will be discussed later. J is Jacobian of the transformation²¹.

Vector quantities appearing in Equation (5-10) are defined as

$$\tilde{\mathbf{U}} = \frac{1}{J} \mathbf{U} \quad (5-12)$$

$$\tilde{\mathbf{F}} = \frac{1}{J} (\xi_{,\tau} \mathbf{U} + \xi_{,x} \mathbf{F} + \xi_{,y} \mathbf{G} + \xi_{,z} \mathbf{H}) \quad (5-13)$$

$$\tilde{\mathbf{G}} = \frac{1}{J} (\eta_{,\tau} \mathbf{U} + \eta_{,x} \mathbf{F} + \eta_{,y} \mathbf{G} + \eta_{,z} \mathbf{H}) \quad (5-14)$$

$$\tilde{\mathbf{H}} = \frac{1}{J} (\zeta_{,\tau} \mathbf{U} + \zeta_{,x} \mathbf{F} + \zeta_{,y} \mathbf{G} + \zeta_{,z} \mathbf{H}) \quad (5-15)$$

$$\tilde{\mathbf{F}}_v = \frac{1}{J} (\xi_{,x} \mathbf{F}_v + \xi_{,y} \mathbf{G}_v + \xi_{,z} \mathbf{H}_v) \quad (5-16)$$

$$\tilde{\mathbf{G}}_v = \frac{1}{J} (\eta_{,x} \mathbf{F}_v + \eta_{,y} \mathbf{G}_v + \eta_{,z} \mathbf{H}_v) \quad (5-17)$$

$$\tilde{\mathbf{H}}_v = \frac{1}{J} (\zeta_{,x} \mathbf{F}_v + \zeta_{,y} \mathbf{G}_v + \zeta_{,z} \mathbf{H}_v) \quad (5-18)$$

With this formulation, the vector of dependent variables \mathbf{U} is given as

$$\mathbf{U} = \frac{1}{J} \rho_a \quad \rho_a v_x \quad \rho_a v_y \quad \rho_a v_z \quad \rho_a E^r \quad (5-19)$$

and the flux vectors are

$$\mathbf{F} = \begin{bmatrix} \rho_a v_x \\ \rho_a v_x^2 + p \\ \rho_a v_x v_y \\ \rho_a v_x v_z \\ (\rho_a E + p)v_x \end{bmatrix}, \quad \mathbf{G} = \begin{bmatrix} \rho_a v_y \\ \rho_a v_x v_y \\ \rho_a v_y^2 + p \\ \rho_a v_y v_z \\ (\rho_a E + p)v_y \end{bmatrix}, \quad \mathbf{H} = \begin{bmatrix} \rho_a v_z \\ \rho_a v_x v_z \\ \rho_a v_y v_z \\ \rho_a v_z^2 + p \\ (\rho_a E + p)v_z \end{bmatrix} \quad (5-20)$$

$$\mathbf{F}_v = 0 \quad \tau_{xx} \quad \tau_{xy} \quad \tau_{xz} \quad v_x \tau_{xx} + v_y \tau_{xy} + v_z \tau_{xz} - q_x^T \quad (5-21a)$$

$$\mathbf{G}_v = 0 \quad \tau_{xy} \quad \tau_{yy} \quad \tau_{yz} \quad v_x \tau_{xy} + v_y \tau_{yy} + v_z \tau_{yz} - q_y^T \quad (5-21b)$$

$$\mathbf{H}_v = 0 \quad \tau_{xz} \quad \tau_{yz} \quad \tau_{zz} \quad v_x \tau_{xz} + v_y \tau_{yz} + v_z \tau_{zz} - q_z^T \quad (5-21c)$$

where the total specific energy per unit is defined as

$$E = \frac{T}{\gamma(\gamma-1)M_\infty^2} + \frac{(v_x^2 + v_y^2 + v_z^2)}{2} \quad (5-22)$$

All variables have been normalized by the appropriate combination of freestream density, velocity and a characteristic length, that is,

$$x = \frac{\hat{x}}{\hat{l}}, \quad y = \frac{\hat{y}}{\hat{l}}, \quad z = \frac{\hat{z}}{\hat{l}}, \quad t = \frac{\hat{t}\hat{V}_\infty}{\hat{l}} \quad (5-23a)$$

$$v_x = \frac{\hat{v}_x}{\hat{V}_\infty}, \quad v_y = \frac{\hat{v}_y}{\hat{V}_\infty}, \quad v_z = \frac{\hat{v}_z}{\hat{V}_\infty}, \quad \mu = \frac{\hat{\mu}}{\hat{\mu}_\infty} \quad (5-23b)$$

$$\rho_a = \frac{\hat{\rho}_a}{\hat{\rho}_\infty}, \quad p = \frac{\hat{p}}{\hat{\rho}_\infty \hat{V}_\infty^2}, \quad T = \frac{\hat{T}}{\hat{T}_\infty} \quad (5-23c)$$

Components of the stress tensor and the heat flux vector may be expressed as

$$\tau_{x_i x_j} = \mu \left(\frac{\partial u_i}{\partial x_j} + \frac{\partial u_j}{\partial x_i} - \frac{2}{3} \delta_{ij} \frac{\partial u_k}{\partial x_k} \right) \quad (5-24)$$

$$q_{x_i} = \left[\frac{1}{(\gamma-1)M_\infty^2} \left(\frac{\mu}{P_r} \right) \frac{\partial T}{\partial x_i} \right] \quad (5-25)$$

where $i = 1, 2, 3$; $u_1, u_2, u_3 = v_x, v_y, v_z$ and $x_1, x_2, x_3 = x, y, z$. Sutherland's law for the molecular viscosity coefficient μ and the perfect gas relationship

$$p = \frac{\rho_a T}{\gamma M_\infty^2} \quad (5-26)$$

are also employed, and Stokes' hypothesis for the bulk viscosity coefficient is assumed.

5.3.3 Geometric Conservation Law

The relationship between the governing equations and the GCL is discussed in the following. The nondimensional Cartesian governing equations can be expressed as

$$\frac{\partial \mathbf{U}}{\partial t} + \frac{\partial}{\partial x} \left(\mathbf{F} - \frac{1}{Re_l} \mathbf{F}_v \right) + \frac{\partial}{\partial y} \left(\mathbf{G} - \frac{1}{Re_l} \mathbf{G}_v \right) + \frac{\partial}{\partial z} \left(\mathbf{H} - \frac{1}{Re_l} \mathbf{H}_v \right) = \mathbf{0} \quad (5-27)$$

Using chain-rule differentiation,

$$\frac{(\cdot)}{\partial t} = \frac{(\cdot)}{\partial \tau} + \frac{(\cdot)}{\partial \xi} \frac{\xi}{\partial t} + \frac{(\cdot)}{\partial \eta} \frac{\eta}{\partial t} + \frac{(\cdot)}{\partial \zeta} \frac{\zeta}{\partial t} \quad (5-28a)$$

$$\frac{(\cdot)}{\partial x} = \frac{(\cdot)}{\partial \xi} \frac{\xi}{\partial x} + \frac{(\cdot)}{\partial \eta} \frac{\eta}{\partial x} + \frac{(\cdot)}{\partial \zeta} \frac{\zeta}{\partial x} \quad (5-28b)$$

$$\frac{(\cdot)}{\partial y} = \frac{(\cdot)}{\partial \xi} \frac{\xi}{\partial y} + \frac{(\cdot)}{\partial \eta} \frac{\eta}{\partial y} + \frac{(\cdot)}{\partial \zeta} \frac{\zeta}{\partial y} \quad (5-28c)$$

$$\frac{(\cdot)}{\partial z} = \frac{(\cdot)}{\partial \xi} \frac{\xi}{\partial z} + \frac{(\cdot)}{\partial \eta} \frac{\eta}{\partial z} + \frac{(\cdot)}{\partial \zeta} \frac{\zeta}{\partial z} \quad (5-28d)$$

and premultiplying by the inverse of the transformation Jacobian, J , equation (5-27) becomes

$$\begin{aligned} \frac{\partial \hat{\mathbf{U}}}{\partial \tau} + \frac{\partial}{\partial \xi} \left(\hat{\mathbf{F}} - \frac{1}{Re_l} \hat{\mathbf{F}}_v \right) + \frac{\partial}{\partial \eta} \left(\hat{\mathbf{G}} - \frac{1}{Re_l} \hat{\mathbf{G}}_v \right) + \frac{\partial}{\partial \zeta} \left(\hat{\mathbf{H}} - \frac{1}{Re_l} \hat{\mathbf{H}}_v \right) = \\ U \left[\frac{\partial J^{-1}}{\partial \tau} + \left(\frac{\xi_{,\tau}}{J} \right)_{,\xi} + \left(\frac{\eta_{,\tau}}{J} \right)_{,\eta} + \left(\frac{\zeta_{,\tau}}{J} \right)_{,\zeta} \right] + \\ \left(\mathbf{F} - \frac{1}{Re_l} \mathbf{F}_v \right) \left[\left(\frac{\xi_{,x}}{J} \right)_{,\xi} + \left(\frac{\eta_{,x}}{J} \right)_{,\eta} + \left(\frac{\zeta_{,x}}{J} \right)_{,\zeta} \right] + \\ \left(\mathbf{G} - \frac{1}{Re_l} \mathbf{G}_v \right) \left[\left(\frac{\xi_{,y}}{J} \right)_{,\xi} + \left(\frac{\eta_{,y}}{J} \right)_{,\eta} + \left(\frac{\zeta_{,y}}{J} \right)_{,\zeta} \right] + \\ \left(\mathbf{H} - \frac{1}{Re_l} \mathbf{H}_v \right) \left[\left(\frac{\xi_{,z}}{J} \right)_{,\xi} + \left(\frac{\eta_{,z}}{J} \right)_{,\eta} + \left(\frac{\zeta_{,z}}{J} \right)_{,\zeta} \right] \end{aligned} \quad (5-29)$$

All four terms on the right hand side of equation (5-29) vanish analytically. The difficulty arises when discrete representations of the temporal and spatial derivatives are used. The discrete form of the last three terms are zero when central differences are used for all metric calculations in 3-D. Unfortunately, this is not true for the first expression due to the mixed temporal and spatial derivatives. The first term set to zero is referred to in the literature as the GCL^{22,23}. The most

straightforward approach of accounting for the GCL is to simply include this term in the discrete governing equations.

5.4 Governing Equations of Thin Plate

The governing equations of the thin plate are the well known von Karman equations for large deflection. Derivations of these equations may be found in a number of sources²⁴. For the von Karman theory the plate is assumed to be isotropic, of uniform small thickness and initially flat. The normal deflection of the plate is assumed to be on the order of the thickness of the plate, while the tangential displacements are assumed infinitesimal. Finally, Kirchoff's hypothesis is employed with tractions on surfaces parallel to the middle surface assumed negligible and strains varying linearly with the plate thickness.

Using these assumptions the governing equations for the plate motion may be written as

$$D\nabla^4\hat{w} + \bar{m}\frac{\partial^2\hat{w}}{\partial t^2} = \hat{p}_z + \hat{n}_x\frac{\partial^2\hat{w}}{\partial\hat{x}^2} + \hat{n}_y\frac{\partial^2\hat{w}}{\partial\hat{y}^2} + 2\hat{n}_{xy}\frac{\partial^2\hat{w}}{\partial\hat{x}\partial\hat{y}} \quad (5-30-a)$$

$$\frac{\partial\hat{n}_x}{\partial\hat{x}} + \frac{\hat{n}_{yx}}{\partial\hat{y}} = 0 \quad (5-30-b)$$

$$\frac{\hat{n}_{xy}}{\partial\hat{x}} + \frac{\hat{n}_y}{\partial\hat{y}} = 0 \quad (5-30-c)$$

where the two-dimensional Laplacian operator and the internal forces are defined as

$$\nabla^4\hat{w} = \frac{\partial^4\hat{w}}{\partial\hat{x}^4} + 2\frac{\partial^4\hat{w}}{\partial\hat{x}^2\partial\hat{y}^2} + \frac{\partial^4\hat{w}}{\partial\hat{y}^4} \quad (5-31)$$

$$\hat{n}_x = B\left\{\frac{\partial\hat{u}}{\partial\hat{x}} + \frac{1}{2}\left(\frac{\partial\hat{w}}{\partial\hat{x}}\right)^2 + v\left[\frac{\partial\hat{v}}{\partial\hat{y}} + \frac{1}{2}\left(\frac{\partial\hat{w}}{\partial\hat{y}}\right)^2\right]\right\} \quad (5-32-a)$$

$$\hat{n}_y = B\left\{\frac{\partial\hat{v}}{\partial\hat{y}} + \frac{1}{2}\left(\frac{\partial\hat{w}}{\partial\hat{y}}\right)^2 + v\left[\frac{\partial\hat{u}}{\partial\hat{x}} + \frac{1}{2}\left(\frac{\partial\hat{w}}{\partial\hat{x}}\right)^2\right]\right\} \quad (5-32-b)$$

$$\hat{n}_{xy} = \frac{B(1-v)}{2}\left(\frac{\partial\hat{u}}{\partial\hat{y}} + \frac{\partial\hat{v}}{\partial\hat{x}} + \frac{\partial\hat{w}}{\partial\hat{x}}\frac{\partial\hat{w}}{\partial\hat{y}}\right) \quad (5-32-c)$$

The rigidity constants for the bending and membrane, D and B , and the mass per unit area are

$$D = \frac{E_s \hat{h}^3}{12(1-v^2)}, \quad B = \frac{E_s \hat{h}}{(1-v^2)}, \quad \bar{m} = \hat{\rho}_s \hat{h} \quad (5-33)$$

In equations (5-30) through (5-33), \hat{u} , \hat{v} , and \hat{w} are the displacements in the x , y , and z directions respectively; \hat{h} and $\hat{\rho}_s$ are, respectively, the thickness and mass density of the plate; \hat{p}_z is external transverse pressure acted on the plate.

The dynamic equations of equilibrium defined above are dimensional. To make them compatible to the governing equations for flow, they are non-dimensionalized with respect to the length of the plate. Suppose the plate is square and the length is \hat{l} , the non-dimensional parameters are defined as

$$u = \frac{\hat{u}}{\hat{l}}, \quad v = \frac{\hat{v}}{\hat{l}}, \quad w = \frac{\hat{w}}{\hat{l}}, \quad h = \frac{\hat{h}}{\hat{l}}, \quad p_z = \frac{\hat{p}_z}{\hat{\rho}_s \hat{V}_\infty^2} \quad (5-34)$$

Using equation (5-34), the non-dimensional form of the dynamic equations of the plate becomes

$$\frac{\mu_s}{\lambda} \nabla^4 w + \frac{\partial^2 w}{\partial t^2} = \mu_s p_z + \mu_s n_x \frac{\partial^2 w}{\partial x^2} + \mu_s n_y \frac{\partial^2 w}{\partial y^2} + 2\mu_s n_{xy} \frac{\partial^2 w}{\partial x \partial y} \quad (5-35-a)$$

$$\frac{\partial n_x}{\partial x} + \frac{n_{yx}}{\partial y} = 0 \quad (5-35-b)$$

$$\frac{n_{xy}}{\partial x} + \frac{n_y}{\partial y} = 0 \quad (5-35-c)$$

and the two-dimensional Laplacian operator and the internal forces are defined as

$$\nabla^4 w = \frac{\partial^4 w}{\partial x^4} + 2 \frac{\partial^4 w}{\partial x^2 \partial y^2} + \frac{\partial^4 w}{\partial y^4} \quad (5-36)$$

$$n_x = t_{nl} \left\{ \frac{\partial u}{\partial x} + \frac{1}{2} \left(\frac{\partial w}{\partial x} \right)^2 + v \left[\frac{\partial v}{\partial y} + \frac{1}{2} \left(\frac{\partial w}{\partial y} \right)^2 \right] \right\} \quad (5-37-a)$$

$$n_y = t_{nl} \left\{ \frac{\partial v}{\partial y} + \frac{1}{2} \left(\frac{\partial w}{\partial y} \right)^2 + v \left[\frac{\partial u}{\partial x} + \frac{1}{2} \left(\frac{\partial w}{\partial x} \right)^2 \right] \right\} \quad (5-37-b)$$

$$n_{xy} = \frac{t_{nl}}{2} \left(\frac{\partial u}{\partial y} + \frac{\partial v}{\partial x} + \frac{\partial w}{\partial x} \frac{\partial w}{\partial y} \right) \quad (5-37-c)$$

The nondimensional dynamic pressure λ , mass ratio μ_s , and internal force coefficient t_{nl} are

$$\lambda = \frac{\hat{\rho}_a \hat{V}_\infty^2 \hat{l}^3}{D}, \quad \mu_s = \frac{\hat{\rho}_a \hat{l}}{\hat{\rho}_s \hat{h}}, \quad t_{nl} = \frac{12}{\lambda} \left(\frac{\hat{l}}{\hat{h}} \right)^2 \quad (5-38)$$

5.5 Numerical Procedure

5.5.1 Aerodynamic

Solutions to equation (5-10) are obtained numerically using the implicit approximately factored finite difference algorithm of Beam and Warming²⁵, employing a Newton like subiteration procedure^{5,6}. The numerical algorithm is obtained from equation (5-10) by utilizing either a two- or three-point backward time differencing and linearizing about the solution at subiteration level . The choice of the first or second-order temporal accuracy is retained in the following iterative approach by specifying $\phi =$ or $\phi = 1/2$, respectively. The numerical algorithm is written in an approximately factored, delta form as

$$\begin{aligned} & \left[\left(J^{-1} \right)^{p+1} + \phi^i \Delta t_s \delta_\xi \left(\frac{\partial \hat{F}^p}{\partial U} - \frac{1}{Re_l} \frac{\partial \hat{F}_v^p}{\partial U} \right) \right] J^{p+1} \cdot \left[\left(J^{-1} \right)^{p+1} + \phi^i \Delta t_s \delta_\eta \left(\frac{\partial \hat{G}^p}{\partial U} - \frac{1}{Re_l} \frac{\partial \hat{G}_v^p}{\partial U} \right) \right] J^{p+1} . \\ & \left[\left(J^{-1} \right)^{p+1} + \phi^i \Delta t_s \delta_\zeta \left(\frac{\partial \hat{H}^p}{\partial U} - \frac{1}{Re_l} \frac{\partial \hat{H}_v^p}{\partial U} \right) \right] \Delta U = -\phi^i \Delta t_s \left\{ \left(J^{-1} \right)^{p+1} \frac{(1+\phi)U^p - (1+2\phi)U^n + \phi U^{n-1}}{\Delta t} \right. \\ & \quad \left. - U^p \left[\left(\frac{\xi_{,t}}{J} \right)_{,\xi} + \left(\frac{\eta_{,t}}{J} \right)_{,\eta} + \left(\frac{\zeta_{,t}}{J} \right)_{,\zeta} \right]^{p+1} + \delta_\xi \left(\hat{F}^p - \frac{1}{Re_l} \hat{F}_v^p \right) + \delta_\eta \left(\hat{G}^p - \frac{1}{Re_l} \hat{G}_v^p \right) + \delta_\zeta \left(\hat{H}^p - \frac{1}{Re_l} \hat{H}_v^p \right) \right\} \end{aligned} \quad (5-39)$$

where

$$\phi^i = \frac{1}{1+\phi}, \quad \Delta U = U^{p+1} - U^p \quad (5-40)$$

Here, U^p is the subiteration approximation of $U^{t+\Delta t}$. Therefore, $U^p = U^t$ for $=$ and $U^p \rightarrow U^{t+\Delta t}$ as $\rightarrow \infty$.

It should be noted that with this subiteration approach the right-hand side of equation (5-39) represents the numerical approximation of the governing equation, while the left-hand side vanishes as $\rightarrow \infty$. The left-hand side, therefore, may be modified without loss of formal accuracy provided a sufficient number of subiterations are employed. In particular, a time step on the left-hand side of the equation, Δt_s , may be chosen independently from the physical time step Δt on the right-hand side to enhance the stability. Also, the right-hand side of equation (5-39) can be modified to include a higher order upwind algorithm, lagged boundary conditions or lagged $k-\varepsilon$ turbulence modeling without

destroying the implicit nature of the algorithm. Left-hand side efficiency improvements can also be implemented. The numerical procedure has been modified to include diagonalization, following the approach by Pulliam and Chaussee²⁶. Although the diagonalized form of the ADI scheme is only first-order time-accurate, when coupled with subiterations, higher order time accuracy may be retained. The numerical scheme (5-39) reverts to the standard first order Beam-Warming procedure for $\phi = \omega$, $\Delta t_s = \Delta t$, and $\beta = 1$.

In equation (5-39) all spatial derivatives are approximated by the second-order accurate differences, and common forms of both implicit and explicit nonlinear dissipation²⁷ are employed in order to preserve numerical stability. The gird speeds x_t , y_t , and z_t are computed in a manner consistent with the temporal derivatives of the conserved variables in equation (5-39).

5.5.2 Structure

The structural equations (5-30) are discretized using a finite difference procedure in space and the Newmark- β method in time.

The Newmark- β integration method is applied to solve the dynamic equilibrium of motion. It is a second-order accurate in time and unconditionally stable approach. In this method the following assumptions for the velocity and displacement in the time interval t to $t + \Delta t$ are employed:

$$\dot{w}_{t+\Delta t} = \dot{w}_t + (1 - \delta)\ddot{w}_t + \delta\ddot{w}_{t+\Delta t} \Delta t \quad (5-41a)$$

$$w_{t+\Delta t} = w_t + \dot{w}_t \Delta t + (1/2 - \alpha)\ddot{w}_t + \alpha\ddot{w}_{t+\Delta t} \Delta t^2 \quad (5-41b)$$

where α and β are integration parameters that determine the stability and accuracy of the method. For an unconditionally stable integration scheme, Newmark originally proposed that $\alpha = 1/4$ and $\delta = 1/2$, in which case equation (5-41) corresponds to the constant average acceleration method.

From equation (5-41), $\ddot{w}_{t+\Delta t}$ may be solved in terms of $w_{t+\Delta t}$ as

$$\ddot{w}_{t+\Delta t} = a_0 w_{t+\Delta t} - w_t - a_2 \dot{w}_t - a_3 \ddot{w}_t \quad (5-42a)$$

Substituting equation (5-42a) for $\ddot{w}_{t+\Delta t}$ in equation (5-41a) yields

$$\dot{w}_{t+\Delta t} = \dot{w}_t + \left[(1 - \delta)\ddot{w}_t + \frac{\delta}{\alpha(\Delta t)^2} (w_{t+\Delta t} - w_t) - \frac{\delta}{\alpha \Delta t} \dot{w}_t - \left(\frac{\delta}{2\alpha} - \delta \right) \ddot{w}_t \right] \Delta t$$

or in a simple form

$$\dot{w}_{t+\Delta t} = a_1 w_{t+\Delta t} - w_t - a_4 \dot{w}_t - a_5 \ddot{w}_t \quad (5-42b)$$

The constants in equation (5-42) are defined as

$$\begin{aligned} a_0 &= \frac{1}{\alpha(\Delta t)^2}, \quad a_1 = \frac{\delta}{\alpha \Delta t}, \quad a_2 = \frac{1}{\alpha \Delta t}, \quad a_3 = \left(\frac{1}{2\alpha} - 1 \right) \\ a_4 &= \frac{\delta}{\alpha} - 1, \quad a_5 = \frac{\Delta t}{2} \left(\frac{\delta}{\alpha} - 2 \right) \end{aligned} \quad (5-43)$$

Both the acceleration $\ddot{w}_{t+\Delta t}$ and velocity $\dot{w}_{t+\Delta t}$ at time $t + \Delta t$ are expressed in terms of the unknown displacement $w_{t+\Delta t}$ at time $t + \Delta t$ and the parameters in time . Using equation (5-42), the governing equation (5-35a) of the plate can be discretized in time domain as

$$a_0 w_{t+\Delta t} + \mu_s / \lambda \nabla^4 w_{t+\Delta t} = \mu_s n_x w_{,xx} + n_y w_{,yy} + 2n_{xy} w_{,xy} + p_{t+\Delta t}^* \quad (5-44)$$

where the equivalent external force is defined as

$$p_{t+\Delta t}^* = \mu_s p_{t+\Delta t} + a_0 w_t + a_2 \dot{w}_t + a_3 \ddot{w}_t \quad (5-45)$$

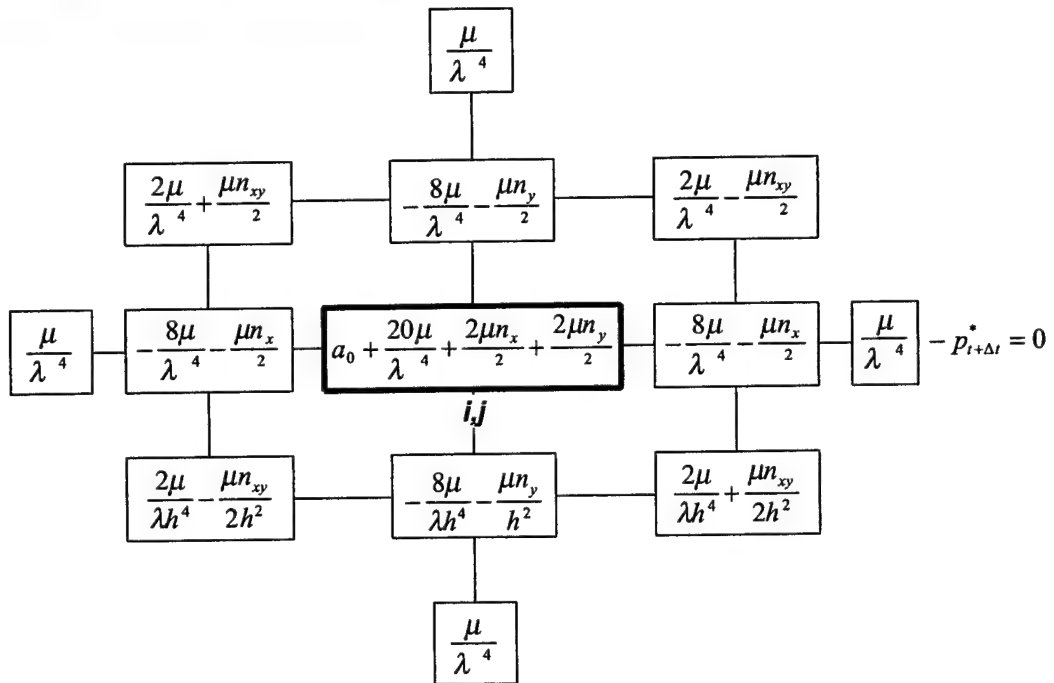
Equations (5-35b) and (5-35c) are static equilibrium, there is no any change for them.

The standard five- and three-point centered finite difference expressions²⁴ are used to approximate the fourth-, second, and first-order spatial derivatives in equations (5-44), (5-35b), (5-35c), and (5-37). The derivatives expressions are given by

$$\begin{aligned} \left(\frac{\partial^4 w}{\partial x^4} \right)_{i,j} &\approx \frac{1}{(\Delta x)^4} (w_{i+2,j} - 4w_{i+1,j} + 6w_{i,j} - 4w_{i-1,j} + w_{i-2,j}) \\ \left(\frac{\partial^4 w}{\partial y^4} \right)_{i,j} &\approx \frac{1}{(\Delta y)^4} (w_{i,j+2} - 4w_{i,j+1} + 6w_{i,j} - 4w_{i,j-1} + w_{i,j-2}) \\ \left(\frac{\partial^4 w}{\partial x^2 \partial y^2} \right)_{i,j} &= \frac{1}{(\Delta x \Delta y)^2} [4w_{i,j} - 2(w_{i+1,j} + w_{i-1,j} + w_{i,j+1} + w_{i,j-1}) + w_{i+1,j+1} + w_{i+1,j-1} + w_{i-1,j+1} + w_{i-1,j-1}] \\ \left(\frac{\partial^2 w}{\partial x^2} \right)_{i,j} &\approx \frac{1}{(\Delta x)^2} (w_{i+1,j} - 2w_{i,j} + w_{i-1,j}), \quad \left(\frac{\partial^2 w}{\partial y^2} \right)_{i,j} \approx \frac{1}{(\Delta y)^2} (w_{i,j+1} - 2w_{i,j} + w_{i,j-1}) \\ \left(\frac{\partial^2 w}{\partial x \partial y} \right)_{i,j} &\approx \frac{1}{4 \Delta x \Delta y} (w_{i+1,j+1} - w_{i+1,j-1} - w_{i-1,j+1} + w_{i-1,j-1}) \\ \left(\frac{\partial w}{\partial x} \right)_{i,j} &= \frac{1}{2 \Delta x} (-w_{i-1,j} + w_{i+1,j}), \quad \left(\frac{\partial w}{\partial y} \right)_{i,j} = \frac{1}{2 \Delta y} (-w_{i,j-1} + w_{i,j+1}) \end{aligned} \quad (5-46)$$

For the fourth-order expressions, $i = i_{ps} + 2$ to $i_{pe} - 2$ (where i_{ps} and i_{pe} denote the beginning and end of the plate in the x direction) and $j = j_{ps} + 2$ to $j_{pe} - 2$ (where j_{ps} and j_{pe} denote the beginning and end of the plate in the y direction). For $i = i_{ps} + 1$ or $i_{pe} - 1$ and $j = j_{ps} + 1$ or $j_{pe} - 1$, these equations are modified by inserting the appropriate boundary condition information.

Introducing the derivative expressions in equation (5-46) into the equivalent static equilibrium (5-44), the finite difference expression of the dynamic equation (5-35a) for $\Delta x = \Delta y = h$ without boundary condition is obtained as



(5-47a)

where μ_s is replaced by μ for simplicity. Similarly, the finite expressions for the governing equations (5-35b) and (5-35c) are given by

$$\begin{aligned}
 & C_{u1} u(i-1, j) + u(i+1, j) + C_{u2} u(i, j-1) + u(i, j+1) + A_u u(i, j) \\
 & + C_v [v(i-1, j-1) - v(i+1, j-1) + v(i+1, j+1) - v(i-1, j+1)] \\
 & + C_{w1} [w(i-1, j-1) - w(i+1, j-1) + w(i+1, j+1) - w(i-1, j+1)] \\
 & \quad [-w(i, j-1) + w(i, j+1)] \\
 & + C_{w2} [-w(i-1, j) + w(i+1, j)] [w(i-1, j) - 2w(i, j) + w(i+1, j)] \\
 & + C_{w3} [-w(i-1, j) + w(i+1, j)] [w(i, j-1) - 2w(i, j) + w(i, j+1)] = 0
 \end{aligned} \tag{5-47b}$$

$$\begin{aligned}
 & C_{u2} v(i-1,j) + v(i+1,j) + C_{u1} v(i,j-1) + v(i,j+1) + A_u v(i,j) \\
 & + C_v [u(i-1,j-1) - u(i+1,j-1) + u(i+1,j+1) - u(i-1,j+1)] \\
 & + C_{w1} [w(i-1,j-1) - w(i+1,j-1) + w(i+1,j+1) - w(i-1,j+1)] \\
 & [-w(i-1,j) + w(i+1,j)] \\
 & + C_{w2} [-w(i,j-1) + w(i,j+1)] [w(i,j-1) - 2w(i,j) + w(i,j+1)] \\
 & + C_{w3} [-w(i,j-1) + w(i,j+1)] [w(i-1,j) - 2w(i,j) + w(i+1,j)] = 0
 \end{aligned} \tag{5-47c}$$

where,

$$C_{u1} = \frac{t_l}{h^2}, \quad C_{u2} = \frac{t_l(1-v)}{2h^2}, \quad C_v = \frac{t_l(1+v)}{8h^2}, \quad C_{w1} = \frac{t_l(1+v)}{16h^3}, \quad C_{w2} = \frac{t_l}{2h^3}, \quad C_{w3} = \frac{t_l(1-v)}{4h^3} \tag{5-48a}$$

$$A_u = -2 C_{u1} + C_{u2} \tag{5-48b}$$

After the proper boundary conditions are applied to Equation (5-47), they can be solved. Assembling equation (5-47), the governing equations of the discrete model of the large deflection plate at the current time step is obtained as

$$A(u, v, w)_w w = B(u, v, w)_w \tag{5-49a}$$

$$A(u, v, w)_u w = B(u, v, w)_u \tag{5-49b}$$

$$A(u, v, w)_v w = B(u, v, w)_v \tag{5-49c}$$

Obviously, the coefficient matrices and vectors on the right-hand sides of equation (5-49) are the functions of the unknowns. This means equation (5-49) is nonlinear. Iterations, not only within equations of the equation (5-49) but also among them, are necessary to solve for the unknowns from this equation.

5.5.3 Fluid-Structure Interaction

The fluid-structure interaction analysis may be performed using the following three main steps in each time step. (1) Calculate the responses of the panel under the fluid pressure and other external forces; (2) Move the fluid grid using the displacements from the panel analysis; (3) Perform the fluid analysis under the moved grid and compute the pressure on the surface of the panel due to its movement. To start the numerical simulation, some initial perturbation, initial displacements, velocity, or accelerations, is usually assigned to the panel. Steps one and three are corresponding to structural and fluid analysis respectively. For each step, iterations are required because the governing equations of the structure and fluid are nonlinear.

The pressure resulted from the fluid side is required when calculating the responses of the panel. On the other hand, the displacements of the panel should be available before performing the analysis of the fluid and obtaining the pressure to be assigned on the panel. Clearly, the fluid and the panel are coupled. If only one cycle, from structure to fluid, is used at each time step, big errors will sometimes be resulted due to the lagged fluid-structure coupling. This error will lead numerical instability when a relatively long time simulation is performed. To eliminate the possible numerical instability, the subiteration between the fluid and structure is implemented.

As we know, the computational effort of the fluid is much more expensive than the structure, the following main logic is used to reduce the computational work.

1. Assign the initial state of the panel;
2. For each time step, do:
 - 2.1. For each subiteration p, do:
 - 2.1.1 Evaluate the equivalent external forces acting on the plate using
$$p_{t+\Delta t} = \mu p^p + a_0 w_t + a_2 \dot{w}_t + a_3 \ddot{w}_t$$
and solve equation (5-49) iteratively;
 - 2.1.2 Move the gird using the displacement vector \mathbf{u} , \mathbf{v} , and \mathbf{w} of the panel;
 - 2.1.3 Perform the fluid analysis and find the pressure acting on the panel;
 - 2.1.4 Set $p = p^p$ and go back to step 2.1.1;
 - 2.2. Evaluate the velocities and accelerations at current time using equation (5-42);
 - 2.3. Output the results;
3. Output the results.

5.6 Results and Discussions

The problem to be investigated is the flow, inviscid flow at this time, over a two-dimensional square flexible panel of length l , as shown in Figure 5.1. Unless otherwise noted the panel has the following properties: thickness $h/l = 0.002$, mass ratio $\mu = 1$ and Poisson's ratio $\nu = 0.3$. For all cases freestream pressure, p_∞ , is specified on the underside of the panel. The coordinate of the flow $-xyz$ and $o_s - x_s y_s$ are shown in Figure 5.1.

Numerical boundary conditions for the panel provide the connection between the aerodynamic and structural equations. For viscous flow computations, a no slip condition is applied on the plate surface. This requires

$$v_x = \dot{x}_b, \quad v_y = \dot{y}_b$$

where \dot{x}_b and \dot{y}_b denote the velocity of the moving boundary with $\dot{x}_b = \dot{y}_b = 0$ in the static case. The remaining two conditions are the adiabatic wall condition and the normal momentum equation:

$$\frac{\partial T}{\partial \eta} = 0, \quad \frac{\partial p}{\partial \eta} = -\left(\frac{\rho_a}{\eta_x^2 + \eta_y^2}\right) (\eta_x \ddot{x}_b + \eta_y \ddot{y}_b)$$

Along the inflow boundary, all dependent variables are assigned their respective freestream values for supersonic flow, whereas for the subsonic flow characteristic boundary conditions²⁸ are applied. On the top boundary, either extrapolation or characteristic conditions are specified for supersonic or subsonic flows respectively. On the outflow boundary, first-order accurate extrapolation of the dependent variables is employed in all cases, corresponding to the condition

$$\frac{U}{\partial x} = 0$$

For the inviscid case, the boundary conditions along the plate are modified by setting the fluid velocity component normal to the surface equal to the corresponding values for the plate. Finally, a slip condition is implemented by using the second-order extrapolation for the tangential velocity component.

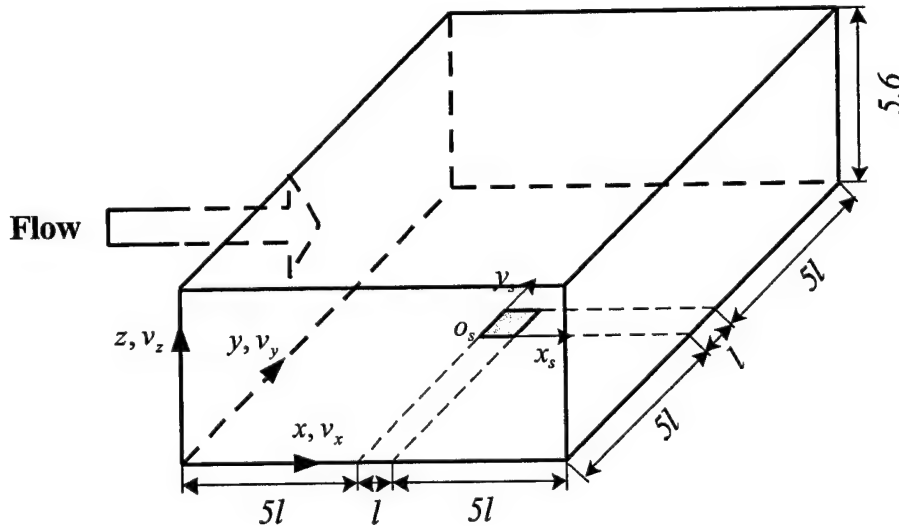


Figure 5.1. Geometry of the flow and panel

Boundary conditions for the plate are specified for simply supported edges. No deflection is allowed along the edges of the plate, i.e., $u = v = w = 0$. No moment is on the edges, that is, $\partial^2 w / \partial n^2 = 0$.

The grid used for the panel is 20×20 with equal space. The finite difference grid for the flow is $x \times y \times z = 4 \times 4 \times 2$ as shown in Figure 5.2. The minimum space in the z-direction is 0.001.

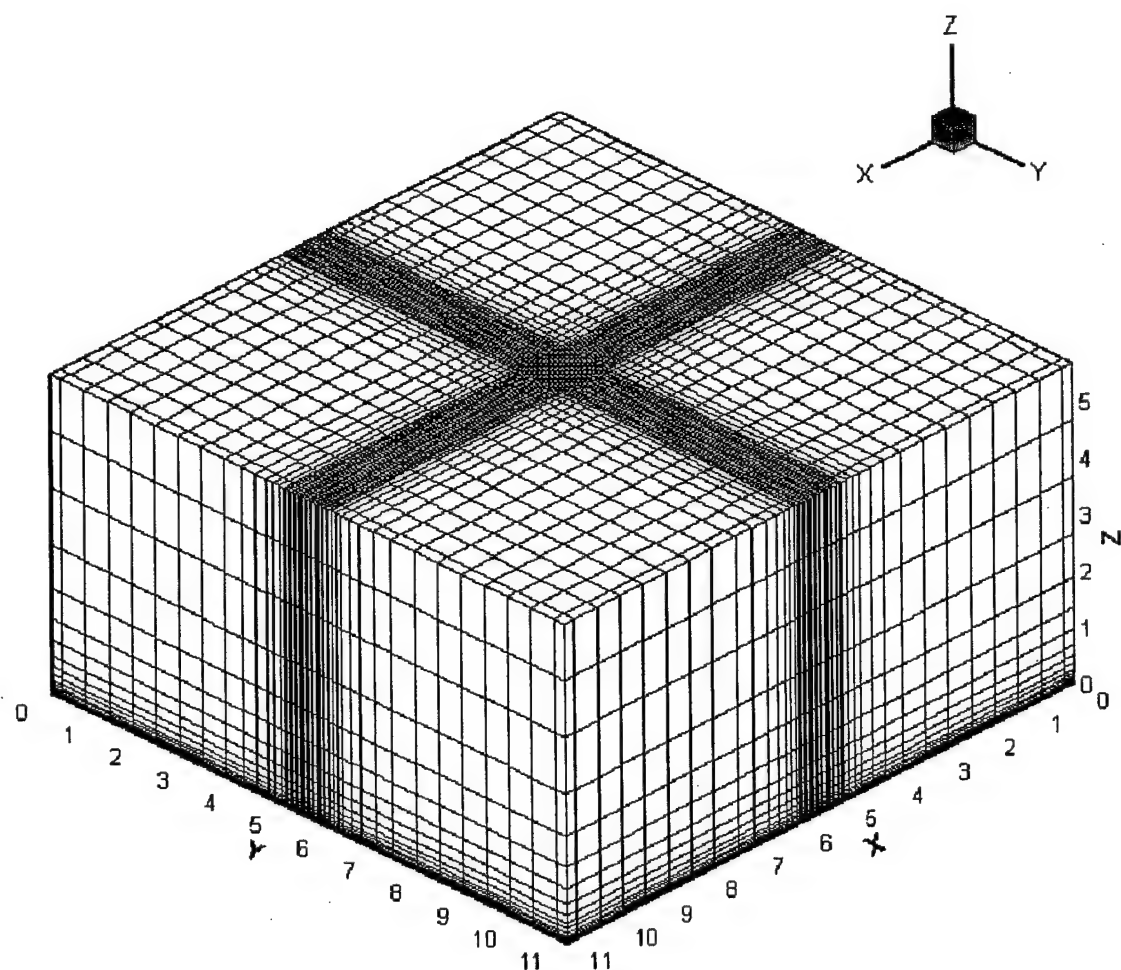


Figure 5.2 Finite difference grid for the range of flow

5.6.1. Amplitudes of Limit Cycle Oscillation (LCO)

As mentioned above, panel flutter is induced by supersonic air flow on a panel. The aerodynamic pressure acting on the panel is a function of the panel motion itself. Therefore, it is very essential to accurately predict the pressure. Even though there are several aerodynamic theories, most of them are linearized, approximate. For the current research, the aerodynamic loads are resulted from the simulation of the Euler flow on the surface of the nonlinear panel. The amplitudes of the limit cycle oscillation resulted from the present computation will be compared with those from approximate aerodynamic theories. Two of them, fully linearized potential flow and quasi-steady piston theory, will be considered at this time.

The fully linearized aerodynamic theory was used to estimate the aerodynamic pressure on the panel by Cunningham²⁹ and Dowell¹⁷ about two decades ago. This theory is based on the inviscid, potential flow. It is usually valid for a low Mach number ($M_\infty = 1$). The amplitudes of the LCO at (0.75, 0.50) in the panel coordinate obtained from this theory and the present calculation are plotted in Figure 5.3. Only three Mach numbers, 1.2, 1.414, and 1.6, are compared due to the availability of the former results.

As shown in Figure 5.3, the critical flutter dynamic pressures, λ , are 216, 462, 608 for the Euler flow while they are 191, 421, and 591 for the linearized potential flow. The former pressures are 13%, 9%, and 3% higher than the latter respectively. The present amplitudes are lower than those from the linearized potential flow theory as shown in Figure 5.3. With the increase of the Mach number, the difference becomes smaller and smaller. The reason might be that the nonlinearity is ignored in the linearized potential theory. The percent difference of the amplitudes resulted from the potential flow with respect to the results from the Euler flow are listed in Table 5.1. Generally, the difference at higher Mach number is much smaller than the lower Mach number.

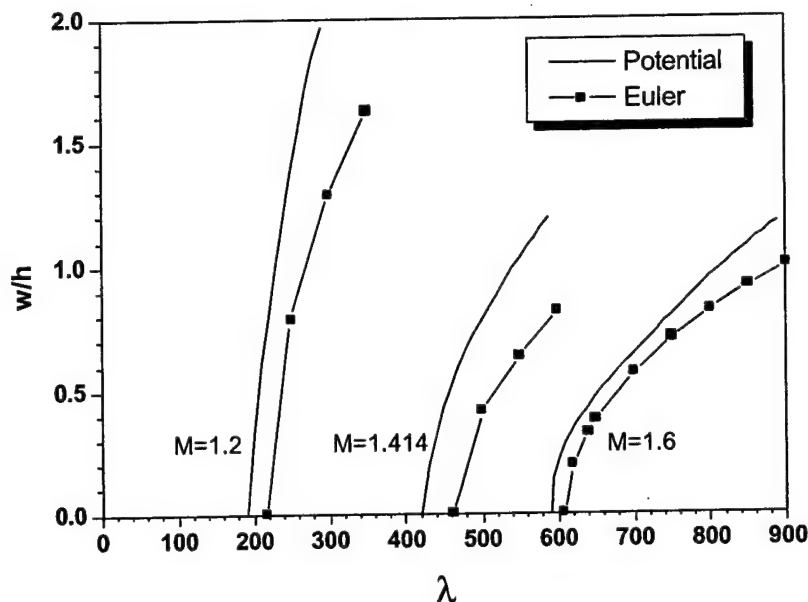


Figure 5.3. Comparison of LCO amplitudes: Potential flow and Euler flow

Table 5.1. Percent differences of the LCO amplitudes

M_∞	λ	Diff.	M_∞	λ	Diff.
1.2	250	75.3	1.6	650	24.9
1.2	300	62.0	1.6	700	14.1
1.414	500	88.7	1.6	750	13.0
1.414	550	60.8	1.6	800	16.5
1.414	600	50.2	1.6	850	18.3

The quasi-steady first order piston theory was proposed to predict the aerodynamic pressure by Ashley and Zartarian in 1956. Since the three dimensionality and the unsteadiness of the air flow was ignored in this theory, it cannot be applied for the air flow with Mach number close to one. It mostly applied for the airflow with large Mach number ($M_\infty > \sqrt{2}$). The LCO amplitudes obtained from the two theories are shown in Figure 5.4. The corresponding difference is listed in Table 5.2. It is shown clearly in Figure 5.4 that the present amplitudes are higher than those from the quasi-steady piston theory. The percent difference reduces with the increase of the dimensionless pressure. The difference for Mach number 1.6, for example, reduces from 44.4% at $\lambda = 650$ to 9.3% at $\lambda = 850$. This also

happens for Mach number 2.0. The most interesting phenomenon is that the shapes of curve resulted from the two theories are almost same for Mach number 1.6 and 2.0 respectively. Therefore, there is only some shifting difference.

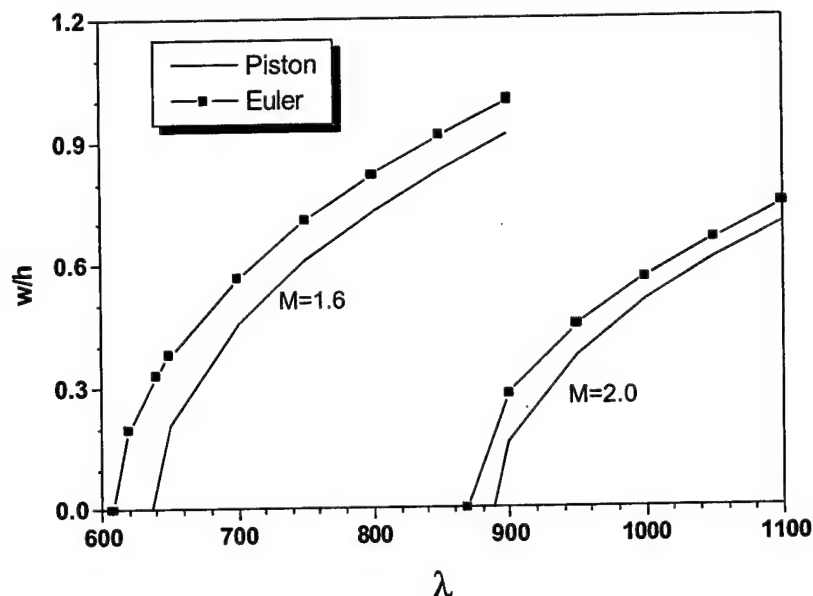


Figure 5.4. Comparison of LCO amplitudes: Piston theory and Euler flow

Table 5.2. Percent differences of the LCO amplitudes

M_∞	λ	Diff.	M_∞	λ	Diff.
1.6	650	44.4	2.0	900	41.8
1.6	700	19.8	2.0	950	17.0
1.6	750	14.0	2.0	1000	10.0
1.6	800	11.2	2.0	1050	7.4
1.6	850	9.3	2.0	1100	6.2

As mentioned in the introduction, Gordnier and Visbal have also used Euler equations to predict the aerodynamic loads very recently. The present amplitudes are compared with theirs in Figure 5.5. Only the results at Mach number 1.2 are shown due to the availability of the later results. They are very close as expected. However, there is a big difference for the critical dynamic pressure. The prediction of the critical dynamic pressure is very computationally expensive when the high fidelity

equations are used to compute the aerodynamic loads. Since the critical pressure can not be predict explicitly, six to ten simulations for the dimensionless pressures around the critical are usually required even though the linear interpolation searching technique is employed. For example, about one week was used to find the critical pressure when the error is required to be less than 1. The computation was performed on a Sun 4500 computer with four of its eight processors.

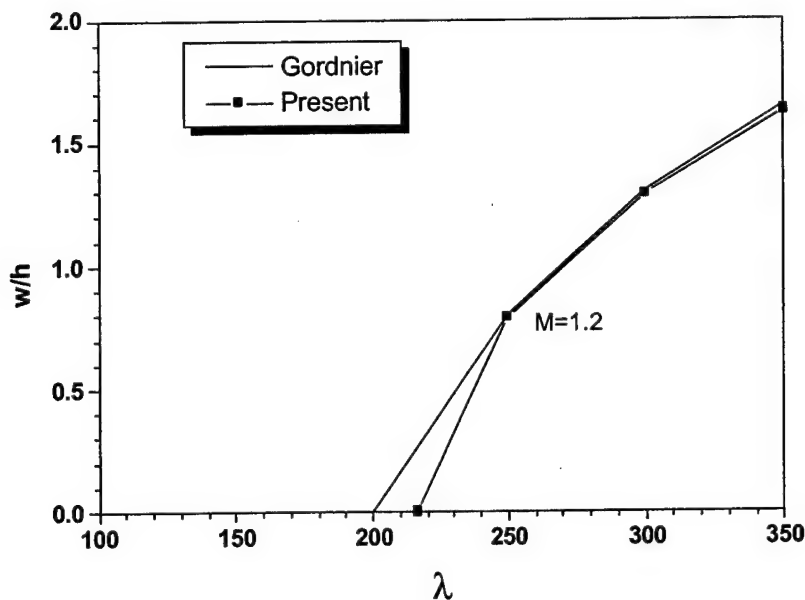
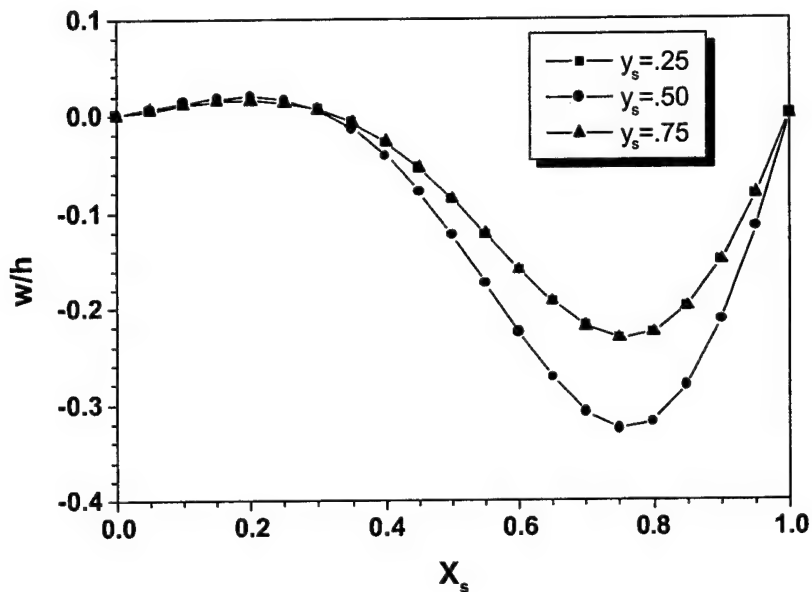
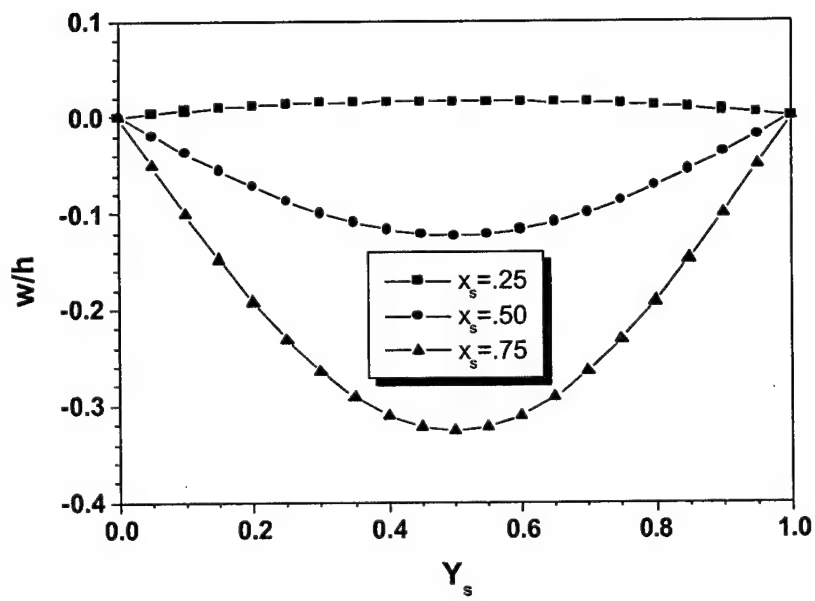


Figure 5.5. Comparison of LCO amplitudes: Euler flow

The deflections of the panel at the end of the 500 dimensionless time are plotted in Figures 5.6 and 5.7. For these figures, Mach number $M_\infty = 1.6$, dimensionless dynamic pressure $\lambda = 650$ and $\lambda = 900$ are used. The following three phenomena may be easily obtained from these plots. (1) The maximum deflection is approximately located on the right one quarter, i.e., $\hat{x}_s/l = 0.75$ and $\hat{y}_s/\hat{l} = 0.5$. This is shown clearly in Figures 5.6(a) and 5.7(a). (2) The deformations are symmetric with respect the central line of the panel in the x direction, that is, $\hat{y}_s = 0.5$. (3) In the y direction, the shape of the deformation is very close to the first modeshape of the panel itself. These three phenomena are very similar to those based on the approximate theories.

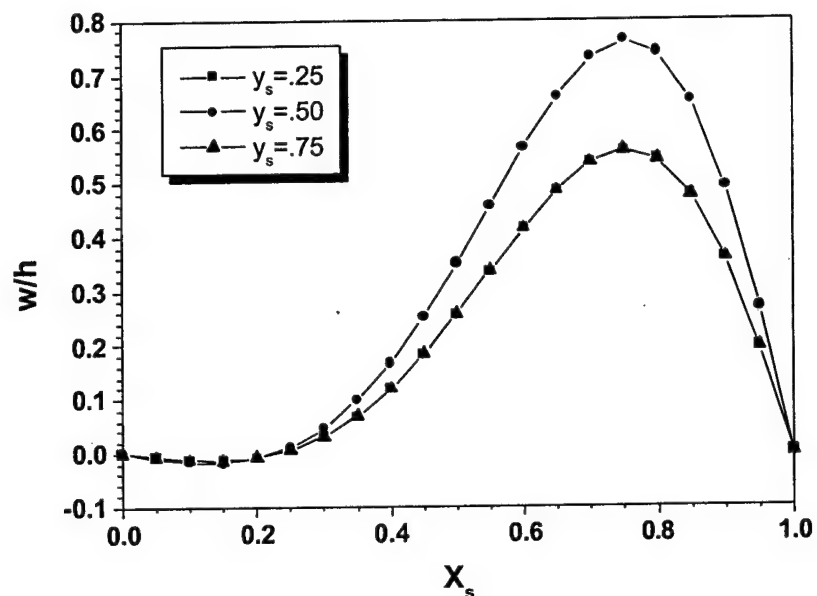


(a)

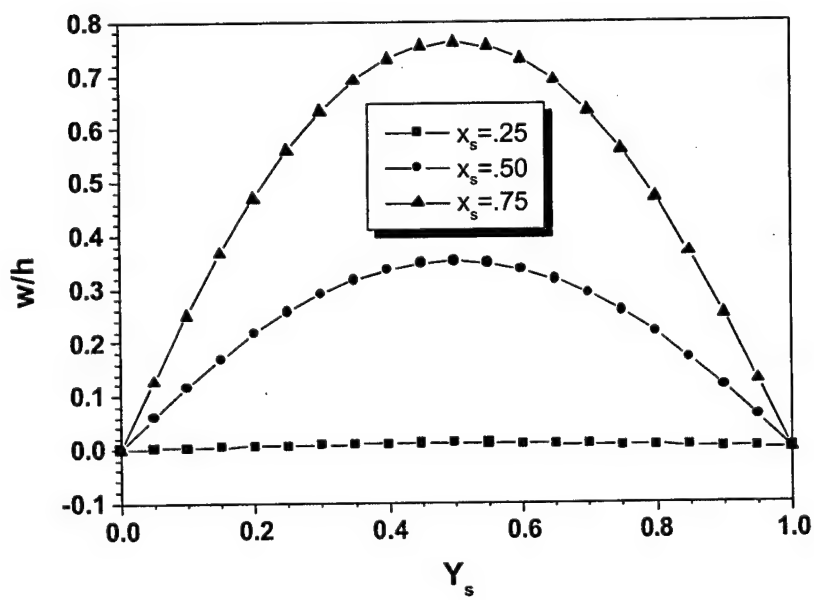


(b)

Figure 5.6. Deflection of the panel for $M_\infty = 1.6$ and $\lambda = 650$: (a) in x direction; (b) in y direction

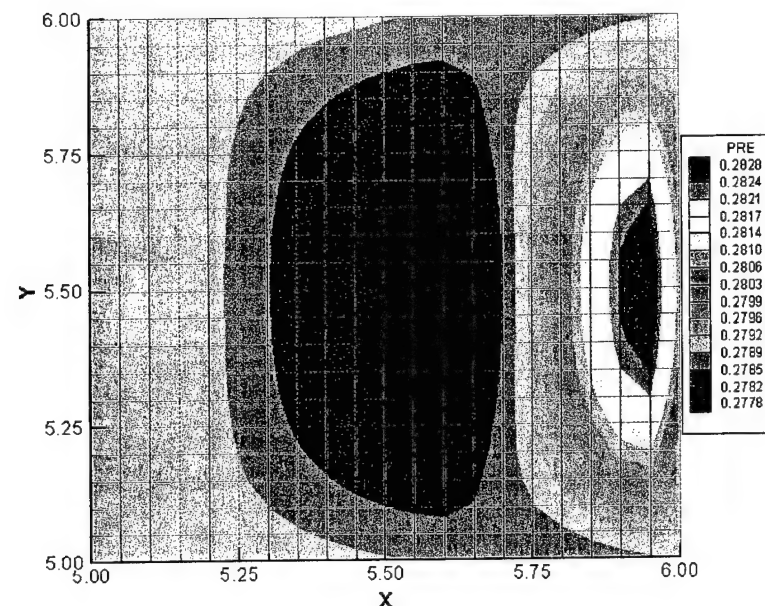


(a)

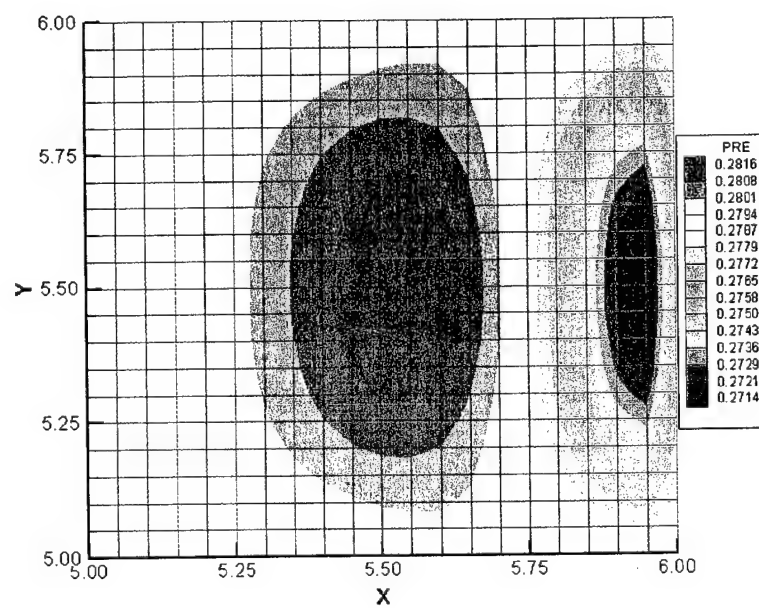


(b)

Figure 5.7. Deflection of the panel for $M_\infty = 1.6$ and $\lambda = 900$: (a) in x direction; (b) in y direction

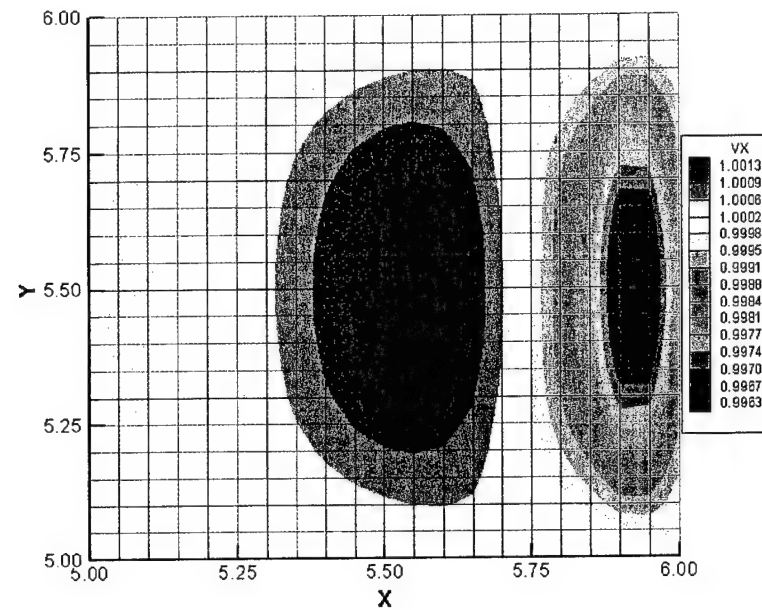


(a)

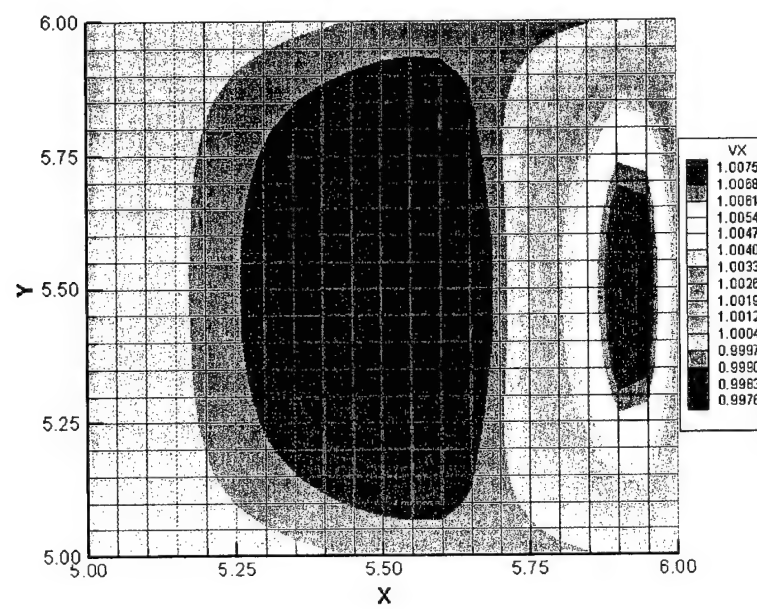


(b)

Figure 5.8. Surface pressure contour of the panel for $M_\infty = 1.6$: (a) $\lambda = 650$, (b) $\lambda = 900$



(a)



(b)

Figure 5.9. Surface flow velocity v_x contour for $M_\infty = 1.6$: (a) $\lambda = 650$, (b) $\lambda = 900$

The pressures and the flow velocity in the x -direction on the surface of the panel at the same time mentioned above are shown in Figures 5.8 and 5.9 respectively. Clearly, they are symmetrical with respect to the central line of the panel in the x -direction, that is $= 5$. As we know, the dimensionless air pressure of the freestream is 0.2790 as shown in the left one fifth part in Figure 5.8. Usually, there are three net pressure ranges. They approximately locate on the left one quarter, middle one half, and right one quarter of the panel respectively as shown in Figure 5.8. For convenience, they are called range I, II, and III from left to right. Since the net pressures in range I are very close to the reference pressure 0.2790, they are not clearly shown in Figure 5.8. The net pressure in range III is much higher than that in range II which is much higher than that in range I. This is the reason that the maximum deflection of the panel is always very close to the three-quarter of the panel from left. Furthermore, the pressure within ranges II and III usually have different sign. Of course, there is a pressure shock between these two ranges. The phenomenon of the distribution of the pressure may be explained from the air velocity distribution on the surface of the panel shown in Figure 5.9.

5.6.2 Flutter Frequency

The LCO in time domain is plotted for $M_\infty = 1.2$ and $\lambda = 300$ in Figure 5.10(a). The FFT transformation of the oscillation in frequency domain is shown in Figure 5.10(b). Initially, the amplitude grows rapidly due to the negative damping from the aerodynamic pressure. With the increase of the amplitude the membrane tensile forces become significant which bound the flutter amplitude at a constant some time later. It can be found from Fig. 5.10(b) that the fundamental flutter frequency of the LCO is 0.0854.

As we know, the natural circular frequencies of the linear simply supported thin plate can be expressed as²⁴

$$\hat{\omega}_{mn} = \frac{\pi^2}{\hat{l}^2} (m^2 + n^2) \sqrt{\frac{\hat{D}}{\hat{\rho}_s \hat{h}}} \quad (5-50)$$

where $m = \dots$. The corresponding nondimensional frequencies are

$$f_{mn} = \frac{\pi}{2\hat{V}_\infty \hat{l}} (m^2 + n^2) \sqrt{\frac{\hat{D}}{\hat{\rho}_s \hat{h}}} \quad (5-51)$$

Using the dimensionless dynamic pressure λ and mass ratio μ_s , equation (5-51) may be rewritten as

$$f_{mn} = \frac{\pi}{2} (m^2 + n^2) \lambda \sqrt{\frac{\mu_s}{\lambda}} \quad (5-52)$$

Hence, the first two natural frequencies are 0.0574 and 0.1434.

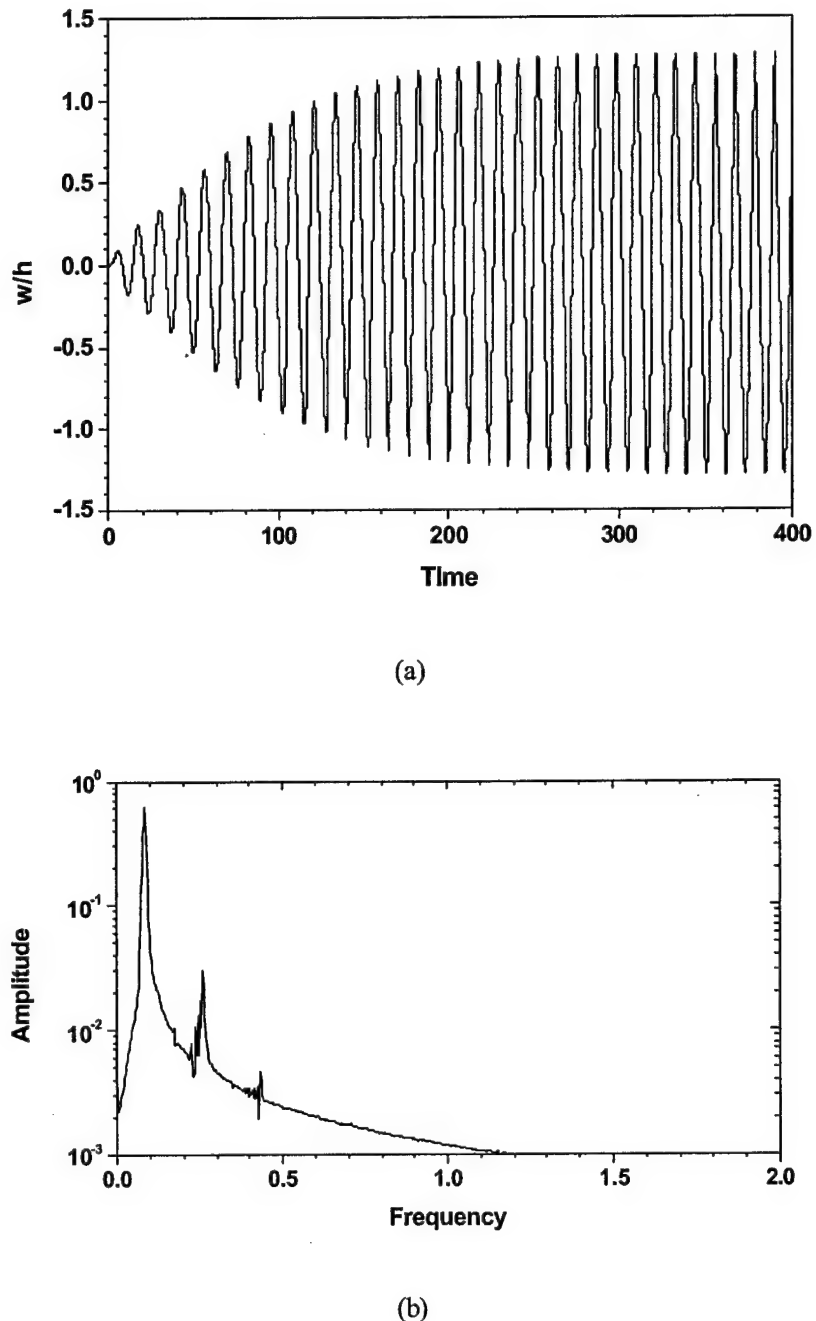
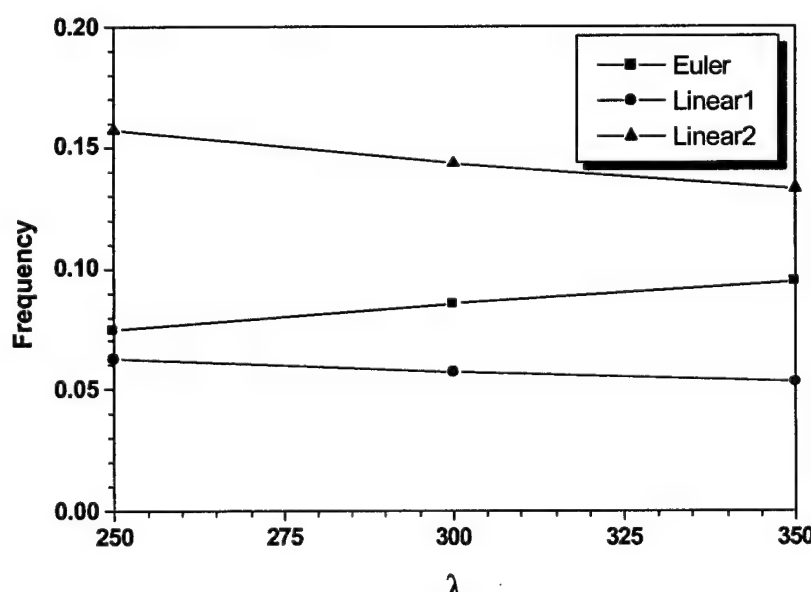
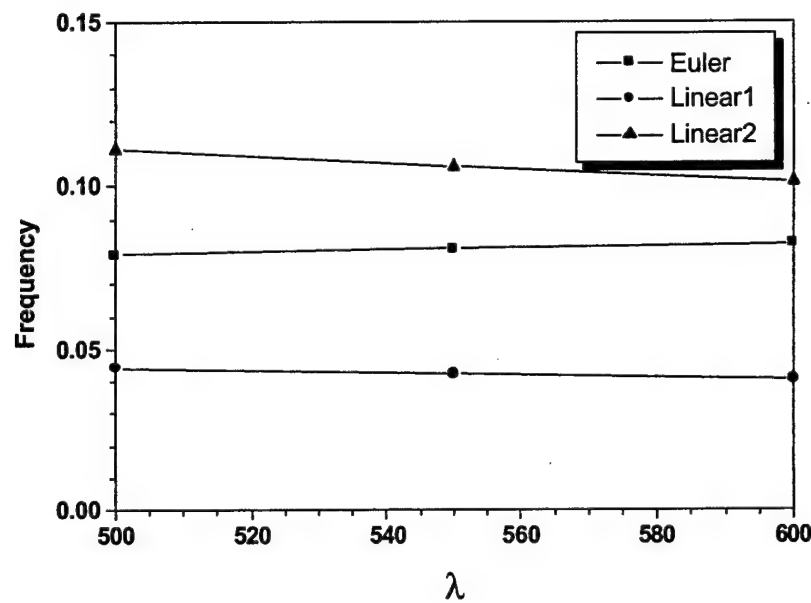


Figure 5.10. LCO for $M_\infty = 1.2$ and $\lambda = 300$: (a) time domain; (b) frequency domain

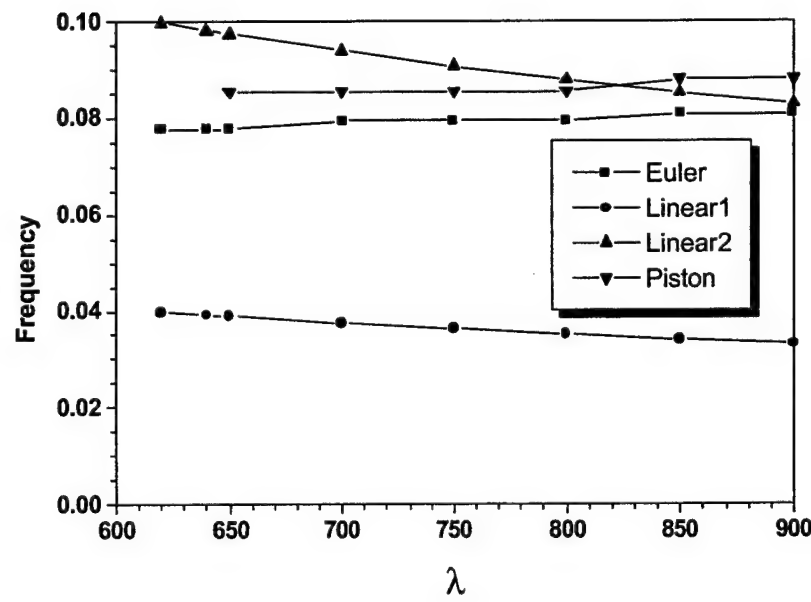
Similarly, the flutter frequencies and the corresponding natural frequencies may be calculated. They are plotted in Fig. 5.11. In these pictures, "Linear1" and "Linear2" denote the first and second natural frequencies respectively. The natural frequencies decrease with the increase of the nondimensional dynamic pressure which can be explained clearly from equation (5-52). As we know, the panel becomes more flexible when the dynamic pressure increases. Under the same air flow, the responses should be bigger for the higher dynamic pressure. The nonlinear effect, therefore, gets more significant. Consequently, the flutter frequencies obtained from both Euler flow theory and piston theory increase very slightly when the dynamic pressure increases even though the corresponding natural frequencies decrease. For the higher Mach numbers, $M_\infty = 1.6$ and $M_\infty = 2.0$, the flutter frequencies are almost constant. The flutter frequencies resulted from the present simulation are a little lower than those from piston theory. Because the flutter frequency is pertaining to the nonlinear model, it should be bigger than the corresponding natural frequency. From Fig. 5.11 we know, almost all the flutter frequencies are located between the first and the second natural frequencies of the corresponding linear models. This means that the lowest two modes, especially the first mode, have significant contribution to the LCO.



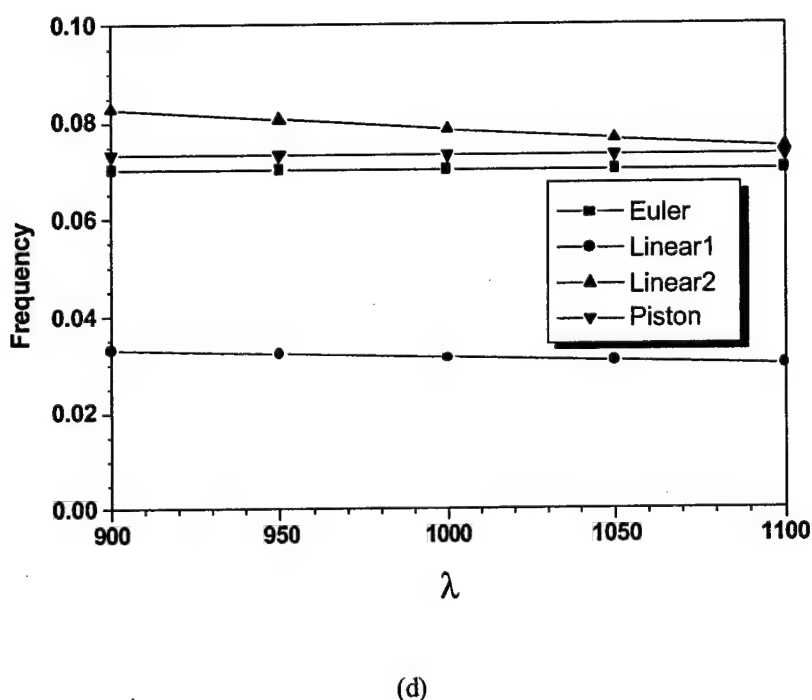
(a)



(b)



(c)



(d)

Figure 5.11. Comparison of the frequencies:

 (a) $M_\infty = 1.2$; (b) $M_\infty = 1.414$; (c) $M_\infty = 1.6$; (d) $M_\infty = 2.0$

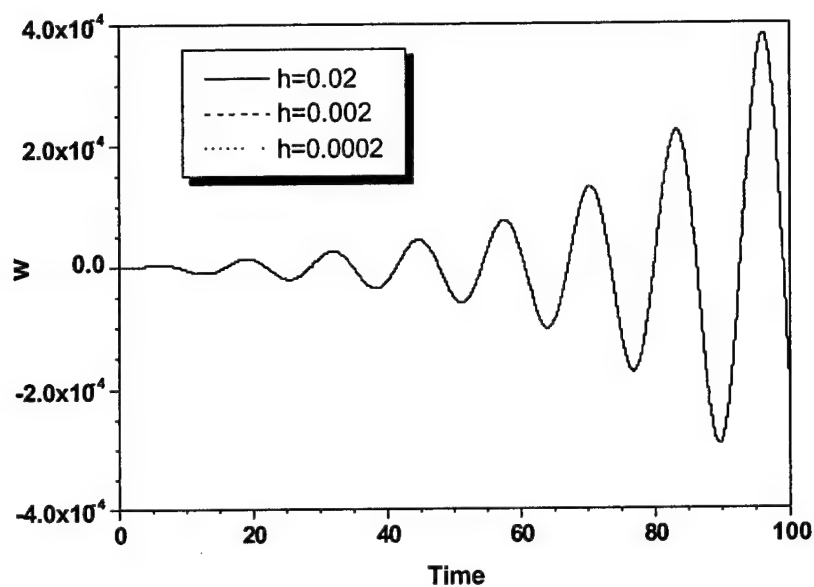
5.6.3. Effect of the Panel Thickness

In the following discussion, we assume the nondimensional dynamic pressure λ , mass ratio μ_s , and the parameters of the air flow are constants when the thickness h changes. This means that the panel and the air flow do not change in the nondimensional sense for different thickness.

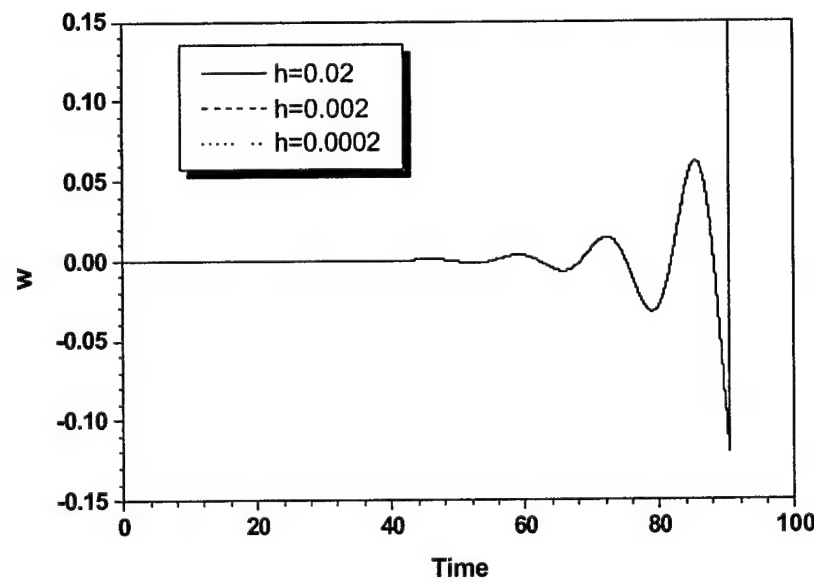
5.6.3.1 Linear Case

The linear governing equations of the panel under the Euler flow can be easily obtained from equation (5-35a) as

$$\frac{\mu_s}{\lambda} \nabla^4 w + \frac{\partial^2 w}{z^2} = \mu_s p_z \quad (5-53)$$



(a)



(b)

Figure 5.12. Linear deflection of the panel: (a) $\lambda = 650$; (b) $\lambda = 900$

As we know, the aerodynamic pressure resulted from the Euler equations is only dependent on the deflection w of the panel during the simulation. Hence, it will not be affected by the thickness. The items on the left-hand side also have nothing to do with the thickness. Therefore, the deflection of the panel is supposed to be independent of the thickness. Since the critical dimensionless dynamic pressure, λ_{cr} , can be determined from the linear panel, it is also independent of the thickness.

The deflections of the panel for $M_\infty = 1.6$, $\lambda = 650$ and $\lambda = 900$ are plotted in Figure 5.12. In these results, three different thicknesses, 0.02, 0.002, and 0.0002, are used. The deformations blow up at time 90.58 in Figure 5.12(b) due to the unreasonable deformation of the panel. The deformations are exactly same for different thicknesses of the panel.

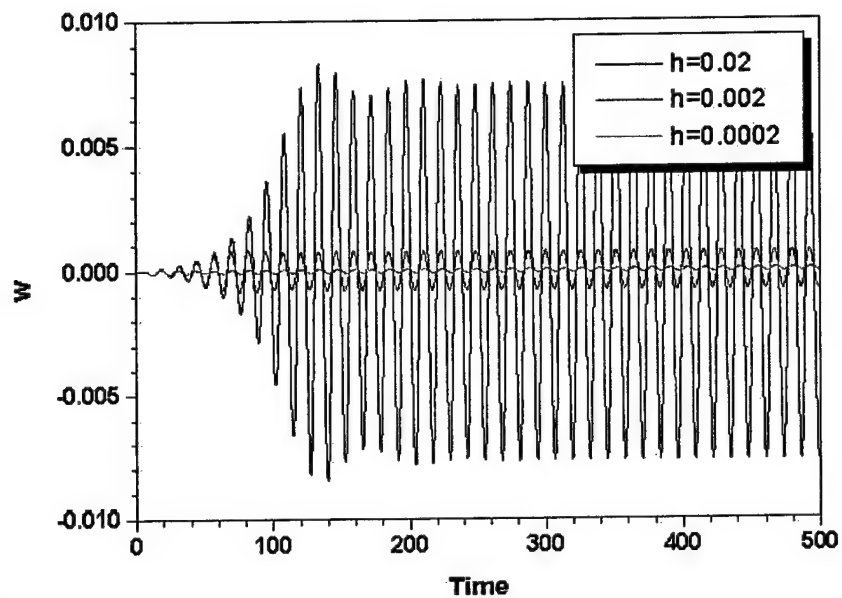
5.6.3.2 Nonlinear Case

For the nonlinear case, the effect of the thickness becomes a little complex. Let's discuss the influence of the thickness on the deformation w at first. Introducing equation (5-37) into equations (5-35b) and (5-35c) leads

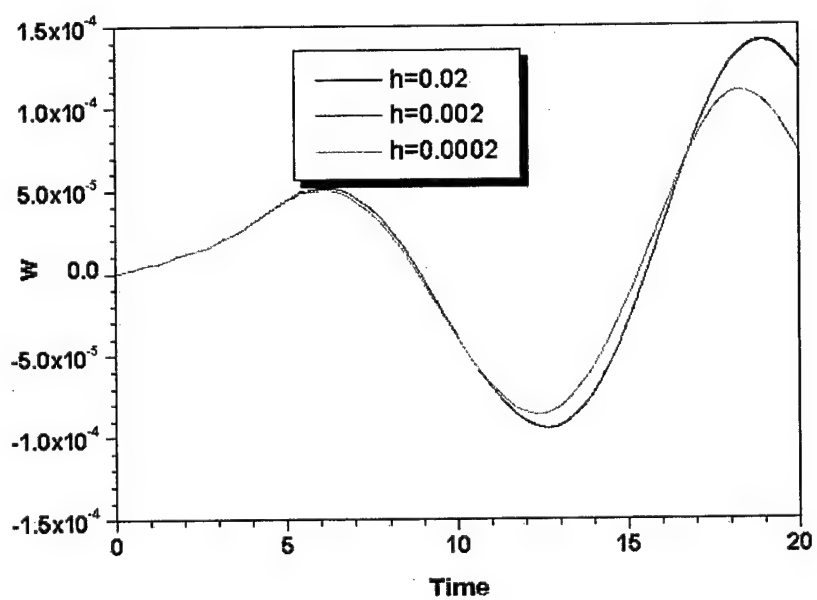
$$2\left[\frac{\partial^2 u}{\partial x^2} + \frac{\partial w}{\partial x} \frac{\partial^2 w}{\partial x^2} + v\left(\frac{\partial^2 v}{\partial x \partial y} + \frac{\partial w}{\partial y} \frac{\partial^2 w}{\partial x \partial y}\right)\right] + (1-v)\left(\frac{\partial^2 u}{\partial y^2} + \frac{\partial^2 v}{\partial x \partial y} + \frac{\partial w}{\partial x} \frac{\partial^2 w}{\partial y^2} + \frac{\partial w}{\partial y} \frac{\partial^2 w}{\partial x \partial y}\right) = 0 \quad (5-54-a)$$

$$2\left[\frac{\partial^2 v}{\partial y^2} + \frac{\partial w}{\partial y} \frac{\partial^2 w}{\partial y^2} + v\left(\frac{\partial^2 u}{\partial x \partial y} + \frac{\partial w}{\partial x} \frac{\partial^2 w}{\partial x \partial y}\right)\right] + (1-v)\left(\frac{\partial^2 u}{\partial x \partial y} + \frac{\partial^2 v}{\partial x^2} + \frac{\partial w}{\partial x} \frac{\partial^2 w}{\partial x \partial y} + \frac{\partial w}{\partial y} \frac{\partial^2 w}{\partial x^2}\right) = 0 \quad (5-54-b)$$

These two equations are independent of the thickness. Therefore, only Equation (5-35a) depends on the thickness through the internal forces expressed in equation (5-37). As shown in equation (5-37), the internal forces reduce with the increase of the thickness. This leads the decrease of the nonlinear effect. Hence, the deflection w will increase. This is shown clearly in Figures 5.13 and 5.14. The deflection of the case $h = 0.02$ is much bigger than the case $h = 0.002$ and the later is much bigger than the case $h = 0.0002$. As shown in Figures 5.13(b) and 5.14(b), the deflections are very close to each other for different thicknesses at beginning. The reason is that these deflections are very small and the nonlinear effect is unimportant. They are close to the linear case.

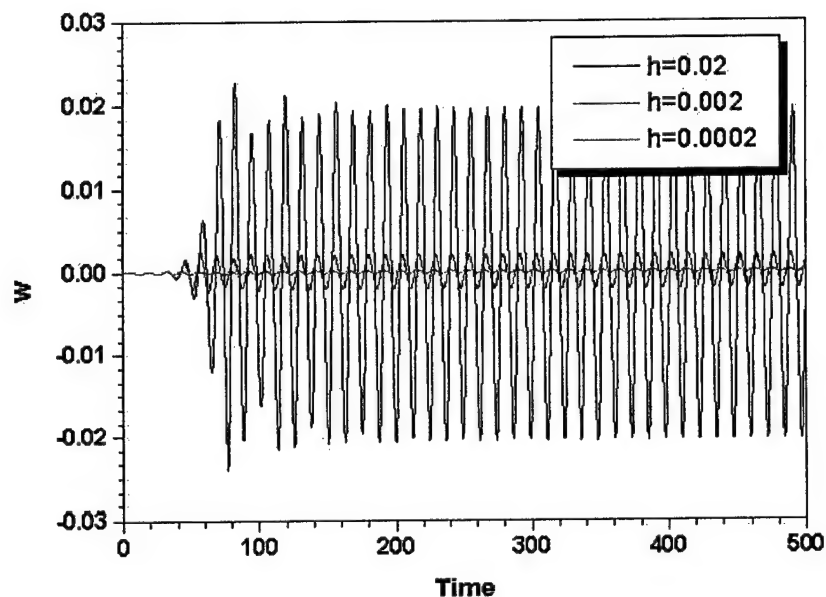


(a)

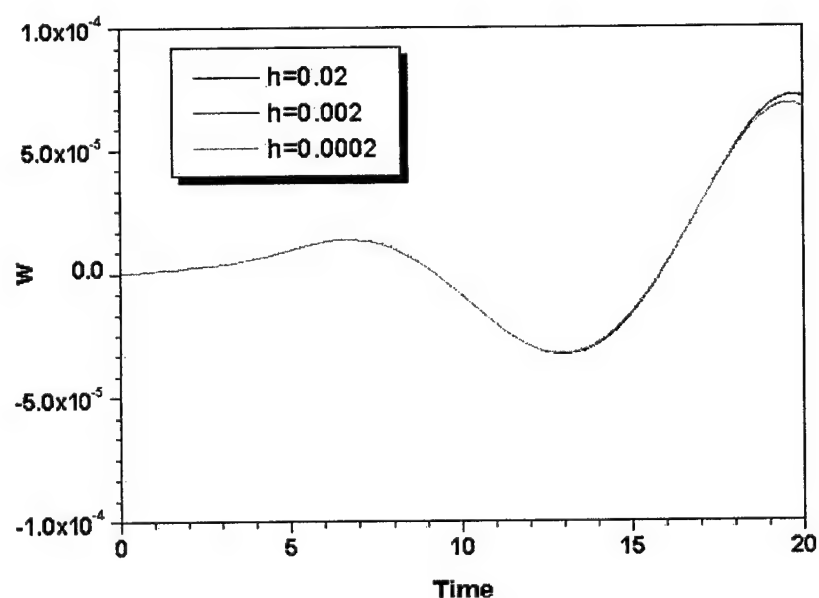


(b)

Figure 5.13. Nonlinear deflection of the panel for $\lambda = 650$



(a)



(b)

Figure 5.14. Nonlinear deflection of the panel for $\lambda = 900$

Defining the ratio of the deflection w with respect to the thickness h as $\tilde{w} = w/h$. Substituting \tilde{w} for w in equations (5-35a) leads

$$\frac{\mu_s}{\lambda} \nabla^4 \tilde{w} + \frac{\partial^2 \tilde{w}}{\partial t^2} = \frac{\mu_s p_z}{h} + \mu_s n_x \frac{\partial^2 \tilde{w}}{\partial x^2} + \mu_s n_y \frac{\partial^2 \tilde{w}}{\partial y^2} + 2\mu_s n_{xy} \frac{\partial^2 \tilde{w}}{\partial x \partial y} \quad (5-55)$$

in which, the internal forces are

$$n_x = \frac{12}{\lambda} \left\{ \frac{\partial \tilde{u}}{\partial x} + \frac{1}{2} \left(\frac{\partial \tilde{w}}{\partial x} \right)^2 + v \left[\frac{\partial \tilde{v}}{\partial y} + \frac{1}{2} \left(\frac{\partial \tilde{w}}{\partial y} \right)^2 \right] \right\} \quad (5-56-a)$$

$$n_y = \frac{12}{\lambda} \left\{ \frac{\partial \tilde{v}}{\partial y} + \frac{1}{2} \left(\frac{\partial \tilde{w}}{\partial y} \right)^2 + v \left[\frac{\partial \tilde{u}}{\partial x} + \frac{1}{2} \left(\frac{\partial \tilde{w}}{\partial x} \right)^2 \right] \right\} \quad (5-56-b)$$

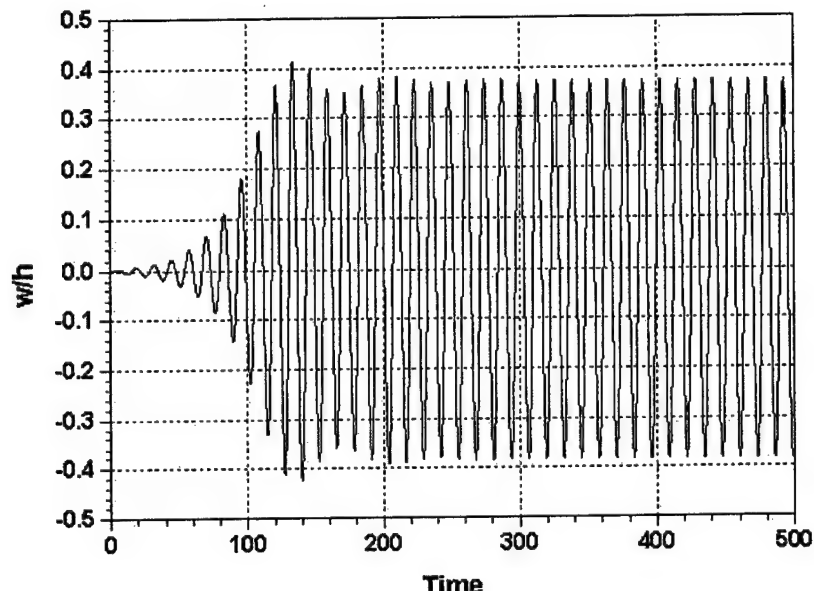
$$n_{xy} = \frac{6(1-v)}{\lambda} \left(\frac{\partial \tilde{u}}{\partial y} + \frac{\partial \tilde{v}}{\partial x} + \frac{\partial \tilde{w}}{\partial x} \frac{\partial \tilde{w}}{\partial y} \right) \quad (5-56-c)$$

where, $\tilde{u} = u/h^2$ and $\tilde{v} = v/h^2$. Using equations (5-56), the governing equations (5-35b) and (5-35c) become

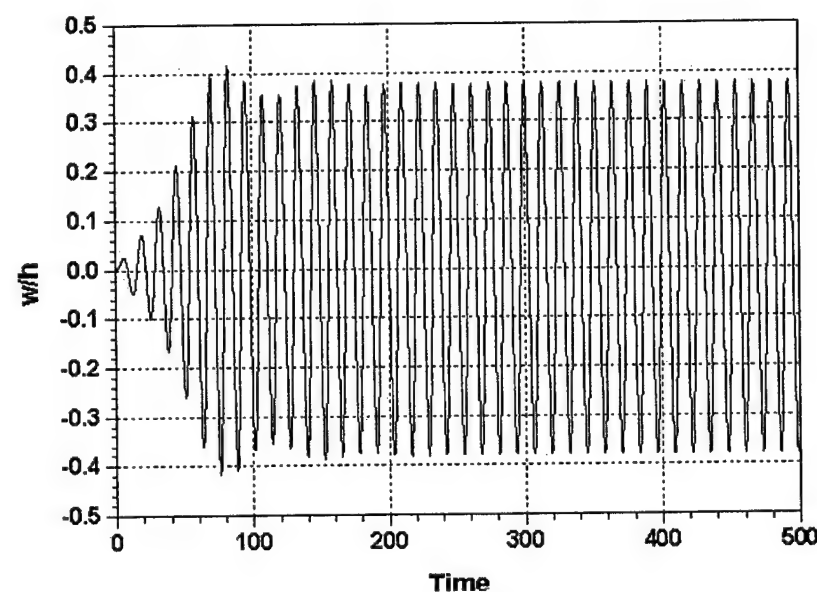
$$2 \left[\frac{\partial^2 \tilde{u}}{\partial x^2} + \frac{\partial \tilde{w}}{\partial x} \frac{\partial^2 \tilde{w}}{\partial x^2} + v \left(\frac{\partial^2 \tilde{v}}{\partial x \partial y} + \frac{\partial \tilde{w}}{\partial y} \frac{\partial^2 \tilde{w}}{\partial x \partial y} \right) \right] + (1-v) \left(\frac{\partial^2 \tilde{u}}{\partial y^2} + \frac{\partial^2 \tilde{v}}{\partial x \partial y} + \frac{\partial \tilde{w}}{\partial x} \frac{\partial^2 \tilde{w}}{\partial y^2} + \frac{\partial \tilde{w}}{\partial y} \frac{\partial^2 \tilde{w}}{\partial x \partial y} \right) = 0 \quad (5-57-a)$$

$$2 \left[\frac{\partial^2 \tilde{v}}{\partial y^2} + \frac{\partial \tilde{w}}{\partial y} \frac{\partial^2 \tilde{w}}{\partial y^2} + v \left(\frac{\partial^2 \tilde{u}}{\partial x \partial y} + \frac{\partial \tilde{w}}{\partial x} \frac{\partial^2 \tilde{w}}{\partial x \partial y} \right) \right] + (1-v) \left(\frac{\partial^2 \tilde{u}}{\partial x \partial y} + \frac{\partial^2 \tilde{v}}{\partial x^2} + \frac{\partial \tilde{w}}{\partial x} \frac{\partial^2 \tilde{w}}{\partial x \partial y} + \frac{\partial \tilde{w}}{\partial y} \frac{\partial^2 \tilde{w}}{\partial x^2} \right) = 0 \quad (5-57-b)$$

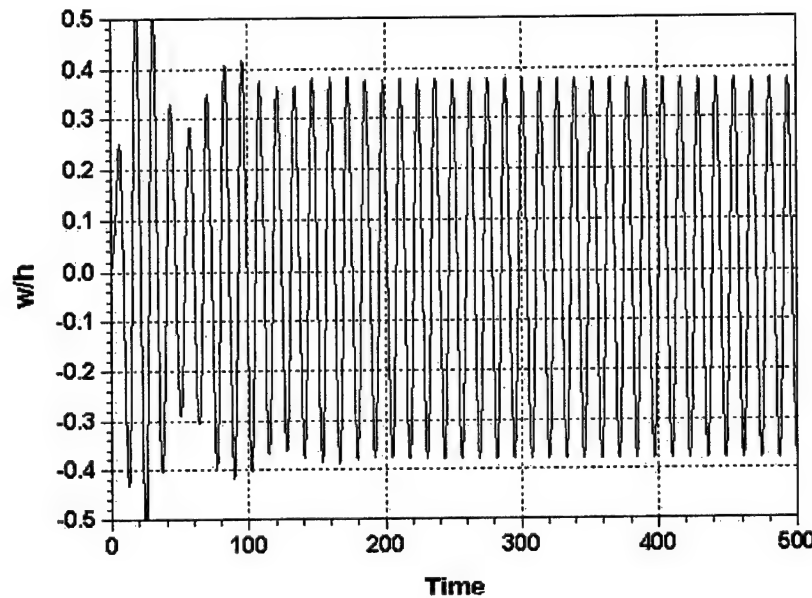
The ratios of the deflection for $\lambda = 650$ and $\lambda = 900$ are shown in Figures 5.15 and 5.16 respectively. It can be seen that the amplitudes of the ratio become stable after some time, 200 for example. The stable amplitudes are very close for the same nondimensional dynamic pressure. This means that the ratio of the LCO amplitude is independent of the thickness. We also can conclude that the ratio of p_z/h has nothing to do with the thickness for the Mach number.



(a)



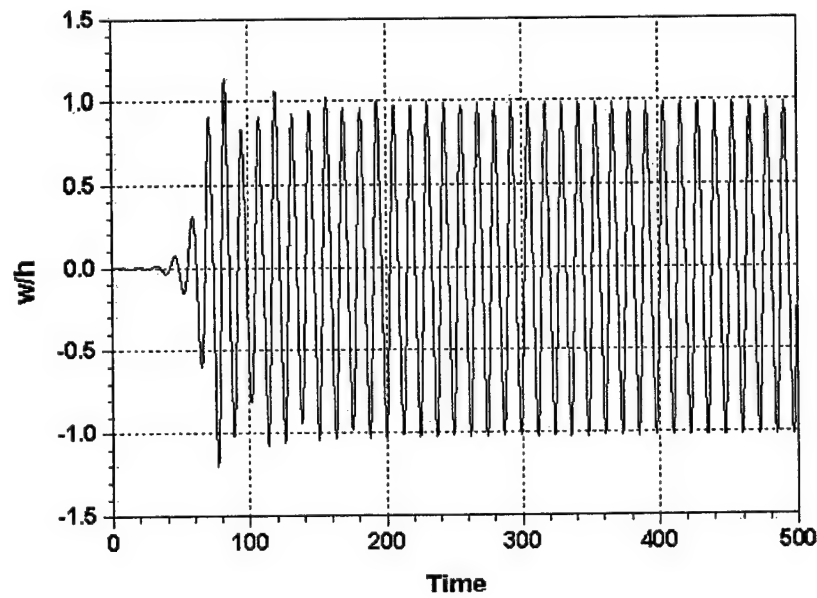
(b)



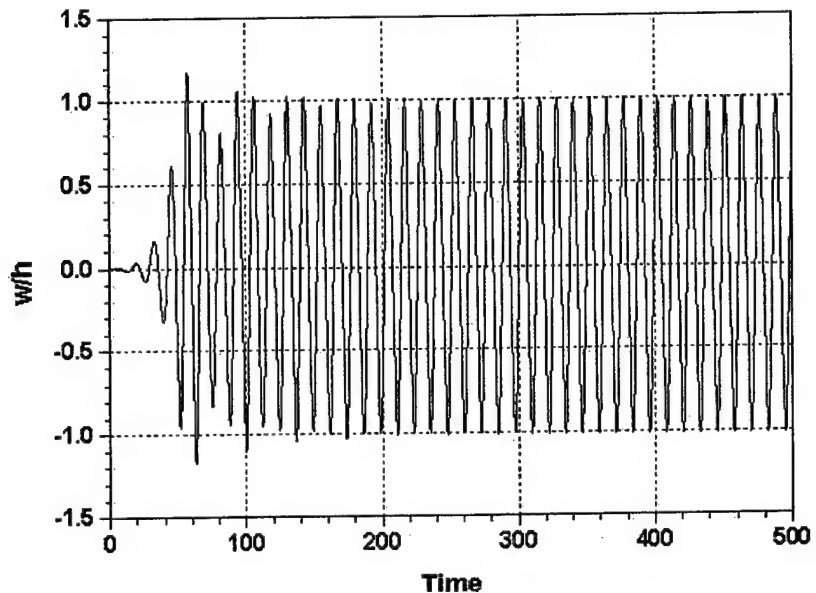
(c)

Figure 5.15. Ratio of the nonlinear deflections for $\lambda = 650$:

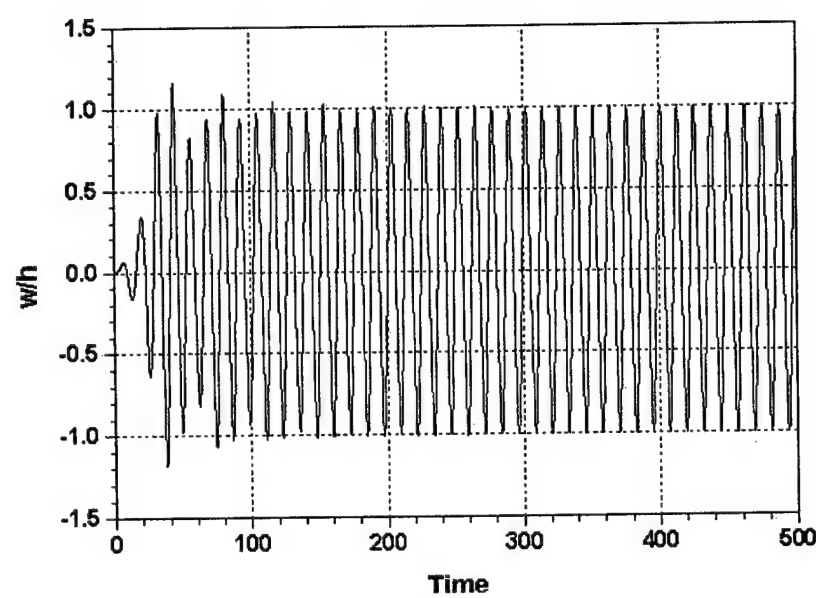
(a) $h = 0.02$; (b) $h = 0.002$; (c) $h = 0.0002$



(a)



(b)



(c)

Figure 5.16. Ratio of the nonlinear deflections for $\lambda = 900$:

(a) $h = 0.02$; (b) $h = 0.002$; (c) $h = 0.0002$

This phenomenon can be explained clearly if the quasi-steady piston aerodynamic theory is considered. In this theory, the aerodynamic pressure acting on the panel is assumed as

$$\hat{p}_z = \frac{\hat{\rho}_a \hat{V}_\infty^2}{\sqrt{M_\infty^2 - 1}} \left(\frac{\partial \hat{w}}{\partial \hat{x}} + \frac{M_\infty^2 - 2}{M_\infty^2 - 1} \frac{1}{\hat{V}_\infty} \frac{\partial \hat{w}}{\partial \hat{t}} \right) \quad (5-58)$$

Its nondimensional form is given by

$$p_z = \frac{\rho_a}{\sqrt{M_\infty^2 - 1}} \left(\frac{\partial w}{\partial x} + \frac{M_\infty^2 - 2}{M_\infty^2 - 1} \frac{\partial w}{\partial t} \right) \quad (5-59)$$

Introducing equation (5-59) into equation (5-55) results

$$\frac{\mu_s}{\lambda} \nabla^4 \tilde{w} + \frac{\partial^2 \tilde{w}}{\partial t^2} = \frac{\mu_s \rho_a}{\sqrt{M_\infty^2 - 1}} \left(\frac{\partial \tilde{w}}{\partial x} + \frac{M_\infty^2 - 2}{M_\infty^2 - 1} \frac{\partial \tilde{w}}{\partial t} \right) + \mu_s n_x \frac{\partial^2 \tilde{w}}{\partial x^2} + \mu_s n_y \frac{\partial^2 \tilde{w}}{\partial y^2} + 2\mu_s n_{xy} \frac{\partial^2 \tilde{w}}{\partial x \partial y} \quad (5-60)$$

Clearly, the above equation has nothing to do with the thickness. Actually, this is true for supersonic flow.

Although the thickness does not affect the ratio of the LCO amplitude after the oscillation become stable, it does affect the way to the LCO. For example, the ratio of the amplitude for $h = 0.02$ increases very slowly as shown in Figure 5.15(a). It takes about 110 nondimensional time for the ratio to close to the stable value. When the thickness decreases by one tenth and one hundredth, the computer times reduce to about 80 and 10, respectively, as shown in Figure 5.15. As we know, the deflection is very small at beginning and fall into the linear or weak nonlinear range. According to the results in Figures 5.13 and 5.14, the amplitudes should be very close. Therefore, the ratio which is scaled by the inversion of the thickness decreases with the increase of the thickness. At the very beginning, the difference is very close to $1/h$. With the increase of the amplitude, the difference decreases very fast. After the oscillation becomes stable, the difference becomes insignificant.

5.7 Summary

The three-dimensional nonlinear panel flutter at supersonic flow is analyzed using the high-fidelity flow equations, Euler equations. These flow equations are solved using the Beam-Warming, alternate-direction, implicit scheme. The governing equations of the large deflection panel are based on the von-Karman theory. Finite difference method is used to discretize the governing equations in space and

Newmark-Beta integration scheme is applied to solve them in time domain. The Newton-like subiteration is implemented to eliminate the lagging errors associated with the exchange of the pressure and deformations between the fluid and panel at their interface. The numerical simulation is performed on a simply supported square panel. The results at the supersonic air flow are compared with those from potential flow theory and quasi-steady supersonic theory.

(1) The present LCO amplitudes are smaller than those resulted from the linear potential flow theory. Generally, the difference at higher Mach number is smaller than the lower Mach number.

(2) The LCO amplitudes obtained from Euler flow are bigger than those obtained from quasi-steady piston theory. Similarly, the difference reduces with the increase of the dynamic pressure.

(3) The current results are very close to those from Reference 14 except for the critical nondimensional dynamic pressure at Mach number 1.2.

(4) The flutter frequencies increase very slightly with the increase of the dynamic pressure. For high supersonic flow, $M_\infty = 2.0$ for example, these frequencies become a constant within a wide dynamic pressure range. The current flutter frequencies are a little lower than those from quasi-steady piston theory. The first mode of the panel has the significant contribution of the panel flutter.

(5) Assume the nondimensional dynamic pressure λ , mass ratio μ_s , and the parameters of the air flow are constants. The deflection of the panel for the linear case, and hence the critical nondimensional dynamic pressure, is independent of the dimensionless thickness of the panel. For the nonlinear case of the panel, the nondimensional thickness does not affect the ratio of the LCO amplitude. However, it does affect the way to the LCO.

References:

¹Guruswamy, G. P., "Unsteady Aerodynamic and Aeroelastic Calculations for Wings Using Euler Equations," *AIAA Journal*, Vol.28, No.3, 1990, pp.461-469.

²Morton, S. A., and Beran, P. S., "Nonlinear Analysis of Airfoil Flutter at Transonic Speeds," *AIAA Paper*, 1995, 95-1905.

³Bendiksen, O. O., and Hwang, G., "Nonlinear Flutter Calculations for Transonic Wings," *Proceedings of International Forum on Aeroelasticity and Structure Dynamics, Rome, Italy*, 1997, pp.105-114.

⁴Bendiksen, O. O., and Davis, G. A., "Nonlinear Traveling Wave Flutter of Plates in Transonic Flow," *AIAA Paper*, 1995, 95-1486.

CHAPTER 5: Three Dimensional Aeroelastic Solver for Nonlinear Panel Flutter

⁵Rizzetta, D. P., and Visbal, M. R., "Comparative Numerical Study of Two Turbulence Models for Airfoil Static and Dynamic Stall," *AIAA Paper*, 1992, 92-4649.

⁶Morton, S. A., and Melville, R. B., and Visbal, M. R., "Accuracy and Coupling Issue of Aeroelastic Navier-Stokes Solutions on Deforming Meshes," *AIAA Paper*, 1997, 97-1085.

⁷Melville, R. B., Morton, S. A., and Rizzetta, D. P., "Implementation of a Fully-Implicit, Aerodynamic Navier-Stokes Solver," *AIAA Paper*, 1997, 97-2039.

⁸Gordnier, R. E., and Melville, R. B., "Accuracy Issues for Transonic Wing Flutter using 3-D Navier-Stokes," *AIAA Paper*, 1998, 98-1729.

⁹Morton, S. A., Rizzetta, D. P., and Melville, R. B., "Numerical simulation of the Interaction Between a Leading-Edge Vortex and a Flexible Vertical Tail," *AIAA Paper*, 1998, 98-1957.

¹⁰Gordnier, R. E., and Melville, R. B., "Physical Mechanisms for Limit-Cycle Oscillations of a Cropped Delta Wing," *AIAA Paper*, 1999, 99-3796.

¹¹Davis, G. A., and Bendiksen, O. O., "Transonic Panel Flutter," *AIAA Paper*, 1993, 93-1476.

¹²Davis, G. A., "Transonic Aeroelasticity Solutions Using Finite Elements in Arbitrary Lagrangian-Eulerian Formulation," Doctoral Dissertation, the University of California at Los Angeles, 1994.

¹³Selvam, R. P., Visbal, M. R., and Morton, S. A., "Computation of Nonlinear Viscous Panel Flutter Using a Fully Implicit Aeroelastic Solver," *AIAA Paper*, 1998, 98-1844.

¹⁴Gordnier, R. E., and Visbal, M. R., "Development of a three-dimensional viscous aeroelastic solver for nonlinear panel flutter," *AIAA Paper*, 2000, 2000-2337.

¹⁵Dowell, E. H., "Aerodynamic of Plates and Shells," Noordhoff International Publishing, Leyden, Netherlands, 1975.

¹⁶Mei, C., Abdel-Motagaly, K., and Chen, R., "Review of Nonlinear Panel Flutter at Supersonic and Hypersonic Speeds," *Applied Mechanics Reviews*, Vol.52, No.10, 1999, pp.321-332.

¹⁷Dowell, E. H., "Nonlinear Oscillations of a Fluttering Plate II," *AIAA Journal*, Vol.5, No.10, 1967, pp.1856-1862.

¹⁸Ashley, H., and Zartarian, G., "Piston Theory – a New Aerodynamic Tool for Aeroelastician," *Journal of Aeronautical Science*, Vol.23, No., 1956, pp.1109-1118.

¹⁹Bisplinghoff, R. L., and Ashley, H., "Principles of Aeroelasticity," John Wiley and Sons, Inc., New York, 1962.

²⁰Krause, H., and Dinkler, D., "The Influence of Curvature on Supersonic Panel Flutter," *AIAA Paper*, 1998, 98-1841.

²¹Garg, V. K., "Applied Computational Fluid Dynamics," New York, USA: Marcel Dekker, Inc., 1998.

²²Thomas, P. D., and Lombard, C. K., "Geometric Conservation Law and Its Application to Flow Computations on Moving Grids," *AIAA Journal*, Vol.17, No.10, 1979, pp.1030-1037.

²³Tamura, Y., and Fujii, K., "Conservation Law for Moving and Transformed Grids," *AIAA Paper*, 1993, 93-3365-CP.

²⁴Szilard, R., "Theory and Analysis of Plates: Classical and Numerical Methods," Englewood Cliffs, N.J.: Prentice-Hall, 1973.

²⁵Beam, R., and Warming, R., "An Implicit Factored Scheme for the Compressible Navier-Stokes Equations," *AIAA Journal*, Vol.16, No.4, 1978, pp.393-402.

²⁶Puliam, T. H., and Chaussee, D. S., "A Diagonal Form of an Implicit Approximate-Factorization Algorithm," *Journal of Computational Physics*, Vol.39, No.2, 1981, pp.347-363.

²⁷Jameson, A., Schmidt, W., and Turkel, E., "Numerical Solutions of the Euler Equations by Finite Volume Methods Using Runge-Kutta Time-Stepping Schemes," *AIAA Paper*, 1981, 81-1259.

²⁸Whitfield, D. L., "Three-Dimensional Unsteady Euler Equation Solutions using a Flux Vector Splitting," *Short Course on Numerical Grid Generation at Mississippi State University*, June, 1984.

²⁹Cunningham, H. J., "Flutter Analysis of Flat Rectangular Panels Based on Three Dimensional Supersonic Potential Flow," *AIAA Journal*, Vol.1, No.8, 1963, pp.1795-1801.

CONCLUSIONS

A three-dimensional solver for the nonlinear panel flutter at supersonic flow has been developed. The solver has been verified using several approximate aerodynamic theories such as the potential flow theory and the quasi-steady supersonic theory on a simply supported square panel at the supersonic flow. The complex problems like wing flutter can be solved with the development of the current work.

Finite element method is the most commonly used approach for discretizing the nonlinear panel. The resulted nonlinear equations of equilibrium may be solved using three formulations. Two of them, the Total Lagrangian formulation and the Co-Rotational formulation, are efficient for the nonlinear panel and have been discussed in details in Chapters 1 and 2 respectively. Because only the panels with very simple geometry are considered at this time, the finite difference method rather than the finite element method for solving the governing equations of the nonlinear panel was implemented into the solver to save the computer time. The Newmark- β integration scheme was applied to solve them in time domain.

In the fluid side, the high-fidelity flow equations - Euler equations was used in this solver. The viscous effect has not been included at this time. The finite volume method is applied to discrete the fluid in space. A three-dimensional aeroelastic solver using QUICK scheme has been developed using the procedure in Chapter 4. Because of the use of sequential solver for a highly nonlinear Euler (NS) equations, the implicit sequential solver becomes overall explicit solver even after subiteration. Hence, a Beam-Warming, alternate-direction, implicit scheme solver has been developed for the elastic solver.

An explicit scheme for the interaction of the fluid and structure was used. The Newton-like subiteration was implemented to eliminate the lagging errors associated with the exchange of the pressure and deformations between the fluid and panel at their interface.

The present amplitudes of the limit cycle oscillation of a simply supported square panel are smaller than those resulted from the linear potential flow and greater than those from quasi-steady piston theory. The difference becomes smaller when the Mach number increases. The flutter frequency and the effects of the panel thickness are also discussed in this report.

Further work of this solver is underway and listed in the following:

- Solve for the nonlinear panel using the finite element method together with both formulations;
- Include the viscous effect in the solver (use NS equations);

- Solve for the panel flutter with complex conditions;
- Extended present solver for the wing flutter problems.